Reaction-diffusion systems on evolving domains with applications to the theory of biological pattern formation

Chandrasekhar Venkataraman

Thesis submitted for the degree of Doctor of Philosophy

11th May 2011

Declaration

I hereby declare that this thesis has not been and will not be submitted in whole or in part to another University for the award of any other degree.

Signature:

Dedication

To Marko.

Acknowledgments

First and foremost I am greatly indebted to my supervisors Drs. Anotida Madzvamuse and Omar Lakkis. It is their patient guidance that has made this work possible. I am grateful to Prof. Toshio Sekimura, Prof. Philip Maini and Dr. Eamonn Gaffney for working with me on the problem of parr mark pattern formation on the Amago trout. I would also like to thank the staff and students of the University of Sussex, Department of mathematics for providing a pleasurable and stimulating environment to carry out research. Special mention in this regard must go to Raquel, Lavina and Tristan.

Finally, I am grateful for the unwavering emotional support of my loving parents Marakatham and Asok, my little sister Uma and my wonderful wife Mirna.

Abstract

In this thesis we investigate a model for biological pattern formation during growth development. The pattern formation phenomenon is described by a reaction-diffusion system on a time-dependent domain.

We prove the global existence of solutions to reaction-diffusion systems on time-dependent domains. We extend global existence results for a class of reaction-diffusion systems on fixed domains to the same systems posed on spatially linear isotropically evolving domains. We demonstrate that the analysis is applicable to many systems that commonly arise in the theory of pattern formation. Our results give a mathematical justification to the widespread use of computer simulations of reaction-diffusion systems on evolving domains.

We propose a finite element method to approximate the solutions to reaction-diffusion systems on time-dependent domains. We prove optimal convergence rates for the error in the method and we derive a computable error estimator that provides an upper bound for the error in the semidiscrete (space) scheme. We have implemented the method in the C programming language and we verify our theoretical results with benchmark computations.

The method is a robust tool for the study of biological pattern formation, as it is applicable to domains with irregular geometries and nonuniform evolution. This versatility is illustrated with extensive computer simulations of reaction-diffusion systems on evolving domains. We observe varied pattern transitions induced by domain evolution, such as stripe to spot transitions, spot-splitting, spot-merging and spot-annihilation. We also illustrate the striking effects of spatially nonuniform domain evolution on the position, orientation and symmetry of patterns generated by reaction-diffusion systems. To improve the efficiency of the method, we have implemented a space-time adaptive algorithm where spatial adaptivity is driven by an error estimator and temporal adaptivity is driven by an error indicator. We illustrate with numerical simulations the dramatic improvements in accuracy and efficiency that are achieved via adaptivity.

To demonstrate the applicability and generality of our methodology, we examine the process of parr mark pattern formation during the early development of the Amago trout. By assuming the existence of chemical concentrations residing on the surface of the Amago fish which react and diffuse during surface evolution, we model the pattern formation process with reaction-diffusion systems posed on evolving surfaces. An important generalisation of our study is the experimentally driven modelling of the fish's developing body surface. Our results add weight to the feasibility of reaction-diffusion system models of fish skin patterning, by illustrating that a reaction-diffusion system posed on an evolving surface generates transient patterns consistent with those experimentally observed on the developing Amago trout. Furthermore, we conclude that the surface evolution profile, the surface geometry and the curvature are key factors which play a pivotal role in pattern formation via reaction-diffusion systems.

Contents

Declaration i

Dedication ii

Acknowledgments iii

Abstract iv

1 Introduction 1
1.1 Layout of the thesis . . . 3

2 RDSs on evolving domains 5
2.1 Introduction . . . 5
2.2 Notation . . . 5
2.3 Domain evolution . . . 6
2.4 Derivation of RDSs on time-dependent domains . . . 7
2.5 Diffusion-driven instability . . . 9
2.5.1 Necessary conditions . . . 10
2.5.2 Reaction kinetics . . . 10
2.6 Lagrangian formulation . . . 12
2.7 Conclusion . . . 13

3 Global existence of classical solutions to RDSs on evolving domains 14
3.1 Introduction . . . 14
3.2 RDSs on continuously evolving domains . . . 15
3.2.1 Lagrangian transformation . . . 15
3.3 Theoretical setting for RDSs on fixed domains . . . 17
3.3.3 Global existence on fixed domains . . . 17
3.3.7 A Lyapunov function approach to proving existence for RDSs . . . 19
3.3.9 Lyapunov stability conditions . . . 20
3.4 Global existence on evolving domains . . . 21
3.4.5 A priori estimates for systems with time-dependent reaction kinetics . . . 23
3.4.7 Global existence results for systems with time-dependent reaction kinetics 25
3.5 Applications . . . 28
3.5.1 Admissible domain evolution . . . 29
3.5.2 Admissible kinetics . . . 29
3.5.4 Examples . . . 31

3.6 Conclusion . . . 32

4 Analysis of a FEM for RDSs on evolving domains 33
4.1 Aims and Outline . . . 33
4.2 Background . . . 33
4.3 Introduction . . . 34
4.4 Problem setup . . . 35
4.4.7 Weak formulations . . . 36
4.4.8 *Cut-off* nonlinear reaction function . . . 37
4.5 Finite element method . . . 37
4.5.1 Semidiscrete approximation . . . 38
4.5.5 Fully discrete approximation . . . 44
4.6 Adaptive schemes for the approximation of RDSs . . . 50
4.6.1 A residual based a posteriori error estimate for the semidiscrete scheme . 51
4.7 Implementation . . . 56
4.8 Numerical experiments . . . 59
4.8.3 Numerical verification of the a priori convergence rate . . . 59
4.8.5 A numerical study of the residual estimator . . . 61
4.9 Conclusion . . . 63

5 Patterns on evolving domains 64
5.1 Introduction . . . 64
5.2 Patterns on time-independent domains . . . 64
5.2.1 Patterns from linear stability analysis . . . 64
5.2.2 Patterns for increasing γ . . . 65
5.3 Transient patterns on evolving domains . . . 66
5.3.1 Verification of the rescaling . . . 66
5.3.2 Stripe to spot transitions and asymmetric patterns on evolving domains . 71
5.3.3 The role of symmetry in pattern transitions . . . 77
5.4 Adaptive schemes . . . 82
5.4.1 Space adaptive scheme . . . 82
5.4.2 Space-time adaptive scheme . . . 92
5.5 Discussion . . . 100

6 A model for parr mark pattern formation during the early development of the Amago trout 102
6.1 Summary . . . 102
6.2 Introduction . . . 103
6.3 Biological observations . . . 104
6.4 Methods . . . 105
6.4.1 Fitting a growth function to the experimental data . . . 107
6.4.3 Modelling the patterned surface . . . 109
6.4.4 Model equations . . . 111
6.4.7 Selection of parameter values . . . 112
6.5 Computer simulations . . . 113
6.5.2 Planar domain . . . 113
6.5.3 Cylindrical surfaces . . . 114

6.6 Conclusion and Discussion 114

7 Summary and Discussion **119**

Bibliography **121**

A Modelling Amago surface patterning **131**
A.1 Extending the FEM to parameterisable surfaces 131
A.2 Numerical schemes for the approximation of pattern formation on the Amago . . 132

List of Figures

1.1 A developmental rule 2

2.1 Mapping from the reference to the evolving domain 8

3.1 Invariant regions 18

4.1 "Triangulation" of the evolving domain 58
4.2 Values, EOC and effectivity index of the residual estimator 62

5.1 Patterns from linear stability analysis on fixed domains 66
5.2 Patterns for increasing γ on fixed domains 66
5.3 Periodic domain evolution (evolving domain) 68
5.4 Periodic domain evolution (rescaled problem) 69
5.5 Spot-merging 70
5.6 Thomas kinetics (stripe to spot transitions) 72
5.7 Schnakenberg kinetics (nonuniform periodic domain evolution) 74
5.8 Schnakenberg kinetics (nonlinear domain evolution 1) 75
5.9 Schnakenberg kinetics (nonlinear domain evolution 2) 76
5.10 Refinements of a mesh with radial symmetry 77
5.11 Spot splitting on a disc (unstructured mesh) 78
5.12 Spot splitting on a disc (D_3 mesh) 79
5.13 Spot splitting on a disc (D_4 mesh) 80
5.14 Spot splitting on a disc (D_6 mesh) 81
5.15 Activator profiles obtained using a space adaptive algorithm on time-independent domains 84
5.16 Adaptive scheme: activator profiles obtained using a space adaptive algorithm on a domain with periodic evolution 85
5.17 Adaptive scheme (continued) 86
5.18 Adaptive scheme (continued) 87
5.19 Adaptive scheme (continued) 88
5.20 Adaptive scheme (continued) 89
5.21 Adaptive scheme (continued) 90
5.22 DOFs and change in discrete solution against time (space adaptive scheme) . . . 91
5.23 Activator profiles obtained using a space-time adaptive algorithm on a domain with periodic evolution 93
5.24 Space-time adaptive scheme (continued) 94
5.25 Space-time adaptive scheme (continued) 95
5.26 Space-time adaptive scheme (continued) 96

5.27 Space-time adaptive scheme (continued) 97
5.28 Space-time adaptive scheme (continued) 98
5.29 DOFs, change in discrete solution and timestep against time (space-time adaptive scheme) 99

6.1 Transient patterns of the developing Amago trout 106
6.2 Final patterned state of the Amago (top down view) 107
6.3 Fitting the growth function to experimental data 108
6.4 Patterned portion of the Amago 109
6.5 A planar approximation to the surface of the Amago 110
6.6 Elliptic cylinder 111
6.7 Cylindrical domains 111
6.8 Approximate activator concentration on planar domains 115
6.9 Approximate activator concentration on cylinders 116

List of Tables

3.1 Parameters from the Lyapunov stability conditions 31

4.1 Experimental order of convergence (spatially linear periodic growth) 61
4.2 Experimental order of convergence (spatially nonlinear periodic growth) 61

5.1 CPU time (spatially linear periodic evolution) 100

Chapter 1

Introduction

Explaining the *emergence of spatial pattern from homogeneity* is a fundamental question in many real world systems. In a seminal work, Turing, A. M. [1952] proposed one of the most elegant explanations for pattern formation; the concept of *diffusion-driven* or *Turing instability*. He showed that a spatially uniform steady state admitted by a system of reaction kinetics could be driven unstable solely by the addition of diffusion, thus showing a reaction-diffusion system (RDS) could account for spatial pattern formation. His idea was one of the first demonstrations of the now widely known concept that the integration of fundamentally stabilising processes can lead to an *emergent* instability.

Turing's original application was a possible explanation for *morphogenesis*: the emergence of shape in the developing embryo. The beauty of Turing's explanation lies in the simplicity and generality of his model. His explanation of morphogenesis requires no explicit recourse to genetics or complex physiology. Thus his work provides a possible underlying mechanism for pattern formation phenomena observed in developmental biology, encompassing diverse seemingly unrelated processes such as the formation of structure in the early embryo [Garfinkel et al., 2004; Miura et al., 2006], or the development of pigment patterns on the imaginal wing disc of butterflies [Sekimura et al., 2000]. Partly due to the generality and simplicity of the proposed patterning mechanism, there remain many controversies amongst the biological community over the validity of Turing pattern formation in biological systems. The foremost of which is that to date experimental studies of biological systems have failed to find definitive proof of the existence of morphogens which behave as the components of an RDS [Kondo and Miura, 2010] (although a recent study by Sick et al. [2006] provides strong evidence that the distribution of hair follicles in mice is determined by a Turing mechanism).

Despite the failure of experimental studies to validate Turing's theory of morphogenesis, Turing patterns have been identified in real world processes. The first and most well known example of a system that exhibits Turing patterns is the chloride-iodide-malonic-acid starch (CIMA) reaction [Vigil et al., 1992]. Since then, Turing patterns have been observed or proposed in many other fields such as semiconductor theory [Ammelt et al., 1997], human influenced ecological systems [Brock and Xepapadeas, 2008], population dynamics [Schmitz et al., 2007] and calcium-voltage dynamics within cardiac cells [Shiferaw and Karma, 2006].

Another widely studied application of Turing's theory is the modelling of skin patterning in vertebrates [Murray et al., 1990; Murray and Myerscough, 1991; Nagorcka and Mooney, 1992]. The importance of mathematical modelling of RDSs in this context is illustrated in a study by

Murray [1988]. He proposes the following *developmental rule*[1]: an animal can have a spotted body and striped tail but never the reverse with larger tails more likely to be spotted, as illustrated in Figure 1.1. This prediction is supported by the observed patterning on the coats of spotted big cats with larger cats having spotted bodies and spotted tails and smaller cats having spotted bodies and striped tails.

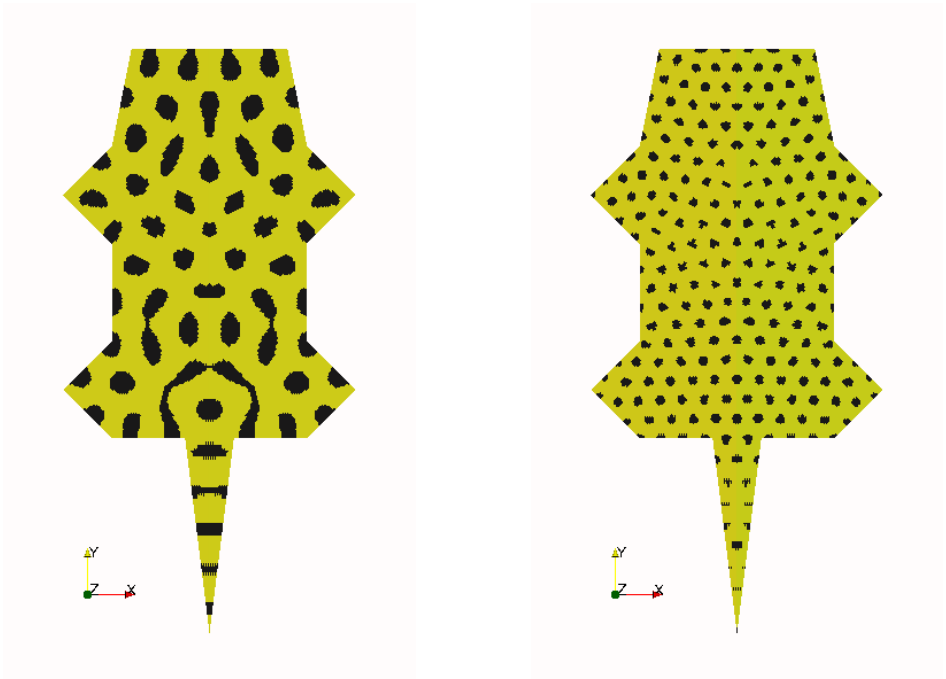

(a) Spotted body, striped tail

(b) Spotted body and tail

Figure 1.1: The developmental rule of striped tails and spotted bodies but not vice-versa. The two numerical simulations are obtained using the same RDS, with a larger scaling parameter in the right hand simulation which is proportional to the area of the domain. Similar patterning is observed in the coats of the spotted big cats, such as the small genet which has a spotted body and striped tail and the larger leopard which has a spotted body and tail.

One of the original controversies of RDSs as a model for skin pigment patterning was the sensitivity of the patterns to small changes in initial conditions. Recently mathematical models for reaction and diffusion of chemicals on continuously growing domains have been derived from first principles [Crampin, 2000] and subsequent theoretical and numerical analysis of these models has shown that *domain growth* can result in robust pattern selection independent of initial conditions [Madzvamuse and Maini, 2007]. Experimental studies have also identified the central role of domain growth in pattern formation such as the regular insertion of stripes that preserve an intrinsic wavelength (distance between stripes) on the skin of the marine angelfish [Kondo and Asai, 1995]. Advances in numerical simulation and experimental biology have meant that computational simulations of RDSs are now being used to design experiments to test the hypoth-

[1]A prediction made using mathematical theory and computational simulations that can be used to test the validity of RDSs as a model for skin patterning in vertebrates.

esis that RDSs account for pattern formation. Examples include the study of stripe formation in the zebrafish [Yamaguchi et al., 2007] and experimental manipulations to cut-out portions of the wings of butterflies to investigate the effects of geometry on patterning [Madzvamuse et al., 2002a]. Typically the reaction kinetics used to model biological pattern formation are nonlinear and do not admit closed form solutions. Therefore it is clear that numerical simulations of RDSs on continuously growing domains will play an important role in the future study of biological pattern formation.

Despite the widespread use of computer simulations of RDSs on fixed and growing domains as both a model for biological pattern formation and as a predictive tool for the design of experiments seeking to validate Turing's hypothesis, fundamental mathematical questions regarding these highly complex models remain. There has thus far been very little work on both the existence and uniqueness of solutions to RDSs on evolving domains and the numerical analysis of computational methods to approximate the solutions to these problems. In this work we attempt to answer some of these questions. We seek to justify the use of computer simulations to model biological pattern formation by examining the stability of RDSs on evolving domains. We then propose and *analyse* a method to approximate the solution to RDSs on evolving domains. To illustrate the versatility of our methodology, we conduct a novel study of an experimentally observed skin pigmentation process. Specifically: We examine the existence and uniqueness of solutions to the continuous problem, an RDS posed on a continuously evolving domain, deriving to our best knowledge the first results in this direction that hold independently of the growth rate. We derive a finite element method to approximate solutions to semilinear RDSs, applicable to problems posed on irregular complex evolving domains. We analyse the method proving optimal convergence rates for the error and deriving a computable error estimator to drive adaptivity. We conduct extensive computer simulations of RDSs posed on evolving domains, in which we observe the significance of changes in domain evolution and domain shape in the pattern formation process. Finally, we illustrate the applications of our results by conducting a study of biological pattern formation on the skin surface of a particular species of fish. A key novelty of our study is the experimentally driven realistic modelling of the biological growth phenomena (from an observational viewpoint).

1.1 Layout of the thesis

The remainder of this work is set out as follows; In Chapter 2 we set the scene for our study, introducing the notation we use in this work and primarily recapping known results. To facilitate our investigation of RDSs on evolving domains, we formally introduce the admissible forms of domain evolution that we consider in this work and then derive the model equations for RDSs on evolving domains. We introduce the concept of diffusion-driven instability (on fixed domains) and present some model reaction kinetics we use to illustrate our theoretical results. We conclude the Chapter by deriving a Lagrangian formulation for an RDS posed on a continuously evolving domain.

In Chapter 3, we present global existence results for solutions of RDSs on evolving domains. We extend global existence results for a class of RDSs on time-independent domains to the same systems posed on domains with spatially linear isotropic evolution. Our results are novel in that they hold without any assumptions on the sign of the growth rate and are thus valid on growing domains, contracting domains or domains that exhibit periods of growth and contraction. The key analytical tools we make use of are a Lyapunov function approach originally introduced by

Morgan [1989] and the invariant region approach of Chueh et al. [1977].

In Chapter 4, we introduce the numerical method with which we seek to approximate the solution to RDSs posed on continuously evolving domains. Our method takes the form of a finite element method in space and a modified backward Euler method in time. We conduct an a priori analysis of the method, proving optimal convergence rates for the error in the $L_2\big([0,T];L_\infty(\Omega)\big)$ norm (where we have exploited the notation introduced in Chapter 2). We derive an a posteriori error estimator in the semidiscrete (space-discrete) case which can be used to drive spatial adaptivity. We illustrate a concrete implementation of the method for some reaction kinetics commonly encountered in developmental biology. We conclude the Chapter by performing some numerical experiments to verify the a priori and the a posteriori estimates.

Chapter 5 contains the results of a series of computer experiments to approximate the solution of RDSs on fixed and evolving domains. We first conduct experiments to provide further verification of our results, by checking the method approximates well spatially nonuniform patterns in cases when linear stability provides a good approximation to the nonuniform steady state. We then verify the Lagrangian transformation by comparing solutions of an RDS on a continuously evolving domain with solutions of the corresponding RDS constructed using the Lagrangian transformation of Chapter 2. We illustrate that under the ad hoc quasistatic approach to modelling domain growth where a scaling pattern is varied; important facets of the pattern formation process such as orientation are lost. By considering different forms of domain evolution, we illustrate both the versatility of the numerical method and the variety of pattern transitions induced by domain evolution, such as stripe to spot transitions, spot-splitting, spot-merging and spot-annihilation. We also observe the striking effects of nonuniform domain evolution on the position orientation and symmetry of patterns generated by RDSs. We conclude the Chapter by presenting results of an adaptive scheme, firstly only with spatial adaptivity driven by the estimator derived in Chapter 4 and then with space-time adaptivity driven by the same estimator and an error indicator for the temporal error. Our results illustrate both the improvements in accuracy and the dramatic increases in efficiency that arise due to the incorporation of adaptivity.

Chapter 6 contains an important application of our work. We investigate the process of parr mark formation on the Amago trout. The Amago is a species of fish native to Japan that is notable for the beautiful patterning it displays. In collaboration with an experimentalist, we mathematically model the observed pattern formation process with RDSs posed on continuously growing surfaces (in Appendix A.1 we extend the numerical method presented in Chapter 4 to the approximation of RDSs posed on surfaces). An important facet of our investigation is the realistic approximation of geometry and growth, both of which are important from the theoretical viewpoint and play important roles in experimentally observed pattern formation processes. Our results illustrate that an RDS is a feasible model for the pattern formation process. We finish the Chapter by discussing the wider implications of our results to the feasibility of RDSs as general models for spatial pattern formation in developmental biology, suggesting future theoretical and experimental research directions.

Finally, in Chapter 7, we briefly summarise our work and make some conclusions. We also indicate possible directions for future research.

Chapter 2

RDSs on evolving domains

2.1 Introduction

In this Chapter we introduce the problems we shall consider in this work which take the form of semilinear RDSs posed on time-dependent domains. To this end, we first define the admissible forms of domain evolution we consider in this study and then derive from first principles model equations for reacting and diffusing chemicals on time-dependent domains. We introduce the concept of diffusion-driven instability by considering RDSs on time-independent domains and present some example reaction kinetics that exhibit diffusion-driven instability. We conclude this Chapter by deriving a Lagrangian transformation of our model problem which plays a central role in the theoretical analysis carried out in the sequel.

The majority of the results contained in this chapter are already known (see for example [Crampin, 2000] or [Madzvamuse, 2000]) and we state them to aid the completeness of the discussion. We also use this Chapter to introduce the majority of our notation.

2.2 Notation

We now introduce some of the notation we shall use in this study. Given an open and bounded domain $\Pi \subset \mathbb{R}^d$ and a function $\boldsymbol{\eta} \in C^1(\Pi; \mathbb{R}^m)$, we define the Jacobian matrix of $\boldsymbol{\eta}$

$$\mathrm{D}\boldsymbol{\eta}(\boldsymbol{x}) := \begin{bmatrix} \partial_{x_1}\eta_1(\boldsymbol{x}) & \dots & \partial_{x_1}\eta_m(\boldsymbol{x}) \\ \vdots & \ddots & \vdots \\ \partial_{x_d}\eta_1(\boldsymbol{x}) & \dots & \partial_{x_d}\eta_m(\boldsymbol{x}) \end{bmatrix}, \text{ for } \boldsymbol{x} \in \Pi, \tag{2.2.1}$$

and the divergence of $\boldsymbol{\eta}$

$$\nabla \cdot \boldsymbol{\eta}(\boldsymbol{x}) := \sum_{i=1}^{d} \partial_{x_i}\eta_i(\boldsymbol{x}). \tag{2.2.2}$$

For the case of a scalar-valued function $\eta \in C^1(\Pi; \mathbb{R})$, we define the gradient of η

$$\nabla\eta(\boldsymbol{x}) := \mathrm{D}_{\boldsymbol{x}}\,\eta(\boldsymbol{x}), \tag{2.2.3}$$

and the Laplacian of η

$$\Delta\eta(\boldsymbol{x}) := \sum_{i=1}^{d} \partial_{x_i x_i}\eta(\boldsymbol{x}). \tag{2.2.4}$$

In an effort to compress notation for spatial derivatives, we introduce the convention used above, that if the variable with respect to which we differentiate is omitted, it should be understood as the spatial argument of the function.

We denote by $L_p(\Pi)$, $W^{p,k}(\Pi)$ and $H^k(\Pi)$ the Lebesgue, Sobolev and Hilbert spaces respectively, defined by the following: for measurable η and for $p, k \in [1, \infty)$

$$L_p(\Pi) := \left\{ \eta : \int_\Pi |\eta|^p < \infty \right\}, \tag{2.2.5}$$

$$L_\infty(\Pi) := \left\{ \eta : \sup_{\boldsymbol{x}\in\Pi} \left|\eta(\boldsymbol{x})\right| < \infty \right\}, \tag{2.2.6}$$

$$W^{p,k}(\Pi) := \left\{ \eta \in L_p(\Pi) : \sum_{\alpha\leq k} \mathrm{D}^\alpha \eta \in L_p(\Pi) \right\}, \tag{2.2.7}$$

$$H^k(\Pi) := W^{2,k}(\Pi). \tag{2.2.8}$$

For measurable functions $\eta, \mu : \Pi \to \mathbb{R}$, we introduce the following notation

$$\langle \eta, \mu \rangle_\Pi := \int_\Pi \eta(\boldsymbol{x})\mu(\boldsymbol{x}) \,\mathrm{d}x, \tag{2.2.9}$$

$$\|\eta\|_{L_2(\Pi)} := \langle \eta, \eta \rangle_\Pi^{1/2}, \tag{2.2.10}$$

$$|\eta|_{H^k(\Pi)} := \left\| \mathrm{D}^k \eta \right\|_{L_2(\Pi)}, \text{ for } k \in \mathbb{Z}_+, \tag{2.2.11}$$

$$\|\eta\|_{H^k(\Pi)} := \left(\|\eta\|^2_{L_2(\Pi)} + \sum_{j=1}^{k} |\eta|^2_{H^j(\Pi)} \right)^{1/2}. \tag{2.2.12}$$

For vector valued functions $\boldsymbol{\eta}, \boldsymbol{\mu} : \Pi \to \mathbb{R}^m$, we denote

$$\langle \boldsymbol{\eta}, \boldsymbol{\mu} \rangle_{\Pi^m} := \sum_{i=1}^{m} \int_\Pi \eta_i(\boldsymbol{x})\mu_i(\boldsymbol{x}) \,\mathrm{d}x, \tag{2.2.13}$$

with the corresponding modifications to the norms and seminorms.

2.3 Domain evolution

We wish to model RDSs posed on continuously evolving domains and we now introduce the forms of domain evolution we consider in this study. Let Ω_t be a continuously evolving time-dependent volume, and let $\hat{\Omega}$ be a simply connected time-independent reference domain with Lipschitz boundary. Throughout this study we assume domain evolution is known and that there exists a "smooth"[1] one to one mapping between the reference and evolving domains as depicted

[1] We shall formalise this assumption in the sequel.

in Figure 2.1. Formally we assume there exists $\boldsymbol{\mathcal{A}} : \hat{\Omega} \times [0,T] \to \Omega_t$ such that at each instant $t \in [0,T]$ and for each $\boldsymbol{x} \in \Omega_t$ there exists a $\boldsymbol{\xi} \in \hat{\Omega}$ such that

$$\boldsymbol{\mathcal{A}}(\boldsymbol{\xi}, t) = \boldsymbol{x}. \tag{2.3.1}$$

The Jacobian of the mapping $\boldsymbol{J}$ and its determinant J are given by

$$\boldsymbol{J}(\boldsymbol{\xi}, t) = \mathrm{D}\boldsymbol{\mathcal{A}}(\boldsymbol{\xi}, t) \quad \text{and} \quad J(\boldsymbol{\xi}, t) = \det\left(\boldsymbol{J}(\boldsymbol{\xi}, t)\right), \tag{2.3.2}$$

with $\boldsymbol{K}$ denoting the Jacobian of the inverse mapping

$$\boldsymbol{K}(\boldsymbol{\xi}, t) = \mathrm{D}\boldsymbol{\mathcal{A}}^{-1}(\boldsymbol{\mathcal{A}}(\boldsymbol{\xi}, t)). \tag{2.3.3}$$

We denote by $\boldsymbol{a}$ the time derivative of the mapping

$$\boldsymbol{a}\left(\boldsymbol{\mathcal{A}}(\boldsymbol{\xi}, t), t\right) = \partial_t \boldsymbol{\mathcal{A}}(\boldsymbol{\xi}, t). \tag{2.3.4}$$

From classical results [Acheson, 1990] we have the following expression for the time derivative of the determinant of the Jacobian

$$\partial_t J\left(\boldsymbol{\xi}, t\right) = J\left(\boldsymbol{\xi}, t\right) \nabla \cdot \boldsymbol{a}\left(\boldsymbol{\mathcal{A}}(\boldsymbol{\xi}, t), t\right). \tag{2.3.5}$$

We now introduce notation to relate functions defined on the evolving domain to functions defined on the reference domain. Given a function $g : (\Omega_t, [0,T]) \to \mathbb{R}$ we consistently denote by $\hat{g} : \hat{\Omega} \times [0,T] \to \mathbb{R}$ its counterpart on the reference domain, defined by the following relationship

$$\hat{g}(\boldsymbol{\xi}, t) := g\left(\boldsymbol{\mathcal{A}}(\boldsymbol{\xi}, t), t\right) \qquad \text{for } t \in [0,T] \text{ and } \boldsymbol{\xi} \in \hat{\Omega}. \tag{2.3.6}$$

Assuming sufficient smoothness on the function g, using (2.3.6) we have the following result that relates the time-differentiation on the reference frame to the evolving domain:

$$\partial_t \hat{g}(\boldsymbol{\xi}, t) = \partial_t g\left(\boldsymbol{\mathcal{A}}(\boldsymbol{\xi}, t), t\right) + \left[\boldsymbol{a} \cdot \nabla g\right]\left(\boldsymbol{\mathcal{A}}(\boldsymbol{\xi}, t), t\right). \tag{2.3.7}$$

The right hand side of (2.3.7) is commonly known as the material derivative of g. The following result relates the norm of a function $g : (\Omega_t, [0,T]) \to \mathbb{R}$ on the evolving domain with its counterpart on the reference domain:

$$\|g\|^2_{L_2(\Omega_t)} = \langle J\hat{g}, \hat{g} \rangle_{\hat{\Omega}}. \tag{2.3.8}$$

For the gradient of a function of a sufficiently smooth function $g : (\Omega_t, [0,T]) \to \mathbb{R}$, we have

$$\|\nabla g\|^2_{L_2(\Omega_t)} = \langle J\boldsymbol{K}\nabla\hat{g}, \boldsymbol{K}\nabla\hat{g} \rangle_{\hat{\Omega}}. \tag{2.3.9}$$

2.4 Derivation of RDSs on time-dependent domains

Following Crampin et al. [1999], we now derive the model equation for an RDS posed on a continuously deforming domain. Our model takes the form of a system of chemicals that are coupled only through the reaction terms and diffuse independently of each other. Let $\boldsymbol{u}\left(\boldsymbol{x}, t\right)$ be an $(m \times 1)$ vector of concentrations of chemical species, with $\boldsymbol{x} \in \Omega_t \subset \mathbb{R}^d$, $d < \infty$, the spatial

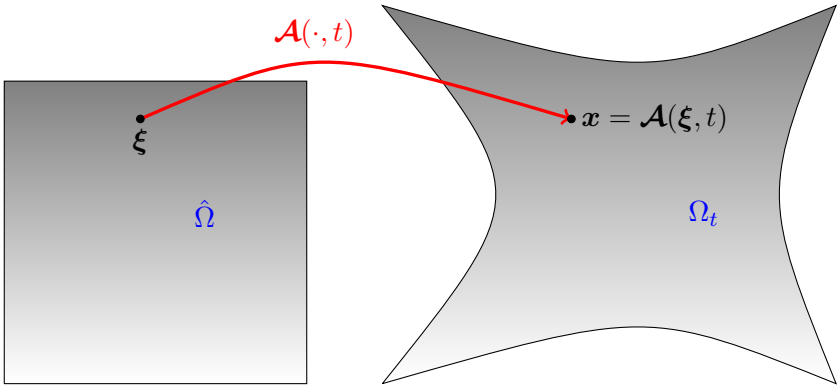

Figure 2.1: The mapping $\mathcal{A}$ from the reference to the evolving domain.

variable and $t \in [0,T]$, $T>0$, the time variable. We assume Ω_t is a simply connected, bounded and continuously deforming domain with respect to t. By the law of conservation of mass, the change of mass in Ω_t is equal to the net flux of mass on the boundary of Ω_t plus the net production of mass within Ω_t i.e., for $i=1,\dots,m$,

$$\frac{\mathrm{d}}{\mathrm{d}t}\int_{\Omega_t} u_i\left(\boldsymbol{x},t\right) = -\int_{\partial\Omega_t}\left[\boldsymbol{q}_i\cdot\boldsymbol{\nu}\right]\left(\boldsymbol{x},t\right) + \int_{\Omega_t} f_i\left(\boldsymbol{u}\left(\boldsymbol{x},t\right)\right), \tag{2.4.1}$$

where $\boldsymbol{q}_i$ is the flux of u_i, $\boldsymbol{\nu}$ is the normal to Ω_t and f_i is the source of u_i in Ω_t. Dealing firstly with the term on the left of (2.4.1), we note that since Ω_t is time-dependent, the time derivative and the spatial integral do not commute. Using the notation of §2.3, we express the time derivative on the reference domain:

$$\begin{aligned}\frac{\mathrm{d}}{\mathrm{d}t}\int_{\Omega_t} u_i &= \frac{\mathrm{d}}{\mathrm{d}t}\int_{\hat{\Omega}} J\hat{u}_i \\ &= \int_{\hat{\Omega}} \hat{u}_i\partial_t J + J\partial_t\hat{u}_i.\end{aligned} \tag{2.4.2}$$

Combining (2.3.5), (2.3.7) and (2.4.2) gives

$$\begin{aligned}\frac{\mathrm{d}}{\mathrm{d}t}\int_{\Omega_t} u_i &= \int_{\hat{\Omega}} J\left(\partial_t\hat{u}_i\left(\boldsymbol{\xi},t\right) + \hat{u}_i\left(\boldsymbol{\xi},t\right)\nabla\cdot\boldsymbol{a}\left(\mathcal{A}(\boldsymbol{\xi},t),t\right)\right) \\ &= \int_{\Omega_t} \partial_t u_i + \boldsymbol{a}\cdot\nabla u_i + u_i\nabla\cdot\boldsymbol{a} \\ &= \int_{\Omega_t} \partial_t u_i + \nabla\cdot\left(\boldsymbol{a}u_i\right).\end{aligned} \tag{2.4.3}$$

2.4.1 Remark (Reynold's transport theorem)**.** Expression (2.4.3) follows from Reynold's transport theorem [Acheson, 1990], which we now state. For a function $g \in C^1(\Omega_t,[0,T])$

$$\frac{\mathrm{d}}{\mathrm{d}t}\int_{\Omega_t} g = \int_{\Omega_t}\partial_t g + \nabla\cdot\left(\boldsymbol{a}g\right). \tag{2.4.4}$$

We derive (2.4.3) explicitly as the intermediate steps where we obtain an expression for the time derivative term on the reference frame will prove useful in the derivation of a finite element scheme in Chapter 4.

To deal with the flux terms, assuming u_i is continuous and applying the divergence theorem gives

$$\int_{\partial\Omega_t} [\boldsymbol{q}_i \cdot \boldsymbol{\nu}] (\boldsymbol{x}, t) = \int_{\Omega_t} \nabla \cdot \boldsymbol{q}_i (\boldsymbol{x}, t) . \tag{2.4.5}$$

We further assume the species diffuse independently according to Fick's law, thus $\boldsymbol{q}_i = -D_i \nabla u$, where $D_i > 0$ is the diffusion coefficient for u_i. We thus have

$$\partial_t u_i(\boldsymbol{x}, t) - D_i \Delta u_i(\boldsymbol{x}, t) + \nabla \cdot [\boldsymbol{a} u_i] (\boldsymbol{x}, t) = f_i \left(\boldsymbol{u}(\boldsymbol{x}, t)\right), \boldsymbol{x} \in \Omega_t, t \in (0, T]. \tag{2.4.6}$$

We are primarily interested in patterns that arise as a result of self-organisation prompting the consideration of homogenous Neumann (also known as zero-flux) boundary conditions. It should be possible to extend the theoretical results we present in subsequent Chapters to encompass more general boundary conditions and we leave this for future work. To maintain physical validity, we take the initial condition for each u_i to be bounded and nonnegative. Our model problem thus takes the following form:

2.4.2 Problem (RDS on a time-dependent domain)**.** Find u_i such that for $i = 1, \ldots, m$, u_i satisfies

$$\begin{cases} \partial_t u_i(\boldsymbol{x}, t) - D_i \Delta u_i(\boldsymbol{x}, t) + \nabla \cdot [\boldsymbol{a} u_i] (\boldsymbol{x}, t) = f_i \left(\boldsymbol{u}(\boldsymbol{x}, t)\right), & \boldsymbol{x} \in \Omega_t, t \in (0, T], \\ [\boldsymbol{\nu} \cdot \nabla u_i](\boldsymbol{x}, t) = 0, & \boldsymbol{x} \in \partial\Omega_t, t > 0, \\ u_i(\boldsymbol{x}, 0) = u_i^0(\boldsymbol{x}), & \boldsymbol{x} \in \Omega_0. \end{cases} \tag{2.4.7}$$

The system is generally nondimensionalised by introducing a length scale L and performing an appropriate rescaling of space and time such that for some $i \in [1, \ldots, m]$ $D_i = 1$ (note the nondimensionalisation of the reactions depends on the kinetics; see the book by Murray [2003] for details).

2.4.3 Remark (Chemotaxis)**.** Our primary focus is applications to pattern formation phenomena in developmental biology. The RDS setup we have assumed is just one possible model for the evolution of chemical concentrations in biological systems. Another important model is the chemotaxis model [Keller and Segel, 1971]. In this setup, cells respond to a chemical in the environment, moving towards higher or lower concentrations of the chemical which is termed a chemo-attractant or chemo-repellent respectively. The models consist of coupled nonlinear reaction-diffusion-advection systems. The addition of chemotaxis generally introduces a nonlinear diffusive term and the extension of our studies to this more general case is an important area for future work.

2.5 Diffusion-driven instability

For the applications we have in mind, we are interested in RDSs as a model for spatial pattern formation. The specific mechanism we shall investigate is *diffusion-driven* or Turing instability [Turing, A. M., 1952]. This is the process whereby a system of the form (2.4.7) admits a homogenous steady state in the absence of diffusion that is driven unstable by the presence of distinct diffusion rates. The theory of diffusion-driven instability on fixed domains is well known and we shall only briefly sketch the details. We refer to the book by Murray [2003, Ch. 2.3 pg. 82] for an in depth discussion. The extension of the relatively well developed mathematical theory for

fixed domains to evolving domains is an important area for future research. The conditions for diffusion-driven instability (on fixed domains) can be readily obtained by linear stability analysis around the steady state. We now state the necessary conditions for diffusion-driven instability for a 2-species RDS posed on a time-independent domain. Although more complex, there are theoretical studies of diffusion-driven instability in multi-species systems [Satnoianu et al., 2000].

2.5.1 Necessary conditions

Firstly we require that the system admits a *linearly stable* steady state $\boldsymbol{u}^* := (u_1^*, u_2^*)$. We denote by $\boldsymbol{J_{f^*}}$, the Jacobian matrix of the reaction function $\boldsymbol{f}$ evaluated at the steady state:

$$\boldsymbol{J_{f^*}} := \left[\begin{array}{cc} \partial_{u_1} f_1 & \partial_{u_2} f_1 \\ \partial_{u_1} f_2 & \partial_{u_2} f_2 \end{array} \right]_{\boldsymbol{u}=\boldsymbol{u}^*}. \tag{2.5.1}$$

The steady state is linearly stable if

$$\mathrm{tr}(\boldsymbol{J_{f^*}}) < 0 \text{ and } \det(\boldsymbol{J_{f^*}}) > 0. \tag{2.5.2}$$

By conducting a linear stability analysis of the full RDS and solving the resulting eigenvalue problem, it can be shown that the steady state $\boldsymbol{u}^*$ is linearly unstable if and only if

$$(d\partial_{u_1} f_1 + \partial_{u_2} f_2)|_{\boldsymbol{u}=\boldsymbol{u}^*} > 0, \tag{2.5.3}$$

$$(d\partial_{u_1} f_1 + \partial_{u_2} f_2)^2|_{\boldsymbol{u}=\boldsymbol{u}^*} > 4d \det(\boldsymbol{J_{f^*}}), \tag{2.5.4}$$

where $d = \frac{D_2}{D_1}$. Thus necessary conditions for a system to exhibit diffusion-driven instability are (2.5.2), (2.5.3) and (2.5.4). The conditions outlined above are necessary but not sufficient for diffusion-driven instability to occur. If all the necessary conditions hold then, for *wavenumbers* k in some interval $[k_1, k_2]$ (the size of which depends on the diffusion coefficients and the reaction kinetics), perturbations of the following form will grow:

$$\boldsymbol{u} - \boldsymbol{u}^* = \boldsymbol{c}_k e^{\lambda(k)t} \psi_k, \tag{2.5.5}$$

where for each k, $\boldsymbol{c}_k$ is the vector of Fourier coefficients and ψ_k is the eigenfunction of the Laplacian on the domain. On finite domains the spectrum of admissible wavenumbers is discrete and thus if there are no admissible wavenumbers in the interval $[k_1, k_2]$ diffusion-driven instability will not occur despite the necessary conditions being fulfilled.

2.5.2 Reaction kinetics

In the 2-species case after a suitable re-ordering of the species, the reaction kinetics for which diffusion-driven instability is possible on fixed domains can be classified into two different forms. The two forms are determined by the signs of the components of the jacobian matrix evaluated at the steady state:

- *Activator-inhibitor*: These have jacobian matrices of the following form

$$\boldsymbol{J_f^*} = \left[\begin{array}{cc} + & - \\ + & - \end{array} \right]. \tag{2.5.6}$$

  In this case one species (u_1) plays the role of activator or growth promoter for both species. The other species (u_2) acts as an inhibitor for both species. Due to the pure activatory (inhibitory) behaviour of the species, these kinetics are sometimes referred to as *pure* kinetics.

- *Activator-substrate*: These systems have jacobian matrices of the following form

$$\boldsymbol{J_f^*} = \begin{bmatrix} + & + \\ - & - \end{bmatrix}. \tag{2.5.7}$$

  In this case the activator (u_1) self-activates and inhibits the production of the other species. The inhibitor (u_2) self-inhibits and activates production of the other species. Due to the mix of activatory and inhibitory behaviour of both species, these kinetics are sometimes referred to as *cross* kinetics.

To illustrate the theoretical results in the sequel, we shall focus on two reaction kinetics models.

- Schnakenberg reaction kinetics: We consider the Schnakenberg or *activator-depleted* substrate model [Gierer and Meinhardt, 1972; Lefever and Prigogine, 1968; Schnakenberg, 1979], arising from a series of hypothetical trimolecular autocatalytic reactions, also known as the Brusselator model:

$$\begin{cases} f_1(u_1, u_2) &= \gamma\left(a - u_1 + u_1^2 u_2\right), \\ f_2(u_1, u_2) &= \gamma\left(b - u_1^2 u_2\right), \end{cases} \tag{2.5.8}$$

  where $0 < a, b, \gamma < \infty$. The homogenous steady state is given by $\left(a + b, \frac{b}{(a+b)^2}\right)$.

- Thomas reaction kinetics: The following model, proposed and studied experimentally by Thomas [1975], is based on a specific reaction involving the substrates oxygen and uric acid which react in the presence of the enzyme uricase:

$$\begin{cases} f_1(u_1, u_2) &= \gamma\left(a - u_1 - g(u_1, u_2)\right), \\ f_2(u_1, u_2) &= \gamma\left(b - \alpha u_2 - g(u_1, u_2)\right), \end{cases} \tag{2.5.9}$$

  where

$$g(u_1, u_2) = \frac{\kappa u_1 u_2}{1 + u_1 + \beta u_1^2}, \tag{2.5.10}$$

  and $0 < \gamma, a, \alpha, b, \kappa, \beta < \infty$.

The above models are in nondimensionalised form, details of the physical models together with nondimensionalisation can be found in the book by Murray [2003]. The theoretical results we derive in the remainder of this work are applicable to most of the reaction kinetics used in the study of biological pattern formation. Other reaction kinetics which fit into the framework of our studies are the Gierer-Meinhardt reaction kinetics introduced by Gierer and Meinhardt [1972] and the BVAM model [Barrio et al., 2009].

The parameter γ is a scaling parameter, originally introduced by Arcuri and Murray [1986], that is proportional to the area of the domain in 2 dimensions. Many earlier studies of pattern formation on evolving domains essentially examined the change in the spatially homogenous steady state for increasing values of γ or took a time-dependent value of γ (in an ad hoc fashion).

A necessary requirement for diffusion-driven instability to occur is that the activator diffuses slower than the inhibitor. Thus the influence of the activator is effectively more local than that of the inhibitor, which has led to the mechanism behind Turing pattern formation being dubbed *short range activation and long range inhibition* or *local activation, lateral inhibition* [Gierer and Meinhardt, 1972].

2.5.3 Remark (Diffusion-driven instability on evolving domains)**.** The effect of domain evolution on the parameter space in which diffusion-driven instability is possible is much more complex and still not fully understood. The discussion above is no longer valid since the eigenvalue theory used to establish the necessary conditions for diffusion-driven instability fails for non-autonomous systems. In a study of RDSs on growing domains, Madzvamuse et al. [2010] show that RDSs with kinetics that are not of activator-substrate or activator-inhibitor type may still exhibit diffusion-driven instability on evolving domains.

2.6 Lagrangian formulation

For the analysis we shall conduct in the sequel, it is easier to work with problems posed on a time-independent domain. We now derive a formulation of (2.4.7) on the reference frame.

2.6.1 Proposition (Reference domain formulation)**.** *Let the mapping $\boldsymbol{\mathcal{A}}$ be sufficiently smooth and suppose $\boldsymbol{u}(\boldsymbol{x},t)$ satisfies (2.4.7). Then, for $i=1,\ldots,m$, $\hat{u}_i(\boldsymbol{\xi},t)$ (cf. (2.3.6)) satisfies the following semilinear reaction-diffusion-convection system posed on the reference domain:*

$$\begin{aligned}
&\partial_t \hat{u}_i\left(\boldsymbol{\xi},t\right)+\hat{u}_i\left(\boldsymbol{\xi},t\right)\nabla\cdot\boldsymbol{a}\left(\boldsymbol{\mathcal{A}}(\boldsymbol{\xi},t),t\right)\\
&\quad=f_i\left(\hat{\boldsymbol{u}}\left(\boldsymbol{\xi},t\right)\right)+D_i\left[\mathrm{D}\boldsymbol{\mathcal{A}}^{-1}:\mathrm{D}\boldsymbol{\mathcal{A}}^{-1}\right]\left(\boldsymbol{\mathcal{A}}\left(\boldsymbol{\xi},t\right)\right)\Delta\hat{u}_i\left(\boldsymbol{\xi},t\right)\\
&\qquad+D_i\left(\left[\Delta\mathcal{A}_1^{-1},\ldots,\Delta\mathcal{A}_d^{-1}\right]\left(\boldsymbol{\mathcal{A}}\left(\boldsymbol{\xi},t\right)\right)\right)\nabla\hat{u}_i\left(\boldsymbol{\xi},t\right)\quad \boldsymbol{\xi}\in\hat{\Omega},t\in(0,T].
\end{aligned}\tag{2.6.1}$$

Furthermore, we note that $\boldsymbol{\mathcal{A}}^{-1}$ and by (2.3.4) $\boldsymbol{a}$ are known.

Proof . Let $\boldsymbol{u}(\boldsymbol{x},t)$ satisfy (2.4.7) and let $\hat{\boldsymbol{u}}\left(\boldsymbol{\mathcal{A}}^{-1}\left(\boldsymbol{x}\right),t\right)$ be the corresponding function on the reference frame (cf. (2.3.6)). From (2.4.7) we obtain for $i=1,\ldots,m$,

$$\begin{aligned}
&\partial_t\hat{u}_i\left(\boldsymbol{\mathcal{A}}^{-1}\left(\boldsymbol{x}\right),t\right)+\hat{u}_i\left(\boldsymbol{\mathcal{A}}^{-1}\left(\boldsymbol{x}\right),t\right)\nabla\cdot\boldsymbol{a}\left(\boldsymbol{x},t\right)\\
&\qquad=f_i\left(\hat{\boldsymbol{u}}\left(\boldsymbol{\mathcal{A}}^{-1}\left(\boldsymbol{x}\right),t\right)\right)+D_i\Delta_{\boldsymbol{x}}\hat{u}_i\left(\boldsymbol{\mathcal{A}}^{-1}\left(\boldsymbol{x}\right),t\right)\ \boldsymbol{x}\in\Omega_t,t\in(0,T],
\end{aligned}\tag{2.6.2}$$

where we have used (2.3.7). Using the chain rule, we express the Laplacian with respect to $\boldsymbol{x}$ as a spatial operator with respect to $\boldsymbol{\mathcal{A}}^{-1}(\boldsymbol{x})$:

$$\begin{aligned}
\Delta_{\boldsymbol{x}}\hat{u}_i\left(\boldsymbol{\mathcal{A}}^{-1}\left(\boldsymbol{x}\right),t\right)=&\nabla_{\boldsymbol{x}}\cdot\left(\mathrm{D}\boldsymbol{\mathcal{A}}^{-1}\left(\boldsymbol{x}\right)\nabla\hat{u}_i\left(\boldsymbol{\mathcal{A}}^{-1}\left(\boldsymbol{x}\right),t\right)\right)\\
=&\,\mathrm{D}\boldsymbol{\mathcal{A}}^{-1}\left(\boldsymbol{x}\right)\nabla_{\boldsymbol{x}}\cdot\left(\nabla\hat{u}_i\left(\boldsymbol{\mathcal{A}}^{-1}\left(\boldsymbol{x}\right),t\right)\right)\\
&+\nabla_{\boldsymbol{x}}\cdot\left(\mathrm{D}\boldsymbol{\mathcal{A}}^{-1}\left(\boldsymbol{x}\right)\right)\nabla\hat{u}_i\left(\boldsymbol{\mathcal{A}}^{-1}\left(\boldsymbol{x}\right),t\right)\\
=&\left[\mathrm{D}\boldsymbol{\mathcal{A}}^{-1}:\mathrm{D}\boldsymbol{\mathcal{A}}^{-1}\right]\left(\boldsymbol{x}\right)\Delta\hat{u}_i\left(\boldsymbol{\mathcal{A}}^{-1}\left(\boldsymbol{x}\right),t\right)\\
&+\left(\Delta\mathcal{A}_1^{-1}\left(\boldsymbol{x}\right),\ldots,\Delta\mathcal{A}_d^{-1}\left(\boldsymbol{x}\right)\right)\nabla\hat{u}_i\left(\boldsymbol{\mathcal{A}}^{-1}\left(\boldsymbol{x}\right),t\right),
\end{aligned}\tag{2.6.3}$$

combining (2.6.2) and (2.6.3) and writing $\boldsymbol{x}$ as $\boldsymbol{\mathcal{A}}(\boldsymbol{\xi},t)$ completes the proof. □

2.7 Conclusion

In this Chapter we have primarily summarised known results. Our main focus in this Chapter was the derivation of the model equations we shall study in the remainder of this work which take the form of an RDS posed on a continuously evolving domain. Since the original derivation from first principles of RDSs on continuously evolving domains [Crampin et al., 1999], many studies have used this framework to study biological pattern formation during growth development. However, fundamental mathematical questions such as the existence and uniqueness of solutions to these models remain unanswered. In light of this, in the next Chapter we study the existence and regularity of solutions to RDSs posed on a class of evolving domains.

Chapter 3

Global existence of classical solutions to RDSs on evolving domains

3.1 Introduction

The importance of RDSs as a framework for the modelling of pattern formation in chemistry and biology has been evident since the work of Turing, A. M. [1952]. Recent advances in mathematical modelling and developmental biology identify the important role of *domain evolution* as central in the formation of patterns, both empirically [Kondo and Asai, 1995] and computationally [Comanici and Golubitsky, 2008; Crampin et al., 1999; Madzvamuse and Maini, 2007]. In this respect, many numerical studies of RDSs on evolving domains are available, such as Madzvamuse [2006] and Barrass et al. [2006]. Yet, fundamental mathematical questions such as existence and regularity of solutions of RDSs on evolving domains remain important open problems [Kelkel and Surulescu, 2009].

Numerous studies on the stability of solutions of RDSs on fixed domains are available, for example Rothe [1984] and Hollis et al. [1987]. Two excellent surveys on existence results for RDSs on fixed domains are the book by Smoller [1994] and the monograph by Pierre [2009]. The former details the useful invariant region approach, which consists in determining a region in "solution space" from which the solution can not escape. The latter provides a detailed survey on the state of the art in terms of existence results for RDSs in which there is "control of mass", i.e., some a priori control on the L_1 norms of the species. There is very little literature regarding the stability of solutions of RDSs on evolving domains. Madzvamuse et al. [2010] provides a linear stability analysis of RDSs on continuously evolving domains and Labadie [2008] examines the stability of solutions of RDSs on monotonically growing surfaces. Our discussion here differs from all these studies in that we focus on planar evolving domains and we show existence, uniqueness and stability for an entire class of RDSs on evolving domains independently of the rate of evolution. In this Chapter we prove the stability of solutions of RDSs on a particular, but fundamentally important, class of time-evolving domains: that of *bounded spatially linear isotropically evolving domains*.

We show that if an RDS fulfils a restricted version of certain *stability conditions*, introduced by Morgan [1989] for fixed domains, then the RDS fulfils the same stability conditions on any bounded spatially linear isotropic evolution of the domain. We thus prove that, under certain conditions, existence and uniqueness for an RDS on a fixed domain implies the existence and uniqueness for the corresponding RDS on an evolving domain. This is, to our best knowledge, the

first result that holds independently of the growth rate and is thus valid on growing or contracting domains as well as domains that exhibit periods of growth and periods of contraction. Our analysis rigorously justifies computations for this type of domain evolution.

The outline of this Chapter goes as follows: In §3.2 we state our model problem together with the form of domain evolution that we consider and present a transformation of our model system to the Lagrangian framework that helps in proving global existence of solutions. In §3.3 we review the existence results for RDSs on fixed domains which will form the basis of our analysis. In §3.4 we state and prove the central results of this Chapter; in particular, we extend the existence results cited in §3.3 to problems posed on evolving domains. In §3.5 we illustrate some specific applications of our results, in particular those of significance in the field of biological pattern formation. We focus on growth functions commonly encountered in the field of developmental biology for which our analysis is valid and show the applicability of our analysis to some of the important reaction kinetics encountered in the theory of biological pattern formation. In §3.6 we summarise our findings and indicate future research directions.

3.2 RDSs on continuously evolving domains

The model problem we wish to consider is Problem (2.4.7) a semilinear RDS posed on a continuously evolving domain (see §2.4 for the details). To avoid technical complications on the boundary, we assume the domain $\Omega_t \subset \mathbb{R}^n$ ($n < \infty$) is a $C^{2+\gamma}(\Omega)$, simply connected, bounded and continuously deforming domain with respect to t. We assume the function $\boldsymbol{f}$ is an $(m \times 1)$ vector of nonlinear coupling terms that is locally Lipschitz. We further assume the diffusion coefficients $\boldsymbol{D}$ are strictly positive. To simplify the exposition, we take boundary conditions to be of homogenous Neumann type, as in (2.4.7). Morgan [1989] considers a much wider class of boundary conditions and our analysis may be extended to this more general setting. We take the initial condition for each u_i to be bounded and nonnegative.

3.2.1 Lagrangian transformation

The approach we shall use to prove the existence of solutions to (2.4.7), is to introduce a transformation that maps Problem (2.4.7) from a time-dependent domain to a fixed domain (cf. §2.3) and to extend existence results for RDSs on fixed domains to the transformed problem. In order to do this, without too many technical complications, we will restrict our attention to special evolutions of the domain, described next.

3.2.2 Assumption (Isotropic domain evolution)**.** We assume the domain Ω_t to evolve by obeying a bounded spatially linear isotropic domain deformation, i.e., at each instant $t \in [0, T]$ and for each $\boldsymbol{x} \in \Omega_t$ there exists a $\boldsymbol{\xi} \in \Omega_0$ such that

$$\boldsymbol{x} := \boldsymbol{\mathcal{A}}(\boldsymbol{\xi}, t) = \rho(t)\boldsymbol{\xi}, \tag{3.2.1}$$

with $\rho \in C^2\left([0,T]; 0, \infty\right)$ and where $\boldsymbol{\xi}$ represents the spatial coordinates of the initial domain.

3.2.3 Assumption (Flow velocity)**.** We assume that the flow velocity induced by the evolution of the domain $\boldsymbol{a}(\boldsymbol{x}, t)$ (cf. (2.3.4)) is identical to the domain velocity, i.e.,

$$\boldsymbol{a} = \partial_t \boldsymbol{\mathcal{A}}$$

as is standard in the derivation of RDSs on evolving domains on application of Reynold's Transport Theorem [Acheson, 1990], (§2.6).

Assumptions 3.2.2 and 3.2.3 imply

$$\boldsymbol{a}(\boldsymbol{x},t) = \dot{\rho}(t)\boldsymbol{\xi} \tag{3.2.2}$$

$$\nabla \cdot \boldsymbol{a}(\boldsymbol{x},t) = n\frac{\dot{\rho}(t)}{\rho(t)} \tag{3.2.3}$$

$$\mathrm{D}\boldsymbol{\mathcal{A}}^{-1}(\boldsymbol{x}) = \begin{bmatrix} \frac{1}{\rho(t)} & 0 & \dots \\ 0 & \ddots & \vdots \\ \vdots & \dots & \frac{1}{\rho(t)} \end{bmatrix} \tag{3.2.4}$$

$$\Delta\boldsymbol{\mathcal{A}}^{-1}(\boldsymbol{x}) = \boldsymbol{0}, \tag{3.2.5}$$

where $\dot{\rho} := \frac{\mathrm{d}\rho}{\mathrm{d}t}$. Hence, we obtain the following transformed problem on the initial domain (see §2.6 for details), with

$$\hat{\boldsymbol{u}}(\boldsymbol{\xi},t) = \boldsymbol{u}(\rho(t)\boldsymbol{\xi},t) \qquad \text{for } t \in [0,T] \text{ and } \boldsymbol{\xi} \in \Omega_0, \tag{3.2.6}$$

we have

$$\begin{cases} \partial_t\hat{\boldsymbol{u}} + n\frac{\dot{\rho}}{\rho}\hat{\boldsymbol{u}} = \boldsymbol{f}(\hat{\boldsymbol{u}}) + \frac{\boldsymbol{D}}{\rho^2}\Delta\hat{\boldsymbol{u}} & \text{on } \Omega_0 \times (0,T], \\ [\boldsymbol{\nu}\cdot\nabla\hat{\boldsymbol{u}}](\boldsymbol{\xi},t) = 0 & \text{on } \partial\Omega_0, t > 0, \\ \hat{\boldsymbol{u}}(\boldsymbol{\xi},0) = \hat{\boldsymbol{u}}_0(\boldsymbol{\xi}) & \boldsymbol{\xi} \in \Omega_0, \\ 0 \le \hat{\boldsymbol{u}}_0(\boldsymbol{\xi}) < \infty, \end{cases} \tag{3.2.7}$$

where the initial spatial domain Ω_0 is taken as the reference domain, n is the spatial dimension and the Laplacian is now taken with respect to $\boldsymbol{\xi}$. The local and global existence results that we utilise from the existing literature require the coefficients on our diffusion term to be independent of time; to this end we introduce the following proposition:

3.2.4 Proposition (Time rescaling [Labadie, 2008])**.** *Let $\boldsymbol{u}$ be a solution of* $(2.4.7)$*, rescaling time via the change of variables*

$$s(t) := \int_0^t \frac{\mathrm{d}r}{\rho(r)^2}, \tag{3.2.8}$$

and denoting $S := s(T)$. We have, $\boldsymbol{u}\left(\rho(t)\boldsymbol{\xi},t\right) = \tilde{\boldsymbol{u}}(\boldsymbol{\xi},s)$, where $\tilde{\boldsymbol{u}}$ satisfies

$$\begin{cases} \partial_s\tilde{\boldsymbol{u}} + n\rho\dot{\rho}\tilde{\boldsymbol{u}} = \rho^2\boldsymbol{f}(\tilde{\boldsymbol{u}}) + \boldsymbol{D}\Delta\tilde{\boldsymbol{u}} & \text{on } \Omega_0 \times (0,S], \\ [\boldsymbol{\nu}\cdot\nabla\tilde{\boldsymbol{u}}](\boldsymbol{\xi},s) = 0 & \boldsymbol{\xi} \in \partial\Omega_0, s > 0, \\ \tilde{\boldsymbol{u}}(\boldsymbol{\xi},0) = \tilde{\boldsymbol{u}}_0(\boldsymbol{\xi}) & \boldsymbol{\xi} \in \Omega_0. \end{cases} \tag{3.2.9}$$

Furthermore, if $\boldsymbol{f}(\boldsymbol{u})$ is locally Lipschitz in $\boldsymbol{u}$ then $\tilde{\boldsymbol{f}}(\tilde{\boldsymbol{u}}(\boldsymbol{\xi},s),s) = \rho^2(s)\boldsymbol{f}(\tilde{\boldsymbol{u}}(\boldsymbol{\xi},s)) - n\rho(s)\dot{\rho}(s)\tilde{\boldsymbol{u}}(\boldsymbol{\xi},s)$, is locally Lipschitz in $\tilde{\boldsymbol{u}}$.

Proof . We note that with domain evolution of the form considered in this study, there exist C_1, C_2 such that $0 < \rho \le C_1 < \infty$ and $\|\dot{\rho}\|_{L_\infty[0,T]} \le C_2 < \infty$. Applying the rescaling (3.2.8), we see that for any function $g \in C^1[0,T]$

$$\partial_s g\,(t) = \partial_s t(s)\partial_t g(t) = \rho^2(t)\partial_t g(t). \tag{3.2.10}$$

Defining $\tilde{\boldsymbol{u}}(\boldsymbol{\xi},s) := \boldsymbol{u}(\rho(t)\boldsymbol{\xi},t)$ and multiplying problem (3.2.7) by ρ^2, we obtain problem (3.2.9). Clearly since $\boldsymbol{f}(\boldsymbol{u})$ is locally Lipschitz in $\boldsymbol{u}$, Assumption 3.2.2 implies $\tilde{\boldsymbol{f}}(\tilde{\boldsymbol{u}},s)$ is locally Lipschitz in $\tilde{\boldsymbol{u}}$ and globally Lipschitz in s. □

3.3 Theoretical setting for RDSs on fixed domains

We now introduce the necessary theoretical background we shall use to prove global existence of solutions to Problem (3.2.9).

3.3.1 Definition (Local existence and uniqueness)**.** Equation (3.2.9) admits a *local solution* on the interval $[0, \delta)$, $\delta > 0$ if there exists

$$\tilde{\boldsymbol{u}} : \Omega_0 \times [0, \delta) \to \mathbb{R}^m, \tag{3.3.1}$$

such that $\tilde{\boldsymbol{u}}$ satisfies (3.2.9) for all $t \in [0, \delta)$. Let $\delta_1, \delta_2 \in (0, \delta)$ and suppose that $\tilde{\boldsymbol{u}}_1$ and $\tilde{\boldsymbol{u}}_2$ are local solutions of (3.2.9) with

$$\operatorname{Dom}(\tilde{\boldsymbol{u}}_1) = \Omega_0 \times [0, \delta_1) \text{ and} \tag{3.3.2}$$

$$\operatorname{Dom}(\tilde{\boldsymbol{u}}_2) = \Omega_0 \times [0, \delta_2). \tag{3.3.3}$$

The local solution (3.3.1) is *unique* if

$$u_1(\cdot, t) = u_2(\cdot, t) \text{ for all } t \in [0, \delta_1) \cap [0, \delta_2). \tag{3.3.4}$$

The following key result gives the local existence of a non-continuable classical solution with non-existence only via blow up in the $L_\infty(\Omega_0)^m$ norm. The proof is a straightforward generalisation of Hollis et al. [1987, Prop. 1].

3.3.2 Theorem (Local existence)**.** *Let Assumption 3.2.1 hold. Problem (3.2.9) admits a unique local solution. Furthermore, defining the unique maximal solution of (3.2.9) by*

$$\tilde{\boldsymbol{u}} : \Omega_0 \times [0, T_{\max}) \to \mathbb{R}^m, \tag{3.3.5}$$

there exists a function $\boldsymbol{N} \in C([0, T_{\max}); \mathbb{R}^m)$ such that,

$$\|\tilde{u}_i(\cdot, s)\|_{L_\infty(\Omega_0)} \leq N_i(t) \quad \text{for } i \in [1, \ldots, m] \text{ and } t \in [0, T_{\max}). \tag{3.3.6}$$

Finally, if $T_{\max} < \infty$,

$$\lim_{s \to T_{\max}^-} \left(\sum_{i=1}^{m} \|\tilde{u}_i(\cdot, s)\|_{L_\infty(\Omega_0)} \right) = \infty. \tag{3.3.7}$$

3.3.3 Global existence on fixed domains

If $\rho(t) = 1$ for all $t \in [0, T]$, Problem (3.2.9) becomes, find $\tilde{\boldsymbol{u}} : \Omega_0 \times (0, T] \to \mathbb{R}_+^m$ such that,

$$\begin{cases} \partial_t \tilde{\boldsymbol{u}} = \boldsymbol{f}(\tilde{\boldsymbol{u}}) + \boldsymbol{D}\Delta\tilde{\boldsymbol{u}}, & \text{on } \Omega_0 \times (0, T], \\ [\boldsymbol{\nu} \cdot \nabla\tilde{\boldsymbol{u}}](\boldsymbol{\xi}, t) = 0, & \boldsymbol{\xi} \in \partial\Omega_0, t > 0, \\ \tilde{\boldsymbol{u}}(\boldsymbol{\xi}, 0) = \tilde{\boldsymbol{u}}_0(\boldsymbol{\xi}), & \boldsymbol{\xi} \in \Omega_0, \end{cases} \tag{3.3.8}$$

where we have used the fact that $s(t) = t$ (cf. (3.2.8)).

3.3.4 Definition (Invariant region [Chueh et al., 1977])**.** $\Sigma \subset \mathbb{R}^m$ is called an invariant region for the solution of the RDS (3.2.9) if for any solution $\tilde{\boldsymbol{u}}$,

$$\tilde{\boldsymbol{u}}(\boldsymbol{\xi}, 0) \in \Sigma \implies \tilde{\boldsymbol{u}}(\boldsymbol{\xi}, t) \in \Sigma \quad \text{for all } (\boldsymbol{\xi}, t) \in \Omega_0 \times (0, T]. \tag{3.3.9}$$

We are primarily interested in RDSs which exhibit diffusion-driven instability, i.e., RDSs with distinct diffusion coefficients. In this case the only admissible (possibly unbounded) invariant regions are products of intervals, i.e., of the form

$$\Sigma = \prod_{i=1}^{m} \{a_i \leq \tilde{u}_i \leq b_i\}. \tag{3.3.10}$$

A sufficient condition for a region Σ of the form (3.3.10) to be invariant is that the reaction function $\boldsymbol{f}$ points strictly into Σ on the boundary [Smoller, 1994]. In Figure 3.3.3, we show the invariant regions admitted by an RDS of the form (3.3.8) equipped with the Thomas kinetics (2.5.9) and Schnakenberg kinetics (2.5.8) respectively.

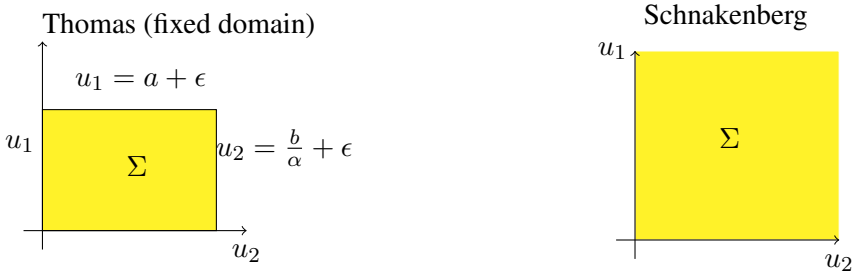

Figure 3.1: Invariant rectangle for the Thomas kinetics (2.5.9) valid in the absence of domain evolution for any $\epsilon > 0$ and the invariant region for the Schnakenberg kinetics (2.5.8).

3.3.5 Assumption (Positive solutions)**.** We assume hereon that

$$f_i(\tilde{\boldsymbol{u}})|_{u_i=0} \geq 0 \text{ for all } \; t \in [0, T], \tag{3.3.11}$$

and for $\boldsymbol{f} \notin C^1(\mathbb{R}^m_+; \mathbb{R}^m)$, the strict inequality

$$f_i(\tilde{\boldsymbol{u}})|_{u_i=0} > 0 \text{ for all } \; t \in [0, T]. \tag{3.3.12}$$

Assumption 3.3.5 together with the positivity of the initial data, implies $\mathbb{R}^m_+$ which we refer to as the positive quadrant, is an invariant region for the solutions of problem (3.3.8) (see Smoller [1994, Th.14.7,14.11 pp.200–203]).

3.3.6 Remark (General invariant regions)**.** Assumption 3.3.5 may be relaxed. The proof of our existence results only requires bounded initial data and the existence of an invariant region. Furthermore, consideration of the positive quadrant alone is sufficient for our studies.

The invariant region approach while useful, especially in proving the positivity of solutions, is very limited for the systems we have in mind. Informally speaking, in the case of distinct diffusion coefficients the invariant region approach effectively requires each of the f_i's to independently provide an upper bound for the u_i's. This means we can not exploit the full structure of the system. We now introduce an alternative approach for systems where sums of the reaction kinetics obey a growth condition.

3.3.7 A Lyapunov function approach to proving existence for RDSs

We use a Lyapunov function approach to extend the stability properties of the system of ordinary differential equations (i.e., in the absence of diffusion) to the full RDS. We illustrate the approach with the following simplified example. Let $\boldsymbol{g} \in C^1(\mathbb{R}^m; \mathbb{R}^m)$ and consider the system of ODEs

$$\begin{aligned} \dot{\boldsymbol{y}}(t) &= \boldsymbol{g}(\boldsymbol{y}(t)), \quad t > 0 \\ \boldsymbol{y}(0) &= \boldsymbol{y}_0, \end{aligned} \tag{3.3.13}$$

with $\boldsymbol{y}_0 \in \mathbb{R}^m$. The local existence and uniqueness of solutions to (3.3.13) follows from classical results. One well known approach to proving global existence of solutions is to construct a function, which we shall call a *Lyapunov function*, that fulfils the following stability criteria. Assume that (3.3.13) admits an invariant region $\boldsymbol{I}$ (possibly unbounded) and suppose that there exists a function $H^* \in C^2(\boldsymbol{I}; [0, \infty))$ such that

$$H^{*\prime\prime}(\boldsymbol{z}) \geq 0 \text{ for all } \boldsymbol{z} \in \boldsymbol{I}, \tag{3.3.14}$$

$$H^*(\boldsymbol{z}) \to \infty \iff |\boldsymbol{z}| \to \infty, \tag{3.3.15}$$

$$[\nabla H^* \cdot \boldsymbol{g}](\boldsymbol{z}) \leq M^* H^*(\boldsymbol{z}) \text{ for some } M^* \in \mathbb{R}. \tag{3.3.16}$$

We state the existence results in the following proposition.

3.3.8 Proposition (Existence in the equal diffusion coefficient case)**.** *If (3.3.15) and (3.3.16) hold, then, (3.3.13) has a global solution. Furthermore, if we introduce diffusion and appropriate boundary conditions to the dynamical system (3.3.13) with equal diffusion coefficients, i.e.,*

$$\begin{aligned} \partial_t \boldsymbol{y}(\boldsymbol{\xi}, t) &= D^* \Delta \boldsymbol{y}(\boldsymbol{\xi}, t) + \boldsymbol{g}(\boldsymbol{y}(\boldsymbol{\xi}, t)) \text{ in } \Omega_0 \times (0, T] \\ [\nabla \boldsymbol{y} \cdot \boldsymbol{\nu}](\boldsymbol{\xi}, t) &= 0 \text{ on } \partial\Omega_0 \times (0, T] \\ \boldsymbol{y}(\boldsymbol{\xi}, 0) &= \boldsymbol{y}_0 \text{ in } \Omega_0, \end{aligned} \tag{3.3.17}$$

with $D^* > 0$. Then, conditions (3.3.14)—(3.3.16) imply the global existence of solutions to (3.3.17).

Proof . We first prove the existence of solutions to Problem (3.3.17). From (3.3.17) we have for $(\boldsymbol{\xi}, t) \in \Omega_0 \times (0, T]$

$$\partial_t H^* \left(\boldsymbol{y}(\boldsymbol{\xi}, t) \right) \leq \left[D^* \Delta_{\boldsymbol{\xi}} H^* + \nabla H^* \cdot \boldsymbol{g} \right] \left(\boldsymbol{y}(\boldsymbol{\xi}, t) \right), \tag{3.3.18}$$

where we have used (3.3.14) to obtain the inequality. Combining (3.3.16) and (3.3.19) gives

$$\partial_t H^* \left(\boldsymbol{y}(\boldsymbol{\xi}, t) \right) \leq \left[D^* \Delta_{\boldsymbol{\xi}} H^* + M^* H^* \right] \left(\boldsymbol{y}(\boldsymbol{\xi}, t) \right). \tag{3.3.19}$$

Defining $v := e^{-\alpha t} H^*$ we have

$$e^{\alpha t} \left[\partial_t v - D^* \Delta v + (\alpha - M^*) v \right] (\boldsymbol{\xi}, t) \leq 0. \tag{3.3.20}$$

By the strong maximum principle for parabolic PDEs [Sperb, 1981, §2.3], for $\alpha \geq M^*$ it follows that v attains its maximum at $t = 0$, thus

$$\|H\|_{L_\infty(\Omega_0 \times (0,T])} \leq e^{\alpha T} \left\| H \left(\boldsymbol{y}(\cdot, 0) \right) \right\|_{L_\infty(\Omega_0)}. \tag{3.3.21}$$

Combining (3.3.15) and (3.3.21) we conclude $\|\boldsymbol{y}\|_{L_\infty(\Omega_0\times[0,T])} < C$. Theorem 3.3.2 completes the proof. The corresponding result for the system of ODEs follows easily once we note (3.3.7) holds with $D^* = 0$. □

In the distinct diffusion coefficient case stability results do not generalise as easily from the ODE system to the RDS. Conditions (3.3.14)—(3.3.16) are no longer sufficient to show existence and we now outline the more complicated framework we need to prove stability in the general case.

3.3.9 Lyapunov stability conditions

We introduce a Lyapunov function for the dynamical system defined by (3.3.8) with distinct diffusion coefficients, when the initial condition $\tilde{\boldsymbol{u}}_0$ varies which is used to prove global existence and a restricted version of the conditions it is required to fulfil [Morgan, 1989].

Suppose $\boldsymbol{f}$ is as defined in problem (3.3.8) and that there exists a function $H \in C^2(\mathbb{R}_+;\mathbb{R})$ and $h_i \in C^2(\mathbb{R}_+;\mathbb{R})$ for each $i = 1,\dots,m$, such that

$$H(\boldsymbol{z}) = \sum_{i=1}^{m} h_i(z_i) \quad \text{for all } \boldsymbol{z} \in \mathbb{R}_+^m, \tag{3.3.22}$$

$$h_i(z_i), h_i''(z_i) \geq 0 \quad \text{for all } \boldsymbol{z} \in \mathbb{R}_+^m, \tag{3.3.23}$$

$$H(\boldsymbol{z}) \to \infty \iff \boldsymbol{z} \to \infty \quad \text{for all } \boldsymbol{z} \in \mathbb{R}_+^m. \tag{3.3.24}$$

Suppose there exists $\boldsymbol{A} = (a_{ij}) \in (\mathbb{R})^{m\times m}$ satisfying $a_{ij} \geq 0, a_{ii} > 0$ with $1 \leq i,j \leq m$ such that for some $r, k_1, k_2 \in \mathbb{R}_+$ independent of j, we have

$$\sum_{i=1}^{j} a_{ij} h_i'(z_i) f_i(\boldsymbol{z}) \leq k_1 (H(\boldsymbol{z}))^r + k_2 \quad \text{for all } \boldsymbol{z} \in \mathbb{R}_+^m, j \leq m. \tag{3.3.25}$$

Suppose there exist $q, k_3, k_4 \in \mathbb{R}_+$ such that for $1 \leq i \leq m$, we have

$$h_i'(z_i) f_i(\boldsymbol{z}) \leq k_3 (H(\boldsymbol{z}))^q + k_4, \quad \text{for all } \boldsymbol{z} \in \mathbb{R}_+^m. \tag{3.3.26}$$

Suppose there exist $k_5, k_6 \geq 0$ such that

$$\nabla H(\boldsymbol{z}) \cdot \boldsymbol{f}(\boldsymbol{z}) \leq k_5 H(\boldsymbol{z}) + k_6 \quad \text{for all } \boldsymbol{z} \in \mathbb{R}_+^m. \tag{3.3.27}$$

Condition (3.3.25), especially the parameter r therein, plays a central role in obtaining existence results. Morgan refers to this condition as an "intermediate sum condition" and we show in §3.5 that it is fulfilled by many important RDSs.

3.3.10 Theorem (a priori estimates [Morgan, 1989])**.** *Let conditions (3.3.22), (3.3.23) and (3.3.27) hold and let $\tilde{\boldsymbol{u}}$ be a solution of problem (3.3.8). The following a priori estimates hold,*

$$\Big\| \int_\tau^t H(\tilde{\boldsymbol{u}}(\cdot,s))\,\mathrm{d}s \Big\|_{L_\infty(\Omega_0)} \leq g(t) \quad \text{for } 0 \leq \tau < t < T_{\max}, \tag{3.3.28}$$

$$\int_0^t \int_{\Omega_0} H(\tilde{\boldsymbol{u}}(\boldsymbol{\xi},s))^2\,\mathrm{d}\boldsymbol{\xi}\,\mathrm{d}s \leq \tilde{g}(t) \quad \text{for } 0 \leq t < T_{\max}, \tag{3.3.29}$$

where $g, \tilde{g} \in C[0,\infty)$.

3.3.11 Theorem (Global existence on fixed domains [Morgan, 1989])**.** *If conditions (3.3.22)—(3.3.26) hold, with r from condition (3.3.25) satisfying $r < (1+a)$, $a \in \mathbb{R}_+$, $\tilde{\boldsymbol{u}}$ is a solution of problem (3.3.8) and if there exists $g \in C[0,\infty)$ such that*

$$\Big\| \int_\tau^t \Big| H\big(\tilde{\boldsymbol{u}}(\cdot,s)\big)\Big|^a \,\mathrm{d}s \Big\|_{L_\infty(\Omega_0)} \leq g(t) \quad \text{for } 0 \leq \tau < t < T_{\max}, \tag{3.3.30}$$

then $T_{\max} = \infty$. Alternatively, if conditions (3.3.22)—(3.3.26) hold, with r from condition (3.3.25) satisfying $r < (1 + \frac{2b}{n+2})$, $b > 0$ and where n represents the spatial dimension, $\tilde{\boldsymbol{u}}$ solves a problem of the form (3.3.8) and if there exists $\tilde{g} \in C[0,\infty)$ such that

$$\int_0^t \int_{\Omega_0} \Big| H(\tilde{\boldsymbol{u}}(\boldsymbol{\xi},s))\Big|^b \,\mathrm{d}\boldsymbol{\xi}\,\mathrm{d}s \leq \tilde{g}(t) \quad \text{for } 0 \leq t < T_{\max}, \tag{3.3.31}$$

then $T_{\max} = \infty$.

Specifically, if r from condition (3.3.25) satisfies $r < 2$ or if $\Omega_0 \subset \mathbb{R}$ with $r < \frac{7}{3}$ and the remaining conditions (3.3.22)—(3.3.27) are satisfied then $T_{\max} = \infty$.

3.4 Global existence on evolving domains

In this section we show that if the stability conditions in §3.3.9 are valid for Problem (3.3.8), then they remain valid under any evolution of the domain fulfilling Assumption 3.2.2, given a suitable assumption on the structure of H. We also extend the previous a priori estimates and existence results of Morgan [1989] to problems with time-dependent reaction functions.

3.4.1 Assumption (Polynomial Lyapunov function)**.** We assume the Lyapunov function introduced in §3.3.9 is of the following form

$$H(\boldsymbol{z}) = \sum_{i=1}^m z_i^{p_i}, \quad p_i \geq 1 \text{ for } i = 1,\ldots,m. \tag{3.4.1}$$

3.4.2 Remark (Polynomial growth restriction)**.** Assumption 3.4.1 is somewhat natural. Condition (3.3.26) is essentially a "polynomial type growth restriction" on the zero order terms [Morgan, 1989]. Assumption 3.4.1 can be viewed as the explicit analogue of the polynomial growth restriction on the zero order terms implicit in (3.3.26).

3.4.3 Lemma (Equivalence of Lyapunov functions)**.** *Suppose Assumptions 3.2.2, 3.3.5 and 3.4.1 hold. Let the Lyapunov stability conditions in §3.3.9 be satisfied by H and $\boldsymbol{f}$. Then the conditions in §3.3.9 with r (cf. (3.3.25)) replaced by $\tilde{r} := \max(1,r)$, are satisfied by H and $\tilde{\boldsymbol{f}}$ (cf. (3.4.2)) in place of $\boldsymbol{f}$.*

Proof . We denote the zero order term in Problem (3.2.9) by

$$\tilde{\boldsymbol{f}}\left(\tilde{\boldsymbol{u}}(\boldsymbol{\xi},s),s\right) := \rho^2(s)\boldsymbol{f}\left(\tilde{\boldsymbol{u}}(\boldsymbol{\xi},s)\right) - n\dot{\rho}(s)\rho(s)\tilde{\boldsymbol{u}}(\boldsymbol{\xi},s). \tag{3.4.2}$$

The positive quadrant remains an invariant region for the solutions of our evolving domain problem since

$$\tilde{f}_i\left(\tilde{\boldsymbol{u}}(\boldsymbol{\xi},s),s\right)|_{u_i=0} = \rho^2(s) f_i\left(\tilde{\boldsymbol{u}}(\boldsymbol{\xi},s)\right)|_{u_i=0}, \tag{3.4.3}$$

thus Assumption 3.3.5 implies $\mathbb{R}^m_+$ is an invariant region for the solutions of problem (3.2.9). Let $k_i, i = 1, \dots, 6, q, r$ and $\boldsymbol{A}$ be as defined in §3.3.9, for which conditions (3.3.22)—(3.3.27) hold for problem (3.3.8). Denote $C_1 := \|\rho\|_{L_\infty[0,T]}$ and $C_2 := \|\dot{\rho}\|_{L_\infty[0,T]}$; these are well defined real numbers thanks to Assumption 3.2.2. We now show that conditions (3.3.22)—(3.3.27) hold with the same H, $\boldsymbol{f}$ replaced by $\tilde{\boldsymbol{f}}$ and r from (3.3.25) replaced by $\tilde{r}$, where $\tilde{r} = \max(1, r)$.

Clearly conditions (3.3.22)—(3.3.24) are still satisfied as they depend only on H which is unchanged. Condition (3.3.25) holds since

$$\sum_{i=1}^{j} a_{ij} h_i' \tilde{f}_i = \sum_{i=1}^{j} a_{ij} h_i' (\rho^2 f_i - n\dot{\rho}\rho\tilde{u}_i) \le (k_1 (H)^r + k_2) C_1^2 + nC_1 C_2 \sum_{i=1}^{j} a_{ij} h_i' \tilde{u}_i, \quad (3.4.4)$$

by the stability of the fixed domain problem. Now Assumption 3.4.1 gives,

$$\begin{aligned} \sum_{i=1}^{j} a_{ij} h_i' \tilde{f}_i &\le (k_1 (H)^r + k_2) C_1^2 + nC_1 C_2 \sum_{i=1}^{j} a_{ij} p_i h_i \\ &\le (k_1 (H)^r + k_2) C_1^2 + k_7 H \le (k_1 C_1^2 + k_7)(H)^{\tilde{r}} + k_8, \end{aligned} \quad (3.4.5)$$

where

$$\tilde{r} = \max(1, r) \text{ and } k_8 := \begin{cases} k_2 C_1^2 + k_1 C_1^2, & \text{if } r < 1, \\ k_2 C_1^2, & \text{if } r = 1, \\ k_2 C_1^2 + k_7, & \text{if } r > 1. \end{cases}$$

Condition (3.3.26) holds since

$$\begin{aligned} h_i' \tilde{f}_i &\le C_1^2 h_i' f_i + nC_1 C_2 p_i h_i \\ &\le k_3 C_1^2 (H)^q + k_4 C_1^2 + nC_1 C_2 \max_i (p_i) H \\ &\le k_{10} H^{\tilde{q}} + k_{11}, \end{aligned} \quad (3.4.6)$$

where

$$\tilde{q} = \max(1, q) \text{ and } k_{11} := \begin{cases} k_4 C_1^2 + k_3 C_1^2, & \text{if } q \le 1, \\ k_4 C_1^2, & \text{if } q = 1, \\ k_4 C_1^2 + k_9, & \text{if } q > 1. \end{cases}$$

Condition (3.3.27) holds since

$$\nabla H . \tilde{\boldsymbol{f}} \le \sum_{i=1}^{m} C_1^2 h_i' f_i + nC_1 C_2 p_i h_i \le (k_5 H + k_6) C_1^2 + k_{12} H. \quad (3.4.7)$$

Thus, the positive quadrant remains an invariant region for the solutions of problem (3.2.9) and the Lyapunov stability conditions in §3.3.9 are satisfied, completing the proof. □

3.4.4 Remark (Applicability of Morgan [1989] to systems with time-dependent zero order terms)**.** Suppose the reaction function $\tilde{\boldsymbol{f}}\left(\tilde{\boldsymbol{u}}(\boldsymbol{\xi}, t), t\right)$ is locally Lipschitz with respect to $\tilde{\boldsymbol{u}}$ and t, and suppose that the Lyapunov function H depends only on $\tilde{\boldsymbol{u}}$. Then, Theorems 3.3.10 and 3.3.11 remain applicable [Morgan, 1989, (5.5)], [Morgan and Hollis, 1995, Th. 1.1] and [Bendahmane and Saad, 2010a, Th. 4]. Thus, the Lipschitz result of Proposition 3.2.4, the structural Assumption

3.4.1 and the equivalence of Lyapunov functions proved in Lemma 3.4.3 imply that Theorems 3.3.10 and 3.3.11 are applicable for solutions of (3.2.9).

For completeness, we include a proof of Theorems 3.3.10 and 3.3.11 for solutions of Problem (3.2.9), in §3.4.5 and 3.4.7 respectively. To remain concise, we prove a sufficient existence result for the examples presented in §3.5 and briefly sketch the full proof of Theorems 3.3.10 and 3.3.11.

The results of Morgan and Hollis [1995] apply for systems with time-dependent diffusion. This may allow treatment of more general domain evolution where the rescaling carried out in §3.2 yields a system with time-dependent diffusion. We leave this generalisation for future studies.

3.4.5 A priori estimates for systems with time-dependent reaction kinetics

In this section we prove Theorem 3.3.10 remains applicable for solutions of Problem (3.2.9). For conciseness we focus on assertion (3.3.28). We adapt the proof of Morgan [1989, Th. 3.2] for our purposes. In §3.4.7, we use the a priori estimates obtained in this section to prove the global existence of classical solutions to Problem (3.2.9). We state the main result of this section in the following Lemma.

3.4.6 Lemma (An a priori estimate for solutions of Problem (3.2.9))**.** *Suppose Assumptions 3.2.2, 3.3.5 and 3.4.1 hold and let (3.3.22)—(3.3.24) and (3.3.27) hold. Then, assertion (3.3.28) is valid with $\tilde{\boldsymbol{u}}$ a solution of Problem (3.2.9).*

Proof . Let $\tilde{\boldsymbol{f}}$ be as defined in (3.4.2). From the proof of Lemma 3.4.1, (3.4.7) holds. We split the remainder of the proof into steps.

Step 1: We first show the following inequality for H:

$$\begin{aligned} H\left(\tilde{\boldsymbol{u}}(\boldsymbol{\xi},t)\right) \leq \int_\tau^t \sum_{i=1}^m D_i \Delta_{\boldsymbol{\xi}} h_i\left(\tilde{u}_i(\boldsymbol{\xi},r)\right) + \left(k_5 C_1^2 + k_{12}\right) H\left(\tilde{\boldsymbol{u}}(\boldsymbol{\xi},r)\right) \mathrm{d}r \\ + H\left(\tilde{\boldsymbol{u}}(\boldsymbol{\xi},\tau)\right) + k_6 C_1^2 (t-\tau) \text{ for } \boldsymbol{\xi} \in \Omega_0. \end{aligned} \tag{3.4.8}$$

From (3.2.9) we have for $(\boldsymbol{\xi},t) \in \Omega_0 \times (0, T_{\max})$,

$$\nabla H\left(\tilde{\boldsymbol{u}}(\boldsymbol{\xi},t)\right) \cdot \partial_t \tilde{\boldsymbol{u}}(\boldsymbol{\xi},t) = \nabla H\left(\tilde{\boldsymbol{u}}(\boldsymbol{\xi},t)\right) \cdot \left(\boldsymbol{D}\Delta\tilde{\boldsymbol{u}}(\boldsymbol{\xi},t) + \tilde{\boldsymbol{f}}\left(\tilde{\boldsymbol{u}}(\boldsymbol{\xi},t),t\right)\right). \tag{3.4.9}$$

Using (3.3.22), (3.4.7) and (3.4.9), we obtain the following generalisation of Morgan [1989, (3.1)],

$$\nabla H\left(\tilde{\boldsymbol{u}}(\boldsymbol{\xi},t)\right) \cdot \partial_t \tilde{\boldsymbol{u}}(\boldsymbol{\xi},t) \leq \sum_{i=1}^m D_i \Delta_{\boldsymbol{\xi}} h_i\left(\tilde{u}_i(\boldsymbol{\xi},t)\right) + \left(k_5 C_1^2 + k_{12}\right) H\left(\tilde{\boldsymbol{u}}(\boldsymbol{\xi},t)\right) + k_6 C_1^2, \tag{3.4.10}$$

where we have used the convexity of H (3.3.23). For $0 \leq \tau < t < T_{\max}$ integrating (3.4.10) in time gives (3.4.8).

Step 2: We use (3.4.8) to construct an appropriate barrier function with a view to applying the maximum principle, corresponding to Morgan [1989, (3.2)—(3.4)]. Introducing an arbitrary $T^* < T_{\max}$, we define

$$w(\boldsymbol{\xi},t) := \int_\tau^t \sum_{i=1}^m \frac{D_i}{D^*} h_i\left(\tilde{u}_i(\boldsymbol{\xi},r)\right) \mathrm{d}r \text{ for } \boldsymbol{\xi} \in \Omega_0 \text{ and } 0 \leq \tau < t \leq T^*, \tag{3.4.11}$$

where $D^* := \max_i(D_i)$. Observe that from (3.3.22) and (3.4.11), we have for $0 \leq \tau < t \leq T^*$

$$\begin{aligned}\left\| \int_\tau^t H(\tilde{\boldsymbol{u}}(\cdot,s))\,\mathrm{d}s \right\|_{L_\infty(\Omega_0)} &= \left\| \int_\tau^t \sum_{i=1}^m h_i(\tilde{u}_i(\cdot,s))\,\mathrm{d}s \right\|_{L_\infty(\Omega_0)} \\ &\leq \max_i \left(\frac{D^*}{D_i}\right) \|w(\cdot,s)\,\mathrm{d}s\|_{L_\infty(\Omega_0)}.\end{aligned} \tag{3.4.12}$$

From (3.4.8) and (3.4.11) we obtain for

$$\begin{cases} \partial_t w(\boldsymbol{\xi},t) \leq [D^*\Delta w + Mw](\boldsymbol{\xi},t) & \\ \qquad\qquad +L + k_6 C_1^2(t-\tau), & \boldsymbol{\xi}\in\Omega_0, t\in(\tau,T^*] \\ [\boldsymbol{\nu}\cdot\nabla w](\boldsymbol{\xi},t) = 0, & \boldsymbol{\xi}\in\partial\Omega_0, t\in(\tau,T^*] \\ w(\boldsymbol{\xi},\tau) = 0, & \boldsymbol{\xi}\in\Omega_0, \end{cases} \tag{3.4.13}$$

where

$$L := \|H\left(\tilde{\boldsymbol{u}}(\cdot,\tau)\right)\|_{L_\infty(\Omega_0)} \text{ and } M := \frac{(k_{12}+C_1^2k_5)D^*}{\min_i(D_i)}. \tag{3.4.14}$$

Note we have used (3.2.9) to obtain the boundary conditions. For the purposes of applying the maximum principle we define a barrier function

$$\hat{w}(\boldsymbol{\xi},t) := w(\boldsymbol{\xi},t) - \frac{L+K_6C_1^2T^*}{M} \text{ for } \boldsymbol{\xi}\in\Omega_0 \text{ and } 0\leq\tau<t\leq T^*. \tag{3.4.15}$$

From (3.4.13) and (3.4.11) we have

$$\begin{cases} \partial_t\hat{w}(\boldsymbol{\xi},t) \leq D^*\Delta\hat{w}(\boldsymbol{\xi},t) + M\hat{w}(\boldsymbol{\xi},t) & \boldsymbol{\xi}\in\Omega_0, 0\leq\tau<t\leq T^* \\ [\boldsymbol{\nu}\cdot\nabla\hat{w}](\boldsymbol{\xi},t) = 0, & \boldsymbol{\xi}\in\partial\Omega_0, t\in(\tau,T^*] \\ \hat{w}(\boldsymbol{\xi},\tau) \leq 0, & \boldsymbol{\xi}\in\Omega_0. \end{cases} \tag{3.4.16}$$

Step 3: We use the maximum principle to complete the proof. Applying the strong maximum principle for parabolic problems [Sperb, 1981][Th. 2.9, Rem. (a) pg. 21] to (3.4.16) and noting the positivity of w, we have

$$-\frac{L+K_6C_1^2T^*}{M} \leq \hat{w}(\boldsymbol{\xi},t) \leq 0 \text{ for all } \boldsymbol{\xi}\in\Omega_0 \text{ and for } t\in(\tau,T^*]. \tag{3.4.17}$$

From (3.4.15) and (3.4.17) we have

$$0 \leq \hat{w}(\boldsymbol{\xi},t) \leq \frac{L+K_6C_1^2T^*}{M} \text{ for all } \boldsymbol{\xi}\in\Omega_0 \text{ and for } t\in(\tau,T^*]. \tag{3.4.18}$$

We conclude from (3.4.18) that

$$\|w(\cdot,t)\|_{L_\infty(\Omega_0)} \leq \frac{L+K_6C_1^2T^*}{M} \text{ for } t\in(\tau,T^*]. \tag{3.4.19}$$

Since T^* was arbitrary, combining (3.4.12) and (3.4.19) completes the proof of the Lemma. □

For completeness, we sketch the proof of assertion (3.3.29) with $\tilde{\boldsymbol{u}}$ a solution of Problem (3.2.9). In (3.4.10) we denote $K_7 := k_5C_1^2 + k_{12}$ and $K_8 := k_6C_1^2$, where K_7, K_8 correspond to the terms on the right hand side of Morgan [1989, (3.1)]. Assertion (3.3.29) follows from the proofs of Morgan [1989, Th. 3.3 and 3.4].

3.4.7 Global existence results for systems with time-dependent reaction kinetics

The main result of this section is Theorem 3.4.11, a special case of Theorem 3.3.11. It is applicable to solutions of Problem (3.2.9). Theorem 3.4.11 is enough for our purposes as seen in the examples in §3.5. To prove the Theorem, we will modify the proof of Morgan [1989, Th. 2.2] with stronger control of the parameter r that appears in (3.3.25).

We start with two Lemmas from Morgan [1989, Lem. 4.1, Lem. 4.2, (4.12)] which follow from the results of Ladyzhenskaya et al. [1968, Th. 9.1 p.341]. We then use a duality approach to prove global existence of classical solutions to (3.2.9).

3.4.8 Lemma (Global existence)**.** *Let $\tilde{\boldsymbol{u}}$ be the solution of Problem (3.2.9). Let the function H fulfil conditions (3.3.22)—(3.3.24) in §3.3.9 and let the polynomial growth restriction on $\tilde{\boldsymbol{f}}$ (3.4.6) hold. Let $T_{\max}$ be as defined in (3.3.5) and suppose that,*

$$\begin{cases} \text{for } 0 \leq \tau < T < T_{\max} \text{ and for all } p \in (1, \dots, \infty) \\ \text{there exist } M_p, N_p > 0 \text{ and } 0 < \delta_p < 1 \text{ such that} \\ \displaystyle\sum_{i=1}^{m} \|h_i(\tilde{u}_i)\|_{L_p\left(\Omega_0 \times (\tau,T)\right)} \leq M_p(T-\tau) + N_p(T-\tau)\|H(\tilde{\boldsymbol{u}})\|^{\delta_p}_{L_p\left(\Omega_0 \times (\tau,T)\right)}, \end{cases} \tag{3.4.20}$$

then $T_{\max} = \infty$.

3.4.9 Definition (Dual problem)**.** A key ingredient of the proof of Theorem 3.4.11 is the dual solution ψ. For $i = 1, \dots, m$, ψ is the solution of the scalar equation

$$\begin{cases} \partial_t \psi(\boldsymbol{\xi}, t) = -D_i \Delta \psi(\boldsymbol{\xi}, t) - \theta(\boldsymbol{\xi}, t) & \text{for } \boldsymbol{\xi} \in \Omega_0 \text{ and } 0 \leq t < T < T_{\max} \\ [\boldsymbol{\nu} \cdot \nabla \psi](\boldsymbol{\xi}, t) = 0, & \boldsymbol{\xi} \in \partial\Omega_0, t \in [0, T) \\ \psi(\boldsymbol{\xi}, T) = 0, & \boldsymbol{\xi} \in \Omega_0, \end{cases} \tag{3.4.21}$$

where $\theta \geq 0$ is such that, for all $p \in (1, \dots, \infty)$, $\|\theta\|_{L_p(\Omega_0 \times [0,T])} = 1$.

3.4.10 Lemma (Control of the solution to the dual problem (3.4.21))**.** *Let ψ be as defined in 3.4.9. For $i = 1, \dots, m$ and for $p \in (1, \dots, \infty)$, there exists $C_{p,T} > 0$ such that,*

$$\|\psi\|_{L_p\left(\Omega_0; L_\infty[0,T]\right)} \leq C_{p,T}. \tag{3.4.22}$$

We now state the main result of this section. Namely, the applicability of a special case of Theorem 3.3.11 to solutions of Problem (3.2.9).

3.4.11 Theorem (Sufficient conditions for global existence of solutions to Problem (3.2.9))**.** *Let Assumptions 3.2.2, 3.3.5 and 3.4.1 hold. Let H, $\boldsymbol{f}$ and r satisfy the conditions in §3.3.9 with $r \leq 1$ (cf. (3.3.25)), i.e., Problem (3.3.8) admits a global classical solution by Theorem 3.3.11. Then, Problem (3.2.9) admits a global classical solution, i.e., $T_{\max} = \infty$ (cf. (3.3.5)).*

Proof . We proceed by contradiction. Assume $T_{\max} < \infty$. Let $\tilde{\boldsymbol{u}}$ and $\tilde{\boldsymbol{f}}$ (cf. 3.4.2) be the solution and zero order term of Problem (3.2.9) respectively. From the proof of Lemma 3.4.3 the polynomial growth restriction (3.4.6) is satisfied by $\tilde{\boldsymbol{f}}$ and H. Since $T_{\max} < \infty$, Lemma 3.4.8 implies that (3.4.20) does not hold. Let $j \in [1, \dots, m]$ denote the smallest k for which $\displaystyle\sum_{i=1}^{k} \|h_i(\tilde{u}_i)\|_{L_p\left(\Omega_0 \times (\tau,T)\right)}$ does not satisfy (3.4.20). From the proof of Lemma 3.4.3, the intermediate sum condition (3.4.5) is satisfied for with $\tilde{r} = 1$ (cf. (3.4.5)). From Lemma 3.4.6, we have the a priori estimate (3.3.28).

We will show (3.3.28) and (3.4.5) imply that (3.4.20) is satisfied for j, obtaining a contradiction. We split the remainder of the proof into steps.

Step 1: We first show the following inequality (corresponding to Morgan [1989, (4.6)—(4.9)]): For $0 < T < T_{\max}$

$$\begin{aligned}\int_{\Omega_0}\int_0^T \sum_{i=1}^{j} a_{ji}\frac{D_i}{D_j} h_i\left(\tilde{u}_i(\boldsymbol{\xi},s)\right)\theta(\boldsymbol{\xi},s)\,\mathrm{d}\boldsymbol{\xi}\,\mathrm{d}s \\ \leq \int_0^T\int_{\Omega_0}\sum_{i=1}^{j-1} a_{ji}\left(1-\frac{D_i}{D_j}\right)h_i\left(\tilde{u}_i(\boldsymbol{\xi},s)\right)\partial_s\psi(\boldsymbol{\xi},s) \\ + \psi(\boldsymbol{\xi},s)\left((k_1C_1^2+k_7)H\left(\tilde{\boldsymbol{u}}(\boldsymbol{\xi},s)\right)+k_8\right)\mathrm{d}s \\ + \sum_{i=1}^{j} a_{ji}\psi(\boldsymbol{\xi},0)h_i\left(\tilde{u}_i^0(\boldsymbol{\xi})\right)\mathrm{d}\boldsymbol{\xi} \\ := I_1 + I_2 + I_3.\end{aligned} \tag{3.4.23}$$

From (3.4.21) we have for $i \in [1,\dots,m]$

$$\begin{aligned}\int_0^T\int_{\Omega_0} h_i\left(\tilde{u}_i(\boldsymbol{\xi},s)\right)\theta(\boldsymbol{\xi},s)\,\mathrm{d}\boldsymbol{\xi}\,\mathrm{d}s \\ = \int_0^T\int_{\Omega_0} -h_i\left(\tilde{u}_i(\boldsymbol{\xi},s)\right)\left[\partial_s\psi + D_j\Delta\psi\right](\boldsymbol{\xi},s)\,\mathrm{d}\boldsymbol{\xi}\,\mathrm{d}s \\ \leq \int_0^T\int_{\Omega_0} -h_i\left(\tilde{u}_i(\boldsymbol{\xi},s)\right)\partial_s\psi(\boldsymbol{\xi},s) \\ - \frac{D_j}{D_i}\psi(\boldsymbol{\xi},s)D_i\Delta_{\boldsymbol{\xi}}h_i\left(\tilde{u}_i(\boldsymbol{\xi},s)\right)\mathrm{d}\boldsymbol{\xi}\,\mathrm{d}s,\end{aligned} \tag{3.4.24}$$

where we have used integration by parts and the homogenous Neumann boundary conditions. From Problem (3.2.9) and the convexity of H (3.3.23), we have

$$\begin{aligned}-\int_0^T\int_{\Omega_0}\psi(\boldsymbol{\xi},s)D_i\Delta_{\boldsymbol{\xi}}h_i\left(\tilde{u}_i(\boldsymbol{\xi},s)\right)\mathrm{d}\boldsymbol{\xi}\,\mathrm{d}s \\ \leq \int_0^T\int_{\Omega_0}\psi(\boldsymbol{\xi},s)h_i'\left(\tilde{u}_i(\boldsymbol{\xi},s)\right)\left(\tilde{f}_i\left(\tilde{\boldsymbol{u}}(\boldsymbol{\xi},s),s\right)-\partial_s\tilde{u}_i(\boldsymbol{\xi},s)\right)\mathrm{d}\boldsymbol{\xi}\,\mathrm{d}s \\ = \int_0^T\int_{\Omega_0}\psi(\boldsymbol{\xi},s)h_i'\left(\tilde{u}_i(\boldsymbol{\xi},s)\right)\tilde{f}_i\left(\tilde{\boldsymbol{u}}(\boldsymbol{\xi},s),s\right) \\ + h_i\left(\tilde{u}_i(\boldsymbol{\xi},s)\right)\partial_s\psi(\boldsymbol{\xi},s)\,\mathrm{d}\boldsymbol{\xi}\,\mathrm{d}s + \int_{\Omega_0}\psi(\boldsymbol{\xi},0)h_i\left(\tilde{u}_i^0(\boldsymbol{\xi})\right)\mathrm{d}\boldsymbol{\xi},\end{aligned} \tag{3.4.25}$$

where we have used integration by parts and the final condition of (3.4.21). Combining

(3.4.25) and (3.4.24), we obtain

$$\begin{aligned}\int_0^T \int_{\Omega_0} h_i\left(\tilde{u}_i(\boldsymbol{\xi},s)\right)\theta(\boldsymbol{\xi},s)\,\mathrm{d}\boldsymbol{\xi}\,\mathrm{d}s \\ \leq \int_{\Omega_0}\int_0^T \left(\frac{D_j}{D_i}-1\right) h_i\left(\tilde{u}_i(\boldsymbol{\xi},s)\right)\partial_s\psi(\boldsymbol{\xi},s) \\ + \frac{D_j}{D_i}\psi(\boldsymbol{\xi},s)h_i'\left(\tilde{u}_i(\boldsymbol{\xi},s)\right)\tilde{f}_i\left(\tilde{\boldsymbol{u}}(\boldsymbol{\xi},s),s\right)\mathrm{d}s \\ + \frac{D_j}{D_i}\psi(\boldsymbol{\xi},0)h_i\left(\tilde{u}_i^0(\boldsymbol{\xi})\right)\mathrm{d}\boldsymbol{\xi}.\end{aligned} \tag{3.4.26}$$

Summing (3.4.26) over $i \leq j$ and using intermediate sum condition (3.4.5) with $\tilde{r}=1$, we obtain (3.4.23). For the case $j=1$, we have introduced the convention $\sum_{i=1}^{0}(\cdot)=0$.

Step 2: We shall use Lemma 3.4.10 and (3.4.23) to obtain the following inequality (as in Morgan [1989, (4.10)—(4.16)]): For all $p \in (1,\ldots,\infty)$ there exists $K_p > 0$ and $0 < \delta_p < 1$ independent of $\tilde{\boldsymbol{u}}$ and θ such that,

$$\begin{aligned}\int_0^T \int_{\Omega_0} \sum_{i=1}^{j} a_{ji}\frac{D_i}{D_j} h_i\left(\tilde{u}_i(\boldsymbol{\xi},s)\right)\theta(\boldsymbol{\xi},s)\,\mathrm{d}\boldsymbol{\xi}\,\mathrm{d}s \\ \leq K_{p,T}\left(1+\|H\left(\tilde{\boldsymbol{u}}\right)\|^{\delta_p}_{L_p\left(\Omega_0\times[0,T]\right)}\right).\end{aligned} \tag{3.4.27}$$

Let $p,q \in (1,\ldots,\infty)$ be such that, $\frac{1}{p}+\frac{1}{q}=1$. Dealing firstly with I_1 (cf. (3.4.23)), we have by Hölder's inequality and the regularity estimate (3.4.22)

$$\begin{aligned}I_1 &\leq \sum_{i=1}^{j-1} a_{ji}\left|1-\frac{D_i}{D_j}\right| C_{q,T}T\|h_i\left(\tilde{u}_i\right)\|_{L_p\left(\Omega_0\times[0,T]\right)} \\ &\leq \sum_{i=1}^{j-1} a_{ji}\left|1-\frac{D_i}{D_j}\right| C_{q,T}T\left(M_p+N_p\|H\left(\tilde{\boldsymbol{u}}\right)\|^{\delta_q}_{L_p\left(\Omega_0\times[0,T]\right)}\right),\end{aligned} \tag{3.4.28}$$

where we have the assumption that (3.4.20) is valid for $i<j$. Dealing with I_2, we have by Hölder's inequality and the regularity estimate (3.4.22)

$$\begin{aligned}I_2 \leq& \int_{\Omega_0}\|\psi(\boldsymbol{\xi},\cdot)\|_{L_\infty[0,T]}\left(\int_0^T((k_1C_1^2+k_7)H\left(\tilde{\boldsymbol{u}}(\boldsymbol{\xi},s)\right)+k_8\,\mathrm{d}s\right)\mathrm{d}\boldsymbol{\xi} \\ \leq& C_{q,T}\left((k_1C_1^2+k_7)\left\|\int_0^T H\left(\tilde{\boldsymbol{u}}(\cdot,s)\right)\right\|_{L_q(\Omega_0)}+k_8T\right) \\ \leq& C_{q,T}\left(g(T)\left|\Omega_0\right|^{1/q}+k_8T\right),\end{aligned} \tag{3.4.29}$$

for some $g \in C[0,\infty)$. Here we have used the a priori estimate (3.3.28). Finally, dealing

with I_3 using Hölder's inequality and estimate (3.4.22) we have

$$\begin{aligned} I_3 &\leq \sum_{i=1}^{j} a_{ji} C_{q,T} \left\| h_i\left(\tilde{u}_i^0\right)\right\|_{L_p\left(\Omega_0\times[0,T]\right)} \\ &\leq \sum_{i=1}^{j} a_{ji} C_{q,T} C_p, \end{aligned} \tag{3.4.30}$$

where we have used the boundedness of $\tilde{\boldsymbol{u}}^0$ and condition (3.3.23). Combining (3.4.28), (3.4.29), (3.4.30) and (3.4.23) yields (3.4.27).

Step 3: We now show (3.4.20) holds for j. Let $p, q \in (1, \ldots, \infty)$, be such that, $\frac{1}{p} + \frac{1}{q} = 1$. We recall, from (3.3.23) and Definition 3.4.9, that for $i \in [1, \ldots, m]$, $h_i, \theta \geq 0$ and $\|\theta\|_{L_q(\Omega_0\times(0,T))} = 1$. Using duality we obtain

$$\begin{aligned} &\min_{i\leq j}\left(a_{ji}\frac{D_i}{D_j}\right)\sum_{i=1}^{j}\|h_i(\tilde{u}_i)\|_{L_p\left(\Omega_0\times(0,T)\right)} \\ &\qquad = \min_{i\leq j}\left(a_{ji}\frac{D_i}{D_j}\right)\int_0^T\int_{\Omega_0}\sum_{i=1}^{j} h_i\left(\tilde{u}_i(\boldsymbol{\xi},s)\right)\theta(\boldsymbol{\xi},s)\,\mathrm{d}\boldsymbol{\xi}\,\mathrm{d}s \\ &\qquad \leq \int_0^T\int_{\Omega_0}\sum_{i=1}^{j} a_{ji}\frac{D_i}{D_j} h_i\left(\tilde{u}_i(\boldsymbol{\xi},s)\right)\theta(\boldsymbol{\xi},s)\,\mathrm{d}\boldsymbol{\xi}\,\mathrm{d}s \\ &\qquad \leq K_{p,T}\left(1+\|H\left(\tilde{\boldsymbol{u}}\right)\|^{\delta_p}_{L_p\left(\Omega_0\times[0,T]\right)}\right), \end{aligned} \tag{3.4.31}$$

where we have used (3.4.27).

Thus, we have a contradiction and we conclude $T_{\max} = \infty$ completing the proof. □

The proof of Theorem 3.3.11 follows from more technical use of Hölder's inequality in (3.4.29) and in the case of assertion (3.3.31) we also require the a priori estimate (3.3.29). We refer to Morgan [1989, (4.13)—(4.16) and (4.27)—(4.19)] for specific details.

3.4.12 Theorem (Global existence of solutions on evolving domains)**.** *Let Assumptions 3.2.2, 3.3.5 and 3.4.1 hold and suppose H, $\boldsymbol{f}$ and r satisfy the conditions in §3.3.9 with $r < 2$ or if $\Omega \subset \mathbb{R}, r < \frac{7}{3}$ (cf. (3.3.25)). Then, Problem (2.4.7) admits a global classical solution.*

Proof . Application of the results in §3.2.1 allows us to show existence for the transformed problem (3.2.9) defined on a fixed domain. Theorem 3.3.2 gives the existence of a unique non-continuable classical solution. From Lemma 3.4.1 the stability conditions in §3.3.9 hold with $\tilde{\boldsymbol{f}}$ (cf. (3.4.2)), H and $r < 2$ or if $\Omega \subset \mathbb{R}$, $r < \frac{7}{3}$. Theorem 3.3.10 gives an a priori estimate for H. Theorem 3.3.11 implies $T_{\max} = \infty$ (cf. (3.3.5)) completing the proof. □

3.5 Applications

In this section we illustrate some applications of Theorem 3.4.12. We present different forms of admissible domain evolution that fulfil Assumption 3.2.2. We show that Assumption 3.4.1 is applicable to some commonly encountered models in chemistry and biology. We concentrate

on RDSs which admit Turing instabilities, as the main focus of our research is biological pattern formation. We identify and describe Lyapunov functions and constants that imply global existence for the fixed domain problem and thus for the evolving domain problem by Theorem 3.4.12.

3.5.1 Admissible domain evolution

We now provide some commonly encountered examples of domain evolution in developmental biology for which Assumption 3.2.2 holds:

- Logistic evolution on any finite positive time interval

$$\rho(t) = \frac{e^{r_g t}}{1 + \frac{1}{K}(e^{r_g t} - 1)}, \quad t \in [0, T], \tag{3.5.1}$$

  where $r_g \geq 0$ is the growth rate and $K > 1$ is the carrying capacity (limiting size of the evolving domain).

- Exponential evolution on any finite positive time interval

$$\rho(t) = e^{r_g t}, \quad t \in [0, T]. \tag{3.5.2}$$

- Linear evolution on any finite positive time interval

$$\rho(t) = 1 + r_g t, \quad t \in [0, T], \tag{3.5.3}$$

  where $r_g > -\frac{1}{T}$.

3.5.2 Admissible kinetics

We now present some of the commonly encountered reaction kinetics of problem (2.4.7) for which the analysis of Morgan [1989] implies global existence of solutions on fixed domains. We first consider the problem (2.4.7) with this general reaction term

$$f_i(\boldsymbol{u}) = \sum_{j=1}^{m} c_{ij} u_j + (-1)^i g(\boldsymbol{u}) + b_i, \tag{3.5.4}$$

with the following restrictions:

$$c_{ij} \geq 0, \quad \text{for} \quad i \neq j. \tag{3.5.5}$$

$$b_i \geq 0, \quad i = 1, \ldots, m. \tag{3.5.6}$$

$$g(\boldsymbol{u})|_{u_i=0} = 0, \quad i = 1, \ldots, m. \tag{3.5.7}$$

$$g(\boldsymbol{u}) \leq \left(\sum_{i=1}^{m} u_i \right)^p, \quad \text{for all } \boldsymbol{u} \in \mathbb{R}^m_+. \tag{3.5.8}$$

$$g \in C^1(\mathbb{R}^m_+; \mathbb{R}). \tag{3.5.9}$$

The motivation of this type of kinetics, as discussed by Murray [2003], is their role in the theory of biological oscillators due to a feedback mechanism.

3.5.3 Proposition (Lyapunov function)**.** *We show that problem (2.4.7) equipped with kinetics (3.5.4) is well posed, with Lyapunov function* $H(\boldsymbol{z}) := \sum_{i=1}^{m} z_i$.

Proof . Recalling that the initial data is bounded and nonnegative, we show that Assumption 3.3.5 is fulfilled, which implies $\mathbb{R}^+_m$ is an invariant region for the solutions. Indeed, from (3.5.7) we have

$$f_i(\boldsymbol{u})|_{u_i=0} = \sum_{j=1}^{m} c_{ij}u_j + b_i = \sum_{j=1}^{i-1} c_{ij}u_j + \sum_{j=i+1}^{m} c_{ij}u_j + b_i. \tag{3.5.10}$$

Conditions (3.5.5) and (3.5.6) imply

$$f_i(\boldsymbol{u})|_{u_i=0} \geq b_i \geq 0 \quad \text{for all} \quad \boldsymbol{u} \in \mathbb{R}^m_+. \tag{3.5.11}$$

Thus, Assumption 3.3.5 is fulfilled due to (3.5.9). We now show conditions (3.3.22)—(3.3.27) are fulfilled with $r = 1$.

Clearly conditions (3.3.22)—(3.3.24) hold.

Condition (3.3.25) holds with

$$a_{ij} := \begin{cases} 1 & \text{if } j = i, \\ 1 & \text{if } j = 1 \text{ and } i \text{ is even}, \\ 0 & \text{otherwise}, \end{cases}$$

$k_1 = \max_{i,j}(c_{ij})$, $k_2 = \sum_{i=1}^{m} b_i$ and $r = 1$.

Condition (3.3.26) holds since

$$h_i' f_i = f_i \leq \max_{i,j}(c_{ij}) \sum_{i=1}^{m} u_i + \max_i(b_i) + g(\boldsymbol{u}). \tag{3.5.12}$$

Using (3.5.8) we have

$$\begin{aligned} h_i' f_i &\leq \max_{i,j}(c_{ij}) \sum_{i=1}^{m} u_i + \max_i(b_i) + (\sum_{i=1}^{m} u_i)^p \\ &\leq \max_{i,j}(c_{ij}) H(u) + H(u)^p + \max_i(b_i) \leq kH(u)^q + b, \end{aligned} \tag{3.5.13}$$

where $k, q, b \in \mathbb{R}_+$ represent constants that depend on the value of p in (3.5.8).

Condition (3.3.27) holds since

$$\nabla H \cdot \boldsymbol{f} = \sum_{i=1}^{m} f_i \leq \max_{i,j}(c_{ij}) \sum_{i=1}^{m} u_i + \sum_{i=1}^{m} b_i \leq kH(u) + b, \tag{3.5.14}$$

where $k = \max_{i,j}(c_{ij})$ and $b = \sum_{i=1}^{m} b_i$.

Application of Theorem 3.4.12 completes the proof. □

3.5.4 Examples

The generic problem for which we showed global existence of solutions actually encompasses some of the more widely studied models in the theory of pattern formation such as the Gray-Scott model and the Brussellator. Below we present two examples of two species reaction terms for which our analysis implies global existence of solutions, the first of which is a restriction of the reaction term above.

- Schnakenberg model: Recalling the Schnakenberg model (2.5.8), the assumption of nonnegative initial data implies that the positive quadrant is invariant for our problem due to the fact that $a, b > 0$. If we take $H(\boldsymbol{u}) = u_1 + u_2$, then conditions (3.3.22)—(3.3.27) are fulfilled with $r = 0$ which implies global existence of solutions on evolving domains via Theorem 3.4.12. The remaining constants for which conditions (3.3.22)—(3.3.27) hold are given in Table 3.1.

- Thomas reaction kinetics: Recalling the Thomas model (2.5.9), once again the assumption of nonnegative initial data implies that the positive quadrant is invariant for our problem due to the fact that $a, b > 0$. If we again take $H(\boldsymbol{u}) = u_1 + u_2$, then conditions (3.3.22)—(3.3.27) are fulfilled with $r = 0$ which implies global existence of solutions on evolving domains via Theorem 3.4.12. The remaining constants for which conditions (3.3.22)—(3.3.27) hold are given in Table 3.1.

Parameters	Schnakenberg model	Thomas model
a_{11}	1	1
a_{12}	0	0
a_{21}	1	0
a_{22}	1	1
k_1	0	0
k_2	$\gamma(a+b)$	$\gamma(a+b)$
k_3	$\frac{\gamma}{2}$	0
q	3	0
k_4	$\gamma(\max(a,b))$	$\gamma(\max(a,b))$
k_5	0	0
k_6	$\gamma(a+b)$	$\gamma(a+b)$

Table 3.1: Terms from §3.3 for which conditions (3.3.22)—(3.3.27) hold for the kinetics defined in (2.5.8) and (2.5.9) respectively.

3.5.5 Remark (Invariant rectangles for the Thomas model)**.** It can be shown, utilising the techniques of Smoller [1994], that there exist bounded invariant rectangles for the solutions of the Thomas model defined in (2.5.9). This implies global existence of solutions via Theorem 3.3.2. However, we can show that it is possible to construct growth functions that fulfil Assumption 3.2.2, for which the bounded invariant rectangle can be made arbitrarily large. This necessitates the Lyapunov function approach to show existence and uniqueness of solutions.

3.5.6 Remark (Further applications)**.** The analysis can be applied to a large number of problems unrelated to the theory of pattern formation. Garvie and Trenchea [2009] provide an example

applicable to ecology and the aforementioned paper of Morgan [1989] contains further examples as well as the numerous citations of said paper that use the approach on various problems.

3.6 Conclusion

Many problems in biology and biomedicine involve growth. In developmental biology recent advances in experimental data collection allow experimentalists to capture the emergence of pattern structure formation during growth development of the organisms or species. Such experiments include the formation of spot patterns on the surface of the eel, patterns emerging on the surface of the Japanese flounder and butterfly wing patterns forming during the growth development of the imaginal wing disc. In all these examples, patterns form during growth development.

Since the seminal paper by Turing, A. M. [1952] which considered linear models that could give rise to spatiotemporal solutions on fixed domains due the process of diffusion-driven instability, a lot of theoretical results on global existence of such solutions have been derived and proved for highly nonlinear mathematical models [Rothe, 1984; Smoller, 1994]. Only recently, mathematical models on growing domains have been derived from first principles in order to incorporate the effects of domain evolution into the models [Crampin et al., 1999; Madzvamuse, 2000]. In all these studies, very little analysis has been done up to now to extend the theoretical global existence results to models defined on evolving domains.

Under suitable assumptions, we have extended existence results from problems posed on fixed domains to problems posed on an evolving domain. We have illustrated the applicability of the existence results of Morgan [1989] to problems on evolving domains. We have shown that global existence of solutions of many commonly encountered RDSs on fixed domains implies global existence of solutions of the same RDSs on a class of evolving domains. The results are significant in the theory of pattern formation especially in fields such as developmental biology where problems posed on evolving domains are commonly encountered. Our results hold with no assumptions on the sign of the growth rate which may prove useful in other fields where monotonic domain growth is not valid from a modelling perspective. The applicability of our results is demonstrated by considering different forms of domain evolution (linear, logistic and exponential). Extension of our work onto domains or surfaces with more complex evolution is an important area for future research.

In this Chapter we have proved some qualitative properties of the solutions to RDSs on evolving domains. In the next Chapter, in order to gain insight into the behaviour of the solutions, we propose a numerical method to approximate RDSs on evolving domains. The theoretical results obtained in this Chapter are an important justification for the assumptions we make on the continuous problem in the analysis of the numerical method.

Chapter 4

Analysis of a FEM for RDSs on evolving domains

4.1 Aims and Outline

Now that we have established existence and uniqueness of solutions to RDSs on a class of evolving domains, we turn to the numerical approximation of solutions to RDSs on evolving domains. In this Chapter we propose and analyse a numerical method to approximate the solution to RDSs on continuously evolving domains.

The layout of the remainder of this Chapter is as follows: We start with §4.2 introducing (very briefly) some background on numerical methods to approximate partial differential equations (PDEs). In §4.3 we motivate the analysis of numerical methods to approximate RDSs on evolving domains and we introduce the content of the proceeding sections. In §4.4 we define our notation, we state our model problem together with the assumptions that we make on the problem data and the domain evolution. We present the weak formulation of the continuous problem and define a modified nonlinear reaction function which we introduce for the analysis. In §4.5 we present the *semidiscrete* (space-discrete) and fully discrete finite element schemes, we show that both schemes converge with optimal order in the $L_\infty\big(0,T;L_2(\Omega_t)^m\big)$ norm. We also derive a stability result in the semidiscrete case, whereby the stabilising effect of domain growth observed in the continuous case is preserved. In §4.6 we derive a residual based a posteriori error estimator for the error in the semidiscrete case with a view to constructing a space-adaptive scheme for the approximation of RDSs. In §4.7 we provide a concrete implementation of the finite element scheme with reaction kinetics commonly encountered in developmental biology, on domains with spatially linear and nonlinear evolution. In §4.8 we perform some numerical experiments to validate our theoretical results. Finally, in §4.9 we summarise our results, draw some conclusions and indicate possible directions for future research.

4.2 Background

In general there is to date no systematic way of constructing exact analytical solutions to nonlinear PDEs (which are usually of most relevance in modelling applications). To gain insight into the solutions of these problems, a *numerical* or *computational* approximation of the solution is therefore desired. The basic idea of constructing a numerical approximation to a continuous problem is to discretise the problem and then to solve the resulting discrete problem computationally.

Many numerical methods have been proposed for the approximation of partial differential equations, one example is the spectral method [Orszag and Patterson, 1972]. In a spectral method we represent the solution of a PDE with a Fourier series which we then approximate often using the fast Fourier transform. Other widely used numerical methods for the approximation of PDEs are finite difference methods, finite volume methods and finite element methods. In all of these methods, the approximate solution is calculated on a *triangulated* (meshed) geometry. In a finite difference method we seek to approximate the solutions to a PDE by replacing the partial derivatives with finite difference (difference quotient) operators [Morton and Mayers, 2005]. In a finite volume method we use the divergence theorem to express volume integral (of divergence) terms over elements (volumes) of the triangulation as surface integrals (fluxes over the volume edges) [Versteeg and Malalasekera, 2007]. In a finite element method (FEM) we seek to approximate solutions to PDEs given in variational form, using a Galërkin procedure that consists of looking for approximate solutions in an appropriate finite dimensional space rather than the infinite dimensional space inhabited by the solution of the variational problem [Braess, 2001]. We shall only consider the conforming FEM, where the finite dimensional space in which we seek to compute an approximate solution is a subspace of the space inhabited by the solution to the variational problem. In practice the FEM has many attractive properties, both from an applications viewpoint such as ease of application to complex geometries and the possibility of varying levels of accuracy and from a mathematical analysis viewpoint, due to the suitability of the well developed analytic frameworks for variational problems.

The problems we are interested in are parabolic systems of PDEs which admit a variational form but may be posed on complex evolving geometries. As is common in most numerical methods for time-dependent problems, we proceed by splitting up the spatial and temporal discretisation. We apply the FEM for the spatial approximation and a finite difference method for the temporal approximation.

4.3 Introduction

RDSs are a useful tool for the modelling of pattern formation phenomena in diverse fields including biology [Cantrell and Cosner, 2003], chemistry [Lee et al., 1994], metallurgy [Onishi and Fujibuchi, 1976] and combustion [Matkowsky and Sivashinsky, 1978]. Our primary focus is applications to the field of developmental biology. Pattern formation within this context generally occurs during growth development [Murray, 2003] and is therefore typically modelled by RDSs that exhibit diffusion-driven instability on growing domains. The nonlinear reaction kinetics inherent in the models and the continuous evolution of the domain means that closed form analytical solutions to the problems can not be obtained and numerical simulations are necessary to gain insight into the nature of solutions.

Numerical simulations of RDSs that attempt to reproduce empirically observed pattern formation processes in developmental biology abound in the literature [Barrio et al., 2009; Kondo and Asai, 1995; Miura et al., 2006] and the analysis of schemes to approximate the solution to RDSs on fixed or evolving domains is an important area of research. On fixed domains, Zhang et al. [2008] analyse a second order implicit-explicit finite element scheme for the Gray-Scott model and Garvie and Trenchea [2007] analyse a first order scheme for an RDS that models predator prey dynamics. Recently Mackenzie and Madzvamuse [2011] analysed a finite difference scheme to approximate the solution of a linear RDS on a domain with continuous spatially linear isotropic evolution. Our study is novel in that, we propose and analyse a finite element method

to approximate RDSs on a domain with continuous (possibly nonlinear) evolution. The finite element method is very robust for the applications we have in mind, as the problems are often posed on complex geometries such as the surface of an organism. We assume prescribed domain evolution and we derive equivalent (up-to numerical quadrature) finite element formulations via the Eulerian and the Lagrangian frameworks, common in fluid dynamics. In the Eulerian framework the problem is discretised on a fixed reference domain while in the Lagrangian framework the problem is discretised on the evolving domain with the movement of the mesh following the flow of the fluid. To deal with the nonlinear reaction kinetics, we make some assumptions on the regularity of the continuous problem guided by the theoretical results in Chapter 3. Although we have in mind applications relating to biological pattern formation, we formulate the scheme with abstract reaction kinetics and domain evolution, so the analysis is applicable to problems in other fields. For simplicity we restrict our discussion to the case where both the reference domain and the evolving domain are embedded in the same spatial dimension. In Appendix A.1 we extend the method derived in this Chapter to the case where the reference domain is planar ($\hat{\Omega} \subset \mathbb{R}^2$) and the evolving domain is an open surface embedded in $\mathbb{R}^3$, that admits an orthogonal parameterisation (cf. (A.1.4)).

4.4 Problem setup

The model problem we wish to consider is Problem (2.4.7), a semilinear RDS posed on a continuously evolving domain (see §2.4 for the details). We assume the domain $\Omega_t \subset \mathbb{R}^d,\ d = 1, 2, 3$ is a simply connected, bounded, continuously deforming domain with respect to t, with Lipschitz boundary $\partial\Omega_t$ at time $t \in [0, T]$. We assume the function $\boldsymbol{f} := (f_1, \ldots, f_m)^{\mathsf{T}}$ is a vector of nonlinear coupling terms that is locally Lipschitz, $\boldsymbol{D} := (D_1, \ldots, D_m)^{\mathsf{T}}$ is a vector of strictly positive diffusion coefficients, $\boldsymbol{a} = (a_1, \ldots, a_d)^{\mathsf{T}}$ is a flow velocity generated by the evolution of the domain and the initial data $\boldsymbol{u}^0(\boldsymbol{x})$ is a bounded vector-valued function. We define the space-time domain

$$\mathcal{Q}_T := \left\{(\boldsymbol{x}, t) : \boldsymbol{x} \in \Omega_t, t \in [0, T]\right\}. \tag{4.4.1}$$

4.4.1 Assumption (Bounded solutions and classically differentiable reaction function)**.** We assume $\boldsymbol{u}$ the solution to (2.4.7) is bounded for all t in $[0, T]$. For $i = 1, \ldots, m$, we define

$$\begin{cases} u_i^- & := \inf_{\mathcal{Q}_T} u_i, \\ u_i^+ & := \sup_{\mathcal{Q}_T} u_i. \end{cases} \tag{4.4.2}$$

We denote by

$$\boldsymbol{I}_{\boldsymbol{u}} := \prod_{i=1}^{m} [u_i^-, u_i^+] \subset \mathbb{R}^m, \tag{4.4.3}$$

the range of $\boldsymbol{u}$. Given $\delta \in \mathbb{R}^+$, we denote by $\boldsymbol{I}_\delta$ the closed region

$$I_\delta := \prod_{i=1}^{m} [u_i^- - \delta, u_i^+ + \delta]. \tag{4.4.4}$$

Furthermore, we assume the nonlinear reaction function $\boldsymbol{f}$ belongs to $C^1(\boldsymbol{I}_\delta)$ for some fixed δ.

4.4.2 Remark (Applicability of Assumption 4.4.1)**.** In Chapter 3, we have shown the global existence of positive classical solutions to problem (2.4.7) for a class of RDSs with positive initial

data on domains with bounded spatially linear isotropic evolution. In this case, if $\boldsymbol{f}$ belongs to $C^1(\mathbb{R}^m_+)$ and $\boldsymbol{u}_0 \geq 0$, then, Assumption 4.4.1 holds with the region $\boldsymbol{I}_\delta$ a subset of $\mathbb{R}^m_+$.

4.4.3 Assumption (Regularity of the mapping)**.** We assume the following regularity on the mapping $\boldsymbol{\mathcal{A}}$ between the evolving domain Ω_t and the reference domain $\hat{\Omega}$, introduced in §2.3.

$$\boldsymbol{\mathcal{A}} \in C^1(0,T) \cap C^{k+1}\big(\hat{\Omega}\big), \tag{4.4.5}$$

where k will be taken equal to the degree of the basis functions of the finite element space defined in the sequel. To ensure the mapping is invertible we assume the determinant of the Jacobian J of the mapping $\boldsymbol{\mathcal{A}}$ (cf. (2.3.2)) satisfies

$$J > 0 \text{ in } \hat{\Omega} \times [0,T]. \tag{4.4.6}$$

4.4.4 Assumption (Flow velocity)**.** We assume that the flow velocity $\boldsymbol{a}$ is identical to the domain velocity, i.e.,

$$\boldsymbol{a}\big(\boldsymbol{\mathcal{A}}(\xi,t),t\big) = \partial_t \boldsymbol{\mathcal{A}}(\boldsymbol{\xi},t) \quad \forall t \in [0,T], \boldsymbol{\xi} \in \hat{\Omega}. \tag{4.4.7}$$

4.4.5 Remark (Regularity under the mapping)**.** Classical results [Adams and Fournier, 2003, Th. 3.41] allow us to relate regularity on the evolving domain to regularity on the reference domain. Let Assumption 4.4.3 hold. For a function $g : \mathcal{Q}_T \to \mathbb{R}$ with the corresponding function on the reference domain $\hat{g} : \hat{\Omega} \times [0,T] \to \mathbb{R}$ defined by (2.3.6), we have for $p = 1, \ldots, \infty$ and $l = 0, \ldots, k+1$,

$$u \in L_p\left(0,T; H^l(\Omega_t)\right) \iff \hat{u} \in L_p\left(0,T; H^l\big(\hat{\Omega}\big)\right). \tag{4.4.8}$$

$$\partial_t u \in L_p\left(0,T; H^l(\Omega_t)\right) \iff \partial_t \hat{u} \in L_p\left(0,T; H^l\big(\hat{\Omega}\big)\right). \tag{4.4.9}$$

4.4.6 Remark (Sufficient but not necessary regularity)**.** For the applications we have in mind the domain velocity is prescribed and Assumption 4.4.3 is valid. Deriving minimal assumptions on the regularity of the mapping is not the focus of this study. Formaggia and Nobile [1999, Pr. 2.1] show that necessary and sufficient conditions for the regularity result (4.4.8) with $k = 0$ are

$$J > 0, \boldsymbol{\mathcal{A}} \in W^{1,\infty}\big(\hat{\Omega}\big) \text{ and } \boldsymbol{\mathcal{A}}^{-1} \in W^{1,\infty}(\Omega_t). \tag{4.4.10}$$

Minimal regularity assumptions would be important if the mapping was determined by the finite element functions. For example, scenarios we wish to consider in future studies are the case of concentration driven domain evolution or the case where evolution of the boundary curve of the domain alone is prescribed and the internal nodes are moved according to principles of elasticity.

4.4.7 Weak formulations

For the purposes of constructing a finite element discretisation, we introduce a *weak formulation* associated with Problem (2.4.7). The problem is to find $u_i \in L_2\big(0,T; H^1(\Omega_t)\big)$ with $\partial_t u_i \in L_2\big(0,T; L_2(\Omega_t)\big)$ such that for $i = 1, \ldots, m$,

$$\big\langle \partial_t u_i + \nabla \cdot (\boldsymbol{a} u_i), \chi \big\rangle_{\Omega_t} + \langle D_i \nabla u_i, \nabla \chi \rangle_{\Omega_t} = \big\langle f_i(\boldsymbol{u}), \chi \big\rangle_{\Omega_t} \quad \forall \chi \in H^1(\Omega_t). \tag{4.4.11}$$

Recalling the notation of §2.3, we use (2.3.7) and (4.4.8) to write an equivalent formulation on the reference domain $\hat{\Omega}$. Find $\hat{u}_i \in L_2\big(0,T; H^1\big(\hat{\Omega}\big)\big)$ with $\partial_t \hat{u}_i \in L_2\big(0,T; L_2\big(\hat{\Omega}\big)\big)$ such that

$$\Big\langle J\left(\partial_t \hat{u}_i + \hat{u}_i \nabla \cdot \boldsymbol{a}(\boldsymbol{\mathcal{A}}(\boldsymbol{\xi},t),t)\right), \hat{\chi} \Big\rangle_{\hat{\Omega}} + \langle D_i J \boldsymbol{K} \nabla \hat{u}_i, \boldsymbol{K} \nabla \hat{\chi} \rangle_{\hat{\Omega}} = \big\langle J f_i(\hat{\boldsymbol{u}}), \hat{\chi} \big\rangle_{\hat{\Omega}} \quad \forall \hat{\chi} \in H^1\big(\hat{\Omega}\big). \tag{4.4.12}$$

Using the expression for the time-derivative of the determinant of the Jacobian (2.3.5), we have

$$\left\langle \partial_t(J\hat{u}_i), \hat{\chi} \right\rangle_{\hat{\Omega}} + \left\langle D_i J \boldsymbol{K} \nabla \hat{u}_i, \boldsymbol{K} \nabla \hat{\chi} \right\rangle_{\hat{\Omega}} = \left\langle J f_i(\hat{\boldsymbol{u}}), \hat{\chi} \right\rangle_{\hat{\Omega}} \quad \forall \hat{\chi} \in H^1\big(\hat{\Omega}\big). \tag{4.4.13}$$

We shall use (4.4.13) to construct a finite element scheme to approximate the solution to Problem (2.4.7) on the reference domain. In §4.7 we illustrate that the resultant scheme may be solved on the reference or the evolving domain. We now define a weak formulation on the evolving domain, where we assume regularity in time on the test functions (we are effectively assuming the test functions have the same regularity in time as the solution). We assume the test functions $\hat{\chi} \in H^1\big(\hat{\Omega}\big)$ and $\partial_t \hat{\chi} \in L_2\big(\hat{\Omega}\big)$. Therefore due to the regularity of the mapping (cf. §2.3) and the relationship between time-differentiation on the reference and evolving domains (2.3.7) $\chi \in H^1(\Omega_t)$ and $\partial_t \chi \in L_2(\Omega_t)$. We obtain the following weak formulation on Ω_t, find $u_i \in L_2\big(0,T; H^1(\Omega_t)\big)$ with $\partial_t u_i \in L_2\big(0,T; L_2(\Omega_t)\big)$ such that

$$\begin{aligned} \frac{\mathrm{d}}{\mathrm{d}t} \left\langle u_i, \chi \right\rangle_{\Omega_t} - \left\langle u_i, \partial_t \chi + \boldsymbol{a} \cdot \nabla \chi \right\rangle_{\Omega_t} + \left\langle D_i \nabla u_i, \nabla \chi \right\rangle_{\Omega_t} = \left\langle f_i(\boldsymbol{u}), \chi \right\rangle_{\Omega_t}, \\ \forall \chi \in H^1(\Omega_t) \text{ and } \partial_t \chi \in L_2(\Omega_t). \end{aligned} \tag{4.4.14}$$

4.4.8 *Cut-off* nonlinear reaction function

In general the techniques used to show Assumption 4.4.1 holds utilise the maximum principle [Smoller, 1994], Chapter 3. In the discrete case, the absence of a maximum principle [Thomée, 2006, pg. 83] means we cannot guarantee the discrete solution remains in the region $\boldsymbol{I}_\delta$. For the purposes of our analysis we introduce a modified *globally Lipschitz* nonlinear reaction function. Recalling $\boldsymbol{I}_\delta$ from Assumption 4.4.1, we define $\widetilde{\boldsymbol{f}} \in C^1(\mathbb{R}^m)$ such that

$$\begin{cases} \widetilde{\boldsymbol{f}}(\boldsymbol{z}) = \boldsymbol{f}(\boldsymbol{z}) \quad \text{for } \boldsymbol{z} \in \boldsymbol{I}_\delta \\ \left| \widetilde{\boldsymbol{f}}'(\boldsymbol{z}) \right| < \widetilde{C} \quad \text{for } \boldsymbol{z} \in \mathbb{R}^m. \end{cases} \tag{4.4.15}$$

The function $\widetilde{\boldsymbol{f}}$ exists due to Assumption 4.4.1 (an extension of $\boldsymbol{f}$ with constant gradient outside $\boldsymbol{I}_\delta$ suffices). We note that due to Assumption 4.4.1, if $\boldsymbol{u}$ is a solution of (2.4.7)

$$\widetilde{\boldsymbol{f}}(\boldsymbol{u}) = \boldsymbol{f}(\boldsymbol{u}). \tag{4.4.16}$$

Thus, we may without restriction replace $\boldsymbol{f}$ with $\widetilde{\boldsymbol{f}}$ in (2.4.7).

4.5 Finite element method

We shall split the spatial and temporal discretisation of Problem (2.4.7) into separate steps. For the spatial approximation, we employ a conforming finite element method. To this end, we define $\hat{\mathscr{T}}$ a triangulation of the reference domain. We shall consistently denote by $\hat{h} := \max_{s \in \hat{\mathscr{T}}} \operatorname{diam}(s)$ the mesh-size of $\hat{\mathscr{T}}$. We assume the triangulation $\hat{\mathscr{T}}$ fulfils the following properties:

- By $\mathsf{s} \in \hat{\mathscr{T}}$ we mean s is an open simplex (interval, triangle or tetrahedron for $d = 1, 2$ or 3 respectively).

- $\hat{\mathscr{T}}$ is conforming, i.e., for any $\mathsf{s}_i, \mathsf{s}_j \in \hat{\mathscr{T}}$, $\bar{\mathsf{s}}_i \cap \bar{\mathsf{s}}_j$ is either $\emptyset$, a vertex, an edge or a face common to s_i and s_j or the full simplex $\bar{\mathsf{s}}_i = \bar{\mathsf{s}}_j$.
- No error due to boundary approximation, i.e., $\cup_{\mathsf{s}\in\hat{\mathscr{T}}}\bar{\mathsf{s}} = \bar{\hat{\Omega}}$ (we make this assumption for ease of exposition and it may be relaxed depending on the applications in mind).

For a sequence $\{\hat{\mathscr{T}}_k\}_{k=1}^{\infty}$ of conforming triangulations, we assume the *quasi-uniformity* of the sequence holds, i.e., there exist C_1, C_2 independent of k such that

$$C_1\hat{h} \leq \hat{h}_s \leq C_2\hat{h}^{\circ}_{\mathsf{s}}, \quad \text{for all } \mathsf{s} \in \hat{\mathscr{T}}_k, k = 1, 2, \ldots, \tag{4.5.1}$$

where $\hat{h}^{\circ}_{\mathsf{s}}$ and $\hat{h}_{\mathsf{s}}$ are the radius of the largest ball contained in s and the diameter of s respectively. Furthermore we note that our assumption of quasi-uniformity implies that the family of triangulations is *shape-regular* [Schwab, 1998, pg. 159].

Given the triangulation $\hat{\mathscr{T}}$, we now define a *finite element space* on the reference configuration,

$$\hat{\mathbb{V}} := \left\{\hat{\Phi} \in H^1\big(\hat{\Omega}\big) : \hat{\Phi}|_s \text{ is piecewise polynomial of degree } \ell\right\}. \tag{4.5.2}$$

We utilise the following known results about the accuracy of the finite element space $\hat{\mathbb{V}}$. By the definition of $\hat{\mathbb{V}}$, we have for $\hat{v} \in H^{\ell+1}\big(\hat{\Omega}\big)$ (see for example Brenner and Scott [2002] or Thomée [2006]),

$$\inf_{\hat{\Phi}\in\hat{\mathbb{V}}} \left\{ \left\|\hat{v} - \hat{\Phi}\right\|_{L_2\left(\hat{\Omega}\right)} + \hat{h}\left\|\nabla(\hat{v} - \hat{\Phi})\right\|_{L_2\left(\hat{\Omega}\right)} \right\} \leq C\hat{h}^{\ell+1}\left|\hat{v}\right|_{H^{\ell+1}\left(\hat{\Omega}\right)}. \tag{4.5.3}$$

In the analysis we shall make use of the fact that (4.5.3) is satisfied by taking the Lagrange interpolant $\Lambda^h\hat{v} : H^{\ell+1}\big(\hat{\Omega}\big) \to \hat{\mathbb{V}}$ in place of $\hat{\Phi}$. Let $\mathcal{I}^h : C^0 \to \hat{\mathbb{V}}$ be a Clément type interpolant [Clément, 1975] and $\ell + 1 > \frac{d}{2}$, where d is the spatial dimension. The following bound holds

$$\left\|\hat{v} - \mathcal{I}^h\hat{v}\right\|_{L_\infty\left(\hat{\Omega}\right)} \leq C\hat{h}^{\ell+1-d/2}\left|\hat{v}\right|_{H^{\ell+1}\left(\hat{\Omega}\right)}. \tag{4.5.4}$$

We shall make use of the following inverse estimate valid on quasiuniform sequences of triangulations:

$$\|\hat{\Phi}\|_{L_\infty(\hat{\mathbb{V}})} \leq C\hat{h}^{-d/2}\|\hat{\Phi}\|_{L_2(\hat{\mathbb{V}})} \quad \forall\hat{\Phi} \in \hat{\mathbb{V}}, \tag{4.5.5}$$

where d is the spatial dimension.

4.5.1 Semidiscrete approximation

We define the *semidiscrete approximation* (space-discrete) to the solution of Problem (2.4.7) to be a function $\hat{u}_i^h : [0, T] \to \hat{\mathbb{V}}$, such that for $i = 1, \ldots, m$,

$$\begin{cases} \left\langle \partial_t(J\hat{u}_i^h), \hat{\Phi}\right\rangle_{\hat{\Omega}} + \left\langle D_i J\boldsymbol{K}\nabla\hat{u}_i^h, \boldsymbol{K}\nabla\hat{\Phi}\right\rangle_{\hat{\Omega}} = \left\langle J\widetilde{f}_i(\hat{\boldsymbol{u}}^h), \hat{\Phi}\right\rangle_{\hat{\Omega}} \quad \forall\hat{\Phi} \in \hat{\mathbb{V}}, \\ \hat{u}_i^h(0) = \Lambda^h\hat{u}_i^0, \end{cases} \tag{4.5.6}$$

where Λ^h is the Lagrange interpolant.

4.5.2 Proposition (Solvability of the semidiscrete scheme)**.** *Let Assumptions 4.4.1 and 4.4.3 hold. Then, the semidiscrete scheme (4.5.6) possesses a unique solution $\hat{\boldsymbol{u}}^h \in L_\infty(0, T)^m$.*

Proof . In (4.5.6) if we write $\hat{u}_i^h(t)$ as $\sum_{j=1}^{\dim(\hat{\mathbb{V}})} \alpha_j \hat{\Phi}_j$, we obtain a system of $\dim(\hat{\mathbb{V}})$ ordinary differential equations for each i. By assumption the initial data for each ODE is bounded. From Assumption 4.4.3 and the construction of $\widetilde{\boldsymbol{f}}$ (4.4.15), we have that J, $\widetilde{\boldsymbol{f}}$ and their product are continuous globally Lipschitz functions. From ODE theory [Schmitt and Thompson, 1998] we conclude that (4.5.6) possesses a unique bounded solution. □

4.5.2.1 The effect of domain evolution on the semidiscrete solution

We now examine the stability of (4.5.6) and show that domain growth has a *diluting* or *stabilising* effect on the semidiscrete solution, mirroring results for the continuous problem [Labadie, 2008]. Taking $\hat{\Phi} = \hat{u}_i^h$ in (4.5.6) gives for $i = 1, \dots, m$,

$$\left\langle \partial_t(J\hat{u}_i^h), \hat{u}_i^h \right\rangle_{\hat{\Omega}} + \left\langle D_i J \boldsymbol{K} \nabla \hat{u}_i^h, \boldsymbol{K} \nabla \hat{u}_i^h \right\rangle_{\hat{\Omega}} = \left\langle J\widetilde{f}_i(\hat{\boldsymbol{u}}^h), \hat{u}_i^h \right\rangle_{\hat{\Omega}}. \tag{4.5.7}$$

For the first term on the left of (4.5.7) we have

$$\left\langle \partial_t(J\hat{u}_i^h), \hat{u}_i^h \right\rangle_{\hat{\Omega}} = \frac{\mathrm{d}}{\mathrm{d}t} \left\langle J\hat{u}_i^h, \hat{u}_i^h \right\rangle_{\hat{\Omega}} - \left\langle J\hat{u}_i^h, \partial_t \hat{u}_i^h \right\rangle_{\hat{\Omega}}. \tag{4.5.8}$$

Using (2.3.6) and (2.3.7) we have

$$\left\langle \partial_t(J\hat{u}_i^h), \hat{u}_i^h \right\rangle_{\hat{\Omega}} = \frac{\mathrm{d}}{\mathrm{d}t} \left\langle u_i^h, u_i^h \right\rangle_{\Omega_t} - \left\langle u_i^h, \partial_t u_i^h + \boldsymbol{a} \cdot \nabla u_i^h \right\rangle_{\Omega_t}. \tag{4.5.9}$$

Application of Reynold's transport theorem (2.4.4) gives

$$\left\langle \partial_t(J\hat{u}_i^h), \hat{u}_i^h \right\rangle_{\hat{\Omega}} = \frac{1}{2} \left(\frac{\mathrm{d}}{\mathrm{d}t} \left\langle u_i^h, u_i^h \right\rangle_{\Omega_t} + \left\langle u_i^h, u_i^h \nabla \cdot \boldsymbol{a} \right\rangle_{\Omega_t} \right). \tag{4.5.10}$$

Now dealing with the right hand side of (4.5.7), using (4.4.15) and the mean-value theorem (MVT) we have

$$\begin{aligned} \left| \widetilde{f}_i(\hat{\boldsymbol{u}}^h) \right| &\leq \left| \widetilde{f}_i(\boldsymbol{0}) \right| + \left| \widetilde{f}_i(\hat{\boldsymbol{u}}^h) - \widetilde{f}_i(\boldsymbol{0}) \right| \\ &\leq \left| \widetilde{f}_i(\boldsymbol{0}) \right| + \widetilde{C} \sum_{j=1}^{m} \left| \hat{u}_j^h \right|, \end{aligned} \tag{4.5.11}$$

where $\widetilde{C}$ is the Lipschitz constant of $\widetilde{\boldsymbol{f}}$. Therefore using (2.3.6) and (4.5.11)

$$\left| \left\langle J\widetilde{f}_i(\hat{\boldsymbol{u}}^h), \hat{u}_i^h \right\rangle_{\hat{\Omega}} \right| \leq \widetilde{C} \left\langle \sum_{j=1}^{m} \left| u_j^h \right|, \left| u_i^h \right| \right\rangle_{\Omega_t} + \left| \left\langle \widetilde{f}_i(0), u_i^h \right\rangle_{\Omega_t} \right|. \tag{4.5.12}$$

Applying Young's inequality gives

$$\begin{aligned} \left| \left\langle J\widetilde{f}_i(\hat{\boldsymbol{u}}^h), \hat{u}_i^h \right\rangle_{\hat{\Omega}} \right| \leq & \widetilde{C} \left(\frac{1}{2} \sum_{j \neq i} \left\| u_j^h \right\|_{L_2(\Omega_t)}^2 + \frac{m+1}{2} \left\| u_i^h \right\|_{L_2(\Omega_t)}^2 \right) \\ & + \frac{1}{2} \left\| u_i^h \right\|_{L_2(\Omega_t)}^2 + C_{\widetilde{f}_i(\boldsymbol{0})}, \end{aligned} \tag{4.5.13}$$

where m is the number of components of the RDS and $C_{\widetilde{f}_i(\mathbf{0})} \in \mathbb{R}^+$ depends on $\left|\widetilde{f}_i(\mathbf{0})\right|$. Summing over i we have

$$\sum_{i=1}^{m} \left| \left\langle J\widetilde{f}_i(\hat{\boldsymbol{u}}^h), \hat{u}_i^h \right\rangle_{\hat{\Omega}} \right| \leq \left(\widetilde{C}m + \frac{1}{2} \right) \left\| \boldsymbol{u}^h \right\|^2_{L_2(\Omega_t)^m} + C_{\widetilde{\boldsymbol{f}}(\mathbf{0})}. \tag{4.5.14}$$

Using (2.3.9), (4.5.10) and (4.5.14) in (4.5.7) gives

$$\begin{aligned} \frac{\mathrm{d}}{\mathrm{d}t} \left\| \boldsymbol{u}^h \right\|^2_{L_2(\Omega_t)^m} + 2\sum_{i=1}^{m} D_i \left\| \nabla u_i^h \right\|^2_{L_2(\Omega_t)} \leq \left\langle \left(2\widetilde{C}m + 1 - \nabla \cdot \boldsymbol{a} \right) \boldsymbol{u}^h, \boldsymbol{u}^h \right\rangle_{\Omega_t{}^m} \\ + 2C_{\widetilde{\boldsymbol{f}}(\mathbf{0})}. \end{aligned} \tag{4.5.15}$$

Finally, integrating in time and applying Gronwall's lemma we have

$$\left\| \boldsymbol{u}^h(t) \right\|^2_{L_2(\Omega_t)^m} \leq \left(\left\| \boldsymbol{u}^h(0) \right\|^2_{L_2(\Omega_0)^m} + 2tC_{\widetilde{\boldsymbol{f}}(\mathbf{0})} \right) \exp\left(\sup_{\mathcal{Q}_T} \left\{ 2\widetilde{C}m + 1 - \nabla \cdot \boldsymbol{a} \right\} t \right). \tag{4.5.16}$$

From (2.3.5), the dilution term $\nabla \cdot \boldsymbol{a}$ has the same sign as $\partial_t J$ and is therefore positive (negative) if the domain is growing (contracting). Thus, domain growth has a diluting effect on the $L_2(\Omega_t)^m$ norm of the solution.

4.5.2.2 A priori analysis of the semidiscrete scheme

We now prove the error between the exact solution and the semidiscrete solution converges with optimal order in the $L_\infty\Big([0,T]; L_2\big(\hat{\Omega}\big)^m\Big)$ norm. A central role in the analysis is played by the Ritz (elliptic) projection originally introduced by Wheeler [1973]. Given $\hat{u}_i \in H^1\big(\hat{\Omega}\big)$, the *Ritz projection* $\mathrm{R}^h : H^1\big(\hat{\Omega}\big) \to \hat{\mathbb{V}}$ is defined to be the finite element solution of a corresponding elliptic problem:

$$\langle \nabla(\hat{u}_i - \mathrm{R}^h\, \hat{u}_i), \nabla\hat{\Phi} \rangle_{\hat{\Omega}} = 0 \quad \forall \hat{\Phi} \in \hat{\mathbb{V}}. \tag{4.5.17}$$

With the Ritz projection as defined above we have the following expression for the time-derivative of (4.5.17):

$$\langle \nabla\partial_t(\hat{u}_i - \mathrm{R}^h\, \hat{u}_i), \nabla\hat{\Phi} \rangle_{\hat{\Omega}} = 0 \quad \forall \hat{\Phi} \in \hat{\mathbb{V}}. \tag{4.5.18}$$

To obtain optimal error estimates, we now decompose the error into an *elliptic error* (the error between the Ritz projection and the exact solution) and a *parabolic error* (the error between the semidiscrete solution and the Ritz projection):

$$\begin{aligned} \left\| \hat{\boldsymbol{u}}^h - \hat{\boldsymbol{u}} \right\|^2_{L_2\left(\hat{\Omega}\right)^m} &\leq \left\| \hat{\boldsymbol{u}} - \mathrm{R}^h\, \hat{\boldsymbol{u}} \right\|^2_{L_2\left(\hat{\Omega}\right)^m} + \left\| \mathrm{R}^h\, \hat{\boldsymbol{u}} - \hat{\boldsymbol{u}}^h \right\|^2_{L_2\left(\hat{\Omega}\right)^m} \\ &= \left\| \hat{\boldsymbol{\varepsilon}} \right\|^2_{L_2\left(\hat{\Omega}\right)^m} + \left\| \hat{\boldsymbol{\rho}}^h \right\|^2_{L_2\left(\hat{\Omega}\right)^m}, \end{aligned} \tag{4.5.19}$$

where the equality defines $\hat{\boldsymbol{\rho}}^h = (\hat{\rho}_1^h, \ldots, \hat{\rho}_m^h)^\mathsf{T}$ and $\hat{\boldsymbol{\varepsilon}} = (\hat{\varepsilon}_1, \ldots, \hat{\varepsilon}_m)^\mathsf{T}$. We warn the reader that $\boldsymbol{\rho}$ which we consistently use in this Chapter to denote the parabolic error was previously used to denote an isotropic growth function in Chapter 3.

4.5.3 Lemma (Elliptic error)**.** *Suppose the exact solution $\boldsymbol{u}$ to Problem (2.4.7) is in $H^{\ell+1}(\Omega_t)^m$ with $\partial_t \boldsymbol{u}$ in $H^{\ell+1}(\Omega_t)^m$ where ℓ is the polynomial degree of the finite element space (4.5.2). Furthermore, suppose Assumptions 4.4.3 (with $k = \ell$) and 4.4.4 hold. Finally, let $\hat{\boldsymbol{u}}$ be as defined in (2.3.6) and R^h be the Ritz projection defined in (4.5.17). Then the following estimates hold for the error in the Ritz projection and its time-derivative.*

$$\begin{aligned}\sup_{t\in[0,T]} \Bigg\{ &\left\| \mathrm{R}^h \hat{\boldsymbol{u}}(t) - \hat{\boldsymbol{u}}(t) \right\|^2_{L_2(\hat{\Omega})^m} \\ &+ \hat{h}^2 \sum_{i=1}^m \left\| \nabla \left(\mathrm{R}^h \hat{u}_i(t) - \hat{u}_i(t) \right) \right\|^2_{L_2(\hat{\Omega})} \Bigg\} \leq C \hat{h}^{2(\ell+1)},\end{aligned} \tag{4.5.20}$$

and

$$\begin{aligned}\sup_{t\in[0,T]} \Bigg\{ &\left\| \partial_t \left(\mathrm{R}^h \hat{\boldsymbol{u}}(t) - \hat{\boldsymbol{u}}(t) \right) \right\|^2_{L_2(\hat{\Omega})^m} \\ &+ \hat{h}^2 \sum_{i=1}^m \left\| \nabla \partial_t \left(\mathrm{R}^h \hat{u}_i(t) - \hat{u}_i(t) \right) \right\|^2_{L_2(\hat{\Omega})} \Bigg\} \leq C \hat{h}^{2(\ell+1)},\end{aligned} \tag{4.5.21}$$

where $C \in \mathbb{R}^+$ is independent of the mesh-size $\hat{h}$.

Proof . Throughout the proof $C \in \mathbb{R}^+$ denotes an arbitrary constant independent of the mesh-size $\hat{h}$. We show the energy norm bound of (4.5.20) first. By (4.5.17), we have for $i = 1, \ldots, m$,

$$\begin{aligned}\|\nabla \hat{\varepsilon}_i\|^2_{L_2(\hat{\Omega})} &= \left| \left\langle \nabla \hat{\varepsilon}_i, \nabla(\hat{\Phi} - \hat{u}_i) \right\rangle_{(\hat{\Omega})} \right| \text{ for } \hat{\Phi} \in \hat{\mathbb{V}}, \\ &\leq \|\nabla \hat{\varepsilon}_i\|_{L_2 \hat{\Omega}} \left\| \nabla(\mathcal{I}^h \hat{u}_i - \hat{u}_i) \right\|_{L_2(\hat{\Omega})} \\ &\leq C \hat{h}^{\ell} \left| \hat{u}_i \right|_{H^{\ell+1}(\hat{\Omega})} \|\nabla \hat{\varepsilon}_i\|_{L_2(\hat{\Omega})} .\end{aligned} \tag{4.5.22}$$

In the above we have used (4.5.3) in the last step. Squaring and summing over i gives

$$\sum_{i=1}^m \|\nabla \hat{\varepsilon}_i\|^2_{L_2(\hat{\Omega})} \leq C \hat{h}^{2\ell} \left| \hat{\boldsymbol{u}} \right|^2_{H^{\ell+1}(\hat{\Omega})^m} . \tag{4.5.23}$$

We show the $L_2(\hat{\Omega})$ estimate of (4.5.20) by a duality (Aubin-Nitsche) argument. Let $\varphi \in L_2(\hat{\Omega})$ and $\omega \in H^2(\hat{\Omega})$ solve,

$$\begin{cases} -\Delta \omega &= \varphi \quad \text{in } \hat{\Omega}, \\ \boldsymbol{\nu} \cdot \nabla \omega &= 0 \quad \text{on } \partial\hat{\Omega}. \end{cases} \tag{4.5.24}$$

Testing (4.5.24) with ω gives

$$\left| \langle \nabla \omega, \nabla \omega \rangle_{\hat{\Omega}} \right| = \left| \langle \varphi, \omega \rangle_{\hat{\Omega}} \right| , \tag{4.5.25}$$

which implies

$$\left| \langle \omega, \Delta \omega \rangle_{\hat{\Omega}} \right| \leq \|\varphi\|_{L_2(\hat{\Omega})} \|\omega\|_{L_2(\hat{\Omega})} . \tag{4.5.26}$$

Using regularity results for elliptic equations, (4.5.24) and (4.5.26), we obtain

$$\begin{aligned} |\omega|_{H^2(\hat{\Omega})} &\leq C \|\Delta\omega\|_{L_2(\hat{\Omega})} \\ &\leq C \|\varphi\|_{L_2(\hat{\Omega})} . \end{aligned} \tag{4.5.27}$$

Testing (4.5.24) with $\hat{\varepsilon}_i$ and using (4.5.17), we have for $i = 1, \ldots, m$,

$$\begin{aligned} \left|\langle \hat{\varepsilon}_i, \varphi \rangle_{\hat{\Omega}}\right| &= \left| \left\langle \nabla\hat{\varepsilon}_i, \nabla(\omega - \hat{\Phi}) \right\rangle_{\hat{\Omega}} \right| \text{ for } \hat{\Phi} \in \hat{\mathbb{V}} \\ &\leq \|\nabla\hat{\varepsilon}_i\|_{L_2(\hat{\Omega})} \left\| \nabla(\omega - \mathcal{I}^h\hat{\omega}) \right\|_{L_2\hat{\Omega}} . \end{aligned} \tag{4.5.28}$$

Using the previous estimate (4.5.22), gives for $i = 1, \ldots, m$,

$$\begin{aligned} \left|\langle \hat{\varepsilon}_i, \varphi \rangle_{\hat{\Omega}}\right| \leq & C\hat{h}^{\ell} |\hat{u}_i|_{H^{\ell+1}(\hat{\Omega})} \left\| \nabla(\omega - \mathcal{I}^h\hat{\omega}) \right\|_{L_2(\hat{\Omega})} \\ \leq & C\hat{h}^{\ell+1} |\omega|_{H^2(\hat{\Omega})} |\hat{u}_i|_{H^{\ell+1}(\hat{\Omega})} , \end{aligned} \tag{4.5.29}$$

where we have used (4.5.3) in the last step. Summing over i and applying estimate (4.5.27) completes the proof of (4.5.20).

For the time-derivative estimates we once again show the energy norm bound first, using (4.5.18) and the fact $\partial_t \left(\mathrm{R}^h \hat{u}_i \right) \in \hat{\mathbb{V}}$, we have for $i = 1, \ldots, m$,

$$\begin{aligned} \|\nabla\partial_t\hat{\varepsilon}_i\|^2_{L_2(\hat{\Omega})} &= \left| \left\langle \nabla\partial_t\hat{\varepsilon}_i, \nabla(\hat{\Phi} - \partial_t\hat{u}_i) \right\rangle_{\hat{\Omega}} \right| \text{ for } \hat{\Phi} \in \hat{\mathbb{V}}. \\ &\leq \|\nabla\partial_t\hat{\varepsilon}_i\|_{L_2(\hat{\Omega})} \left\| \nabla(\mathcal{I}^h\partial_t\hat{u}_i - \partial_t\hat{u}_i) \right\|_{L_2(\hat{\Omega})} . \end{aligned} \tag{4.5.30}$$

Now using (4.5.3) gives for $i = 1, \ldots, m$,

$$\|\nabla\partial_t\hat{\varepsilon}_i\|^2_{L_2(\hat{\Omega})} \leq C\hat{h}^{\ell} |\partial_t\hat{u}_i|_{H^{\ell+1}(\hat{\Omega})} \|\nabla\partial_t\hat{\varepsilon}_i\|_{L_2(\hat{\Omega})} . \tag{4.5.31}$$

This completes the energy norm estimate in (4.5.21). For the $L_2(\hat{\Omega})$ estimate in (4.5.21), we use a duality argument. Testing (4.5.24) with $\partial_t\varepsilon_i$, we have for $i = 1, \ldots, m$,

$$\left|\langle \partial_t\hat{\varepsilon}_i, \varphi \rangle_{\hat{\Omega}}\right| = \left|\langle \nabla\partial_t\hat{\varepsilon}_i, \nabla\omega \rangle_{\hat{\Omega}}\right| . \tag{4.5.32}$$

Using (4.5.18) and the fact $\partial_t \left(\mathrm{R}^h \hat{u}_i \right) \in \hat{\mathbb{V}}$, we have for $i = 1, \ldots, m$,

$$\begin{aligned} \left|\langle \partial_t\hat{\varepsilon}_i, \varphi \rangle_{\hat{\Omega}}\right| &= \left| \left\langle \nabla\partial_t\hat{\varepsilon}_i, \nabla(\omega - \hat{\Phi}) \right\rangle_{\hat{\Omega}} \right| \text{ for } \hat{\Phi} \in \hat{\mathbb{V}}, \\ &\leq \|\nabla\partial_t\hat{\varepsilon}_i\|_{L_2(\hat{\Omega})} \left\| \nabla(\omega - \mathcal{I}^h\omega) \right\|_{L_2(\hat{\Omega})} . \end{aligned} \tag{4.5.33}$$

Using (4.5.3) and (4.5.31), we obtain for $i = 1, \ldots, m$,

$$\left|\langle \partial_t\hat{\varepsilon}_i, \varphi \rangle_{\hat{\Omega}}\right| \leq C\hat{h}^{\ell+1} |\omega|_{H^2(\hat{\Omega})} |\partial_t\hat{u}_i|_{H^{\ell+1}(\hat{\Omega})} . \tag{4.5.34}$$

Application of the estimate (4.5.27) completes the proof of (4.5.21). □

4.5.4 Theorem (A priori estimate for the semidiscrete scheme)**.** *Suppose the exact solution $\boldsymbol{u}$ to Problem (2.4.7) is in $H^{\ell+1}(\Omega_t)^m$ with $\partial_t \boldsymbol{u}$ in $H^{\ell+1}(\Omega_t)^m$ where ℓ is the polynomial degree of the finite element space (4.5.2). Furthermore, suppose Assumptions 4.4.3 (with $k = \ell$) and 4.4.4 hold. Finally let $\hat{\boldsymbol{u}}$ be as defined in (2.3.6) and let $\hat{\boldsymbol{u}}^h$ be the solution to Problem (4.5.6). Then, the following optimal a priori error estimate holds for the error in the semidiscrete scheme:*

$$\sup_{t\in[0,T]} \left\{ \left\| \hat{\boldsymbol{u}}^h(t) - \hat{\boldsymbol{u}}(t) \right\|^2_{L_2\left(\hat{\Omega}\right)^m} \right\} \leq C \hat{h}^{2(\ell+1)}, \tag{4.5.35}$$

where $C \in \mathbb{R}^+$ is independent of the mesh-size $\hat{h}$.

Proof . Throughout the proof $C \in \mathbb{R}^+$ denotes an arbitrary constant independent of the mesh-size $\hat{h}$. Using decomposition (4.5.19) and Lemma 4.5.3 we have a bound on the elliptic error and it simply remains to estimate the parabolic error $\hat{\boldsymbol{\rho}}^h$. To this end, we use (4.5.6) to construct a PDE for $\hat{\rho}_i^h$ by inserting $\hat{\rho}_i^h$ in place of $\hat{u}_i^h$ and taking $\hat{\Phi} = \hat{\rho}_i^h$. Using (2.3.9) we obtain for $i = 1, \ldots, m$,

$$\begin{aligned} \left\langle \partial_t \left(J\hat{\rho}_i^h \right), \hat{\rho}_i^h \right\rangle_{\hat{\Omega}} + D_i \left\| \nabla \rho_i^h \right\|^2_{L_2(\Omega_t)} &= \left\langle \widetilde{f}_i(\hat{\boldsymbol{u}}^h), J\hat{\rho}_i^h \right\rangle_{\hat{\Omega}} \\ &\quad - \left\langle \partial_t \left(J \, \mathrm{R}^h \, \hat{u}_i \right), \hat{\rho}_i^h \right\rangle_{\hat{\Omega}} - \left\langle J\boldsymbol{K} \nabla \, \mathrm{R}^h \, \hat{u}_i, \boldsymbol{K} \nabla \hat{\rho}_i^h \right\rangle_{\hat{\Omega}}. \end{aligned} \tag{4.5.36}$$

Using (4.4.13), (4.4.16) and (4.5.17) gives

$$\begin{aligned} \left\langle \partial_t \left(J\hat{\rho}_i^h \right), \hat{\rho}_i^h \right\rangle_{\hat{\Omega}} + D_i \left\| \nabla \rho_i^h \right\|^2_{L_2(\Omega_t)} &= \left\langle \widetilde{f}_i(\hat{\boldsymbol{u}}^h) - \widetilde{f}_i(\hat{\boldsymbol{u}}), J\hat{\rho}_i^h \right\rangle_{\hat{\Omega}} \\ &\quad - \left\langle \partial_t \left(J\hat{\varepsilon}_i \right), \hat{\rho}_i^h \right\rangle_{\hat{\Omega}}. \end{aligned} \tag{4.5.37}$$

Dealing with the first term on the left of (4.5.37) as in (4.5.10):

$$\left\langle \partial_t \left(J\hat{\rho}_i^h \right), \hat{\rho}_i^h \right\rangle_{\hat{\Omega}} = \frac{1}{2} \left(\frac{\mathrm{d}}{\mathrm{d}t} \left\| \rho_i^h \right\|^2_{L_2(\Omega_t)} + \left\langle \rho_i^h \nabla \cdot \boldsymbol{a}, \rho_i^h \right\rangle_{\Omega_t} \right). \tag{4.5.38}$$

Dealing with the first term on the right of (4.5.37) using (4.5.19) and the MVT we have

$$\left| \left\langle \widetilde{f}_i(\hat{\boldsymbol{u}}^h) - \widetilde{f}_i(\hat{\boldsymbol{u}}), J\hat{\rho}_i^h \right\rangle_{\hat{\Omega}} \right| \leq \widetilde{C} \left(\left\langle \sum_{j=1}^m \left(\left| \hat{\varepsilon}_j \right| + \left| \hat{\rho}_j^h \right| \right), J \left| \hat{\rho}_i^h \right| \right\rangle_{\hat{\Omega}} \right). \tag{4.5.39}$$

Applying Young's inequality:

$$\begin{aligned} \left| \left\langle \widetilde{f}_i(\hat{\boldsymbol{u}}^h) - \widetilde{f}_i(\hat{\boldsymbol{u}}), J\hat{\rho}_i^h \right\rangle_{\hat{\Omega}} \right| \leq \widetilde{C} \Bigg(& \left(m + \frac{1}{2} \right) \left\| \rho_i^h \right\|^2_{L_2(\Omega_t)} + \sum_{j \neq i} \frac{1}{2} \left\| \rho_j^h \right\|^2_{L_2(\Omega_t)} \\ & + \frac{1}{2} \left\| J \right\|_{L_\infty(\hat{\Omega}\times[0,T])} \left\| \hat{\boldsymbol{\varepsilon}} \right\|^2_{L_2\left(\hat{\Omega}\right)^m} \Bigg). \end{aligned} \tag{4.5.40}$$

Summing over i we have

$$\begin{aligned} \sum_{i=1}^m \left| \left\langle \widetilde{f}_i(\hat{\boldsymbol{u}}^h) - \widetilde{f}_i(\hat{\boldsymbol{u}}), J\hat{\rho}_i^h \right\rangle_{\hat{\Omega}} \right| \leq \widetilde{C} \Bigg(& \frac{3m}{2} \left\| \boldsymbol{\rho}^h \right\|^2_{L_2(\Omega_t)^m} \\ & + \frac{m}{2} \left\| J \right\|_{L_\infty(\hat{\Omega}\times[0,T])} \left\| \hat{\boldsymbol{\varepsilon}} \right\|^2_{L_2\left(\hat{\Omega}\right)^m} \Bigg). \end{aligned} \tag{4.5.41}$$

Dealing with the second term on the right of (4.5.37):

$$\begin{aligned}\left|\left\langle \partial_t \left(J\hat{\varepsilon}_i\right), \hat{\rho}_i^h \right\rangle_{\hat{\Omega}}\right| \leq & \left|\left\langle J\partial_t\hat{\varepsilon}_i, \hat{\rho}_i^h \right\rangle_{\hat{\Omega}}\right| + \left|\left\langle \partial_t\left(J\right)\hat{\varepsilon}_i, \hat{\rho}_i^h \right\rangle_{\hat{\Omega}}\right| \\ \leq & \frac{1}{2}\Bigg(\left\|\rho^h\right\|^2_{L_2(\Omega_t)} + \langle J\partial_t\hat{\varepsilon}_i, \partial_t\hat{\varepsilon}_i\rangle_{\hat{\Omega}} \\ & + \left\langle \left|\partial_t(J)\right| \hat{\rho}_i^h, \hat{\rho}_i^h \right\rangle_{\hat{\Omega}} + \left\langle \left|\partial_t(J)\right| \hat{\varepsilon}_i, \hat{\varepsilon}_i \right\rangle_{\hat{\Omega}} \Bigg),\end{aligned} \tag{4.5.42}$$

where we have used Young's inequality for the second step. Now using (2.3.5) and summing over i we have

$$\begin{aligned}\sum_{i=1}^m \left|\left\langle \partial_t \left(J\hat{\varepsilon}_i\right), \hat{\rho}_i^h \right\rangle_{\hat{\Omega}}\right| \leq \frac{1}{2}\Bigg(& \left\|\boldsymbol{\rho}^h\right\|^2_{L_2(\Omega_t)^m} + \left\langle \boldsymbol{\rho}^h \left|\nabla\cdot\boldsymbol{a}\right|, \boldsymbol{\rho}^h \right\rangle_{{\Omega_t}^m} \\ & + \|J\|_{L_\infty(\hat{\Omega}\times[0,T])} \left\|\partial_t\hat{\boldsymbol{\varepsilon}}\right\|^2_{L_2\left(\hat{\Omega}\right)^m} \\ & + \|\partial_t J\|_{L_\infty(\hat{\Omega}\times[0,T])} \left\|\hat{\boldsymbol{\varepsilon}}\right\|^2_{L_2\left(\hat{\Omega}\right)^m} \Bigg).\end{aligned} \tag{4.5.43}$$

Combining (4.5.38), (4.5.41), (4.5.43)

$$\begin{aligned}\frac{\mathrm{d}}{\mathrm{d}t}\left\|\boldsymbol{\rho}^h\right\|^2_{L_2(\Omega_t)^m} + 2\sum_{i=1}^m D_i \left\|\nabla\rho_i^h\right\|^2_{L_2(\Omega_t)} \leq C\Bigg(& \left\|\boldsymbol{\rho}^h\right\|^2_{L_2(\Omega_t)^m} + \left\|\hat{\boldsymbol{\varepsilon}}\right\|^2_{L_2\left(\hat{\Omega}\right)^m} \\ & + \left\|\partial_t\hat{\boldsymbol{\varepsilon}}\right\|^2_{L_2\left(\hat{\Omega}\right)^m} \Bigg),\end{aligned} \tag{4.5.44}$$

where we have used the fact that Assumption 4.4.3 implies $J, \partial_t J \in L_\infty\left(\hat{\Omega}\times[0,T]\right)$. Integrating in time, using Lemma 4.5.3 and applying Gronwall's Lemma we have

$$\left\|\boldsymbol{\rho}^h(t)\right\|^2_{L_2(\Omega_t)^m} \leq C\left(\left\|\boldsymbol{\rho}^h(0)\right\|^2_{L_2(\Omega_0)^m} + \hat{h}^{2(\ell+1)}\right). \tag{4.5.45}$$

To estimate $\boldsymbol{\rho}^h(0)$, we note

$$\begin{aligned}\left\|\boldsymbol{\rho}^h(0)\right\|_{L_2(\Omega_0)^m} \leq & C\left(\left\|\hat{\boldsymbol{u}}(0) - \Lambda^h\hat{\boldsymbol{u}}(0)\right\|_{L_2\left(\hat{\Omega}\right)^m} + \left\|\hat{\boldsymbol{\varepsilon}}^h\right\|_{L_2\left(\hat{\Omega}\right)^m}\right) \\ \leq & C\hat{h}^{\ell+1},\end{aligned} \tag{4.5.46}$$

where we have used (4.5.3), the assumption on the regularity of the exact solution and Lemma 4.5.3 in the last step. Assumption 4.4.3 and the equivalence of norms on the reference and evolving domains (2.3.8) completes the proof. □

4.5.5 Fully discrete approximation

We now propose a time discretisation of (4.5.6). To this end, we divide the time interval $[0,T]$ into a partition of N uniform subintervals, $0 = t_0 < \ldots < t_N = T$ and denote by $\tau := t_n - t_{n-1}$

the time step. We consistently use the following shorthand for a function of time: $f^n := f(t_n)$, we denote by $\bar{\partial} f^n := \tau^{-1}\left(f^n - f^{n-1}\right)$.

For the approximation in time we use a finite difference scheme, specifically the 1-SBEM a modified implicit Euler method where linear reaction terms and the diffusive term are treated implicitly while the nonlinear reaction terms are treated semi-implicitly using values from the previous timestep (a 1-step Picard linearisation). Our choice of timestepping scheme stems from the numerical investigation conducted by Madzvamuse [2006], where the 1-SBEM was deemed to be robust for the applications we have in mind.

The fully discrete scheme we employ to approximate the solution of Problem (2.4.7) is thus, find $\hat{U}_i^n \in \hat{\mathbb{V}}$, for $n = 1, \ldots, N$, such that for $i = 1 \ldots, m$, we have

$$\begin{cases} \left\langle \bar{\partial}\left[J\hat{U}_i\right]^n, \hat{\Phi}\right\rangle_{\hat{\Omega}} + D_i \left\langle [J\boldsymbol{K}\nabla\hat{U}_i]^n, \boldsymbol{K}^n\nabla\hat{\Phi}\right\rangle_{\hat{\Omega}} \\ \qquad\qquad = \left\langle J^n f_i\left(\hat{U}_i^n, \hat{\boldsymbol{U}}^{n-1}\right), \hat{\Phi}\right\rangle_{\hat{\Omega}} \qquad \forall \hat{\Phi} \in \hat{\mathbb{V}} \\ \hat{U}_i^0 = \Lambda^h \hat{u}_i^0, \end{cases} \tag{4.5.47}$$

where Λ^h is the Lagrange interpolant.

Alternatively we may look to approximate the solution to (2.4.7) on a conforming subspace of the evolving domain. To this end we define a family of finite dimensional spaces $\mathbb{V}_{t^n} \subset \Omega_{t^n}$, $n = [0, \ldots, N]$ such that

$$\mathbb{V}_{t^n} := \left\{\Phi^n : \Phi^n(\mathcal{A}(\boldsymbol{\xi}, t_n)) = \hat{\Phi}(\boldsymbol{\xi})\right\}, \tag{4.5.48}$$

which also defines the *triangulation* $\mathscr{T}^n$, $n = [0, \ldots, N]$ on the evolving domain. Using (4.5.47) and (4.5.48) we have the following equivalent finite element formulation on the evolving domain: find $U_i^n \in \mathbb{V}_{t^n}$, for $n = 1, \ldots, N$, such that for $i = 1 \ldots, m$,

$$\begin{cases} \bar{\partial}\left[\langle U_i, \Phi\rangle_{\Omega_t}\right]^n + D_i \langle \nabla U_i^n, \nabla\Phi^n\rangle_{\Omega_{t^n}} = \left\langle f_i\left(U_i^n, \boldsymbol{U}^{n-1}\right), \Phi^n\right\rangle_{\Omega_{t^n}} \\ U_i^0 = \Lambda^h u_i^0, \end{cases} \tag{4.5.49}$$

where $\Lambda^h : H^1(\Omega_0) \to \mathbb{V}_0$ is the Lagrange interpolant. By (2.3.7) and (4.5.48)

$$\partial_t \hat{\Phi}(\boldsymbol{\xi}) = \left[\partial_t\Phi + \boldsymbol{a}\cdot\nabla\Phi\right]\left(\boldsymbol{\mathcal{A}}(\boldsymbol{\xi}, t)\right) = 0. \tag{4.5.50}$$

Thus, (4.5.49) may be viewed as the finite element discretisation of formulation (4.4.14).

4.5.6 Theorem (A priori estimate for the fully discrete scheme)**.** *Suppose the exact solution $\boldsymbol{u}$ to Problem (2.4.7) is in $H^{\ell+1}(\Omega_t)^m$ with $\partial_t\boldsymbol{u}$ in $H^{\ell+1}(\Omega_t)^m$ where ℓ is the polynomial degree of the finite element space (4.5.2). Furthermore, suppose Assumptions 4.4.3 (with $k = \ell$) and 4.4.4 hold. Let $\hat{\boldsymbol{u}}$ be as defined in (2.3.6) and let $\hat{\boldsymbol{U}}$ be the solution to (4.5.47). Finally, suppose the timestep satisfies a stability condition defined in (4.5.61). Then, the following optimal a priori estimate holds for the error in the fully discrete scheme:*

$$\left\|\hat{\boldsymbol{U}}^n - \hat{\boldsymbol{u}}^n\right\|^2_{L_2\left(\hat{\Omega}\right)^m} \leq C\left(\hat{h}^{2(\ell+1)} + \tau^2\right) \quad \text{for } n \in [0, \ldots, N], \tag{4.5.51}$$

where $C \in \mathbb{R}^+$ is independent of the mesh-size $\hat{h}$ and the timestep τ.

Proof . Throughout the proof $C \in \mathbb{R}^+$ denotes an arbitrary constant independent of the mesh-size $\hat{h}$ and the timestep τ. Decomposing the error as in (4.5.19) we have

$$\begin{aligned}\left\|\hat{\boldsymbol{U}}^n - \hat{\boldsymbol{u}}^n\right\|^2_{L_2(\hat{\Omega})^m} &\leq \left\|\mathrm{R}^h\,\hat{\boldsymbol{u}}^n - \hat{\boldsymbol{u}}^n\right\|^2_{L_2(\hat{\Omega})^m} + \left\|\hat{\boldsymbol{U}}^n - \mathrm{R}^h\,\hat{\boldsymbol{u}}^n\right\|^2_{L_2(\hat{\Omega})^m} \\ &= \|\hat{\boldsymbol{\varepsilon}}^n\|^2_{L_2(\hat{\Omega})^m} + \|\hat{\boldsymbol{\rho}}^n\|^2_{L_2(\hat{\Omega})^m}\,.\end{aligned} \tag{4.5.52}$$

From Lemma 4.5.3 we have the following bound on the elliptic error:

$$\|\hat{\boldsymbol{\varepsilon}}^n\|^2_{L_2(\hat{\Omega})^m} \leq C\hat{h}^{2(\ell+1)} \quad \text{for } n \in [0,\ldots,N]. \tag{4.5.53}$$

It therefore only remains to estimate $\hat{\boldsymbol{\rho}}^n$. Constructing an expression for $\hat{\boldsymbol{\rho}}^n$ as in (4.5.36), using (4.5.47) and (4.5.17) we obtain for $i = 1,\ldots,m$,

$$\begin{aligned}\left\langle \bar{\partial}[J\hat{\rho}_i]^n, \hat{\rho}_i^n\right\rangle_{\hat{\Omega}} + D_i\,\|\nabla\rho_i^n\|^2_{L_2(\Omega_t)} &= \left\langle \widetilde{f}_i(\hat{U}_i^n, \hat{\boldsymbol{U}}^{n-1}), [J\hat{\rho}_i]^n\right\rangle_{\hat{\Omega}} \\ &\quad - \left\langle \bar{\partial}[J\,\mathrm{R}^h\,\hat{u}_i]^n, \hat{\rho}_i^n\right\rangle_{\hat{\Omega}} - D_i\left\langle [J\boldsymbol{K}\nabla\hat{u}_i]^n, [\boldsymbol{K}\nabla\hat{\rho}_i]^n\right\rangle_{\hat{\Omega}} \\ &= \left\langle \widetilde{f}_i(\hat{U}_i^n, \hat{\boldsymbol{U}}^{n-1}) - \widetilde{f}_i(\hat{\boldsymbol{u}}^n), [J\hat{\rho}_i]^n\right\rangle_{\hat{\Omega}} \\ &\quad - \left\langle \bar{\partial}[J\hat{\varepsilon}_i]^n, \hat{\rho}_i^n\right\rangle_{\hat{\Omega}} + \left\langle \left(\bar{\partial} - \partial_t\right)[J\hat{u}_i]^n, \hat{\rho}_i^n\right\rangle_{\hat{\Omega}},\end{aligned} \tag{4.5.54}$$

where we have used (4.4.13) for the second step. Using Young's inequality for the first term on the left hand side of (4.5.54) gives

$$\begin{aligned}\left\langle \bar{\partial}[J\hat{\rho}_i]^n, \hat{\rho}_i^n\right\rangle_{\hat{\Omega}} \geq \frac{1}{\tau}\Bigg(&\|\rho_i^n\|^2_{L_2(\Omega_{t^n})} \\ &- \frac{1}{2}\left(\left\langle J^{n-1}\hat{\rho}_i^n, \hat{\rho}_i^n\right\rangle_{\hat{\Omega}} + \left\langle J^{n-1}\hat{\rho}_i^{n-1}, \hat{\rho}_i^{n-1}\right\rangle_{\hat{\Omega}}\right)\Bigg),\end{aligned} \tag{4.5.55}$$

where we have used (2.3.8). Summing over i we have

$$\begin{aligned}\sum_{i=1}^m \left\langle \bar{\partial}[J\hat{\rho}_i]^n, \hat{\rho}_i^n\right\rangle_{\hat{\Omega}} \geq \frac{1}{\tau}\left(1 - \frac{1}{2}\left\|\frac{J^{n-1}}{J^n}\right\|_{L_\infty(\hat{\Omega})}\right)\|\boldsymbol{\rho}^n\|^2_{L_2(\Omega_{t^n})^m} \\ - \frac{1}{2\tau}\left\|\boldsymbol{\rho}^{n-1}\right\|^2_{L_2(\Omega_{t^{n-1}})^m}.\end{aligned} \tag{4.5.56}$$

Using 4.5.52 and the MVT for the first term on the right of (4.5.54) gives

$$\begin{aligned}&\left|\left\langle \widetilde{f}_i(\hat{U}_i^n, \hat{\boldsymbol{U}}^{n-1}) - \widetilde{f}_i(\hat{\boldsymbol{u}}^n), [J\hat{\rho}_i]^n\right\rangle_{\hat{\Omega}}\right| \\ &\quad\leq \widetilde{C}\sum_{j=1}^m \left\langle \left|\hat{\varepsilon}_j^{n-1}\right| + \left|\hat{\rho}_j^{n-1}\right| + \left|\tau\bar{\partial}\hat{u}_j^n\right| + |\hat{\varepsilon}_i^n| + |\hat{\rho}_i^n|\,, J^n\,|\hat{\rho}_i^n|\right\rangle_{\hat{\Omega}} \\ &\quad\leq C\widetilde{C}\Bigg(\|\rho_i^n\|^2_{L_2(\Omega_{t^n})} + \left\|\frac{J^n}{J^{n-1}}\right\|_{L_\infty(\hat{\Omega})}\left\|\boldsymbol{\rho}^{n-1}\right\|^2_{L_2(\Omega_{t^{n-1}})^m} \\ &\qquad + \|J^n\|_{L_\infty(\hat{\Omega})}\left(\|\hat{\varepsilon}_i^n\|^2_{L_2(\hat{\Omega})} + \left\|\hat{\boldsymbol{\varepsilon}}^{n-1}\right\|^2_{L_2(\hat{\Omega})^m} + \left\|\tau\bar{\partial}\hat{\boldsymbol{u}}^n\right\|^2_{L_2(\hat{\Omega})^m}\right)\Bigg),\end{aligned} \tag{4.5.57}$$

where we have used Young's inequality for the second step. Summing over i we have

$$\begin{aligned}
&\sum_{i=1}^{m} \left| \left\langle \widetilde{f}_i(\hat{U}_i^n, \hat{\boldsymbol{U}}^{n-1}) - \widetilde{f}_i(\hat{\boldsymbol{u}}^n), [J\hat{\rho}_i]^n \right\rangle_{\hat{\Omega}} \right| \\
&\quad \leq C\widetilde{C} \Bigg(\|\boldsymbol{\rho}^n\|^2_{L_2(\Omega_{t^n})^m} + \left\| \frac{J^n}{J^{n-1}} \right\|_{L_\infty(\hat{\Omega})} \left\| \boldsymbol{\rho}^{n-1} \right\|^2_{L_2(\Omega_{t^{n-1}})^m} \\
&\quad + \|J^n\|_{L_\infty(\hat{\Omega})} \left(\|\hat{\boldsymbol{\varepsilon}}^n\|^2_{L_2(\hat{\Omega})^m} + \left\|\hat{\boldsymbol{\varepsilon}}^{n-1}\right\|^2_{L_2(\hat{\Omega})^m} + \left\|\tau\bar{\partial}\hat{\boldsymbol{u}}^n\right\|^2_{L_2(\hat{\Omega})^m} \right) \Bigg).
\end{aligned} \tag{4.5.58}$$

Applying Young's inequality to the second and third term on the right of (4.5.54) gives

$$\begin{aligned}
&\left| \left\langle \bar{\partial}[J\hat{\varepsilon}_i]^n, \hat{\rho}_i^n \right\rangle_{\hat{\Omega}} \right| + \left| \left\langle \left(\bar{\partial} - \partial_t\right)[J\hat{u}_i]^n, \hat{\rho}_i^n \right\rangle_{\hat{\Omega}} \right| \\
&\quad \leq \|\rho_i^n\|^2_{L_2(\Omega_{t^n})} + \frac{1}{2} \left\| \frac{1}{J^n} \right\|_{L_\infty(\hat{\Omega})} \left(\left\|\bar{\partial}[J\hat{\varepsilon}_i]^n\right\|^2_{L_2(\hat{\Omega})} + \left\| \left(\bar{\partial} - \partial_t\right)[J\hat{u}_i]^n \right\|^2_{L_2(\hat{\Omega})} \right).
\end{aligned} \tag{4.5.59}$$

Using (4.5.56), (4.5.58) and (4.5.59) in (4.5.54) gives

$$\begin{aligned}
&\frac{1}{\tau} \left(1 - \frac{1}{2} \left\| \frac{J^{n-1}}{J^n} \right\|_{L_\infty(\hat{\Omega})} - C\widetilde{C}\tau \right) \|\boldsymbol{\rho}^n\|^2_{L_2(\Omega_{t^n})^m} + \sum_{i=1}^{m} D_i \|\nabla\rho_i^n\|^2_{L_2(\Omega_t)} \\
&\quad \leq \left(\frac{1}{2\tau} + C\widetilde{C} \left\| \frac{J^n}{J^{n-1}} \right\|_{L_\infty(\hat{\Omega})} \right) \left\| \boldsymbol{\rho}^{n-1} \right\|^2_{L_2(\Omega_{t^{n-1}})^m} \\
&\quad + C\widetilde{C} \|J^n\|_{L_\infty(\hat{\Omega})} \left(\|\hat{\boldsymbol{\varepsilon}}^n\|^2_{L_2(\hat{\Omega})^m} + \left\|\hat{\boldsymbol{\varepsilon}}^{n-1}\right\|^2_{L_2(\hat{\Omega})^m} + \left\|\tau\bar{\partial}\hat{\boldsymbol{u}}^n\right\|^2_{L_2(\hat{\Omega})^m} \right) \\
&\quad + \frac{1}{2} \left\| \frac{1}{J^n} \right\|_{L_\infty(\hat{\Omega})} \left(\left\|\bar{\partial}[J\hat{\boldsymbol{\varepsilon}}]^n\right\|^2_{L_2(\hat{\Omega})^m} + \left\| \left(\bar{\partial} - \partial_t\right)[J\hat{\boldsymbol{u}}]^n \right\|^2_{L_2(\hat{\Omega})^m} \right).
\end{aligned} \tag{4.5.60}$$

Let $\tau' > 0$ be such that, for $\tau < \tau'$

$$1 - \frac{1}{2} \left\| \frac{J^{n-1}}{J^n} \right\|_{L_\infty(\hat{\Omega})} - C\widetilde{C}\tau > 0. \tag{4.5.61}$$

Such a τ' exists since

$$\lim_{\tau\to 0} \left\{ \frac{1}{2} \left\| \frac{J^{n-1}}{J^n} \right\|_{L_\infty(\hat{\Omega})} + C\widetilde{C}\tau \right\} = \frac{1}{2}. \tag{4.5.62}$$

For $\tau < \tau'$, we have

$$\|\boldsymbol{\rho}^n\|^2_{L_2(\Omega_{t^n})^m} + \sum_{i=1}^{m} C\tau D_i \|\nabla\rho_i^n\|^2_{L_2(\Omega_t)} \leq C \left(\bar{C}^n \left\| \boldsymbol{\rho}^{n-1} \right\|^2_{L_2(\Omega_{t^{n-1}})^m} + \tau\mathcal{R}^n \right), \tag{4.5.63}$$

where $\bar{C}^n = 1 + \tau\widetilde{C}\left\|\frac{J^n}{J^{n-1}}\right\|_{L_\infty\left(\hat{\Omega}\right)}$ and

$$\begin{aligned}\mathcal{R}^n := \widetilde{C}\left\|J^n\right\|_{L_\infty\left(\hat{\Omega}\right)}\left(\left\|\hat{\boldsymbol{\varepsilon}}^n\right\|^2_{L_2\left(\hat{\Omega}\right)^m} + \left\|\hat{\boldsymbol{\varepsilon}}^{n-1}\right\|^2_{L_2\left(\hat{\Omega}\right)^m} + \left\|\tau\bar{\partial}\hat{\boldsymbol{u}}^n\right\|^2_{L_2\left(\hat{\Omega}\right)^m}\right)\\ +\frac{1}{2}\left\|\frac{1}{J^n}\right\|_{L_\infty\left(\hat{\Omega}\right)}\left(\left\|\bar{\partial}[J\hat{\boldsymbol{\varepsilon}}]^n\right\|^2_{L_2\left(\hat{\Omega}\right)^m} + \left\|\left(\bar{\partial}-\partial_t\right)[J\hat{\boldsymbol{u}}]^n\right\|^2_{L_2\left(\hat{\Omega}\right)^m}\right).\end{aligned} \tag{4.5.64}$$

Therefore, for $n \in [1, \ldots, N]$,

$$\begin{aligned}\left\|\boldsymbol{\rho}^n\right\|^2_{L_2(\Omega_{t^n})^m} + \sum_{i=1}^m C\tau D_i\left\|\nabla\rho_i^n\right\|^2_{L_2(\Omega_t)}\\ \leq C\left(\prod_{k=1}^n \bar{C}^k\left\|\boldsymbol{\rho}^0\right\|^2_{L_2(\Omega_0)^m} + \tau\sum_{j=1}^n\prod_{i=j}^n \bar{C}^i\mathcal{R}^j\right).\end{aligned} \tag{4.5.65}$$

Considering the first two terms on the right of (4.5.64), we have for $n \in [1, \ldots, N]$

$$\begin{aligned}\widetilde{C}\left\|J^n\right\|_{L_\infty\left(\hat{\Omega}\right)}\left(\left\|\hat{\boldsymbol{\varepsilon}}^n\right\|^2_{L_2\left(\hat{\Omega}\right)^m} + \left\|\hat{\boldsymbol{\varepsilon}}^{n-1}\right\|^2_{L_2\left(\hat{\Omega}\right)^m}\right)\\ \leq 2\widetilde{C}\sup_{s\in[0,\ldots,N]}\left\|J^s\right\|_{L_\infty\left(\hat{\Omega}\right)}\left\|\hat{\boldsymbol{\varepsilon}}^s\right\|^2_{L_2\left(\hat{\Omega}\right)^m}\\ \leq \widetilde{C}C\hat{h}^{2(\ell+1)},\end{aligned} \tag{4.5.66}$$

where we have used Assumption 4.4.3 and Lemma 4.5.3. Dealing with the third term on the right of (4.5.64), we have

$$\begin{aligned}\widetilde{C}\left\|J^n\right\|_{L_\infty\left(\hat{\Omega}\right)}\left\|\tau\bar{\partial}\hat{\boldsymbol{u}}^n\right\|^2_{L_2\left(\hat{\Omega}\right)^m} = \widetilde{C}\left\|J^n\right\|_{L_\infty\left(\hat{\Omega}\right)}\left\|\int_{t^{n-1}}^{t^n}\partial_t\hat{\boldsymbol{u}}^s\,\mathrm{d}s\right\|^2_{L_2\left(\hat{\Omega}\right)^m}\\ \leq \widetilde{C}C\tau^2,\end{aligned} \tag{4.5.67}$$

where we have used Assumptions 4.4.1, 4.4.3 and (4.4.8). For the fourth term on the right of (4.5.64) we have

$$\begin{aligned}\frac{1}{2}\left\|\frac{1}{J^n}\right\|_{L_\infty\left(\hat{\Omega}\right)}\left\|\bar{\partial}[J\hat{\boldsymbol{\varepsilon}}]^n\right\|^2_{L_2\left(\hat{\Omega}\right)^m} &\leq \frac{1}{2}\left\|\frac{1}{J^n}\right\|_{L_\infty\left(\hat{\Omega}\right)}\left\|\frac{1}{\tau}\int_{t^{n-1}}^{t^n}\partial_t[J\hat{\boldsymbol{\varepsilon}}]^s\,\mathrm{d}s\right\|^2_{L_2\left(\hat{\Omega}\right)^m}\\ &\leq C\sup_{s\in[t^{n-1},t^n]}\left\|\hat{\boldsymbol{\varepsilon}}^s\right\|^2_{L_2\left(\hat{\Omega}\right)^m}\\ &\leq C\hat{h}^{2(\ell+1)},\end{aligned} \tag{4.5.68}$$

where we have used Assumption 4.4.3 for the second step and Lemma 4.5.3 for the final step.

Finally, for the fifth term on the right of (4.5.64) we have

$$\begin{aligned}
&\left\|\frac{1}{J^n}\right\|_{L_\infty(\hat\Omega)} \left\|\left(\bar\partial - \partial_t\right)[J\hat{\boldsymbol{u}}]^n\right\|^2_{L_2(\hat\Omega)^m} \\
&\qquad = \left\|\frac{1}{J^n}\right\|_{L_\infty(\hat\Omega)} \left\|\frac{1}{\tau}\int_{t^{n-1}}^{t^n}\left(s - t^{n-1}\right)\partial_{tt}[J\hat{\boldsymbol{u}}]^s\,\mathrm{d}s\right\|^2_{L_2(\hat\Omega)^m} \\
&\qquad \le C\tau^2 \sup_{s\in[t^{n-1},t^n]}\left(\|\partial_t\hat{\boldsymbol{u}}^s\|^2_{L_2(\hat\Omega)^m} + \|\hat{\boldsymbol{u}}^s\|^2_{L_2(\hat\Omega)^m}\right) \\
&\qquad \le C\tau^2,
\end{aligned} \tag{4.5.69}$$

where we have used Assumption 4.4.3 for the second step and Assumption 4.4.1 for the final step. Combining (4.5.66), (4.5.67), (4.5.68) and (4.5.69) we have

$$\mathcal{R}^n \le C\left(\hat h^{2(\ell+1)} + \tau^2\right) \text{ for } n \in [1,\dots,N]. \tag{4.5.70}$$

Using (4.5.46) we have

$$\left\|\boldsymbol{\rho}^0\right\|^2_{L_2(\Omega_0)^m} = \left\|\boldsymbol{\rho}^h(0)\right\|^2_{L_2(\Omega_0)^m} \le C\hat h^{2(\ell+1)}. \tag{4.5.71}$$

Applying estimates (4.5.70) and (4.5.71) in (4.5.63) completes the proof of Theorem 4.5.6. □

4.5.7 Remark (Qualitative estimates on the exact solution)**.** In practice only qualitative a priori estimates are generally available for the exact solution and the region $\boldsymbol{I}_\delta$ defined in Assumption 4.4.1 is not explicitly known. Thus, we can not construct the function $\widetilde{\boldsymbol{f}}$ defined in (4.4.15). To this end, we introduce the following assumption to circumvent the construction of $\widetilde{\boldsymbol{f}}$.

4.5.8 Assumption (Dimension dependent polynomial degree)**.** We wish to invoke estimate (4.5.4) with a positive power of $\hat h$ and thus we require the degree of the finite element space to satisfy

$$\ell > \frac{d}{2} - 1, \tag{4.5.72}$$

where d is the spatial dimension. Thus, we require piecewise linear or higher basis functions for $d \le 2$ and at least piecewise quadratics for $d = 3$.

4.5.9 Proposition (Point-wise convergence of the discrete solution)**.** *Let Assumption 4.5.8 hold and Theorem 4.5.6 be valid. For sufficiently small mesh-size $\hat h$ the discrete solution $\hat{\boldsymbol{U}}^n$ to Problem (4.5.47) is in the region $\boldsymbol{I}_\delta$ for all $n \in [0,\dots,N]$. Thus, we may replace $\widetilde{\boldsymbol{f}}$ in (4.5.47) by $\boldsymbol{f}$.*

Proof . For $n \in [0,\dots,N]$ we have for $\mathcal{I}^h$ the Clément interpolant

$$\left\|\hat{\boldsymbol{u}}^n - \hat{\boldsymbol{U}}^n\right\|_{L_\infty(\hat\Omega)^m} \le \left\|\mathcal{I}^h\hat{\boldsymbol{u}}^n - \hat{\boldsymbol{U}}^n\right\|_{L_\infty(\hat\Omega)^m} + \left\|\hat{\boldsymbol{u}}^n - \mathcal{I}^h\hat{\boldsymbol{u}}^n\right\|_{L_\infty(\hat\Omega)^m}. \tag{4.5.73}$$

By (4.5.4) we have

$$\begin{aligned}
\left\|\hat{\boldsymbol{u}}^n - \hat{\boldsymbol{U}}^n\right\|_{L_\infty(\hat\Omega)^m} \le C\Bigg(&\hat h^{\ell+1-d/2}\,|\hat{\boldsymbol{u}}^n|_{H^{\ell+1}(\hat\Omega)^m} \\
&+ \hat h^{\ell-d/2}\left\|\mathcal{I}^h\hat{\boldsymbol{u}}^n - \hat{\boldsymbol{U}}^n\right\|_{L_\infty(\hat\Omega)^m}\Bigg).
\end{aligned} \tag{4.5.74}$$

Using (4.5.5) gives

$$\begin{aligned}\left\|\hat{\boldsymbol{u}}^n - \hat{\boldsymbol{U}}^n\right\|_{L_\infty\left(\hat{\Omega}\right)^m} \leq C\Bigg(&\hat{h}^{\ell+1-d/2}\left|\hat{\boldsymbol{u}}^n\right|_{H^{\ell+1}\left(\hat{\Omega}\right)^m} \\ &+ \hat{h}^{-d/2}\left(\left\|\mathcal{I}^h\hat{\boldsymbol{u}}^n - \hat{\boldsymbol{u}}^n\right\|_{L_2\left(\hat{\Omega}\right)^m} + \left\|\hat{\boldsymbol{u}}^n - \hat{\boldsymbol{U}}^n\right\|_{L_2\left(\hat{\Omega}\right)^m}\right)\Bigg).\end{aligned} \tag{4.5.75}$$

Now using (4.5.3) and Theorem 4.5.6 we have

$$\left\|\hat{\boldsymbol{u}}^n - \hat{\boldsymbol{U}}^n\right\|_{L_\infty\left(\hat{\Omega}\right)^m} \leq C\hat{h}^{\varepsilon}, \tag{4.5.76}$$

where $\varepsilon = \ell + 1 - \frac{d}{2} > 0$ by Assumption 4.5.8. Thus, if $\hat{h}$ is taken sufficiently small we have

$$\sup_{n\in[0,\ldots,N]}\left\|\hat{\boldsymbol{u}}^n - \hat{\boldsymbol{U}}^n\right\|_{L_\infty\left(\hat{\Omega}\right)^m} \leq \frac{\delta}{2}. \tag{4.5.77}$$

Therefore, $\hat{\boldsymbol{U}}^n \in \boldsymbol{I}_\delta$ for all $n \in [0,\ldots,N]$ and thus, $\widetilde{\boldsymbol{f}}(\hat{\boldsymbol{U}}) = \boldsymbol{f}(\hat{\boldsymbol{U}})$ completing the proof. □

4.6 Adaptive schemes for the approximation of RDSs

In this section we construct a space-adaptive scheme for the solution of RDSs on continuously growing domains. The goal of an adaptive scheme may be viewed as an attempt to minimise the computational cost of a numerical scheme for a given tolerance of the error. To this end, many techniques have been suggested to improve the efficiency of finite element methods.

One example is the *moving finite element* method, where nodal movement is regarded as an unknown (even on fixed domain problems) and at each timestep nodes are moved, usually with the goal of equidistributing the error [Baines, 1994]. Zegeling and Kok [2004] describe an adaptive moving mesh FEM to approximate solutions of the Gray-Scott RDS on a *fixed* domain. Nodal movement is determined by the solution of an adaptive moving mesh PDE which is effectively the minimisation of a mesh-energy functional given by the Euler-Lagrange equations. This approach, while attractive, necessitates an ALE formulation which allows the consideration of arbitrary mesh velocities which are not necessarily Lagrangian in nature, i.e., scenarios where the mesh velocity is different to the underlying domain velocity.

Another well known method to improve the efficiency of the FEM is local refinement with a view to increasing the resolution of the scheme where the error is high. This commonly takes the form of *p-refinement* where the polynomial degree (or approximating properties of the basis functions for non-polynomial methods) is increased locally or *h-refinement* where the mesh-size is reduced locally by local mesh refinement [Schwab, 1998]. We have implemented our numerical methods using the toolbox ALBERTA [Schmidt and Siebert, 2005]. One attractive feature of the toolbox is the implementation of algorithms for error estimation and mesh refinement. This has been exploited by Kimura et al. [2005] who conducted a numerical study of adaptive mesh refinement for RDSs on fixed domains using ALBERTA. However, they provide no details of the numerical method they use concentrating only on the results of their simulations with the Gray-Scott model in 2 and 3 dimensions. In light of this, we now attempt to derive an *h-adaptive* scheme for the solution of RDSs on continuously growing domains.

To drive an adaptive algorithm, some knowledge of the quality of the approximation (ideally knowledge of the error) is needed to guide the local refinement. The estimates (4.5.35) and (4.5.51) provide knowledge of the rate of convergence of the error (as the mesh-size is refined), but both estimates depend on the exact solution (through the constant C) which is unknown and thus, the bound is not computable. To drive a space-adaptive scheme we shall derive bounds for the error (in the semidiscrete scheme) which are *computable*, i.e., they depend on the approximate solution rather than the exact solution. The process of deriving such bounds is known as a posteriori error estimation.

4.6.1 A residual based a posteriori error estimate for the semidiscrete scheme

The goal of this section is to show the error in the semidiscrete scheme (4.5.6) can be bounded by a computable quantity namely an a posteriori error estimator. Our estimator is based on the element *residual*, which may be viewed as the remainder that results from applying the continuous differential operator to the discrete solution. Many other a posteriori estimates exist such as recovery based estimators where the difference between the gradient of the discrete solution and a post-processed gradient of the discrete solution estimates the error in the energy norm. For an in-depth discussion of a posteriori error estimation we refer to the book by Ainsworth and Oden [1997].

Our strategy to derive an a posteriori error estimate is similar to that employed by Kruger et al. [2003]. We use energy arguments to show the residual is an upper bound for the error and the analysis is similar to the a priori case considered previously (though we work with the energy norm in the a posteriori setting). Other analytical techniques exist to relate the residual to the true error, with *duality* perhaps being the most important. Estep et al. [2000] use duality techniques to construct residual based a posteriori estimates for systems of coupled RDEs and ODEs. Their approach, although in some ways more general in scope (since ODEs are admissible) than the one we shall follow, necessitates the solution of a linearised dual problem at each timestep which may be computationally inefficient over the long timescales we have in mind and is limited to constant diffusion coefficients.

We start by recalling the semidiscrete scheme, find $\hat{u}_i^h : [0,T] \to \hat{\mathbb{V}}$, such that for $i = 1, \dots, m$,

$$\begin{cases} \left\langle \partial_t (J\hat{u}_i^h), \hat{\Phi} \right\rangle_{\hat{\Omega}} + \left\langle D_i J \boldsymbol{K} \nabla \hat{u}_i^h, \boldsymbol{K} \nabla \hat{\Phi} \right\rangle_{\hat{\Omega}} = \left\langle J \widetilde{f}_i(\hat{\boldsymbol{u}}^h), \hat{\Phi} \right\rangle_{\hat{\Omega}} \quad \forall \hat{\Phi} \in \hat{\mathbb{V}}, \\ \hat{u}_i^h(0) = \Lambda^h \hat{u}_i^0, \end{cases} \tag{4.6.1}$$

where $\Lambda^h : H^1(\hat{\Omega}) \to \hat{\mathbb{V}}$ is the Lagrange interpolant.

4.6.2 Assumption (Applicability of the MVT)**.** In addition to Assumption 4.4.1, we assume the mesh is sufficiently refined (cf. (4.5.77)) such that $\hat{\boldsymbol{u}}^h(t) \in \boldsymbol{I}_\delta$ for all $t \in [0,T]$. We thus (cf. (4.4.15)) may without restriction replace $\widetilde{\boldsymbol{f}}(\hat{\boldsymbol{u}}^h)$ with $\boldsymbol{f}(\hat{\boldsymbol{u}}^h)$ in (4.6.1) and we have

$$\left\| \boldsymbol{f}' \right\|_{L_\infty\left(\mathrm{dom}(\hat{\boldsymbol{u}}^h)\right)} < \tilde{C}. \tag{4.6.2}$$

We define the error in the semidiscrete scheme

$$\hat{\boldsymbol{e}}(t) := \hat{\boldsymbol{u}}^h(t) - \hat{\boldsymbol{u}}(t), \text{ for } t \in [0,T]. \tag{4.6.3}$$

4.6.3 Assumption (Dominant energy norm error)**.** Since we are primarily interested in problems posed on long time intervals, obtaining an a posteriori analogue of estimate (4.5.35) is not that

useful due to the exponential dependence on time. Thus, to circumvent the use of Gronwall's inequality we assume the error in the $L_2(0,T;L_2(\hat{\Omega}))$ norm converges faster than the error in the $L_2(0,T;H^1(\hat{\Omega}))$ norm. Formally we assume there exists $C>0$ and $r\in(0,1]$ independent of the mesh-size $\hat{h}$ such that

$$\int_0^T \|\hat{\boldsymbol{e}}\|^2_{L_2(\hat{\Omega})^m} \leq C\hat{h}^{2r}\sum_{i=1}^m \int_0^T \|\nabla \hat{e}_i\|^2_{L_2(\hat{\Omega})}\,. \tag{4.6.4}$$

Due to the equivalence of norms between the reference and evolving domains (2.3.8) and (2.3.9), we have for some $C\in\mathbb{R}^+$ and for r as defined in (4.6.4)

$$\int_0^T \|\boldsymbol{e}\|^2_{L_2(\Omega_t)^m} \leq C\hat{h}^{2r}\sum_{i=1}^m \int_0^T \|\nabla e_i\|^2_{L_2(\Omega_t)}\,. \tag{4.6.5}$$

We note assumptions of this type have been used previously by Kruger et al. [2003] and by Medina et al. [1996] to obtain a posteriori estimates for a quasilinear reaction-diffusion problem and a stationary nonlinear convection-diffusion problem respectively.

We start by introducing the *residual* $\hat{R}_i \in H^1(\hat{\Omega})'$ (the dual of $H^1(\hat{\Omega})$) a.e. in $[0,T]$ which satisfies

$$\left\langle \hat{R}_i \,|\, \hat{\chi}\right\rangle := \left\langle \partial_t(J\hat{u}^h{}_i) - D_i\nabla\cdot\left(J\boldsymbol{K}\boldsymbol{K}^{\mathsf{T}}\nabla\hat{u}_i^h\right) - Jf_i(\hat{\boldsymbol{u}}^h)\,|\,\hat{\chi}\right\rangle \quad \forall\hat{\chi}\in H^1(\hat{\Omega}), \tag{4.6.6}$$

where $\langle\cdot\,|\,\cdot\rangle$ denotes the duality pairing between H^1 and its dual. We now show the residual is an upper bound for the error.

4.6.4 Proposition (Upper bound for the error)**.** *Suppose Assumptions 4.4.1, 4.6.2 and 4.6.3 hold. Let $\hat{\boldsymbol{u}}$ satisfy (4.4.13) and let the error $\hat{e}_i$ and the residual $\hat{R}_i$ be as in (4.6.3) and (4.6.6) respectively. If the mesh-size satisfies $\hat{h}\leq\hat{h}_0$ defined in (4.6.15), then*

$$\left\|\boldsymbol{e}(T)\right\|^2_{L_2(\Omega_t)^m} + \sum_{i=1}^m D_i\int_0^T \|\nabla e_i\|^2_{L_2(\Omega_t)} \leq \left\|\boldsymbol{e}(0)\right\|^2_{L_2(\Omega_0)^m} + 2\sum_{i=1}^m\int_0^T \left\langle \hat{R}_i\,|\,\hat{e}_i\right\rangle. \tag{4.6.7}$$

Proof . Using (4.4.13) and (4.6.1) we have for $i=1,\dots,m$,

$$\begin{aligned}\left\langle\partial_t(J\hat{e}_i),\hat{\chi}\right\rangle_{\hat{\Omega}} + D_i\left\langle J\boldsymbol{K}\nabla\hat{e}_i,\boldsymbol{K}\nabla\hat{\chi}\right\rangle_{\hat{\Omega}}&\\ = \left\langle f_i(\hat{\boldsymbol{u}}^h) - f_i(\hat{\boldsymbol{u}}), J\hat{\chi}\right\rangle_{\hat{\Omega}} + \left\langle \hat{R}_i\,|\,\hat{\chi}\right\rangle &\quad \forall\hat{\chi}\in H^1(\hat{\Omega}),\end{aligned} \tag{4.6.8}$$

Taking $\hat{\chi}=\hat{e}_i$, we use the results of §2.3 and Reynold's transport theorem (cf. §4.5.2.1) to express the integrals on the evolving domain

$$\begin{aligned}\frac{1}{2}\left(\frac{\mathrm{d}}{\mathrm{d}t}\left\langle e_i,e_i\right\rangle_{\Omega_t} + \left\langle(\nabla\cdot\boldsymbol{a})e_i,e_i\right\rangle_{\Omega_t}\right) + D_i\left\langle\nabla e_i,\nabla e_i\right\rangle_{\Omega_t}&\\ = \left\langle f_i(\boldsymbol{u}^h) - f_i(\boldsymbol{u}), e_i\right\rangle_{\Omega_t} + \left\langle\hat{R}_i\,|\,\hat{\chi}\right\rangle.&\end{aligned} \tag{4.6.9}$$

Integrating in time, we obtain

$$\begin{aligned}\left\|e_i(T)\right\|^2_{L_2(\Omega_t)} + \int_0^T\left\langle(\nabla\cdot\boldsymbol{a})\,e_i,e_i\right\rangle_{\Omega_t} + 2\int_0^T D_i\,\|\nabla e_i\|^2_{L_2(\Omega_t)}&\\ = \left\|e_i(0)\right\|^2_{L_2(\Omega_0)} + 2\int_0^T\left\langle f_i(\boldsymbol{u}^h) - f_i(\boldsymbol{u}^h), e_i\right\rangle_{\Omega_t} + 2\left\langle\hat{R}_i\,|\,\hat{e}_i\right\rangle.&\end{aligned} \tag{4.6.10}$$

Focussing on the second term on the right of (4.6.10), using the MVT and Assumption 4.6.2 we have

$$\begin{aligned}\left|\left\langle f_i(\boldsymbol{u}) - f_i(\boldsymbol{u}^h), e_i\right\rangle_{\Omega_t}\right| &\leq \tilde{C}\left\langle \sum_{j=1}^{m}\left|e_j\right|, \left|e_i\right|\right\rangle_{\Omega_t} \\ &\leq \tilde{C}\left(\frac{m+1}{2}\left\|e_i\right\|^2_{L_2(\Omega_t)} + \sum_{j\neq i}\frac{1}{2}\left\|e_j\right\|^2_{L_2(\Omega_t)}\right),\end{aligned} \tag{4.6.11}$$

where we have used Young's inequality. Summing over i we have

$$\sum_{i=1}^{m}\left|\left\langle f_i(\boldsymbol{u}) - f_i(\boldsymbol{u}^h), e_i\right\rangle_{\Omega_t}\right| \leq \tilde{C}m\left\|\boldsymbol{e}\right\|^2_{L_2(\Omega_t)^m}. \tag{4.6.12}$$

Combining (4.6.10) and (4.6.12) gives

$$\begin{aligned}&\sum_{i=1}^{m}\left(\left\|e_i(T)\right\|^2_{L_2(\Omega_t)} + \int_0^T 2D_i\left\|\nabla e_i\right\|^2_{L_2(\Omega_t)}\right) \\ &\qquad\leq \sum_{i=1}^{m}\left(\left\|e_i(0)\right\|^2_{L_2(\Omega_0)} + \int_0^T\left\langle\left(2\tilde{C}m - \nabla\cdot\boldsymbol{a}\right)e_i, e_i\right\rangle_{\Omega_t} + \int_0^T 2\left\langle\hat{R}_i\,|\,e_i\right\rangle\right).\end{aligned} \tag{4.6.13}$$

Thus, we have

$$\begin{aligned}&\left\|\boldsymbol{e}(T)\right\|^2_{L_2(\Omega_t)^m} + \sum_{i=1}^{m}\int_0^T 2D_i\left\|\nabla e_i\right\|^2_{L_2(\Omega_t)} \\ &\leq \left\|\boldsymbol{e}(0)\right\|^2_{L_2(\Omega_t)^m} + \int_0^T \sup_{\mathcal{Q}_T}\{2\tilde{C}m - \nabla\cdot\boldsymbol{a}\}\left\|\boldsymbol{e}\right\|^2_{L_2(\Omega_t)^m} + \sum_{i=1}^{m}\int_0^T 2\left\langle\hat{R}_i\,|\,e_i\right\rangle,\end{aligned} \tag{4.6.14}$$

where $\mathcal{Q}_T$ is as defined in §4.4. If $\sup_{\mathcal{Q}_T}\{2\tilde{C}m - \nabla\cdot\boldsymbol{a}\} > 0$, we assume the following global mesh-size condition:

$$\hat{h} \leq \hat{h}_0 := \min_i\left(\frac{D_i}{\sup_{\mathcal{Q}_T}\{2\tilde{C}m - \nabla\cdot\boldsymbol{a}\}}\right)^{1/2r}, \tag{4.6.15}$$

with C, r as in (4.6.5). Combining (4.6.5), (4.6.14) and (4.6.15) we have

$$\left\|\boldsymbol{e}(T)\right\|^2_{L_2(\Omega_t)^m} + \sum_{i=1}^{m}\int_0^T D_i\left\|\nabla e_i\right\|^2_{L_2(\Omega_t)^m} \leq \left\|\boldsymbol{e}(0)\right\|^2_{L_2(\Omega_t)^m} + \sum_{i=1}^{m}\int_0^T 2\left\langle\hat{R}_i\,|\,e_i\right\rangle, \tag{4.6.16}$$

which completes the proof. □

4.6.5 Assumption (Piecewise linear basis functions)**.** To simplify the remainder of the analysis, we now assume $\ell = 1$, i.e., the finite element space $\hat{\mathbb{V}}$ is made up of piecewise linear functions. This assumption sufficies for our purposes but may be relaxed depending on the applications in mind.

We now introduce an explicit computable *estimator* in order to provide an upper bound for the residuals $\hat{R}_i$ defined in (4.6.6). Estimators of this type were first introduced by Babuška, I. and Rheinboldt, W.C. [1978]. For any simplex s of the triangulation $\hat{\mathscr{T}}$ we denote by $\hat{h}_{\mathsf{s}}$ the mesh-size of s. Let E_{s} be the set of three edges of s. Let E_{i} be an edge on the interior of $\hat{\Omega}$, with outward pointing (with respect to s) normal $\boldsymbol{\nu}$. We denote by $[\![\nabla\phi\cdot\boldsymbol{\nu}]\!]_{\mathsf{E}_{\mathsf{i}}}$ the jump of $\nabla\phi\cdot\boldsymbol{\nu}$ across the edge E_{i}. For boundary edges we take $[\![\nabla\phi\cdot\boldsymbol{\nu}]\!]=2\nabla\phi\cdot\boldsymbol{\nu}$. The local error indicator is given by

$$(\hat{\mathscr{E}}_{i|\mathsf{s}})^2=\left(\hat{\epsilon}_{i|\mathsf{s}}\right)^2+\left(\hat{\mathsf{J}}_{i|\mathsf{s}}\right)^2, \tag{4.6.17}$$

where the interior ($\hat{\epsilon}_i$) and jump ($\hat{\mathsf{J}}_i$) components are given by

$$\left(\hat{\epsilon}_{i|\mathsf{s}}\right)^2=\hat{h}_{\mathsf{s}}^2\left\|\partial_t(J\hat{u}_i^h)-D_i\nabla\cdot\left(J\boldsymbol{K}\boldsymbol{K}^{\mathsf{T}}\nabla\hat{u}_i^h\right)-Jf_i(\hat{\boldsymbol{u}}^h)\right\|^2_{L_2(\mathsf{s})}, \tag{4.6.18}$$

and

$$\left(\hat{\mathsf{J}}_{i|\mathsf{s}}\right)^2=\frac{1}{2}\sum_{e\in\mathsf{E}_{\mathsf{s}}}|e|\left\|D_i\left[\!\left[J\boldsymbol{K}\boldsymbol{K}^{\mathsf{T}}\nabla\hat{u}_i^h\cdot\boldsymbol{\nu}\right]\!\right]\right\|^2_{L_2(e)}. \tag{4.6.19}$$

4.6.6 Proposition (Residual bound)**.** *Let R_i and $\hat{\mathscr{E}}_i$, $i=1,\dots,m$ be defined by (4.5.64) and (4.6.17) respectively and let Assumption 4.6.5 hold. There exists a $C>0$ that depends only on the shape regularity of the triangulation $\hat{\mathscr{T}}$ such that for $i=1,\dots,m$,*

$$\begin{aligned}&\left|\int_0^T\left\langle\hat{R}_i\,|\,\hat{\chi}\right\rangle\right|\\&\quad\le C\int_0^T\left(\sum_{\mathsf{s}\in\hat{\mathscr{T}}}(\hat{\mathscr{E}}_{i|\mathsf{s}})^2\right)^{1/2}\int_0^T\left(\|\hat{\chi}\|^2_{L_2(\hat{\Omega})}+\|\nabla\hat{\chi}\|_{L_2(\hat{\Omega})}\right)^{1/2}\forall\hat{\chi}\in H^1(\hat{\Omega}).\end{aligned} \tag{4.6.20}$$

Proof . By Galërkin orthognality the residual is orthogonal to the finite element space, therefore for $\hat{\chi}\in H^1(\hat{\Omega})$,

$$\int_0^T\left\langle\hat{R}_i\,|\,\hat{\chi}\right\rangle=\int_0^T\left\langle\hat{R}_i\,|\,\hat{\chi}-\hat{\Phi}\right\rangle\quad\forall\hat{\Phi}\in\hat{\mathbb{V}}. \tag{4.6.21}$$

Using (4.6.6)

$$\begin{aligned}&\left\langle\hat{R}_i\,|\,\hat{\chi}-\hat{\Phi}\right\rangle\\&\quad=\sum_{\mathsf{s}\in\hat{\mathscr{T}}}\left\{\left\langle\partial_t(Ju_i^h)-Jf_i(\hat{\boldsymbol{u}}^h),\hat{\chi}-\hat{\Phi}\right\rangle_{(s)}+\left\langle D_iJ\boldsymbol{K}\boldsymbol{K}^{\mathsf{T}}\nabla u_i^h,\nabla(\hat{\chi}-\hat{\Phi})\right\rangle_{(s)}\right\}.\end{aligned} \tag{4.6.22}$$

Integrating by parts we have

$$\begin{aligned}\left\langle\hat{R}_i\,|\,\hat{\chi}-\hat{\Phi}\right\rangle=\sum_{\mathsf{s}\in\hat{\mathscr{T}}}\Bigg\{&\left\langle\partial_t(Ju_i^h)-D_i\nabla\cdot\left(J\boldsymbol{K}\boldsymbol{K}^{\mathsf{T}}\nabla u_i^h\right)-Jf_i(\hat{\boldsymbol{u}}^h),\hat{\chi}-\hat{\Phi}\right\rangle_{(s)}\\&+\frac{1}{2}\sum_{e\in\mathsf{E}_{\mathsf{s}}}\left\langle D_i\left[\!\left[J\boldsymbol{K}\boldsymbol{K}^{\mathsf{T}}\nabla u_i^h\cdot\boldsymbol{\nu}\right]\!\right],\hat{\chi}-\hat{\Phi}\right\rangle_{(e)}\Bigg\}.\end{aligned} \tag{4.6.23}$$

By the Cauchy-Bunyakovsky-Schwarz inequality

$$\begin{aligned}
&\left| \left\langle \hat{R}_i \,|\, \hat{\chi} - \hat{\Phi} \right\rangle \right| \\
&\quad \leq \sum_{\mathsf{s} \in \hat{\mathscr{T}}} \left\{ \left\| \partial_t (J u_i^h) D_i \nabla \cdot \left(J \boldsymbol{K} \boldsymbol{K}^{\mathsf{T}} \nabla u_i^h \right) - J f_i(\hat{\boldsymbol{u}}^h) \right\|_{L_2(s)} \left\| \hat{\chi} - \hat{\Phi} \right\|_{L_2(s)} \right. \\
&\qquad \left. + \frac{1}{2} \sum_{e \in \mathsf{E}_\mathsf{s}} \left\| D_i \left[\!\!\left[J \boldsymbol{K} \boldsymbol{K}^{\mathsf{T}} \nabla u_i^h \cdot \boldsymbol{\nu} \right]\!\!\right] \right\|_{L_2(e)} \left\| \hat{\chi} - \hat{\Phi} \right\|_{L_2(e)} \right\}.
\end{aligned} \tag{4.6.24}$$

Taking $\hat{\Phi} = \mathcal{I}^h \hat{\chi}$ the Clément interpolant of $\hat{\chi}$ and recalling the assumption that $\ell = 1$, we state the following two known results [Ainsworth and Oden, 1997] a posteriori analogues of (4.5.3). There exists $C > 0$ that depends only on the shape regularity of the triangulation $\hat{\Omega}$ such that,

$$\begin{cases}
\left\| \hat{\chi} - \mathcal{I}^h \hat{\chi} \right\|^2_{L_2(\mathsf{p}_\mathsf{s})} & \leq C \hat{h}_s^2 \left(\|\hat{\chi}\|^2_{L_2(\mathsf{p}_\mathsf{s})} + \|\nabla \hat{\chi}\|^2_{L_2(\mathsf{p}_\mathsf{s})} \right), \\
\left\| \hat{\chi} - \mathcal{I}^h \hat{\chi} \right\|^2_{L_2(e)} & \leq C \, |e| \left(\|\hat{\chi}\|^2_{L_2(\mathsf{p}_\mathsf{s})} + \|\nabla \hat{\chi}\|^2_{L_2(\mathsf{p}_\mathsf{s})} \right),
\end{cases} \tag{4.6.25}$$

where p_s denotes a *patch* of simplices that share a common edge or vertex with s. Since the mesh is regular there exists $C > 0$, dependent only on the shape regularity of the elements, such that

$$\left(\sum_{\mathsf{s} \in \hat{\mathscr{T}}} \|\hat{\chi}\|^2_{L_2(\mathsf{p}_\mathsf{s})} + \|\nabla \hat{\chi}\|^2_{L_2(\mathsf{p}_\mathsf{s})} \right) \leq C \left(\|\hat{\chi}\|^2_{L_2(\Omega)} + \|\nabla \hat{\chi}\|^2_{L_2(\Omega)} \right). \tag{4.6.26}$$

Application of (4.6.25) in (4.6.24) gives,

$$\left| \left\langle \hat{R}_i \,|\, \hat{\chi} - \hat{\Phi} \right\rangle \right| \leq C \left(\sum_{\mathsf{s} \in \hat{\mathscr{T}}} (\hat{\mathscr{E}}_{i|\mathsf{s}})^2 \right)^{1/2} \left(\sum_{\mathsf{s} \in \hat{\mathscr{T}}} \|\hat{\chi}\|^2_{L_2(\mathsf{p}_\mathsf{s})} + \|\nabla \hat{\chi}\|^2_{L_2(\mathsf{p}_\mathsf{s})} \right)^{1/2}. \tag{4.6.27}$$

Using (4.6.26) in (4.6.27) and integrating in time yields for $i = 1, \ldots, m$,

$$\left| \int_0^T \left\langle \hat{R}_i \,|\, \hat{\chi} - \hat{\Phi} \right\rangle \right| \leq C \int_0^T \left(\sum_{\mathsf{s} \in \hat{\mathscr{T}}} (\hat{\mathscr{E}}_{i|\mathsf{s}})^2 \right)^{1/2} \left(\|\hat{\chi}\|^2_{L_2(\Omega)} + \|\nabla \hat{\chi}\|^2_{L_2(\Omega)} \right)^{1/2}, \tag{4.6.28}$$

whereupon application of the Cauchy-Bunyakovsky-Schwarz inequality completes the proof. □

To complete the bound of the error by the estimator, we make an assumption about the error in the approximation of the initial data.

4.6.7 Assumption (Dominated initial error)**.** We assume that the initial error in the $L_2(\hat{\Omega})$ norm converges faster than the error in the $L_2(0, T; H^1(\hat{\Omega}))$. Formally we assume there exists $C > 0$ and $r \in (0, 1]$ independent of the mesh-size $\hat{h}$ such that

$$\left\| \hat{\boldsymbol{e}}(0) \right\|^2_{L_2(\hat{\Omega})} \leq C \hat{h}^{2r} \sum_{i=1}^m \int_0^T \|\nabla \hat{e}_i\|^2_{L_2(\hat{\Omega})}. \tag{4.6.29}$$

4.6.8 Theorem (A posteriori error estimate for the semidiscrete scheme)**.** *Let Assumptions 4.6.2, 4.6.3 and 4.6.7 hold. Let the error $\hat{e}_i$ and $\hat{\mathscr{E}}_i$ $i = 1, \dots, m$ be defined by and (4.6.3) and (4.6.17) respectively. If the mesh-size is sufficiently small. Then for some $C > 0$,*

$$\sum_{i=1}^{m} D_i \int_0^T \|\nabla e_i\|^2_{L_2(\Omega_t)} \leq \sum_{i=1}^{m} C \int_0^T \sum_{\mathsf{s}\in\hat{\mathscr{T}}} (\hat{\mathscr{E}}_{i|\mathsf{s}})^2. \tag{4.6.30}$$

Proof . Combining (4.6.7) and (4.6.20) we have

$$\begin{aligned}\sum_{i=1}^{m} 2D_i \int_0^T \|\nabla e_i\|^2_{L_2(\Omega_t)} &\leq \left\|\boldsymbol{e}(0)\right\|^2_{L_2(\Omega_0)^m} \\ &+ \sum_{i=1}^{m} 2C \int_0^T \left(\sum_{\mathsf{s}\in\hat{\mathscr{T}}} (\hat{\mathscr{E}}_{i|\mathsf{s}})^2\right)^{1/2} \int_0^T \left(\|\hat{e}_i\|^2_{L_2(\hat{\Omega})} + \|\nabla \hat{e}_i\|^2_{L_2(\hat{\Omega})}\right)^{1/2}.\end{aligned} \tag{4.6.31}$$

By Assumptions 4.6.3 and 4.6.7 for $\hat{h}$ sufficiently small we have

$$\sum_{i=1}^{m} D_i \int_0^T \|\nabla e_i\|^2_{L_2(\Omega_t)} \leq 2C \sum_{i=1}^{m} \int_0^T \left(\sum_{\mathsf{s}\in\hat{\mathscr{T}}} (\hat{\mathscr{E}}_{i|\mathsf{s}})^2\right)^{1/2} \int_0^T \left(\|\nabla \hat{e}_i\|^2_{L_2(\hat{\Omega})}\right)^{1/2}. \tag{4.6.32}$$

The equivalence of norms on the evolving and the reference frame (2.3.8) and Young's inequality complete the proof. □

Since the estimator $\hat{\mathscr{E}}$ is an upper bound for the error, we use it to drive a space-adaptive scheme. To ensure the efficiency of the adaptive scheme, we would have to show the estimator was also a lower bound for the error and we leave this extension for future work. We give the details of the adaptive algorithm we employ in Chapter 5.

Although we have only derived an estimator for the semidiscrete error, in §5.4.2 we propose a space-time adaptive algorithm based on the spatial error estimator $\hat{\mathscr{E}}$ and a heuristic error indicator for the error in the time discretisation. An important analytical tool that is likely to make the derivation of optimal a posteriori estimates for the fully discrete scheme possible is the *elliptic reconstruction* the a posteriori analogue of the Ritz projection, introduced by Makridakis and Nochetto [2004] and extended to the fully discrete (linear) case by Lakkis and Makridakis [2006].

4.7 Implementation

In this section we illustrate the implementation of the finite element scheme with explicit nonlinear reaction functions. We demonstrate that scheme (4.5.47) on the reference domain or scheme (4.5.49) on the evolving domain give rise to equivalent linear systems. To illustrate concrete implementations of the proposed finite element scheme, we present explicitly the implementation when the scheme is used to solve an RDS with the Schnakenberg (2.5.8) or Thomas (2.5.9) kinetics.

In matrix vector form scheme (4.5.47) equipped with kinetics (2.5.8) or (2.5.9) and appropriate initial approximations $\boldsymbol{W}_1^0, \boldsymbol{W}_2^0$ is: To solve for $\boldsymbol{W}_1^n, \boldsymbol{W}_2^n$, $n = [1, \dots, N]$, the linear systems given by

$$\begin{cases} \left(\frac{1}{\tau}\hat{\boldsymbol{M}}^n + D_1\hat{\boldsymbol{S}}^n + \gamma\hat{\boldsymbol{N}}_1^n\right)\hat{\boldsymbol{W}}_1^n &= \frac{1}{\tau}\hat{\boldsymbol{M}}^{n-1}\hat{\boldsymbol{W}}_1^{n-1} + \gamma a\hat{\boldsymbol{F}}^n \\ \left(\frac{1}{\tau}\hat{\boldsymbol{M}}^n + D_2\hat{\boldsymbol{S}}^n + \gamma\hat{\boldsymbol{N}}_2^n\right)\hat{\boldsymbol{W}}_2^n &= \frac{1}{\tau}\hat{\boldsymbol{M}}^{n-1}\hat{\boldsymbol{W}}_2^{n-1} + \gamma b\hat{\boldsymbol{F}}^n, \end{cases} \tag{4.7.1}$$

where $\boldsymbol{W}_1$ and $\boldsymbol{W}_2$ represent the nodal values of the discrete solutions corresponding to $\hat{u}_1$ and $\hat{u}_2$ respectively. The components of $\hat{\boldsymbol{M}}, \hat{\boldsymbol{S}}$ and $\hat{\boldsymbol{F}}$ are given by

$$\hat{M}^n_{\alpha\beta} := \int_{\hat{\Omega}} J^n \hat{\Phi}_\alpha \hat{\Phi}_\beta, \tag{4.7.2}$$

$$\hat{S}^n_{\alpha\beta} := \int_{\hat{\Omega}} [J\boldsymbol{K}]^n \nabla\hat{\Phi}_\alpha \cdot \boldsymbol{K}^n \nabla\hat{\Phi}_\beta, \tag{4.7.3}$$

and

$$\hat{F}^n_\alpha := \int_{\hat{\Omega}} J^n \hat{\Phi}_\alpha. \tag{4.7.4}$$

For reaction kinetics (2.5.8) the components of $\hat{\boldsymbol{N}}_1$ and $\hat{\boldsymbol{N}}_2$ are given by

$$\left(\hat{N}_1\right)_{\alpha\beta} := \sum_{\eta=1}^{\dim(\hat{\mathbb{V}})} \sum_{\vartheta=1}^{\dim(\hat{\mathbb{V}})} \left[(W_2)_\eta (W_2)_\vartheta\right]^{n-1} \int_{\hat{\Omega}} J^n \hat{\Phi}_\alpha \hat{\Phi}_\beta \hat{\Phi}_\eta \hat{\Phi}_\vartheta, \tag{4.7.5}$$

and

$$\left(\hat{N}_2\right)_{\alpha\beta} := \int_{\hat{\Omega}} J^n \hat{\Phi}_\alpha \hat{\Phi}_\beta + \sum_{\eta=1}^{\dim(\hat{\mathbb{V}})} \sum_{\vartheta=1}^{\dim(\hat{\mathbb{V}})} \left[(W_1)_\eta (W_2)_\vartheta\right]^{n-1} \int_{\hat{\Omega}} J^n \hat{\Phi}_\alpha \hat{\Phi}_\beta \hat{\Phi}_\eta \hat{\Phi}_\vartheta, \tag{4.7.6}$$

respectively. For kinetics (2.5.9)

$$\begin{aligned}\left(\hat{N}_1\right)_{\alpha\beta} &:= \int_{\hat{\Omega}} J^n \hat{\Phi}_\alpha \hat{\Phi}_\beta \\ &\quad + \sum_{\eta,\vartheta,\zeta,\varrho=1}^{\dim(\hat{\mathbb{V}})} \kappa \left[\frac{(W_2)_\eta}{1 + (W_1)_\vartheta + k(W_1)_\zeta (W_1)_\varrho}\right]^{n-1} \int_{\hat{\Omega}} J^n \hat{\Phi}_\alpha \hat{\Phi}_\beta \hat{\Phi}_\eta \hat{\Phi}_\vartheta \hat{\Phi}_\zeta \hat{\Phi}_\varrho,\end{aligned} \tag{4.7.7}$$

and

$$\begin{aligned}\left(\hat{N}_2\right)_{\alpha\beta} &:= \int_{\hat{\Omega}} cJ^n \hat{\Phi}_\alpha \hat{\Phi}_\beta \\ &\quad + \sum_{\eta,\vartheta,\zeta,\varrho=1}^{\dim(\hat{\mathbb{V}})} \kappa \left[\frac{(W_1)_\eta}{1 + (W_1)_\vartheta + k(W_1)_\zeta (W_1)_\varrho}\right]^{n-1} \int_{\hat{\Omega}} J^n \hat{\Phi}_\alpha \hat{\Phi}_\beta \hat{\Phi}_\eta \hat{\Phi}_\vartheta \hat{\Phi}_\zeta \hat{\Phi}_\varrho.\end{aligned} \tag{4.7.8}$$

We now illustrate the implementation of scheme (4.5.49) where the linear systems are assembled on the evolving domain. By the definition of $\mathbb{V}_{t^n}$ (4.5.48) we obtain the following system matrices if we assemble the linear systems on the evolving domain

$$M^n_{\alpha\beta} := \int_{\Omega_{t^n}} \Phi^n_\alpha \Phi^n_\beta = \hat{M}^n_{\alpha\beta}, \tag{4.7.9}$$

$$S^n_{\alpha\beta} := \int_{\Omega_{t^n}} \nabla\Phi^n_\alpha \cdot \nabla\Phi^n_\beta = \hat{S}^n_{\alpha\beta}, \tag{4.7.10}$$

and

$$F^n_\alpha := \int_{\Omega_{t^n}} \Phi^n_\alpha = \hat{F}^n_\alpha. \tag{4.7.11}$$

We thus obtain the following linear systems:

$$\begin{cases} \left(\frac{1}{\tau}\boldsymbol{M}^n + D_1\boldsymbol{S}^n + \gamma\boldsymbol{N}_1^n\right)\boldsymbol{W}_1^n &= \frac{1}{\tau}\boldsymbol{M}^{n-1}\boldsymbol{W}_1^{n-1} + \gamma a\boldsymbol{F}^n \\ \left(\frac{1}{\tau}\boldsymbol{M}^n + D_2\boldsymbol{S}^n + \gamma\boldsymbol{N}_2^n\right)\boldsymbol{W}_2^n &= \frac{1}{\tau}\boldsymbol{M}^{n-1}\boldsymbol{W}_2^{n-1} + \gamma b\boldsymbol{F}^n, \end{cases} \tag{4.7.12}$$

where for reaction kinetics (2.5.8) the components of $\boldsymbol{N}_1 = \hat{\boldsymbol{N}}_1$ are given by

$$(N_1)_{\alpha\beta} := \sum_{\eta=1}^{\dim(\hat{\mathbb{V}})}\sum_{\vartheta=1}^{\dim(\hat{\mathbb{V}})}\left[(W_2)_\eta(W_2)_\vartheta\right]^{n-1}\int_{\Omega_{tn}}\Phi_\alpha^n\Phi_\beta^n\Phi_\eta^n\Phi_\vartheta^n \tag{4.7.13}$$

with analogous modifications for $\boldsymbol{N}_2$ and for kinetics (2.5.9).

Both formulations (4.7.1) and (4.5.49) result in the same linear algebra problem. Solve for vectors $\boldsymbol{b}_i^n, i = 1, \ldots, m$,

$$\boldsymbol{A}^n\boldsymbol{b}_i^n = \boldsymbol{c}_i^{n-1}, \text{ for } n = 1, \ldots, N. \tag{4.7.14}$$

The matrix $\boldsymbol{A}^n$ is symmetric sparse and positive definite. We therefore use the conjugate gradient (CG) algorithm [Hestenes and Stiefel, 1952] to compute the solution to the linear systems.

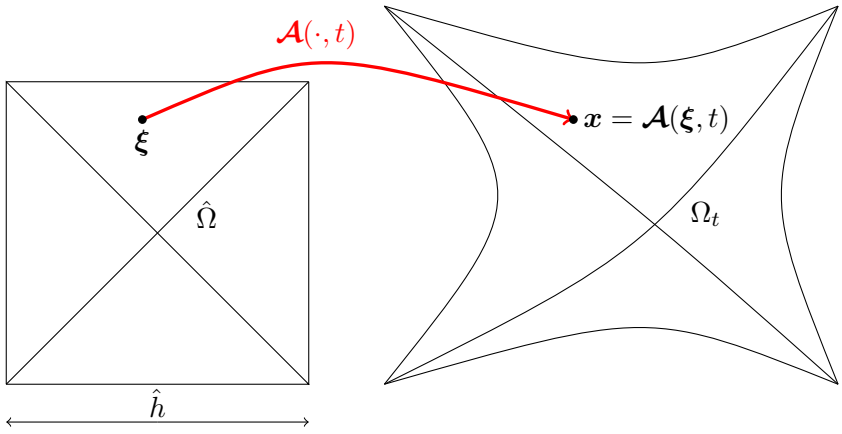

Figure 4.1: An example of the reference and evolving domain with the associated mapping, mesh-size and triangulations.

4.7.1 Remark (Quadrature on the evolving domain)**.** As we do not have to compute the Jacobian of the mapping, assemblage of the linear systems is faster on the evolving domain. However, in the previous analysis we have neglected errors due to variational crimes, such as the fact that integrals of finite element functions must be evaluated by some numerical quadrature. In light of this, it should be noted that the finite dimensional space $\mathbb{V}_t$ on the evolving domain will not in general consist of piecewise polynomial functions. Furthermore, simplices on the evolving domain will not in general be affine transformations of the reference simplex (see Figure 4.1 for an example). If formulation (4.5.49) is used and domain evolution is not spatially linear, the influence of numerical quadrature on the accuracy of the scheme should be considered. We leave this extension for future studies.

4.8 Numerical experiments

We now provide numerical evidence to back-up the estimates of Theorems 4.5.6 and 4.6.8. We start by verifying the a priori estimate of the convergence rate (4.5.51). We use as a test problem the Schnakenberg kinetics (2.5.8), although any other reaction kinetics that fulfil our assumptions could have been used.

4.8.1 Remark (Existence of solutions to Problem (2.4.7) with spatially linear isotropic evolution)**.** In Chapter 3, we show that Problem (2.4.7) equipped with reaction kinetics (2.5.8) or (2.5.9) and $\Omega_t \in C^2(\Omega_t)$ is well posed under any bounded spatially linear isotropic evolution of the domain. If we assume the analysis holds for polygonal domains, we have sufficient regularity on the continuous problem to apply Theorem 4.5.6 and thus, scheme (4.5.47) converges with optimal order with $\mathbb{P}^1$ elements.

4.8.2 Definition (Experimental order of convergence)**.** We denote the $L_\infty\big(0,T;L_2(\Omega)^m\big)$ error in the numerical scheme on a series of uniform refinements of a triangulation $\big\{\hat{\mathscr{T}}_i\big\}_{i=0,\dots,N}$ by $\{\boldsymbol{e}_i\}_{i=0,\dots,N}$. The experimental order of convergence (EOC) is defined to be the numerical measure of rate of convergence of the scheme as $\hat{h}_n \to 0$, where $\hat{h}_n$ denotes the maximum mesh-size of $\hat{\mathscr{T}}_n$.

$$\mathrm{EOC}_i(\boldsymbol{e}_{i,i+1},\hat{h}_{i,i+1}) = \frac{\ln(\boldsymbol{e}_{i+1}/\boldsymbol{e}_i)}{\ln(\hat{h}^{i+1}/\hat{h}_i)}. \tag{4.8.1}$$

4.8.3 Numerical verification of the a priori convergence rate

We examine the EOC of scheme (4.5.47) to approximate the solution to (2.4.7) with $\mathbb{P}^1$, $\mathbb{P}^2$ and $\mathbb{P}^3$ basis functions and with timestep $\tau \approx \hat{h}^2$, $\tau \approx \hat{h}^3$ and $\tau \approx \hat{h}^4$ respectively (since the scheme is first order in time). In all cases we take a time interval of $[0,1]$ and the initial domain as the unit square.

We consider two different forms of domain evolution that include both domain growth and contraction to illustrate the versatility of the proposed finite element scheme.

- Spatially linear periodic evolution:

$$\boldsymbol{\mathcal{A}}(\boldsymbol{\xi},t) = \boldsymbol{\xi}\left(1+\sin\left(\frac{\pi t}{T}\right)\right). \tag{4.8.2}$$

- Spatially nonlinear periodic evolution:

$$\mathcal{A}_i(\xi_i,t) = \xi_i\left(1+\sin\left(\frac{\pi t}{T}\right)\xi_i\right), \tag{4.8.3}$$

  for $i = 1,\dots,d$.

Thus, in both cases the domain grows to a square of length 2 at $t = 0.5$ before contracting back to the initial domain at end time. We take the diffusion coefficients $\boldsymbol{D} = (0.01,1)^{\mathsf{T}}$ and the parameter $\gamma = 1$. Problem (2.4.7) equipped with the nonlinear reaction kinetics (2.5.8) does not admit any closed form solutions. In order to provide numerical verification of the convergence rate, we insert a source term such that the exact solution is,

$$\begin{aligned}\hat{u}_1(\boldsymbol{\xi},t) &= \sin(\pi t)\exp(-10\,|\boldsymbol{\xi}|^2),\\ \hat{u}_2(\boldsymbol{\xi},t) &= -\sin(\pi t)\exp(-10\,|\boldsymbol{\xi}|^2).\end{aligned} \tag{4.8.4}$$

We use the PDE for $\hat{\boldsymbol{u}}$ derived in (2.6.1) to construct the benchmark problems by applying the differential operator therein to the exact solution (4.8.4) to obtain $\boldsymbol{g}(\boldsymbol{\xi}, t)$ the right hand side for the benchmark problems. Thus, our benchmark example is:

4.8.4 Example (Benchmark problem)**.** Find (u_1, u_2) such that for $(\boldsymbol{\xi}, t) \in \hat{\Omega} \times (0, T]$,

$$\begin{cases} \left[\partial_t u_1 - 0.01\Delta u_1 + \nabla \cdot (\boldsymbol{a} u_1)\right] \left(\boldsymbol{\mathcal{A}}(\boldsymbol{\xi}, t), t\right) = g_1(\boldsymbol{\xi}, t) - \left[u_1 - u_1^2 u_1\right] \left(\boldsymbol{\mathcal{A}}(\boldsymbol{\xi}, t), t\right) \\ \left[\partial_t u_2 - \Delta u_2 + \nabla \cdot (\boldsymbol{a} u_2)\right] \left(\boldsymbol{\mathcal{A}}(\boldsymbol{\xi}, t), t\right) = g_2(\boldsymbol{\xi}, t) - \left[u_1^2 u_1\right] \left(\boldsymbol{\mathcal{A}}(\boldsymbol{\xi}, t), t\right), \end{cases} \tag{4.8.5}$$

with homogenous Neumann boundary conditions and zero initial data (the exact solution (4.8.4) evaluated at $t = 0$). For our first example (linear periodic growth (4.8.2)) the function $\boldsymbol{g}(\boldsymbol{\xi}, t)$ takes the form

$$\begin{cases} g_1(\boldsymbol{\xi}, t) = & \partial_t \hat{u}_1(\boldsymbol{\xi}, t) + 2\frac{\pi \cos(\pi t)}{1+\sin(\pi t)} \hat{u}_1(\boldsymbol{\xi}, t) - \frac{0.01}{\left(1+\sin(\pi t)\right)^2} \Delta \hat{u}_1(\boldsymbol{\xi}, t) \\ & + [\hat{u}_1 - \hat{u}_1^2 \hat{u}_2](\boldsymbol{\xi}, t), \\ g_2(\boldsymbol{\xi}, t) = & \partial_t \hat{u}_2(\boldsymbol{\xi}, t) + 2\frac{\pi \cos(\pi t)}{1+\sin(\pi t)} \hat{u}_2(\boldsymbol{\xi}, t) - \frac{1}{\left(1+\sin(\pi t)\right)^2} \Delta \hat{u}_2(\boldsymbol{\xi}, t) \\ & + [\hat{u}_1^2 \hat{u}_2](\boldsymbol{\xi}, t). \end{cases} \tag{4.8.6}$$

For the second example (nonlinear periodic growth (4.8.3)) the function $\boldsymbol{g}(\boldsymbol{\xi}, t)$ takes the form

$$\begin{cases} g_1(\boldsymbol{\xi}, t) = \partial_t \hat{u}_1(\boldsymbol{\xi}, t) + 2\pi \cos(\pi t) \left(\frac{\xi_1}{1+\sin(\pi t)\xi_1} + \frac{\xi_2}{1+\sin(\pi t)\xi_2}\right) \hat{u}_1(\boldsymbol{\xi}, t) \\ -0.01 \left(\left(1 + 2\sin(\pi t)\,\xi_1\right)^{-2} \partial_{\xi_1\xi_1} \hat{u}_1(\boldsymbol{\xi}, t) + \left(1 + 2\sin(\pi t)\,\xi_2\right)^{-2} \partial_{\xi_2\xi_2} \hat{u}_1(\boldsymbol{\xi}, t) \right) \\ \quad - \sum_{i=1}^{2} \frac{0.02\sin(\pi t)}{1+(1+2\xi_i \sin(\pi t))^3} \partial_{\xi_i} \hat{u}_1(\boldsymbol{\xi}, t) + [\hat{u}_1 - \hat{u}_1^2 \hat{u}_2](\boldsymbol{\xi}, t), \\ \\ g_2(\boldsymbol{\xi}, t) = \partial_t \hat{u}_2(\boldsymbol{\xi}, t) + 2\pi \cos(\pi t) \left(\frac{\xi_1}{1+\sin(\pi t)\xi_1} + \frac{\xi_2}{1+\sin(\pi t)\xi_2}\right) \hat{u}_2(\boldsymbol{\xi}, t) \\ - \left(\left(1 + 2\sin(\pi t)\,\xi_1\right)^{-2} \partial_{\xi_1\xi_1} \hat{u}_2(\boldsymbol{\xi}, t) + \left(1 + 2\sin(\pi t)\,\xi_2\right)^{-2} \partial_{\xi_2\xi_2} \hat{u}_2(\boldsymbol{\xi}, t) \right) \\ \quad - \sum_{i=1}^{2} \frac{2\sin(\pi t)}{1+(1+2\xi_i \sin(\pi t))^3} \partial_{\xi_i} \hat{u}_2(\boldsymbol{\xi}, t) + [\hat{u}_1^2 \hat{u}_2](\boldsymbol{\xi}, t). \end{cases} \tag{4.8.7}$$

In both cases $\hat{\boldsymbol{u}}$ is the function defined in (4.8.4).

Tables 4.1 and 4.2 show the EOCs for the two benchmark examples. For the first benchmark example where domain growth is linear with respect to space, we assemble the linear systems on the evolving domain corresponding to scheme (4.7.12). For the second benchmark example, as domain evolution is nonlinear, we assemble the linear systems on the reference frame corresponding to scheme (4.7.1). In both cases we observe that the error converges at the expected rate of $\ell + 1$ where ℓ is the degree of the finite element basis functions, providing numerical evidence for the a priori estimate of Theorem 4.5.6.

$\hat{h}$	2^{-2}	2^{-3}	2^{-4}	2^{-5}
$\mathbb{P}^1$	1.055	2.214	2.073	2.019
$\mathbb{P}^2$	1.947	2.873	2.977	2.898
$\mathbb{P}^3$	-1.958	3.959	3.956	3.918

Table 4.1: EOC in the $L_\infty\big(0,T;L_2(\Omega_t)^m\big)$ norm for Problem (2.4.7) with kinetics (2.5.8) and spatially linear domain evolution (4.8.2). The linear systems are assembled on the evolving frame corresponding to system (4.7.12).

$\hat{h}$	2^{-2}	2^{-3}	2^{-4}	2^{-5}
$\mathbb{P}^1$	1.554	2.253	2.076	1.823
$\mathbb{P}^2$	1.999	2.973	2.971	2.963
$\mathbb{P}^3$	-0.9758	3.959	3.952	3.953

Table 4.2: EOC in the $L_\infty\Big(0,T;L_2(\hat{\Omega})^m\Big)$ norm for Problem (2.4.7) with kinetics (2.5.8) and nonlinear domain evolution (4.8.3). The linear systems are assembled on the reference frame corresponding to system (4.7.1).

4.8.5 A numerical study of the residual estimator

We have implemented the residual estimator for the case of spatially linear domain evolution and $\mathbb{P}^1$ basis functions. We now conduct an experiment to back-up the a posteriori estimate of Theorem 4.6.8. We expect the estimator to behave asymptotically like the error in the $H^1\big(\hat{\Omega}\big)^m$ norm. To examine this behaviour, we examine the EOC of the estimator (by taking $\hat{\mathscr{E}}$ in place of $\boldsymbol{e}$ in (4.8.1)) for the benchmark problem on the domain with periodic linear growth (4.8.2). To minimise the error due to the time-discretisation, we take a very refined timestep ($\tau = 10^{-5}$) and examine the convergence of the estimator in the $L_2\big([0,T]\big)$ norm. We plot the log of the estimator values for successive mesh refinements (which we use to calculate the EOC) and the EOC in Figure 4.2(a). We observe the EOC$\approx$1, backing up the theoretical results (if we assume the error converges with optimal order).

To examine the practical usefulness of the estimator, we also calculate the *effectivitiy index* of the estimator which is a numerical measure of the constant C that appears in (4.6.30) and is often used as a measure of the quality of the estimator. The effectivity index is defined as:

$$\mathrm{EI}_i^n := \frac{\hat{\mathscr{E}}_i^n}{D_i \left\| \nabla \left([\hat{u} - \hat{U}_i]^n \right) \right\|_{L_2\left(\hat{\Omega}\right)}}. \tag{4.8.8}$$

We present the effectivity index for the most refined mesh in the above benchmark computation ($h = 2^{-5}, \tau = 10^{-5}$). We use the estimator and error of the activator species ($\hat{u}_1$), the rationale being that the diffusion coefficient for this species is lower and thus, the approximation is likely to be less accurate. Figure 4.2(b) shows the inverse of the effectivity index over time (we plot the inverse as the initial error is zero). We see the inverse of the effectivity index is well behaved and appears to approach a constant value of around 0.3 giving an effectivity index of around 3.3.

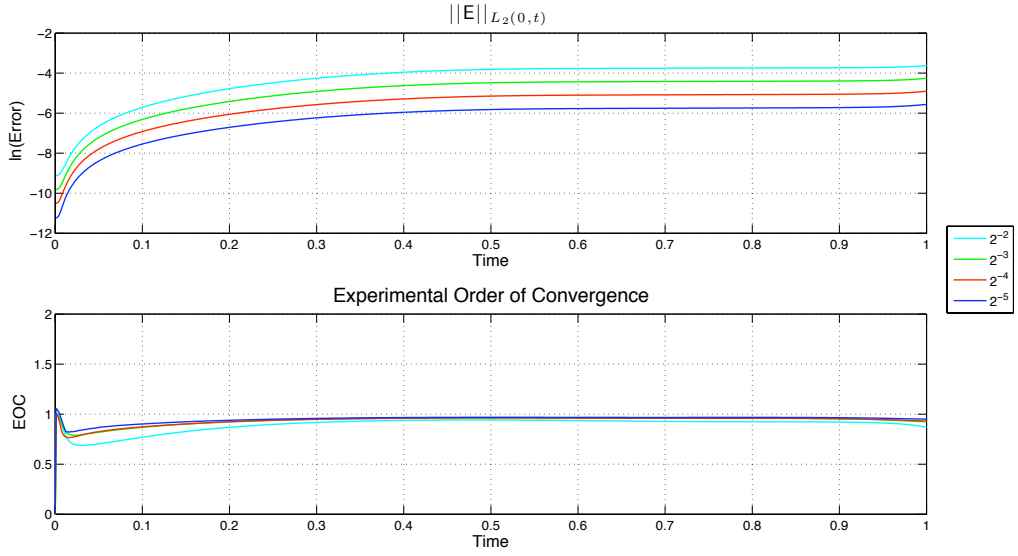

(a) Estimator values and EOC

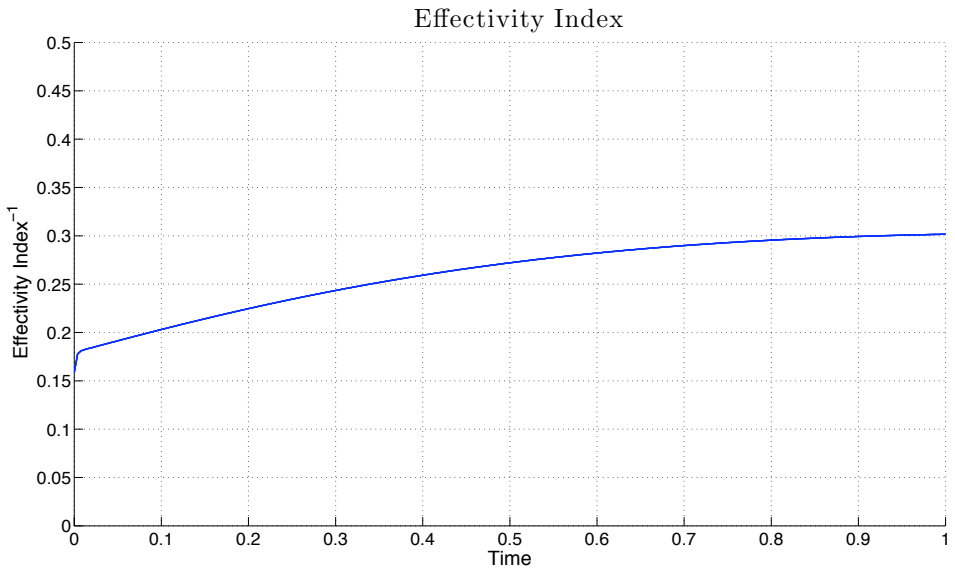

(b) Inverse effectivity index

Figure 4.2: The log of the $L_2\big([0,T]\big)$ norm of the estimator $\hat{\mathscr{E}}$ (cf. (4.6.17)), the EOC of the estimator and the inverse of the effectivity index all against time. The legend in Figure 4.2(a) indicates the mesh-size $\hat{h}$ taken for each simulation.

4.9 Conclusion

We have presented and analysed a fully discrete finite element scheme to approximate the solution to semilinear RDSs posed on continuously evolving domains. Given suitable assumptions on the reaction kinetics and domain evolution we have shown that the proposed scheme converges at an optimal rate in the $L_\infty\big(0,T;L_2(\Omega_t)^m\big)$ norm.

The computational method considered in this work has applications to the study of biological pattern formation, a field in which computer simulations of RDSs on evolving domains are widespread. The scheme presented provides a practical numerical method that should prove useful to scientists in the field of developmental biology and in other fields where semilinear RDSs are encountered.

Domain evolution may be viewed as changing the coefficients of the PDE (in the reference framework) or altering the mesh-size of the triangulation (in the evolving framework), thus adaptive schemes for the solution of RDSs are likely to dramatically improve computational efficiency. For the purposes of deriving a space-adaptive scheme, the a priori analysis carried out in this study was used as a guide in the a posteriori analysis of the error in the semidiscrete scheme. A residual based a posteriori error estimate was derived which can be used to drive adaptive mesh-refinement. We presented the details of the implementation of the method for two reaction kinetics that have applications to the theory of biological pattern formation. Finally, we conducted some numerical experiments with a view to backing-up our theoretical results.

The problems we have in mind are inherently posed on long time-scales and an important area for future work will be the a posteriori analysis of the fully discrete scheme. We also wish to extend our analysis the ALE formulation [Donea et al., 2004] (of which the Eulerian and Lagrangian formulations considered in this study are special cases). This formulation would allow consideration of adaptive moving mesh methods and for suitably chosen time-discretisations has attractive stability properties when domain evolution is nonlinear with respect to space [Boffi and Gastaldi, 2004; Mackenzie and Mekwi, 2011]. RDSs posed on evolving surfaces or domains with topological changes are becoming increasingly important in applications and extension of the analysis to these scenarios is an important subject for future work. We also wish to consider cases where domain evolution is unknown or stochastic as these scenarios have applications to cell motility and tumour growth.

In the next Chapter, we illustrate the versatility of the numerical method derived in this Chapter by simulating RDSs on domains with varied evolution.

Chapter 5

Patterns on evolving domains

5.1 Introduction

In this chapter we conduct computer simulations to validate the theoretical results of Chapters 3 and 4. We then use the FEM of Chapter 4 to investigate the behaviour of solutions to RDSs on time-independent and evolving domains.

We start in §5.2.1 by checking that patterns predicted by linear stability analysis are accurately approximated by the method for problems on time-independent domains. In §5.2.2 we investigate the patterns that arise as a result of varying a scaling parameter on fixed domains, an approach that has widely been used as an ad hoc model for domain evolution. We use §5.3.1 to back-up the rescaling of §2.6, by presenting numerical results for an RDS posed on a domain with periodic evolution and an equivalent transformed problem on a time-independent domain. We also compare this approach of modelling domain evolution with the approach used in §5.2.2. We use §5.3.2 to illustrate some of the spectacular pattern transitions that occur even with the relatively simple form of domain evolution considered in Chapter 3. We also examine the patterns that result when domain evolution is spatially nonlinear. In §5.3.3 we examine the role of domain and mesh symmetry in the bifurcation of solutions to an RDS on a growing disc. We show that changes in domain or mesh symmetry can dramatically affect the bifurcation sequence. §5.4 contains results obtained using an adaptive algorithm driven by the estimator derived in Chapter 4 and an error indicator for the time-discretisation. Our results indicate that spatial and temporal adaptivity is worthwhile for problems posed on time-dependent domains.

All the numerical simulations were carried out utilising the adaptive finite element toolbox ALBERTA [Schmidt and Siebert, 2005]. In all the simulations the FE space (at least on the reference domain cf. Chapter 4) was taken to be the space of piecewise linear functions. The linear systems were solved using the CG algorithm. The graphics presented were created using PARAVIEW.

5.2 Patterns on time-independent domains

5.2.1 Patterns from linear stability analysis

To examine the EOC of the numerical scheme, we considered modified reaction kinetics such that we knew the exact solution to Problem (2.4.7). We now present some examples on time-independent domains where we attempt to test the accuracy of the code without modifying the kinetics. To this end, we utilise the fact that near primary bifurcation points linear stability analysis provides a good approximation to the full nonlinear RDS [Dillon et al., 1994]. Thus, if we

take parameter values, under which only a single (low) wavenumber is unstable (cf. §2.5) and we consider a domain where the eigenfunctions of the Laplacian are known, the solution to the RDS should correspond to the unstable mode obtained from linear stability analysis. We consider the unit square domain. Thus, eigenfunctions of the Laplacian with homogenous Neumann boundary conditions are of the form:

$$\psi_{m,n} = \cos(m\pi x_1) + cos(n\pi x_2), \tag{5.2.1}$$

where m and n are the wavenumbers of the unstable mode. Recalling the Thomas kinetics

$$\begin{cases} f_1(u_1, u_2) &= \gamma\left(a - u_1 - g(u_1, u_2)\right), \\ f_2(u_1, u_2) &= \gamma\left(b - \alpha u_2 - g(u_1, u_2)\right), \end{cases} \tag{5.2.2}$$

where

$$g(u_1, u_2) = \frac{\kappa u_1 u_2}{1 + u_1 + \beta u_1^2}, \tag{5.2.3}$$

we set $a = 150, b = 150, \alpha = 1.5, \kappa = 13$, $\beta = 0.05$ and $\gamma = 252$. Madzvamuse [2000] shows that the $(2, 2)$ mode is isolated (i.e., the only unstable mode) if we take the diffusion coefficients $\boldsymbol{D} = (1, 30.9152)^{\mathsf{T}}$. Similarly recalling the Schnakenberg kinetics

$$\begin{cases} f_1(u_1, u_2) &= \gamma\left(a - u_1^2 u_2\right), \\ f_2(u_1, u_2) &= \gamma\left(b - u_1 + u_1^2 u_2\right), \end{cases} \tag{5.2.4}$$

with $a = 0.1, b = 0.9$ and $\gamma = 435.99$. Madzvamuse [2000] shows that the $(4, 0)$ mode is isolated (or the equivalent (0,4) mode) if we take the diffusion coefficients $\boldsymbol{D} = (1, 8.6676)^{\mathsf{T}}$.

Figure 5.1(b) shows the spatially nonuniform steady state of the discrete activator concentration (u_1) obtained using the FEM outlined in Chapter 4. In both cases we took a uniform mesh with 8321 degrees of freedom (DOFs) and a fixed timestep of 10^{-4}. We used the change in the discrete solutions as a stopping criteria, terminating the simulation when the system reached the spatially nonuniform steady state. The substrate (inhibitor) profile (u_2) has been omitted as it is in phase (out of phase) with the activator. The solution profiles as expected correspond to the (2,2) mode and (4,0) mode on the unit square respectively (cf. (5.2.1)).

5.2.2 Patterns for increasing γ

We now investigate the effect of varying the the scaling parameter γ, which is proportional to the area of the domain in 2 dimensions. This parameter was introduced by Arcuri and Murray [1986] and since then, many studies of RDSs have modelled domain growth by simply increasing the value of γ. We take an initial domain of $[-0.25, 0.25]^2$ and consider the Schnakenberg equations with the following parameter values: $a = 0.1, b = 0.9$ and $\boldsymbol{D} = (0.01, 1)^{\mathsf{T}}$. We take a uniform mesh with 8321 DOFs and a fixed timestep of 10^{-2}. The change in the discrete solution was used to determine the end time of the simulation. Figure 5.2 shows the spatially non-uniform steady states obtained for increasing values of γ. Since we are considering square domains, $\gamma^{1/2}$ is proportional to the length of the domain, thus Figures 5.2(a), 5.2(b) and 5.2(c) can equivalently be viewed as the solution of the RDS with the parameter $\gamma = 1$ on a square of length $10^{1/2}, 50^{1/2}$

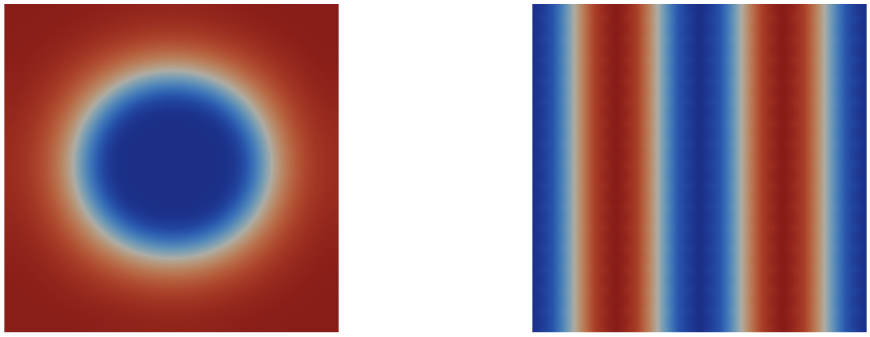

(a) Thomas kinetics (b) Schnakenberg kinetics

Figure 5.1: Spatially nonuniform steady states on the unit square for the Thomas and Schnakenberg kinetics with parameter values that promote growth of the (2,2) mode and the (4,0) mode respectively.

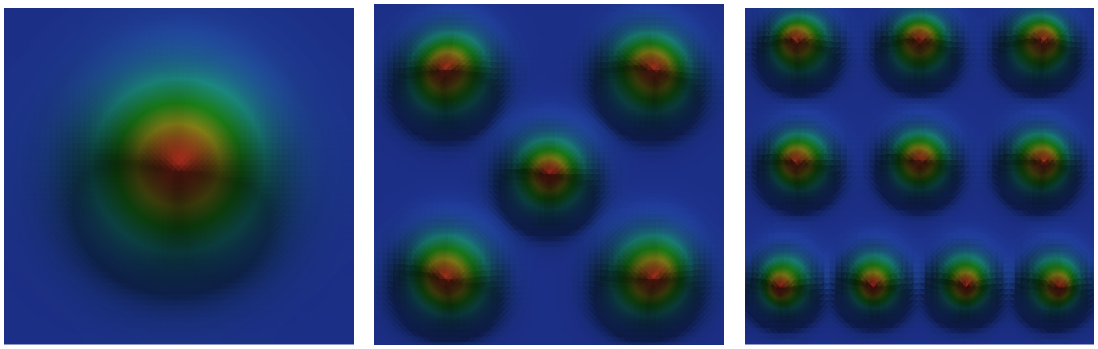

(a) $\gamma = 10$ (b) $\gamma = 50$ (c) $\gamma = 100$

Figure 5.2: Spatially nonuniform steady states for the Schnakenberg kinetics on a time-independent domain with increasing values of γ. For parameter values see text. As γ is increased more complicated patterns (higher mode-numbers) are expressed.

and 10 times the original length respectively. We see that as γ is increased for this set of parameter values an increasing number of spots are produced. In §5.3.1 we compare these results with results of an RDS posed on an evolving domain with identical length scales and parameter values to investigate the validity of using a scaling parameter as an ad hoc model of domain evolution.

5.3 Transient patterns on evolving domains

5.3.1 Verification of the rescaling

In this section we present numerical results on two-dimensional evolving domains firstly to support the rescaling we use to prove our theoretical results and secondly to illustrate the limitations

of using the scaling parameter γ to model domain growth. We present results for the aforementioned Schnakenberg model (2.5.8) with the following parameter values: $a = 0.1, b = 0.9, \gamma = 1$ and $\boldsymbol{D} = (0.01, 1)^{\mathsf{T}}$. We consider domain evolution of the form:

$$\boldsymbol{\mathcal{A}}(\boldsymbol{\xi}, t) = \left(1 + 9\sin\left(\frac{\pi t}{T}\right)\right)\boldsymbol{\xi}. \tag{5.3.1}$$

Thus, the domain grows to 10 times the original size before contracting back to the initial domain, which we take to be $[-0.25, 0.25]^2$. To validate the rescaling of §3.2, we compare the approximate solution of an RDS posed on the evolving domain and the approximate solution of the equivalent transformed system on a fixed domain as in §2.6. For example, on the evolving domain the problem is stated as follows:

$$\begin{cases} \left[\partial_t u_1 + \nabla\cdot(\boldsymbol{a}u_1) - 0.01\Delta u_1\right](\boldsymbol{x}, t) = 0.1 - u_1(\boldsymbol{x}, t) + [u_1^2 u_2](\boldsymbol{x}, t), \\ \left[\partial_t u_2 + \nabla\cdot(\boldsymbol{a}u_2) - \Delta u_2\right](\boldsymbol{x}, t) = 0.9 - [u_1^2 u_2](\boldsymbol{x}, t), \ \boldsymbol{x} \in \Omega_t, t \in (0, T], \\ [\boldsymbol{\nu}\cdot\nabla\boldsymbol{u}](\boldsymbol{x}, t) = 0, \quad \boldsymbol{x} \in \partial\Omega_t, t > 0, \end{cases} \tag{5.3.2}$$

where $\boldsymbol{x} = \boldsymbol{\mathcal{A}}(\boldsymbol{\xi}, t)$ and $\boldsymbol{a}(\boldsymbol{x}, t) = \partial_t\boldsymbol{\mathcal{A}}(\boldsymbol{\xi}, t)$. Equivalently, the following transformed equations are obtained on a fixed domain (cf. §2.6),

$$\begin{cases} \partial_t u_1 + 2\frac{\dot\rho}{\rho}u_1 - \frac{0.01}{\rho^2}\Delta u_1 = 0.1 - u_1 + u_1^2 u_2, & \text{on } \Omega_0 \times (0, T], \\ \partial_t u_2 + 2\frac{\dot\rho}{\rho}u_2 - \frac{1}{\rho^2}\Delta u_2 = 0.9 - u_1^2 u_2, & \\ [\boldsymbol{\nu}\cdot\nabla\boldsymbol{u}](\boldsymbol{\xi}, t) = 0, & \boldsymbol{\xi} \in \partial\Omega_0, t > 0, \end{cases} \tag{5.3.3}$$

where $\rho(t) = 1 + 9\sin\left(\frac{\pi t}{T}\right)$. In both cases we take identical initial conditions as small perturbations around the homogenous steady state of (1.0, 0.9) valid on fixed domains. We solve (5.3.2) with the FEM detailed in Chapter 4. The finite element scheme to approximate the solution to equation (5.3.3) aims to find $W_1^n, W_2^n \in \mathbb{V}^0, n = 1, \ldots, N$ such that

$$\begin{cases} \frac{1}{\tau}\langle W_1^n - W_1^{n-1}, \Phi\rangle + \frac{0.01}{(\rho^n)^2}\langle\nabla W_1^n, \nabla\Phi\rangle & + \frac{2\dot\rho^n}{\rho^n}\langle W_1^n, \Phi\rangle \\ & = \langle 0.9 - W_1^n + W_1^{n-1}W_2^n W_1^n, \Phi\rangle, \\ \frac{1}{\tau}\langle W_2^n - W_2^{n-1}, \Phi\rangle + \frac{1}{(\rho^n)^2}\langle\nabla W_2^n, \nabla\Phi\rangle & + \frac{2\dot\rho^n}{\rho^n}\langle W_2^n, \Phi\rangle \\ & = \langle 0.1 - \left(W_1^{n-1}\right)^2 W_2^n, \Phi\rangle, \end{cases} \tag{5.3.4}$$

for all $\Phi \in \mathbb{V}^0$. Note that this is not equivalent to the reference formulation of the FEM in Chapter 4. We have used the fact that the flow velocity $\boldsymbol{a}$ is known to compute explicitly the $\partial_t(J)u$ term rather than approximating the $\partial_t(J\hat{u})$ term with an implicit Euler method and thus, we are comparing two different discretisations.

We took an initial triangulation $\mathcal{T}^0$ with 8321 DOFs, a uniform mesh diameter of 2^{-6} and a fixed timestep of 10^{-2}.

Figures 5.3 and 5.4 show snapshots of the activator profile. The inhibitor profiles have been omitted as they are 180° out of phase to the activator profiles. We observe identical pattern transitions in the discrete activator concentration under both schemes, validating the results in §2.6.

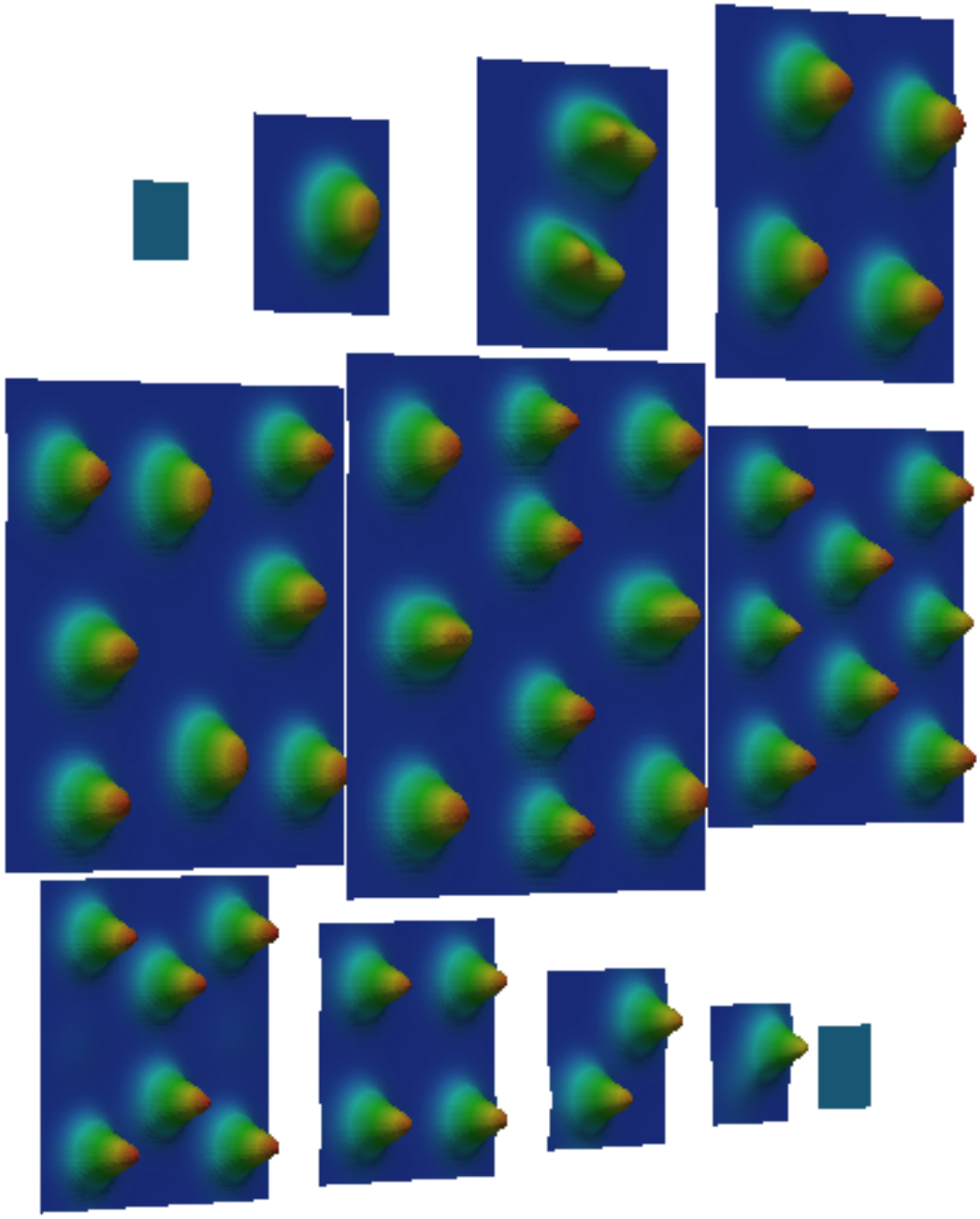

Figure 5.3: Snapshots of the discrete activator profile obtained using the FEM of Chapter 4, at times 0, 50, 160, 220, 380, 500, 700, 740, 820, 900, 980 and 1000 reading from left to right and then top to bottom. For parameter and numerical values see text. The solution exhibits a mode doubling sequence of 1,2,4, 8 and finally, 10 as the domain grows. As the domain contracts, the spots are annihilated in a sequence of 8, 6, 4, 2 and the final transition to a single spot occurs via merging, with the final domain exhibiting no patterns.

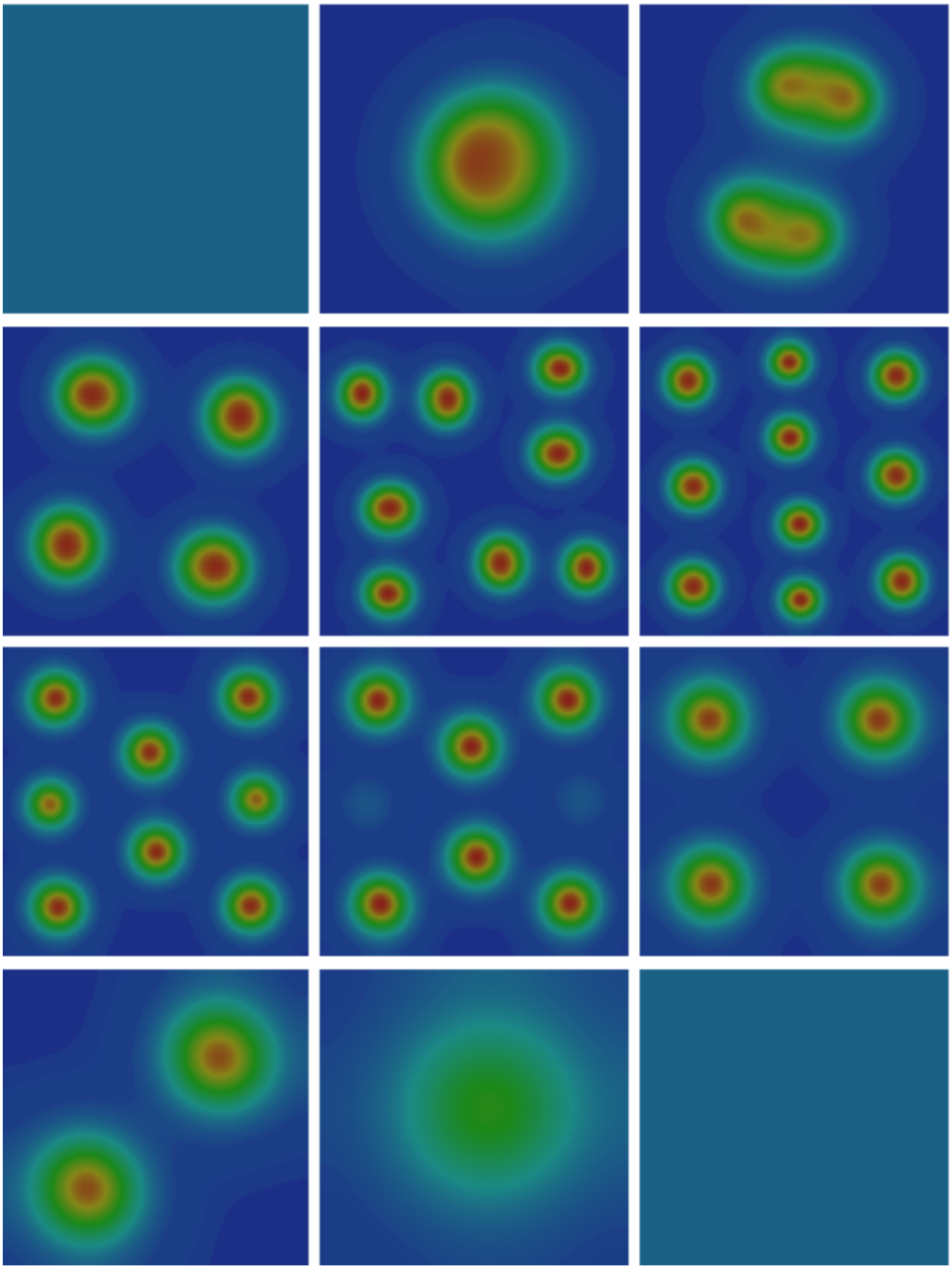

Figure 5.4: Snapshots of the discrete solution W_2 corresponding to system (5.3.4) at times 0, 50, 160, 220, 380, 500, 700, 740, 820, 900, 980 and 1000 reading from left to right and then top to bottom. For parameter and numerical values see text. The mode transition follows exactly that of Figure 5.3, corroborating the results in §2.6.

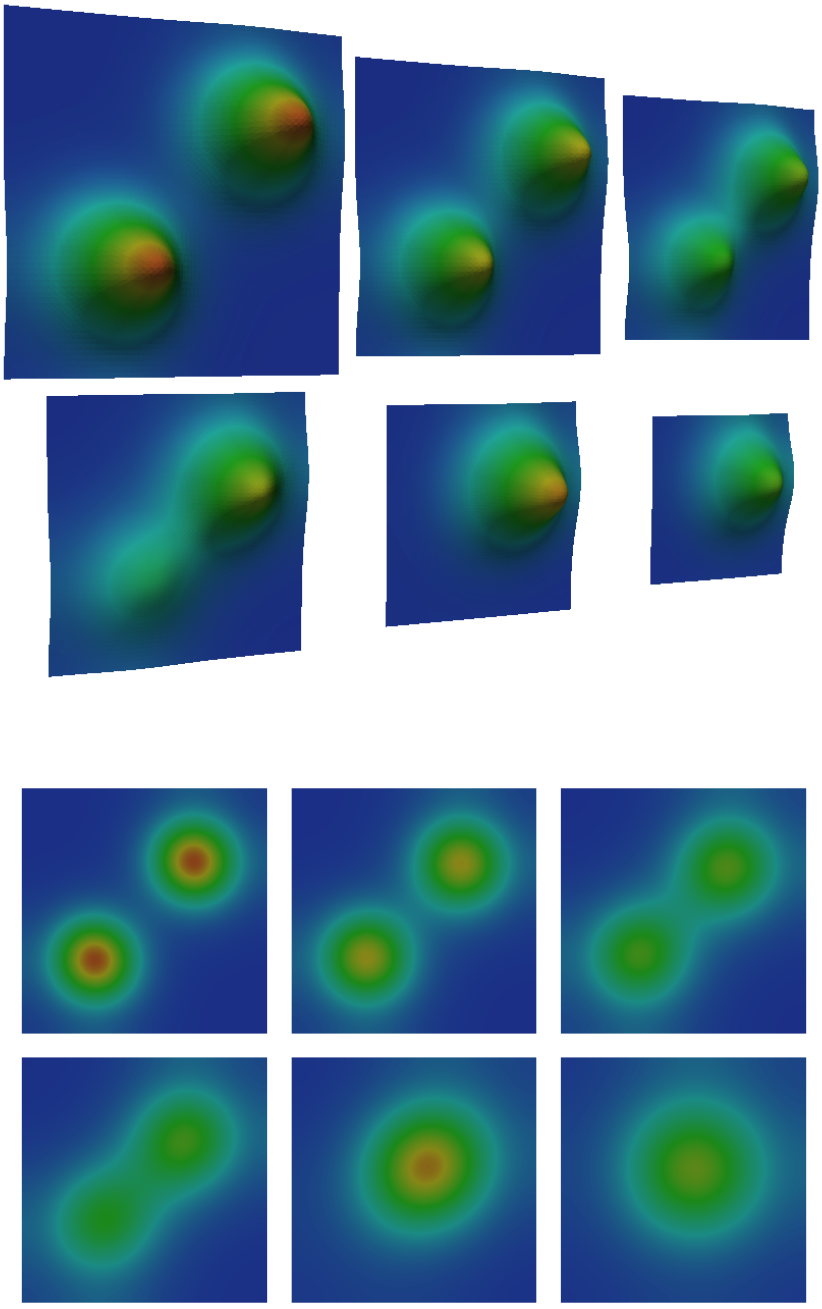

Figure 5.5: Snapshots of the discrete solution U_2 corresponding to continuous problems (5.3.2) (top) and (5.3.3) (bottom) at times 930, 940, 950, 955, 965, 975. The spot merging phenomena observed in the transition from two spots to one spot is displayed.

The figures illustrate the mode doubling phenomena that occurs as the domain grows as well as the spot-annihilation and spot-merging phenomena that occurs as the domain contracts. In Figure 5.5 we present in more detail the novel spot-merging phenomena observed on the contracting domain. It is still unclear whether spot-merging is in fact a special case of the spot-annihilation phenomenon, that occurs when the modes are of sufficient proximity to influence each other. We note that despite the periodic domain evolution, the mode transition sequence is not periodic and the bifurcation of solutions is markedly different when the domain grows to when it contracts.

Comparing the results to the patterns obtained by increasing γ in §5.2.2, we firstly note that the sequence of spots we observe on the evolving domain is constrained by the mechanism by which bifurcations occur (spot-splitting or spot-annihilation/merging). We never observe for example the 5 spot solution visible in Figure 5.2(b). The pattern displayed in Figure 5.2(c) should be compared with the pattern in Figure 5.3 at $t = 500$ (in both cases a domain effectively 10 times the original length). We see that in this case the patterning is similar qualitatively, with the patterned state in both simulations being 10 spots (although as evidenced by the absence of a 5 spot solution this is coincidental). However, the orientation of the spots is markedly different and it is clear from the simulations that domain evolution significantly influences the orientation of patterns, a factor that is completely lost using the scaling parameter approach.

5.3.2 Stripe to spot transitions and asymmetric patterns on evolving domains

We now illustrate some of the spectacular and varied patterns that can be expressed by RDSs on continuously evolving domains, which has led to their widespread use in the context of developmental biology. In the applications we have in mind domain evolution occurs on a much slower timescale than pattern formation allowing each transient pattern mode to be expressed before the domain size changes sufficiently to admit a new mode. In all the numerical simulations of this section we took a timestep of 10^{-2} and a uniform mesh with 8321 nodes.

For the first example we consider the Thomas reaction kinetics with parameter values (cf. (5.2.2)) $a = 92, b = 96, c = 1.5, \kappa = 18.5, \beta = 0.1, \gamma = 16$ and diffusion coefficients $\boldsymbol{D} = (1, 27.1)^{\mathsf{T}}$. For the initial data we take small trigonometric perturbations around the homogenous steady state (9.93, 9.29) valid on time-independent domains. We consider isotropic exponential domain evolution of the form

$$\boldsymbol{\mathcal{A}}(\boldsymbol{\xi}, t) = \exp(0.002t), \tag{5.3.5}$$

with final time $T = 1500$. The initial domain is taken as the unit square and thus at final time $\Omega_{1500} = [0, e^3]^2$.

Figure 5.6 shows snapshots of the activator profile corresponding to $\boldsymbol{W}_1$ in system (4.7.12) with the Thomas reaction kinetics (2.5.9). The substrate ($\boldsymbol{W}_2$) profiles have been omitted as they are in phase with those of the activator. Stripes initially form (with the parameter values we have chosen the initial pattern is a single stripe independent of initial conditions up to orientation) which transients into spots as the domain grows. The initial pattern is a single stripe (Figure 5.6(b)) and subsequent domain growth leads to regular stripe insertion (Figure 5.6(c)), as the domain approaches its final size the striped patterning breaks down (Figure 5.6(d)) and the final domain exhibits only spots (Figure 5.6(e)). The results demonstrate the varied pattern transitions induced by this relatively simple domain evolution, which has led to its widespread use in models for biological pattern formation [Barrass et al., 2006; Crampin et al., 2002a; Madzvamuse and Maini, 2007].

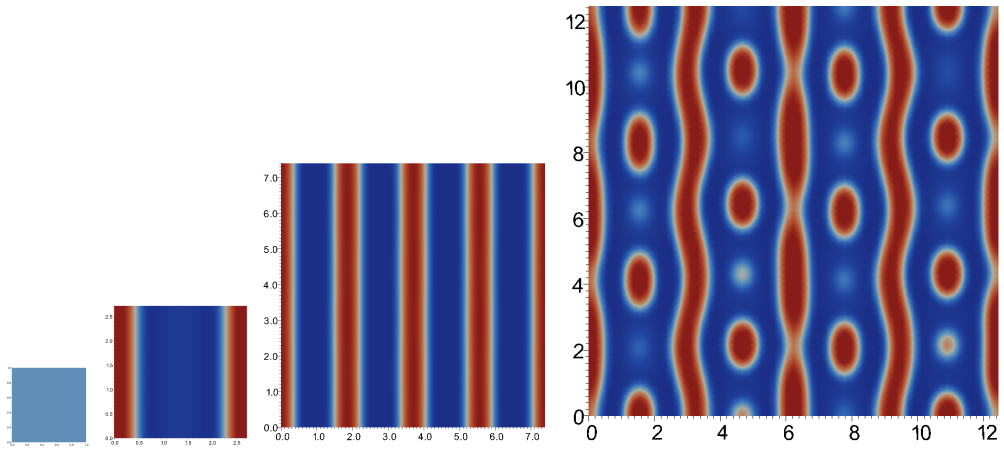

(a) $t = 0$ (b) $t = 500$ (c) $t = 1000$ (d) $t = 1260$

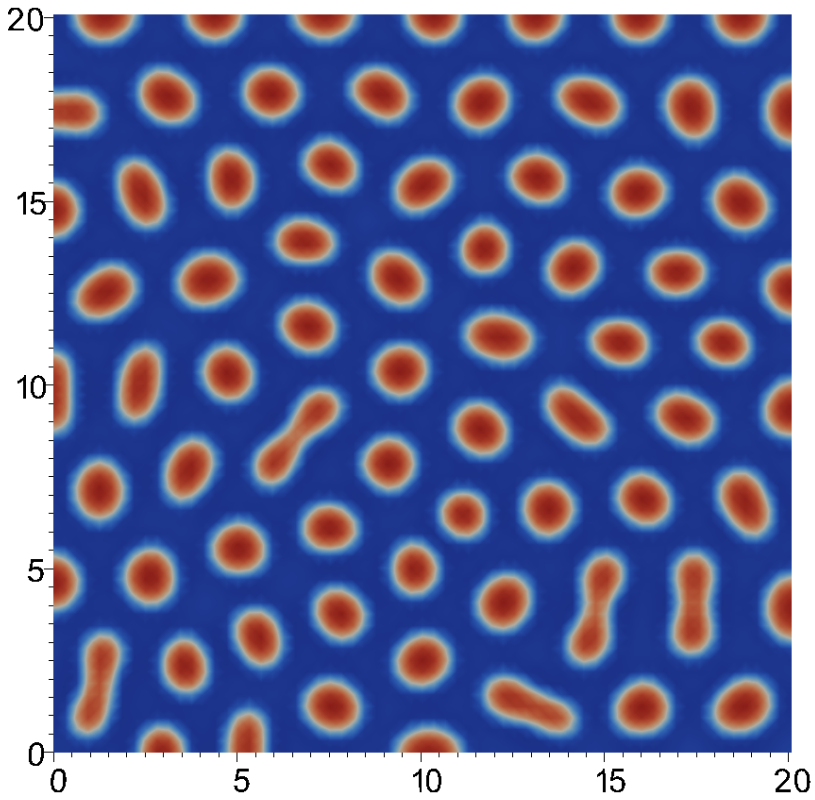

(e) $t = 1500$

Figure 5.6: The discrete activator profile on the evolving domain corresponding to system (4.7.12) with the Thomas kinetics (2.5.9) and exponential domain growth. For parameter values see text. Initially stripes are exhibited with insertion of stripes and finally transition to spots as the domain grows.

We next consider the Schnakenberg kinetics with the same kinetic parameter values as the experiments in §5.2.2 and 5.3.1, on a domain with nonlinear periodic domain evolution of the form

$$\mathcal{A}_i(\boldsymbol{\xi}, t) = \left(1 + 18\sin\left(\frac{\pi t}{T}\right)\xi_i\right)\xi_i, \tag{5.3.6}$$

with final time $T = 1000$. We took the initial domain as a square of length 0.5 and the reference domain as the initial domain i.e., $\hat{\Omega} = [0, .5]^2$. The evolving domain therefore grows to a square of length 5 before contracting back to the initial domain. The evolution of the boundary of the domain is similar to the spatially linear periodic case (5.3.1) however the growth rate within the domain is now non-uniform.

Figure 5.7 shows snapshots of the activator profile corresponding to W_1 in system (4.7.1) with the Schnakenberg kinetics (2.5.8). The inhibitor profiles (W_2) have been omitted as they are 180° out of phase to the activator profiles. Similar to the spatially linear periodic evolution case considered in §5.3.1, we observe spot-splitting phenomena as the domain grows as well as the novel spot-annihilation phenomena that occurs as the domain contracts. Comparing the results to the uniform isotropic periodic evolution case depicted in Figure 5.3 we see that due to nonuniform domain evolution, there is a breakdown of symmetry in the lattice of spots generated on the evolving domain. The results clearly illustrate that patterning is driven by domain evolution and that changes in domain evolution strongly influence the patterns expressed, as observed previously by Crampin et al. [2002b] and Madzvamuse and Maini [2007].

In all of the previous examples the forms of domain evolution considered did not alter the shape of the domain. To further illustrate the versatility of the method, we now present examples of an RDS with the Schnakenberg kinetics and the same set of parameter values as considered in §5.3.1 posed on domains with spatially nonlinear evolution where the domain shape changes drastically during the evolution. We first consider domain evolution of the form

$$\mathcal{A}_i(\boldsymbol{\xi}, t) = \left(1 + 18\sin\left(\frac{\pi t}{T}\right)\xi_j\right)\xi_i, \tag{5.3.7}$$

with final time $T = 1000$ and the initial domain (and reference domain) taken as the square $[0, 0.5]^2$. Under this form of evolution the square continuously grows into a quadrilateral at $t = 500$ with vertices $(0, 0), (0, 1), (1, 0)$ and $(5, 5)$, before contracting back to the original square. Figure 5.8 shows the activator concentrations on a domain with evolution of the form (5.3.7). The bifurcations of solutions occur via the same splitting or annihilation mechanisms previously observed. However, the spatially nonuniform domain evolution clearly influences the shape and position of the spots, which are no longer radially symmetric as was previously observed but now appear stretched in the direction towards which the domain is growing. We next consider the same Schnakenberg system on a domain with evolution of the form

$$\mathcal{A}_i(\boldsymbol{\xi}, t) = \left(1 + 2\sin\left(\frac{\pi t}{T}\right)|\boldsymbol{\xi}|^2\right)\xi_i, \tag{5.3.8}$$

with final time $T = 1000$ and the initial domain (and reference domain) taken as the square $[-1, 1]^2$. Figure 5.9 shows the activator concentrations on a domain with evolution of the form

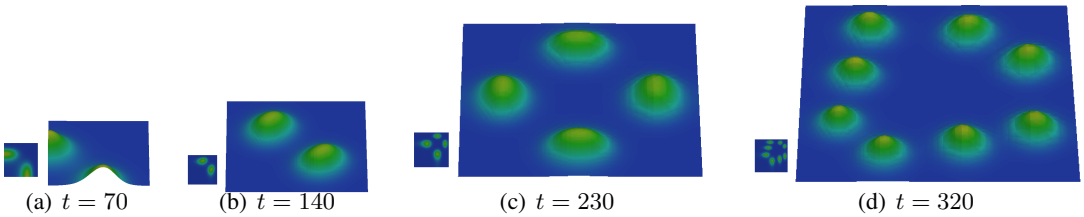

(a) $t = 70$ (b) $t = 140$ (c) $t = 230$ (d) $t = 320$

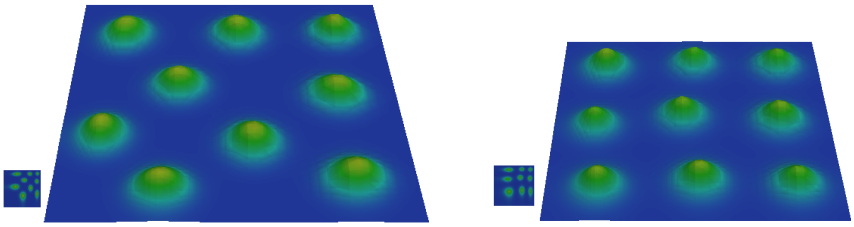

(e) $t = 500$ (f) $t = 750$

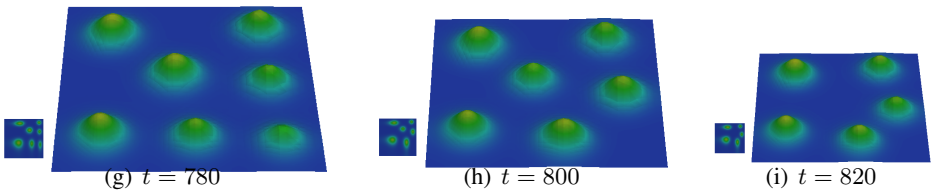

(g) $t = 780$ (h) $t = 800$ (i) $t = 820$

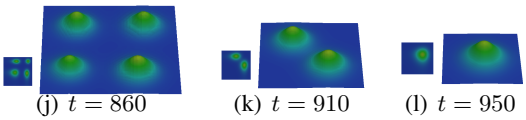

(j) $t = 860$ (k) $t = 910$ (l) $t = 950$

Figure 5.7: The discrete activator profile on the reference domain and mapped to the evolving domain corresponding to system (4.7.1) with the Schnakenberg kinetics (2.5.8) and nonlinear periodic domain evolution (5.3.6). For parameter values see text. The solution exhibits a spot-splitting bifurcation sequence of 2, 4, 8 and 9 as the domain grows. As the domain contracts, spot-annihilation occurs in a 9, 7, 6, 5, 4, 2 and 1 sequence. Although the evolution of the boundary curve of the domain is similar to the spatially linear case (Figure 5.3), we observe a completely different pattern transition sequence. A striking effect of the nonuniform domain evolution is a breakdown in symmetry of the lattice of spots on the evolving domain.

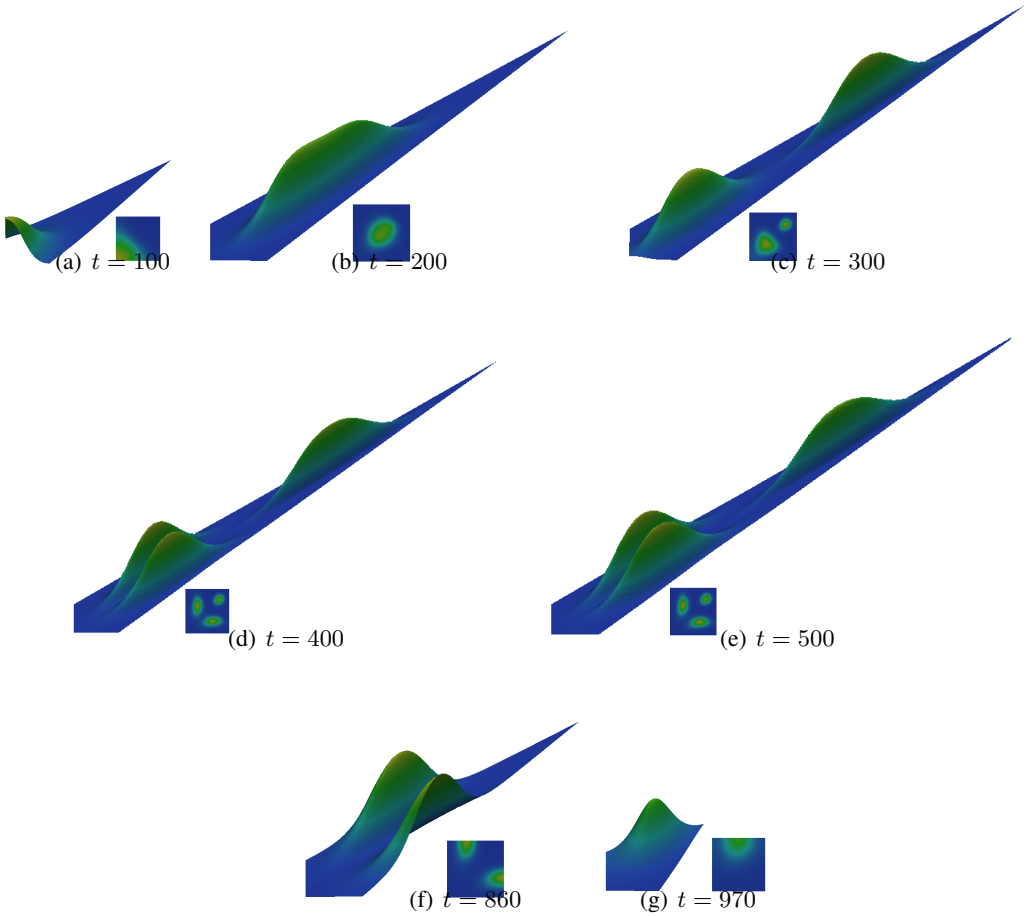

(a) $t = 100$ (b) $t = 200$ (c) $t = 300$

(d) $t = 400$ (e) $t = 500$

(f) $t = 860$ (g) $t = 970$

Figure 5.8: The discrete activator profile on the reference domain and mapped to the evolving domain corresponding to system (4.7.1) with the Schnakenberg kinetics (2.5.8) and nonlinear domain evolution of the form (5.3.7). For parameter values see text. We observe the formation of an initial spot which splits as the domain grows and then a second spot-splitting event occurs with the largest domain exhibiting three spots elongated in the direction of growth. As the domain contracts, the spots are annihilated leaving a single half-spot on the domain at final time.

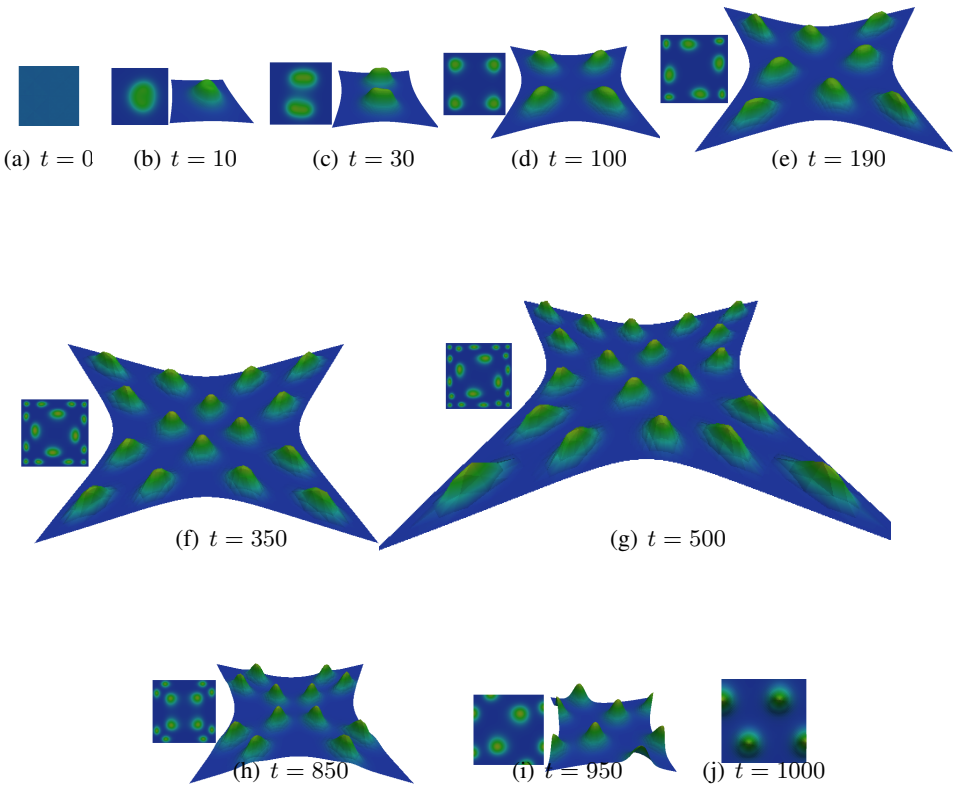

(a) $t = 0$ (b) $t = 10$ (c) $t = 30$ (d) $t = 100$ (e) $t = 190$

(f) $t = 350$ (g) $t = 500$

(h) $t = 850$ (i) $t = 950$ (j) $t = 1000$

Figure 5.9: The discrete activator profile on the reference domain and mapped to the evolving domain corresponding to system (4.7.1) with the Schnakenberg kinetics (2.5.8) and nonlinear domain evolution of the form (5.3.8). For parameter values see text. We see that spots form and increase in number (via splitting) as the domain grows and decrease in number (via annihilation) as the domain contracts. The spots appear to maintain a relatively uniform separation distance on the evolving domain.

(5.3.8). We observe the now familiar spot-splitting behaviour as the domain grows and spot-annihilation as the domain contracts. Interestingly, we observe that the spots appear to orient themselves to maintain a relatively uniform level of separation (which is a characteristic of Turing patterns due to their intrinsic wavelength) as the domain evolves even with this highly nonlinear form of domain evolution.

5.3.3 The role of symmetry in pattern transitions

The influence of domain symmetry on pattern formation processes is well recognised [Gunaratne et al., 1994]. To our knowledge the only study of the role of symmetry in the bifurcation sequence of RDSs on *evolving domains* is the work of Comanici and Golubitsky [2008]. They examine patterns on growing square domains and indicate why for example diagonal stripes are never expressed by invoking arguments from group theory and exploiting the "*hidden symmetries*" that arise from the equivalence between an RDS with homogenous Neumann boundary conditions on a square of length l and an RDS with periodic boundary conditions on a square of length $2l$.

To examine numerically the role of domain symmetry in the bifurcation of solutions on evolving domains, we conduct experiments on polygonal approximations to a *growing disc* of initial radius 0.25. We consider a domain with no radial symmetry (unstructured mesh), and a series of domains where the initial triangulations have D_3, D_4 and D_6 symmetry respectively (where D_n is the dihedral group consisting of the symmetries of a regular polygon with n vertices). To construct our computational domains, we refine the initial triangulation projecting new boundary nodes onto the circle of radius 0.25. Figure 5.10 shows a series of refinements of the initially D_3 symmetric approximation to the disc (equilateral triangle with vertices on the circumference of a circle). The resulting domains have $D_{3(n+1)}$ symmetry where n is the number of global refinements, but the mesh itself has only D_3 symmetry. We take the Schnakenberg kinetics with

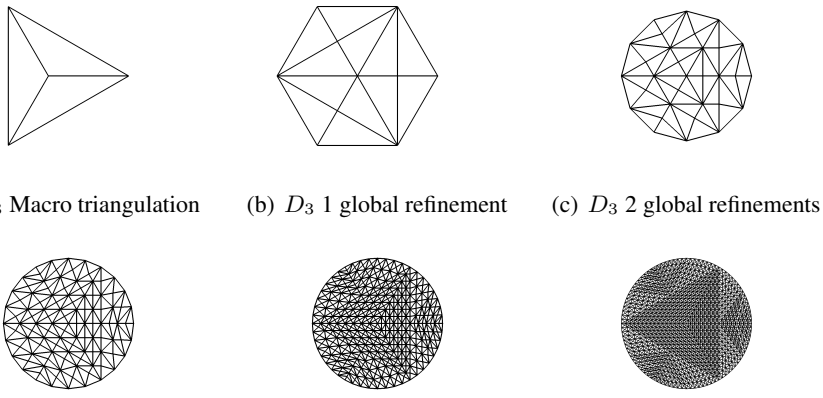

(a) D_3 Macro triangulation (b) D_3 1 global refinement (c) D_3 2 global refinements

(d) D_3 3 global refinements (e) D_3 4 global refinements (f) D_3 5 global refinements

Figure 5.10: A series of refinements of a polygonal approximation to the disc, each refinement is a domain with $D_{3(n+1)}$ symmetry where n is the number of global refinements.

the same parameter values as §5.2.2 as our model problem. We consider exponential domain evolution of the form

$$\mathcal{A}(\boldsymbol{\xi}, t) = \exp(0.001t), \tag{5.3.9}$$

on a time interval $[0, 2350]$. Thus, at the final time the domain is a circle with approximate radius 2.7. Kolokolnikov et al. [2008] examined the mode transitions of an RDS with the Schnakenberg kinetics on fixed 2-dimensional domains and they concluded that peak doubling via a "peanut instability" (see Figure 5.11(d) for an example) was the dominant bifurcation. They conjectured this result was valid on slowly growing domains and they presented numerical simulations on fixed domains to validate their theoretical findings. We now investigate their conjecture by numerically examining bifurcations of the Schnakenberg RDS on a growing disc. In all the simulations we present only the activator concentration (the inhibitor profile is out of phase with the activator profile).

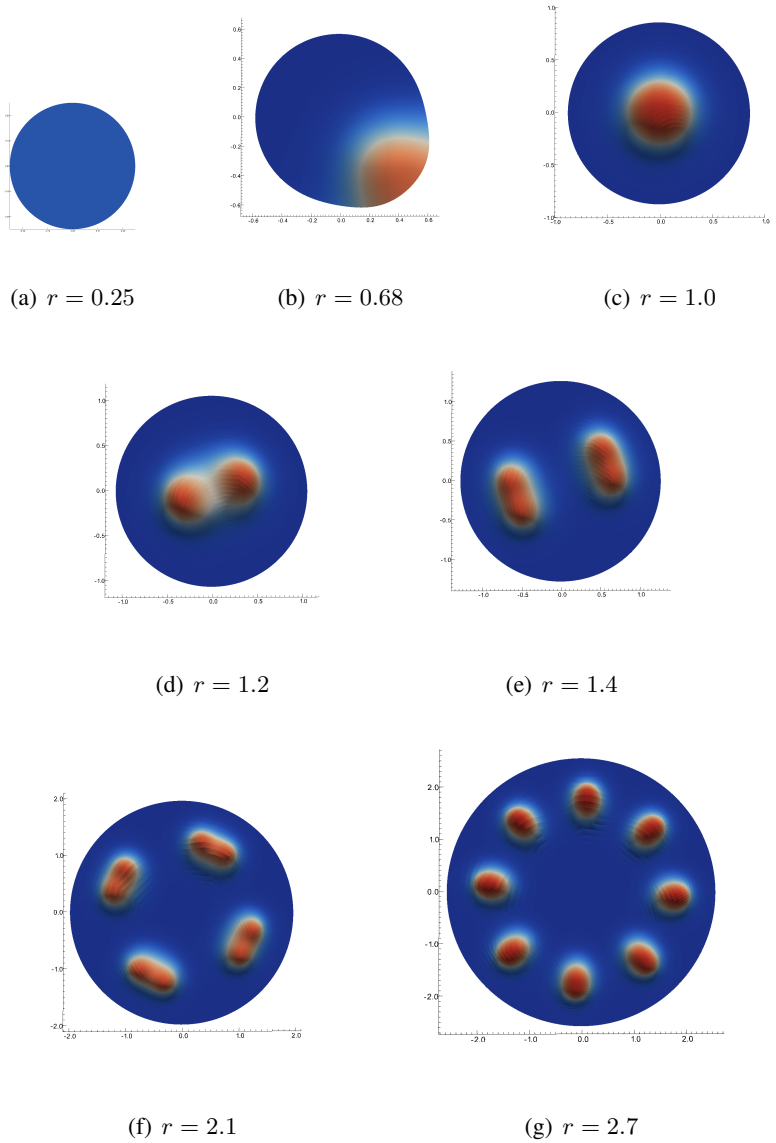

(a) $r = 0.25$ (b) $r = 0.68$ (c) $r = 1.0$

(d) $r = 1.2$ (e) $r = 1.4$

(f) $r = 2.1$ (g) $r = 2.7$

Figure 5.11: The bifurcation sequence on a polygonal approximation to a disc with no radial symmetry. Peak insertion occurs by regular peak-splitting via a "peanut instability" in a 1, 2, 4, 8 sequence.

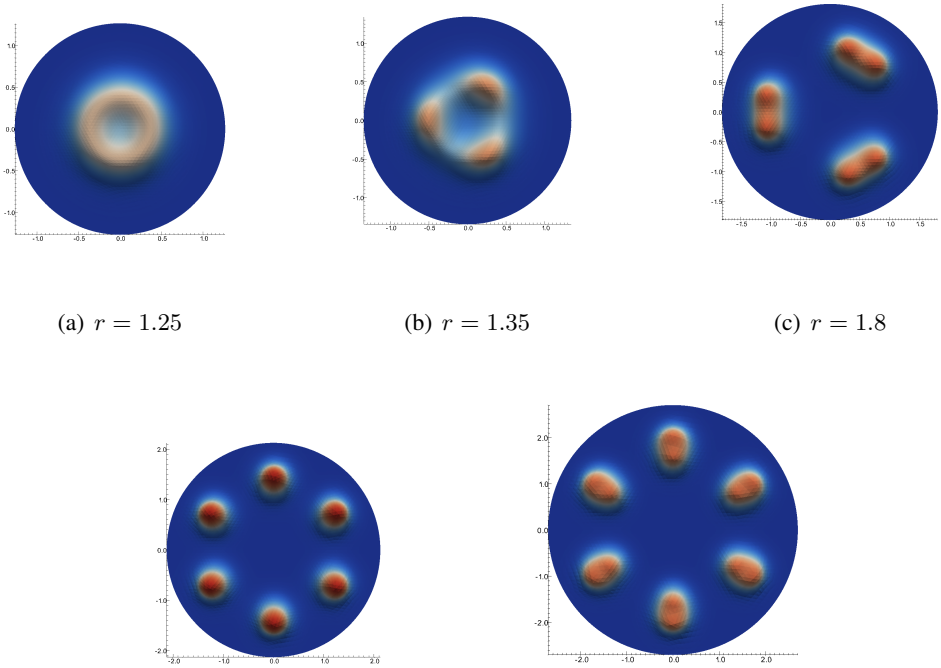

(a) $r = 1.25$ (b) $r = 1.35$ (c) $r = 1.8$

(d) $r = 2.1$ (e) $r = 2.7$

Figure 5.12: The bifurcation sequence on a polygonal approximation to the disc where the mesh has D_3 symmetry. An annulus forms and in the initial bifurcation from one to three spots we observe the breakdown of peak doubling. The peak insertion occurs by splitting in a 1, 3, 6 sequence.

Figure 5.11 shows the pattern transition on the unstructured mesh (with no radial symmetry). We see the initiation of a half-spot which reorients to a single spot positioned at the centre of the domain as it grows. As the domain grows further, the single spot splits into two identical peaks via the characteristic "peanut instability" (Figure 5.11(d)). Subsequently, a second and third wave of peak splitting occurs. The pattern transition takes the form of regular mode doubling with spots splitting in a 1, 2, 4, 8 sequence. The pattern expressed on the domain at end-time is an eight spot radially symmetric lattice.

Figure 5.12 shows the pattern transition on the D_3 symmetric mesh. We have omitted the results up to the stage where a single spot forms in the centre of the domain as it is identical to the unstructured case (Figure 5.11). At a similar time to the first spot-splitting bifurcation on the unstructured mesh, we observe the formation of an annulus in the centre of the domain (Figure 5.12(a)). The spot-splitting behaviour completely breaks down with the first transition being peak tripling (Figure 5.12(b)). Subsequent pattern transitions occur via "peanut" spot-splitting with the final pattern expressed this time being a six spot lattice on the verge of splitting. The pattern transition follows a 1, 3, 6 sequence.

Figures 5.13 and 5.14 show the pattern transition on the D_4 and D_6 symmetric mesh respectively. The pattern transition on both of these domains is very similar we observe the formation

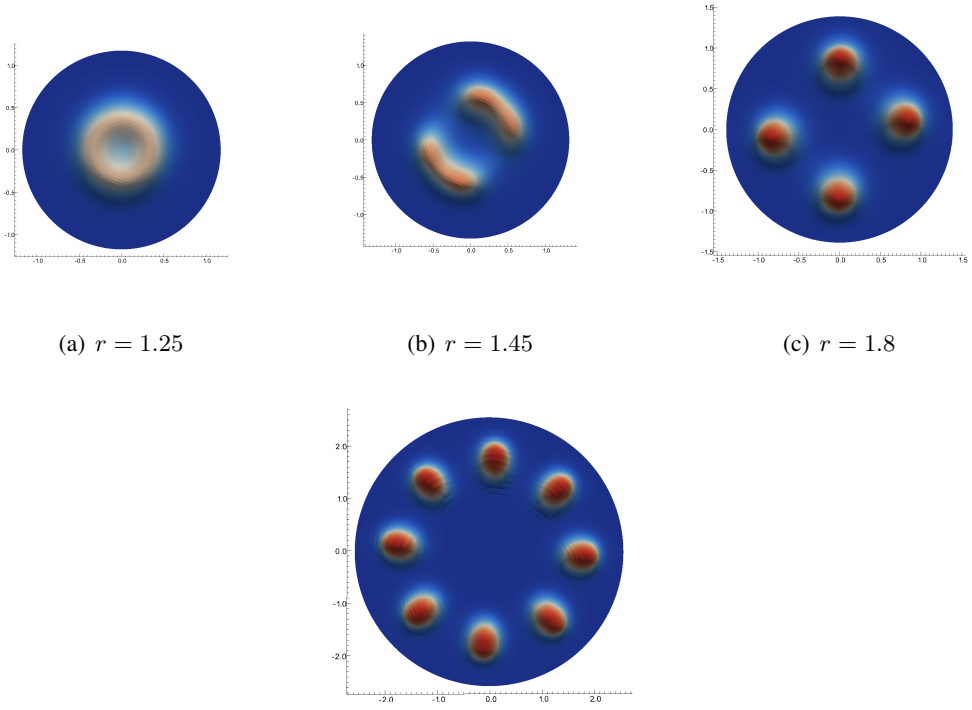

(a) $r = 1.25$ (b) $r = 1.45$ (c) $r = 1.8$

(d) $r = 2.7$

Figure 5.13: The bifurcation sequence on a polygonal approximation to the disc where the mesh has D_4 symmetry. An annulus forms and subsequently, peak insertion occurs by splitting in a 1, 2, 4, 8 sequence.

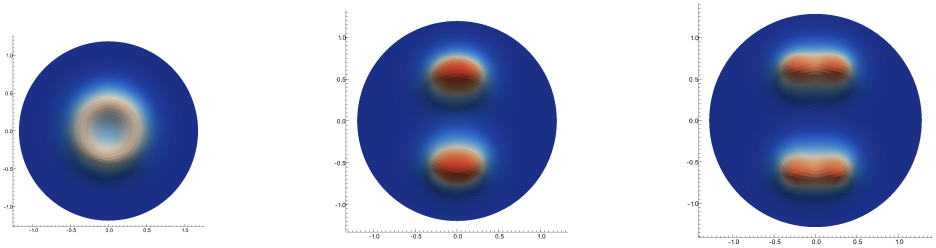

(a) $r = 1.25$ (b) $r = 1.35$ (c) $r = 1.45$

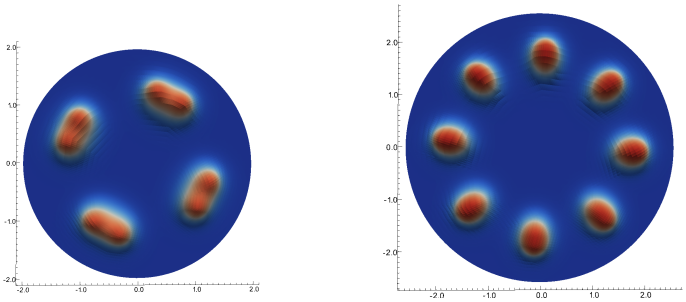

(d) $r = 2.1$ (e) $r = 2.7$

Figure 5.14: The bifurcation sequence on a polygonal approximation to the disc where the mesh has D_6 symmetry. An annulus forms and subsequently, peak insertion occurs by splitting in a 1, 2, 4, 8 sequence.

of annulus structure in both cases which splits into a two spot solution. After that the pattern transitions are similar to the unstructured case with regular spot-splitting occurring via the "peanut instability". The final pattern on both domains is an eight spot lattice identical to the unstructured case.

The results raise interesting observations. On all the domains considered, the initial stage of pattern formation is similar with a half-spot forming which evolves into a single spot located at the centre of the domain. The single spot pattern in the centre of the domain is an example of a robust pattern that arises due to domain evolution and is independent of initial conditions. We do observe the onset of spot-splitting via a "peanut instability" on unstructured meshes and on radially symmetric meshes if we introduce small perturbations into the source term (results omitted). This provides evidence for the conjecture of Kolokolnikov et al. [2008], that spot-splitting via a "peanut instability" is the dominant bifurcation on growing discs for the Schnakenberg RDS with this set of parameter values. However, on radially symmetric domains we note the formation of an annulus structure with the onset of spot-splitting delayed. In the case of the mesh that is D_3 symmetric, peak splitting breaks down completely in favour of peak tripling. We have observed similar behaviour on square domains with spot-splitting breaking down in favour of spot-quadrupling. This leads us to believe that both the onset and the specific form of peak splitting that occurs is highly dependent on the level of radial symmetry of the domain.

The role of mesh and domain symmetry in finite element methods and the ability of finite element methods to preserve symmetries of the continuous problem is still an open question even on fixed domains [McKenna and Reichel, 2007]. Our results indicate the need for further work in this direction. Asymptotically we would expect the simulations to converge, but the nature of the exact solution on the disc, specifically the symmetry of the lattice and the nature of the peak splitting is still an open question. We note that in practice due to the sensitivity of the annulus structure to small changes in geometry or small perturbations of the source term spot-splitting may be the only relevant instability for this set of parameter values for real-word problems. Finally, we remark that this behaviour is not observed for other forms of domain evolution even in the isotropic case due to the time dependence of the $\nabla \cdot \boldsymbol{a}$ dilution term. Our results suggests care must be taken when approximating the solution to RDSs on evolving domains as small changes in domain geometry that disrupt symmetry can strongly influence the patterns expressed.

5.4 Adaptive schemes

5.4.1 Space adaptive scheme

We start by proposing a space adaptive algorithm controlled by the spatial error estimator $\hat{\mathscr{E}}$ defined in (4.6.17), which is kept under a given tolerance by local mesh refinement. The idea of our adaptive algorithm is that a marking strategy is chosen whereby mesh elements are marked for refinement or coarsening (the inverse operation to refinement where degrees of freedom are removed) according to the value of the local error indicator $\hat{\mathscr{E}}_{|\mathsf{S}}$ (cf. §4.6.1) on the element. The mesh is then refined at which point all elements marked for refinement are bisected, at this stage further refinement of elements not originally marked for refinement maybe required as we require that the triangulation contains no hanging nodes (a vertex of one simplex which is not a vertex of a neighbouring simplex). Elements marked for coarsening are then coarsened only if all elements involved in the coarsening step are marked for coarsening (such that the triangulation contains no hanging nodes). The marking strategy we employ is the Equidistribution Strategy [Schmidt and Siebert, 2005, Alg. 1.19, pg. 45], where elements are marked for refinement and coarsening

with the goal of equidistributing the estimator value over all mesh elements. The marking strategy takes two parameters the tolerance of the adaptive algorithm tol and a parameter $\theta \in (0, 1)$. At each timestep elements are marked for refinement according to the following algorithm:

5.4.1.1 Equidistribution strategy (refinement)

Start with $\hat{\mathscr{T}}_0^n$ the initial triangulation at time n, tolerance tol and parameter θ
$k := 0$
solve the discrete linear problem on the mesh $\hat{\mathscr{T}}_k^n$
compute global error estimator $\hat{\mathscr{E}}$ and local error indicators $\hat{\mathscr{E}}_{|\mathsf{s}}$ ▷ cf. §4.6.1
while $\hat{\mathscr{E}} > \mathrm{tol}$ **do**
  for all $\mathsf{s} \in \hat{\mathscr{T}}_k^n$ **do**
    if $\hat{\mathscr{E}}_{|\mathsf{s}} > \theta\,\mathrm{tol}\,/N$ **then** ▷ where N is the number of DOFs of the triangulation
      mark s for refinement ▷ elements are also marked for coarsening at this stage
    end if
  end for
  adapt mesh $\hat{\mathscr{T}}_k^n$ to give $\hat{\mathscr{T}}_{k+1}^n$
  k:=k+1
  solve the discrete linear problem on the mesh $\hat{\mathscr{T}}_k^n$
  Compute global error estimator $\hat{\mathscr{E}}$ and local error indicators $\hat{\mathscr{E}}_{|\mathsf{s}}$
end while

Elements are marked for coarsening in a similar way to the above, the difference being that if the local error indicator plus a coarsening indicator is less than a given tolerance on an element then the element is marked for coarsening [Schmidt and Siebert, 2005, pg. 48]. It is beyond the scope of this work to demonstrate that this algorithm terminates; the design and analysis of adaptive algorithms is an extensive research area and is not the primary focus of this work, we refer to the ALBERTA manual [Schmidt and Siebert, 2005] for an in-depth discussion of adaptive algorithms, marking strategies and their properties.

To compare the results obtained with the adaptive algorithm to the results obtained with the uniform mesh, we first consider two of the problems posed on time-independent domains presented in §5.2.2. Specifically those with $\gamma = 10$ and 50. We use the same timestep (10^{-2}) as in the uniform mesh case. We select parameters tol and θ equal to 10^{-3} and 0.9 respectively. Figure 5.15 shows the resulting non-uniform steady states and we observe the patterns obtained using the adaptive algorithm are identical to those obtained with a uniform mesh. The mesh also appears locally well refined around the spots suggesting the estimator is a good guide for adaptivity.

Intuition suggests adaptivity is likely to be most useful on evolving domains as effectively the mesh-size is now a function of time. To investigate this, we now apply the adaptive algorithm to the solution of problem (5.3.2). Figures 5.16 — 5.21 show the discrete activator profiles obtained by the adaptive scheme for problem (5.3.2) with periodic domain evolution (5.3.1), as considered in §5.3.1. The pattern transitions are identical to those obtained with the uniform mesh (Figure 5.3) validating the adaptive scheme. The mesh is locally well refined around the spots, both as the

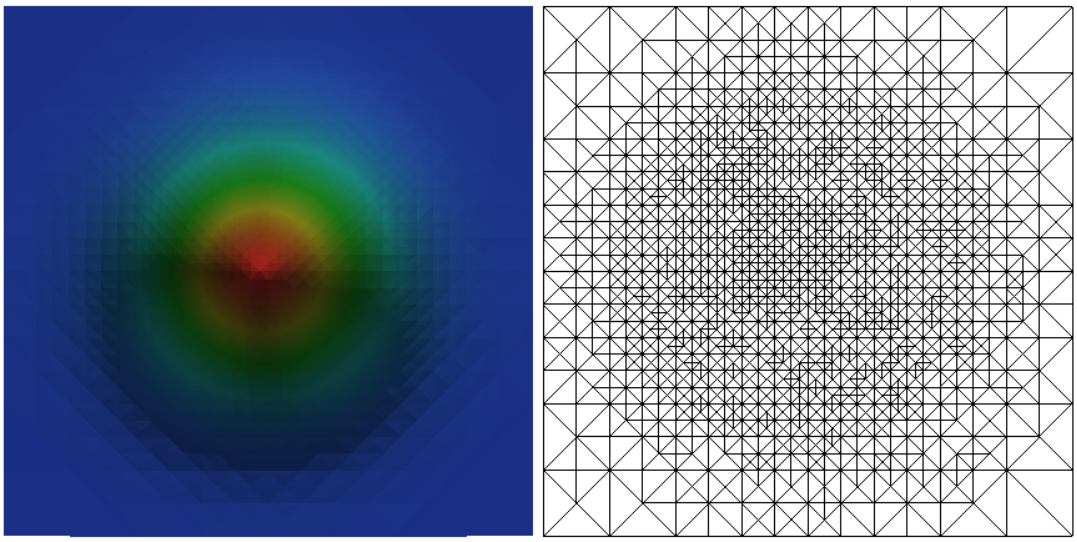

(a) $\gamma = 10$

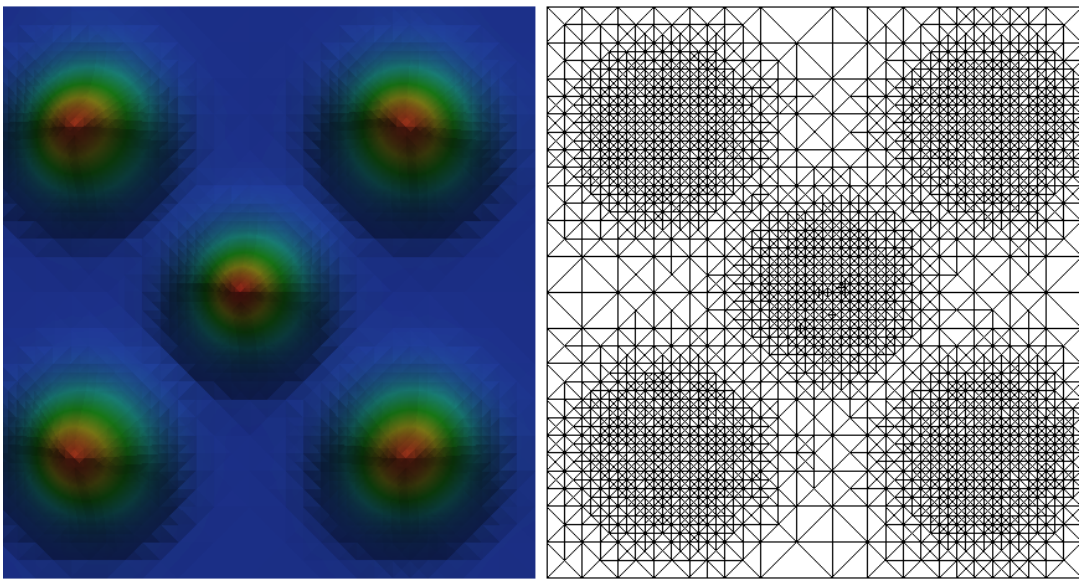

(b) $\gamma = 50$

Figure 5.15: Adaptive approximation of the spatially nonuniform steady states for the Schnakenberg kinetics on a time-independent domain with increasing values of γ. For parameter values see text. The mesh is well refined around the spots and the resulting pattern is identical to the uniform mesh-size case of Figure 5.2.

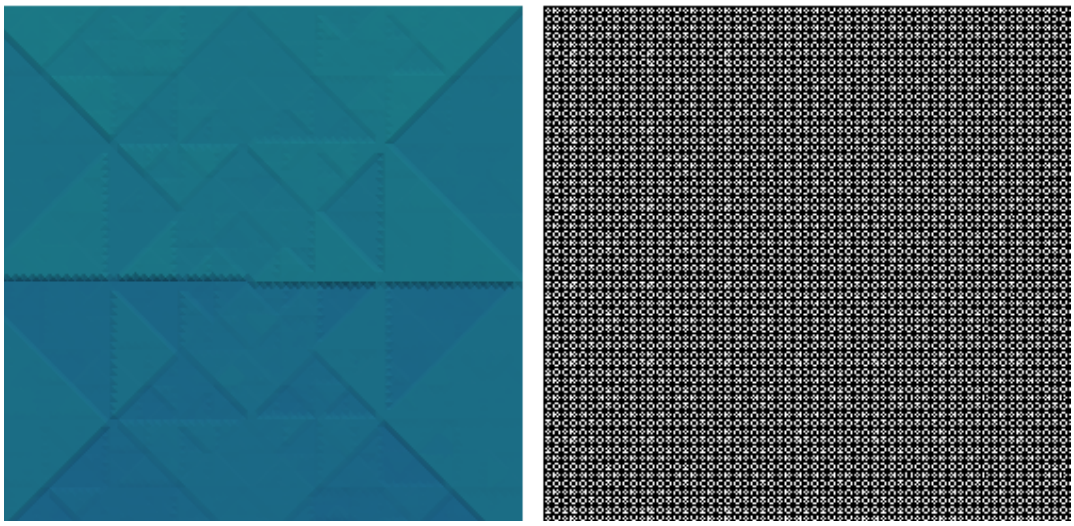

(a) $t = 0$

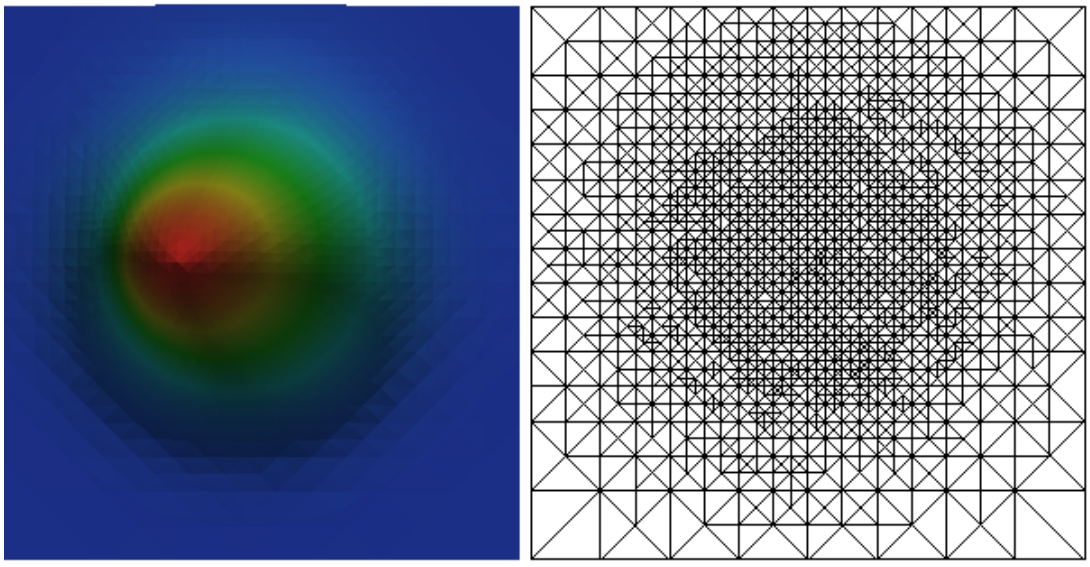

(b) $t = 50$

Figure 5.16: The discrete activator profile for the Schnakenberg kinetics on a domain with periodic evolution under adaptive mesh refinement (for parameter values see text). The mode transitions follow exactly that of Figures 5.3 and 5.4.

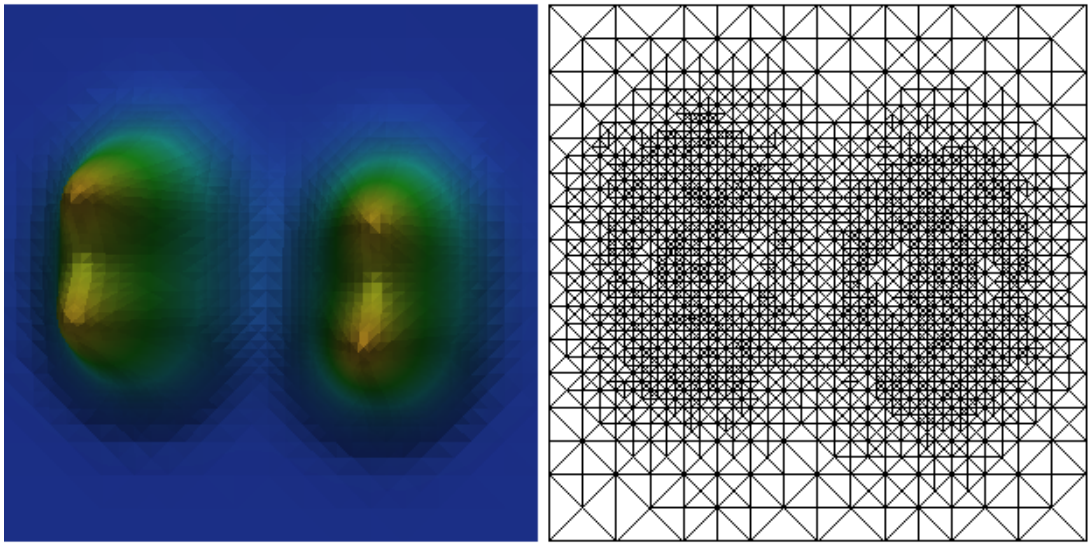

(a) $t = 160$

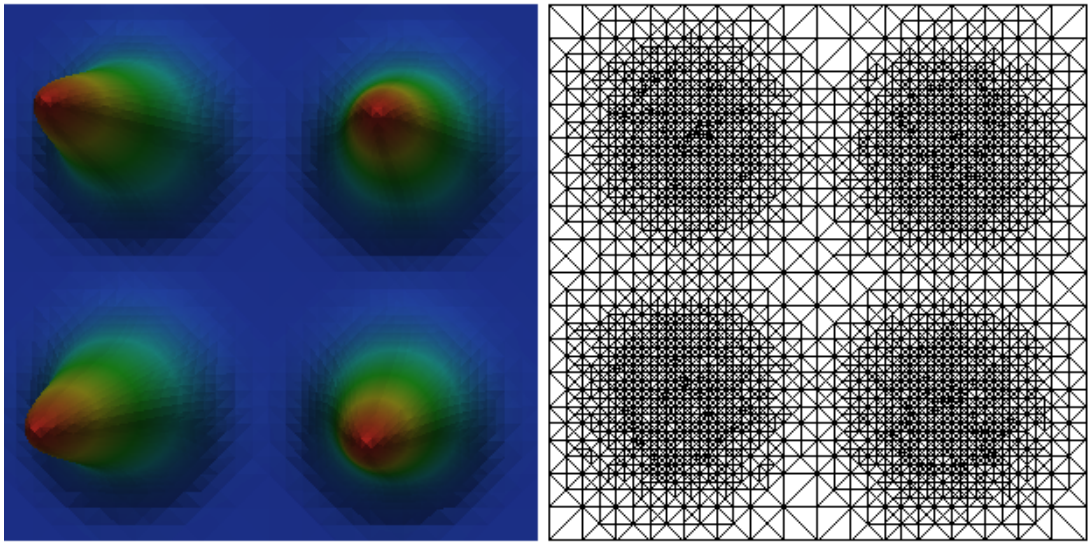

(b) $t = 220$

Figure 5.17: (continuation of Figure 5.16) The discrete activator profile for the Schnakenberg kinetics on a domain with periodic evolution under adaptive mesh refinement (for parameter values see text). The mode transitions follow exactly that of Figures 5.3 and 5.4.

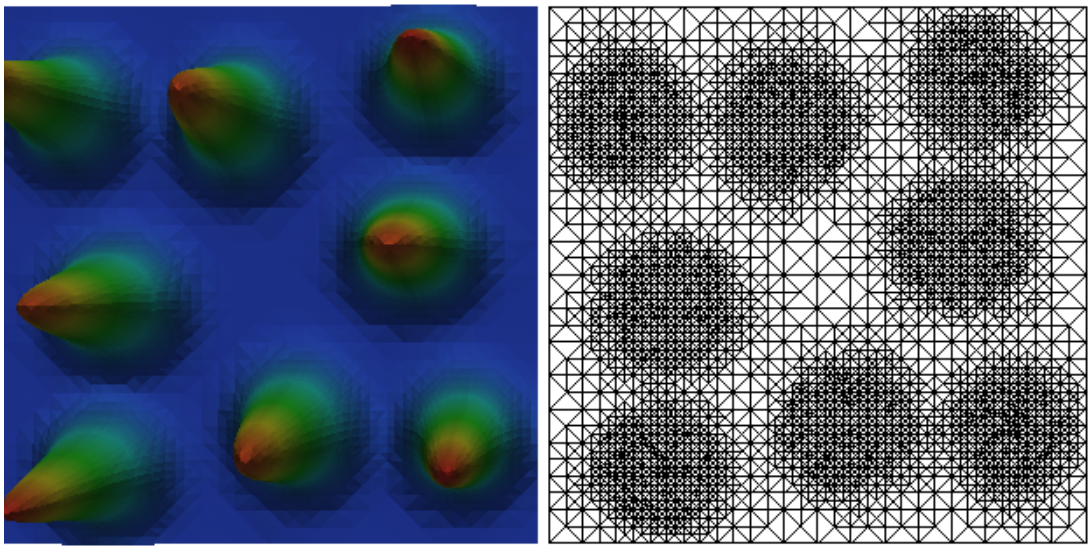

(a) $t = 380$

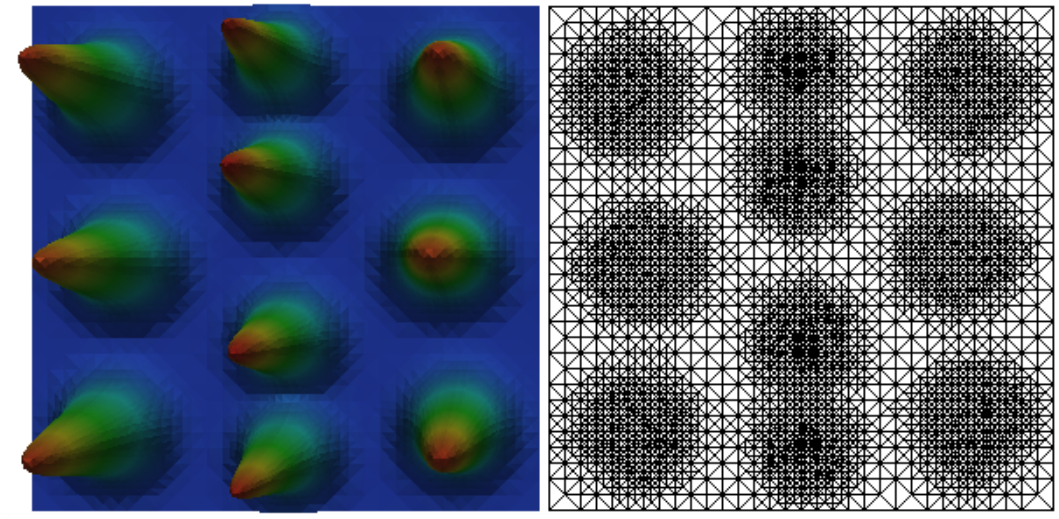

(b) $t = 500$

Figure 5.18: (continuation of Figure 5.17) The discrete activator profile for the Schnakenberg kinetics on a domain with periodic evolution under adaptive mesh refinement (for parameter values see text). The mode transitions follow exactly that of Figures 5.3 and 5.4.

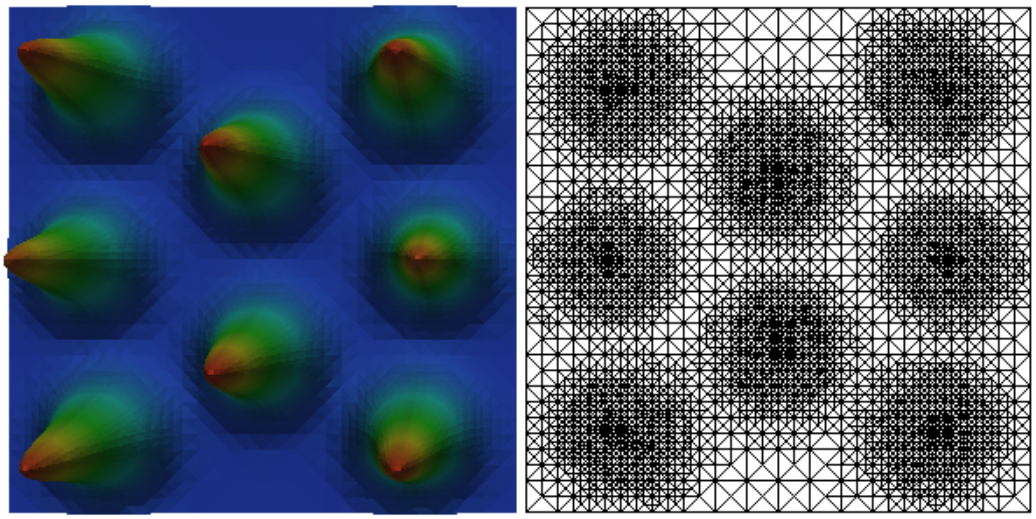

(a) $t = 700$

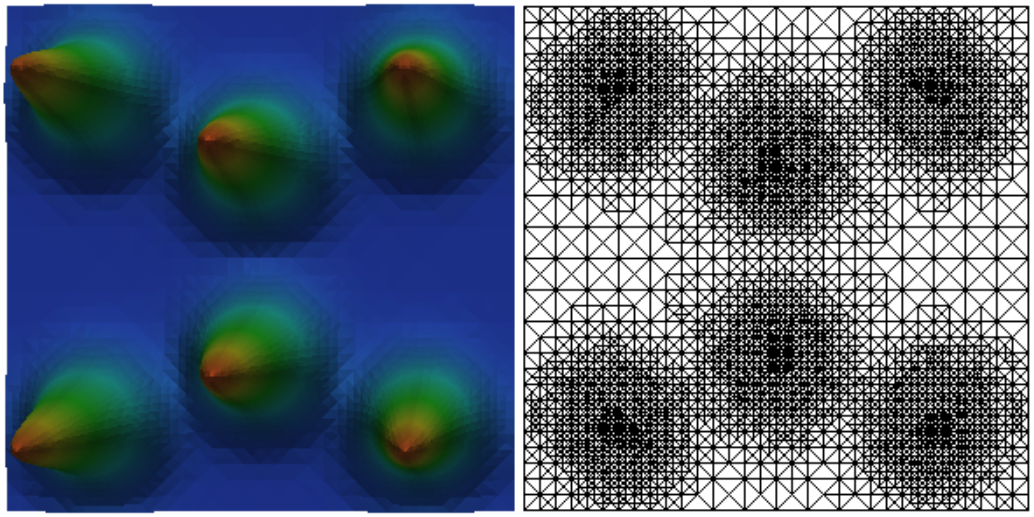

(b) $t = 740$

Figure 5.19: (continuation of Figure 5.18) The discrete activator profile for the Schnakenberg kinetics on a domain with periodic evolution under adaptive mesh refinement (for parameter values see text). The mode transitions follow exactly that of Figures 5.3 and 5.4.

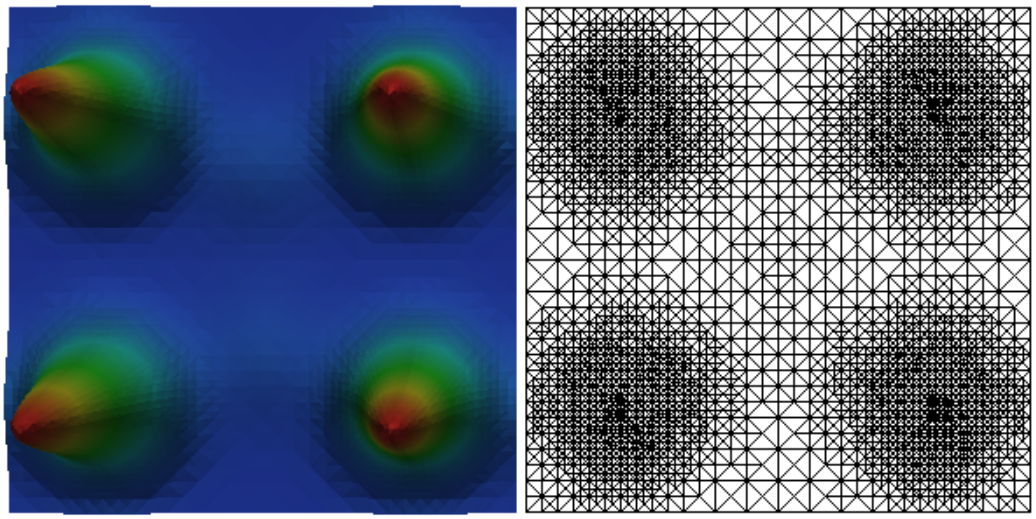

(a) $t = 820$

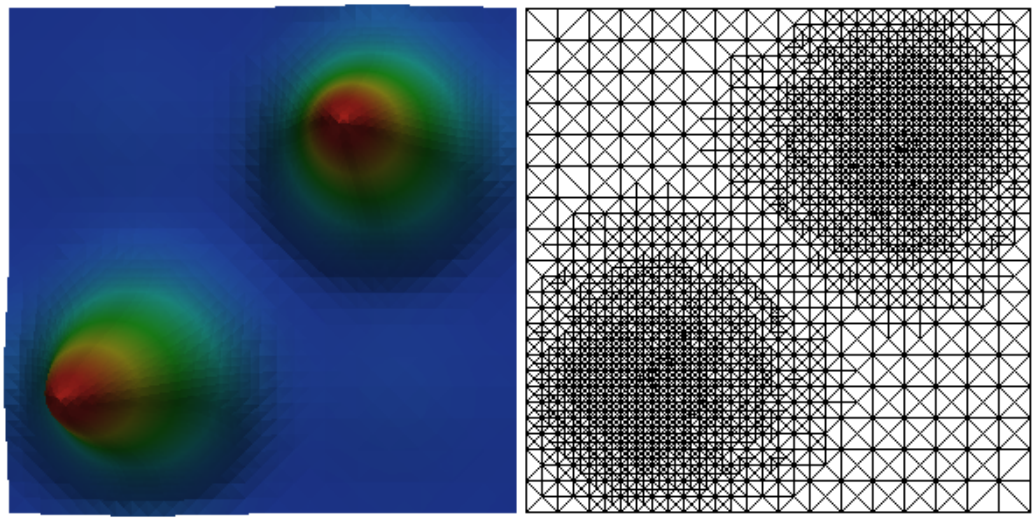

(b) $t = 900$

Figure 5.20: (continuation of Figure 5.19) The discrete activator profile for the Schnakenberg kinetics on a domain with periodic evolution under adaptive mesh refinement (for parameter values see text). The mode transitions follow exactly that of Figures 5.3 and 5.4.

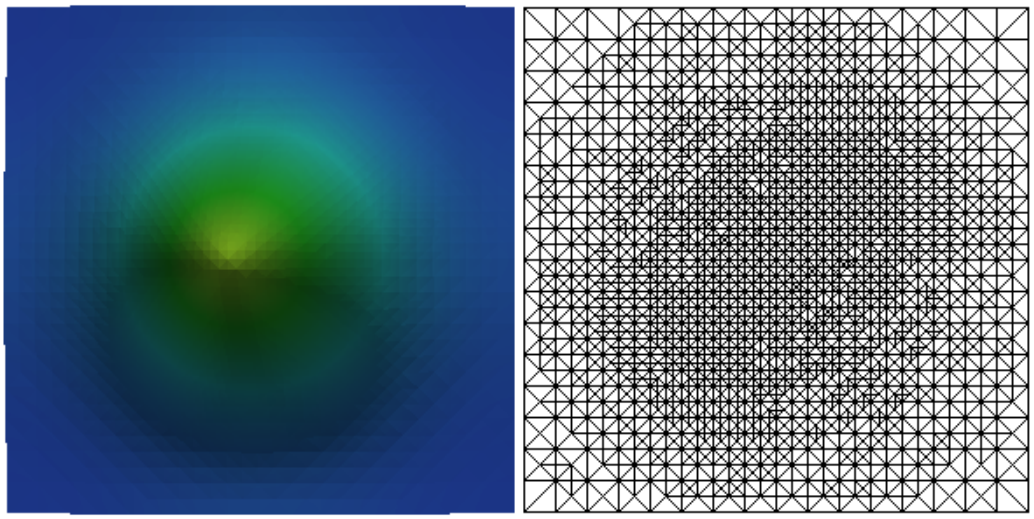

(a) $t = 980$

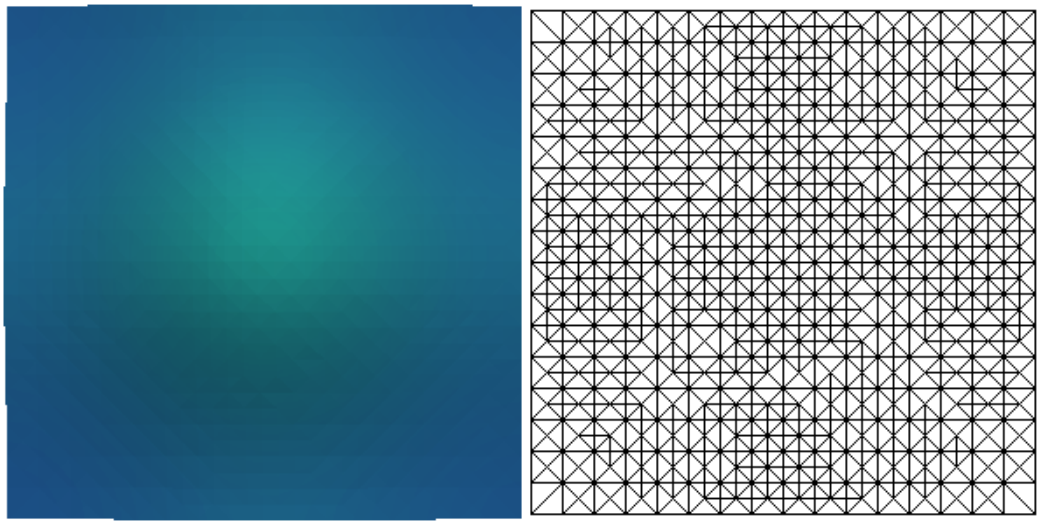

(b) $t = 1000$

Figure 5.21: (continuation of Figure 5.20) The discrete activator profile for the Schnakenberg kinetics on a domain with periodic evolution under adaptive mesh refinement (for parameter values see text). The mode transitions follow exactly that of Figures 5.3 and 5.4.

domain grows and as it contracts.

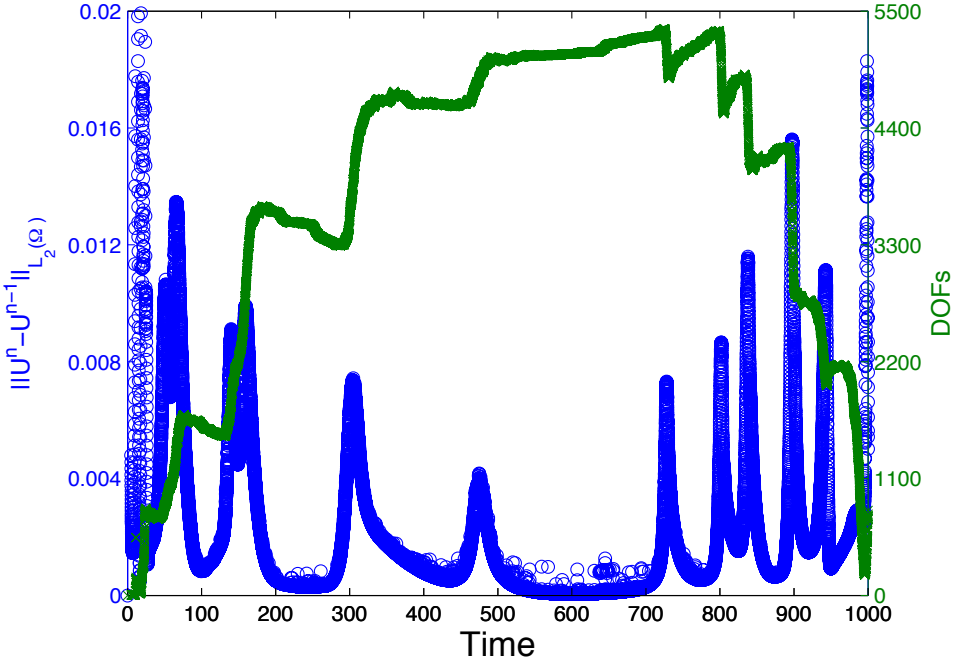

Figure 5.22: The number of DOFs and the change in the discrete solution over time (periodic domain evolution). Overall the number of DOFs of freedom increases as the domain grows ($t < 500$) and decreases as the domain contracts. As the domain grows, bifurcations of solutions (spot-splitting) correspond to an increase in the change in the discrete solution and an increase in the number of DOFs. As the domain contracts, the behaviour is reversed with bifurcations (now spot-annihilation or merging) corresponding to an increase in the change in the discrete solution and a decrease in the number of DOFs.

In Figure5.22, we plot the number of degrees of freedom and the norm of the change in discrete solution over time. Since the mesh at time n and the mesh at time $n-1$ are not necessarily the same, we define the $\|\cdot\|_{L_2(\hat{\Omega})}$ of the change in discrete solution as

$$\left\| \hat{U}^n - \Lambda^{h^n} \hat{U}^{n-1} \right\|_{L_2(\hat{\Omega})}, \tag{5.4.1}$$

where Λ^h is the Lagrange interpolant. As the domain grows, at each bifurcation point (spot-splitting) both the change in discrete solution and the number of DOFs increase sharply. As the domain contracts, at each bifurcation point (spot-annihilation or merging) the change in discrete solution increases sharply while the number of DOFs falls sharply. This is in accordance with intuition as bifurcations on a growing domain correspond to the insertion of new localised structures (spots) and bifurcations on the contracting domain correspond to annihilation or merging of localised structures. Loosely speaking, the number of degrees of freedom appears proportional to the domain size, providing strong evidence that the efficient solution of RDSs on evolving domains requires some form of spatial adaptivity. As domain evolution is spatially linear, the

mesh-size on the evolving domain is given by

$$h = \left(1 + 9\sin\left(\frac{\pi t}{T}\right)\right)\hat{h}. \tag{5.4.2}$$

Thus, although we are solving on the reference domain, the adaptive algorithm could very roughly be viewed as maintaining a constant (but not uniform) mesh-size on the evolving domain.

5.4.2 Space-time adaptive scheme

The results of §5.4.1 indicate that adaptive mesh refinement is worthwhile especially in the case of domain evolution. Inspection of the previous results of this Chapter suggests that with the slow growth rates considered in this study, the solution profiles evolve via a series of effectively steady state patterns with sharp transition stages where bifurcations occur. In light of this, adaptive time-stepping is also likely to prove worthwhile on evolving domains and we now introduce adaptive time-stepping into the algorithm. The error estimator $\hat{\mathscr{E}}$ (4.6.17) is based on the error in the semidiscrete scheme and neglects the error due to time discretisation. To estimate the error introduced due to the time-discretisation, we introduce a heuristic time error indicator $\boldsymbol{\eta}$ defined by the following: for $i = 1, \ldots, m$,

$$\eta_i^n = \left\| U_i^n - \Lambda^h U_i^{n-1} \right\|_{L_2(\hat{\Omega})}, \tag{5.4.3}$$

where Λ^h is the Lagrange interpolant. To incorporate time adaptivity into the algorithm we conduct the time and space adaptivity separately. In the first step we compute the value of a time error indicator $\tilde{\boldsymbol{\eta}}^n$ by computing the discrete solution $\boldsymbol{U}^n$ on the old mesh $\hat{\mathscr{T}}^{n-1}$. We select a sufficiently small timestep such that this indicator is below a certain tolerance and then proceed with the space adaptive algorithm outlined in §5.4.1 ensuring the estimator $\hat{\mathscr{E}}$ is below a given tolerance. Finally, after computing the discrete solution $\boldsymbol{U}^n$ on the new mesh $\hat{\mathscr{T}}^n$ we check that the value of the time error indicator $\boldsymbol{\eta}^n$ is below the desired tolerance. This adaptive algorithm is given in detail in [Schmidt and Siebert, 2005, Alg. 1.25 pg. 52].

To compare the results of the space-time adaptive scheme with the previous results of this Chapter, we apply the scheme to the solution of Problem (5.3.2) with periodic domain evolution (5.3.1). We select the same values of 10^{-3} and 0.9 for parameters tol and θ respectively. We select a value of 5×10^{-2} for the tolerance on the time error indicator $\boldsymbol{\eta}$. Figures 5.23 — 5.28 show the discrete activator profile obtained using a space-time adaptive scheme. The pattern transitions are identical to those obtained with the uniform mesh (Figure 5.3) and the space adaptive scheme (Figures 5.16—5.21). The mesh is locally well refined around the spots, both as the domain grows and as it contracts.

In Figure 5.29(a) we plot the change in the discrete solution and the number of DOFs over time. As the domain grows, we observe similar behaviour to the space adaptive case with each bifurcation of solutions corresponding to a sharp increase in the change in discrete solution and a sharp increase in the number of DOFs. As the domain contracts, the number of DOFs stays

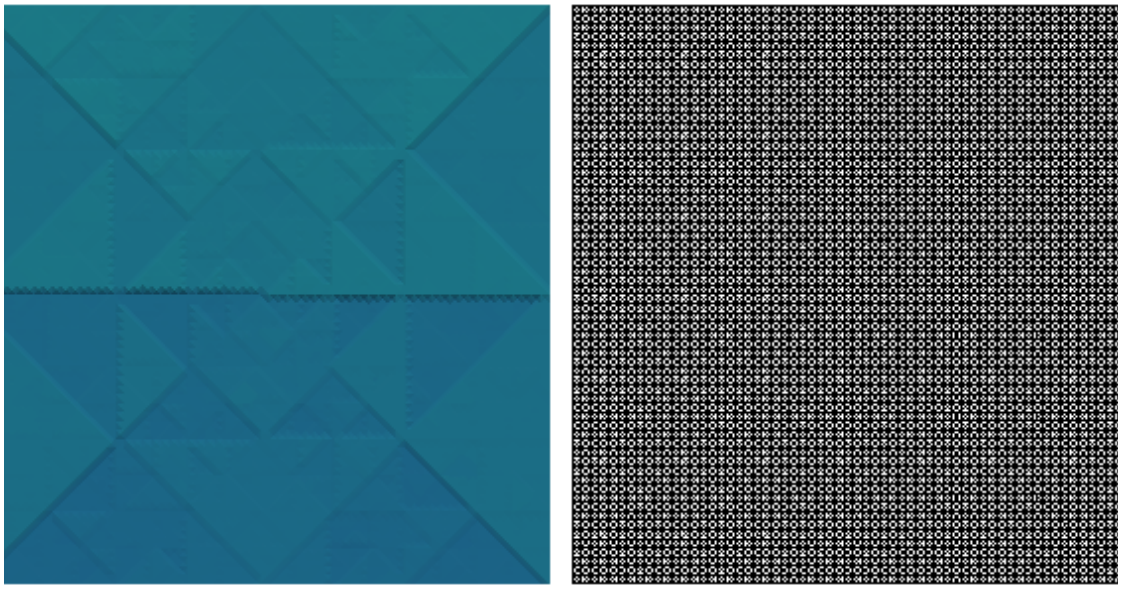

(a) $t = 0$

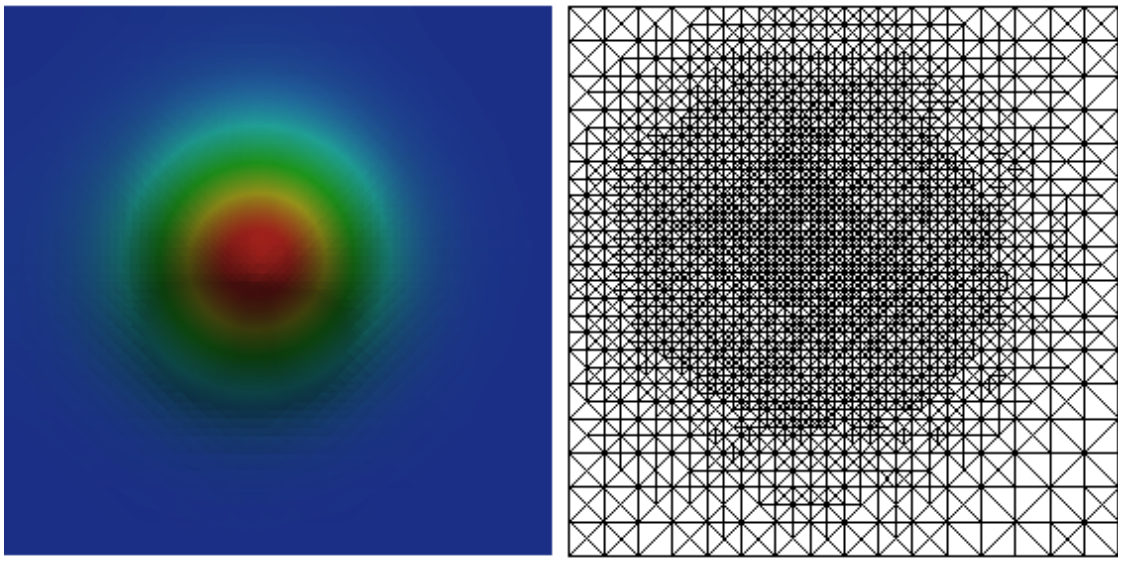

(b) $t = 50$

Figure 5.23: The discrete activator profile for the Schnakenberg kinetics on a domain with periodic evolution under adaptive timestep and mesh refinement (for parameter values see text). The mode transitions follow exactly that of Figures 5.3, 5.4 and 5.16.

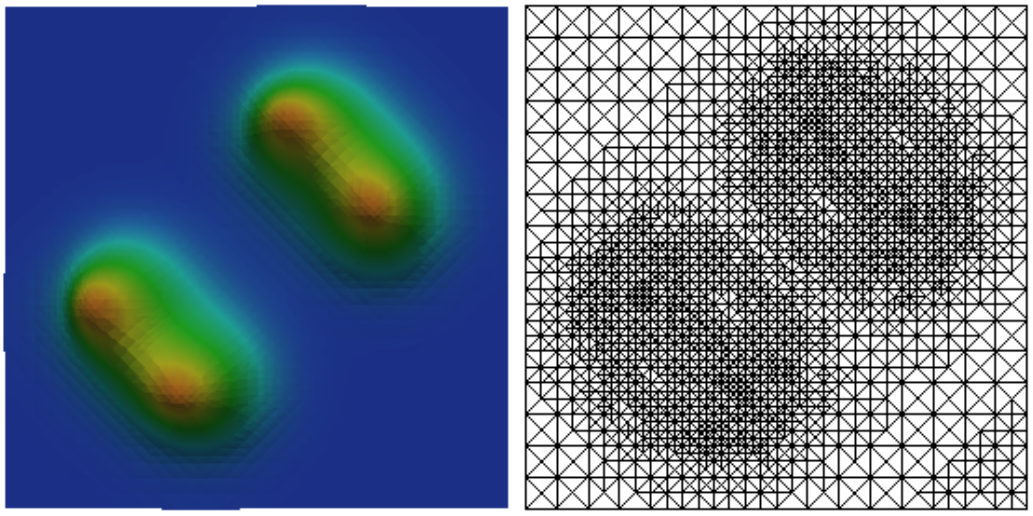

(a) $t = 160$

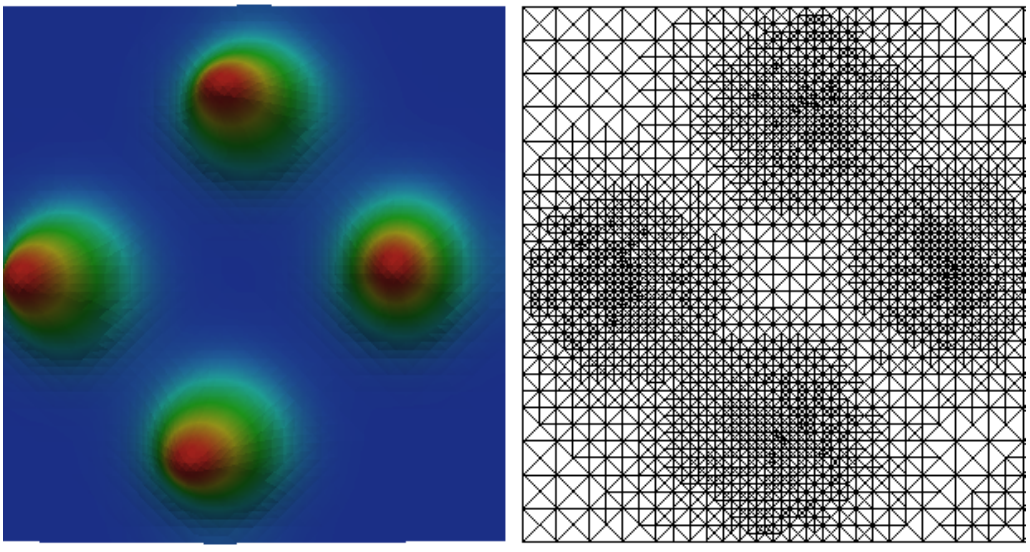

(b) $t = 220$

Figure 5.24: (continuation of Figure 5.23) The discrete activator profile for the Schnakenberg kinetics on a domain with periodic evolution under adaptive timestep and mesh refinement (for parameter values see text). The mode transitions follow exactly that of Figures 5.3, 5.4 and 5.17.

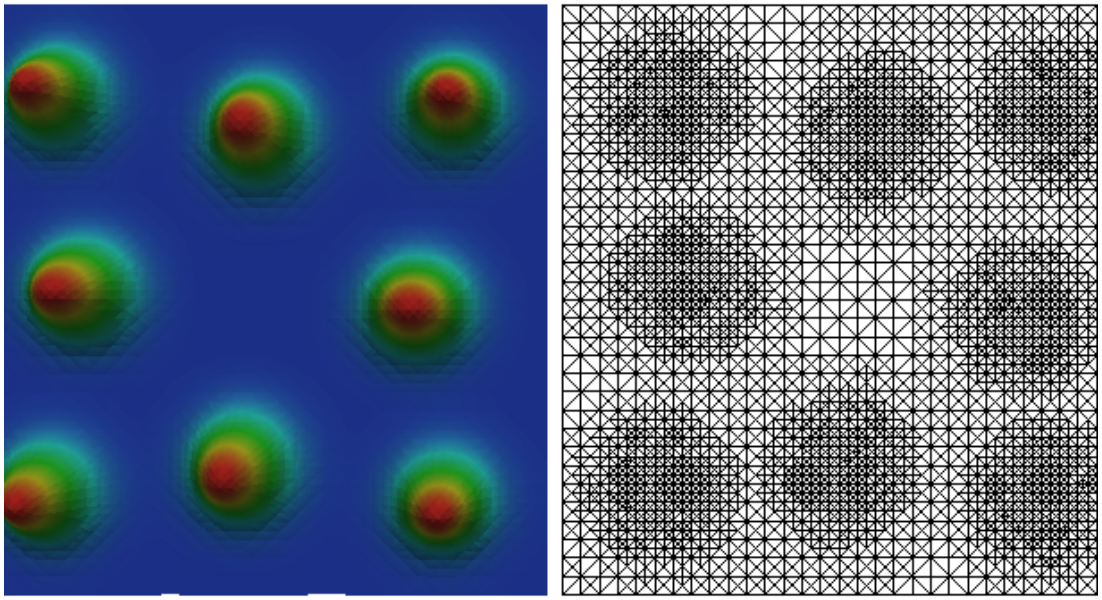

(a) $t = 380$

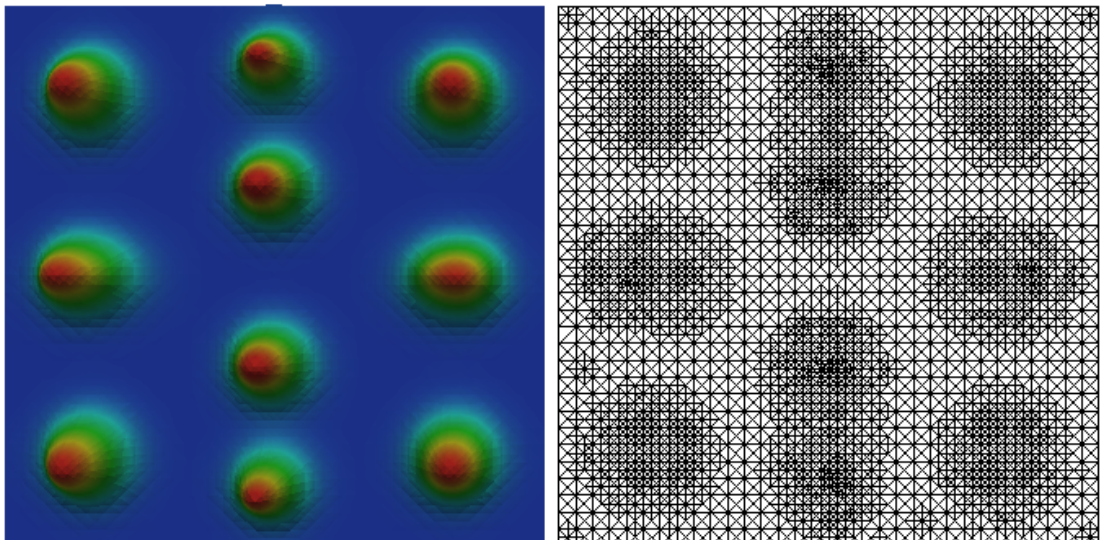

(b) $t = 500$

Figure 5.25: (continuation of Figure 5.24) The discrete activator profile for the Schnakenberg kinetics on a domain with periodic evolution under adaptive timestep and mesh refinement (for parameter values see text). The mode transitions follow exactly that of Figures 5.3, 5.4 and 5.18.

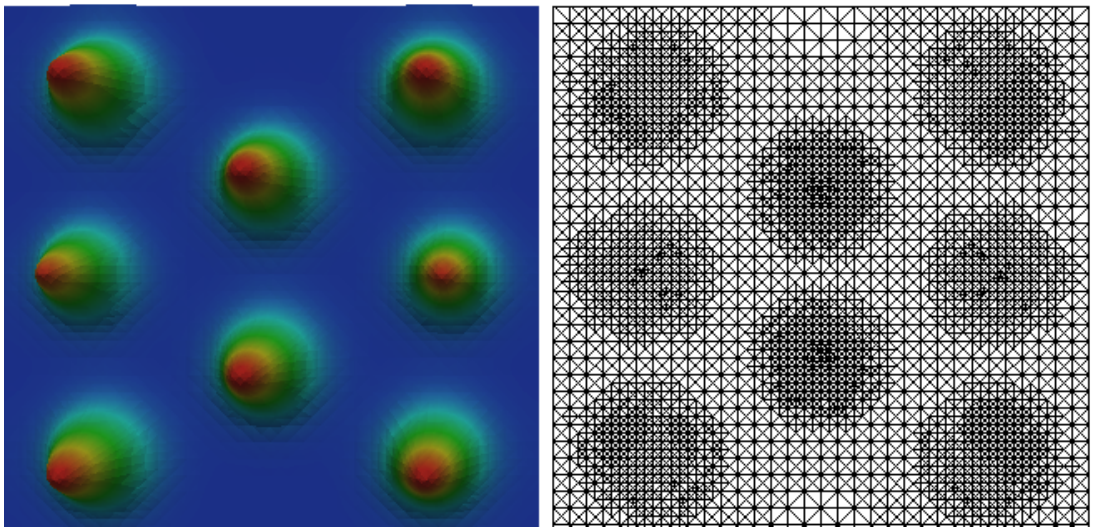

(a) $t = 700$

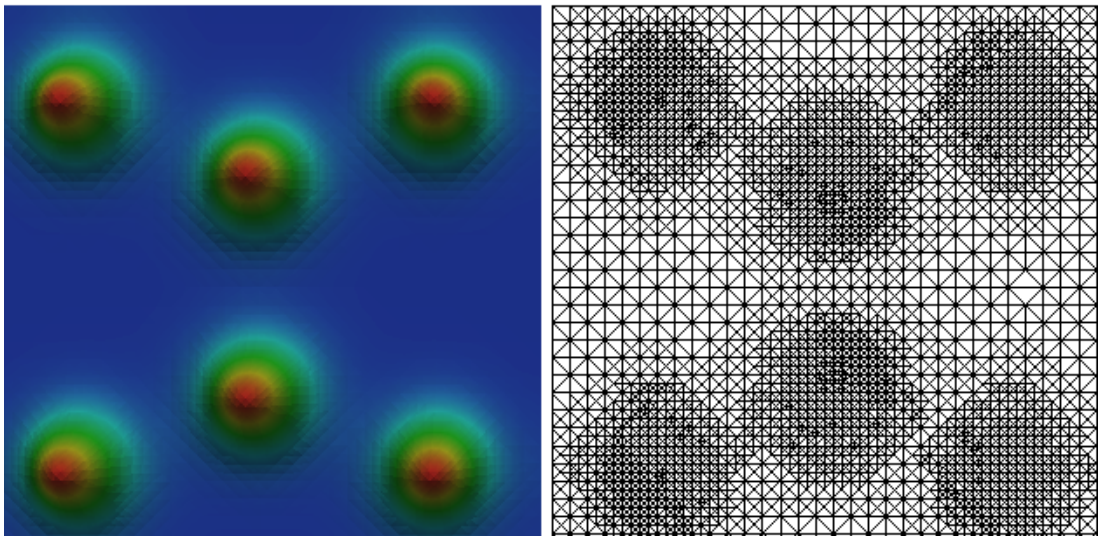

(b) $t = 740$

Figure 5.26: (continuation of Figure 5.25) The discrete activator profile for the Schnakenberg kinetics on a domain with periodic evolution under adaptive timestep and mesh refinement (for parameter values see text). The mode transitions follow exactly that of Figures 5.3, 5.4 and 5.19.

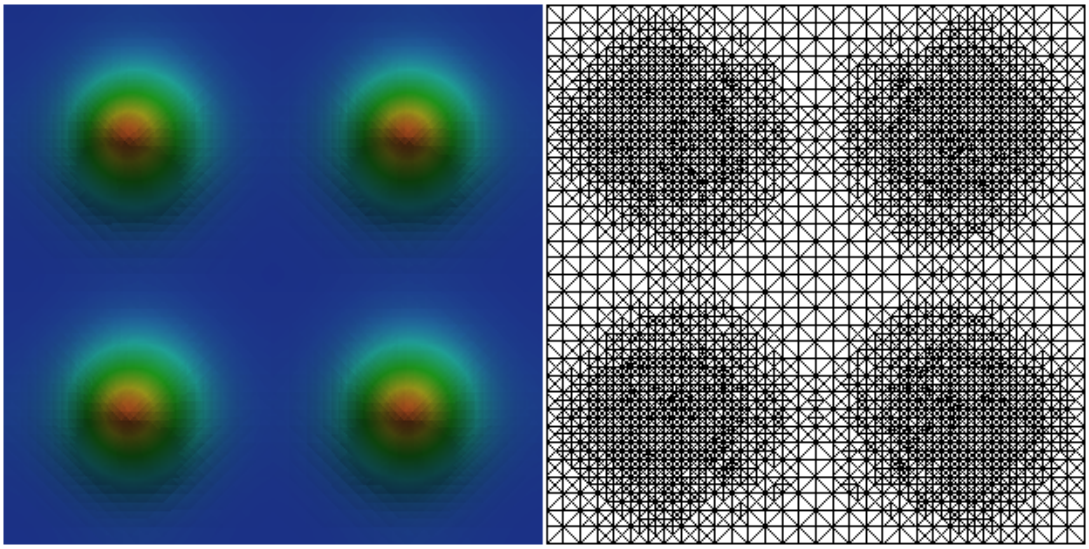

(a) $t = 820$

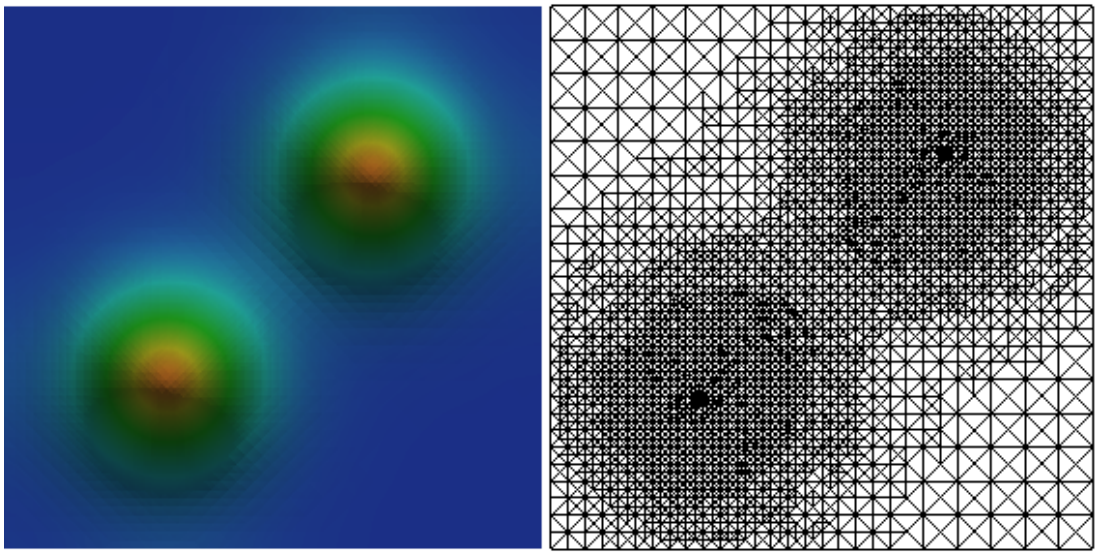

(b) $t = 900$

Figure 5.27: (continuation of Figure 5.26) The discrete activator profile for the Schnakenberg kinetics on a domain with periodic evolution under adaptive timestep and mesh refinement (for parameter values see text). The mode transitions follow exactly that of Figures 5.3, 5.4 and 5.20.

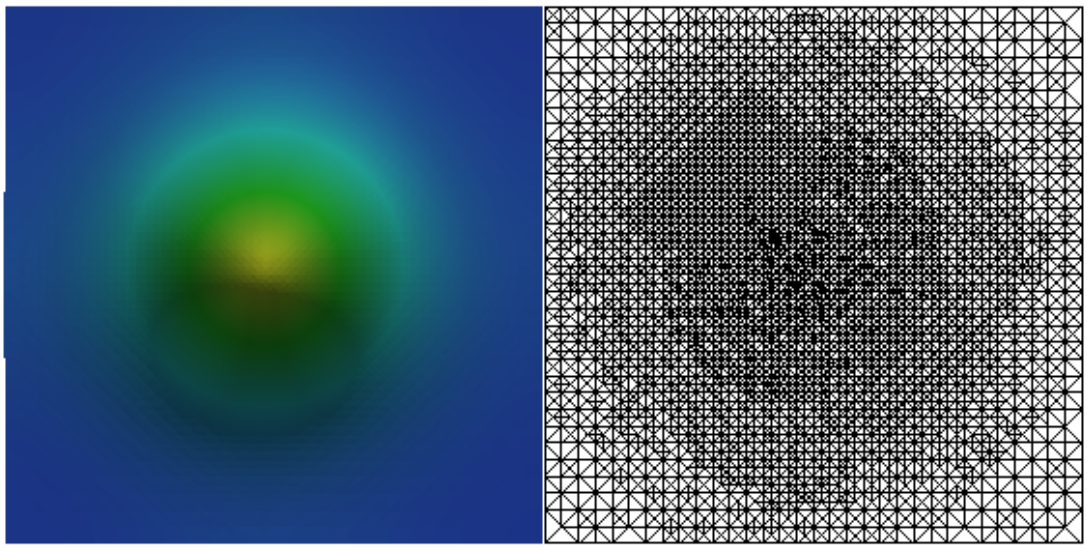

(a) $t = 980$

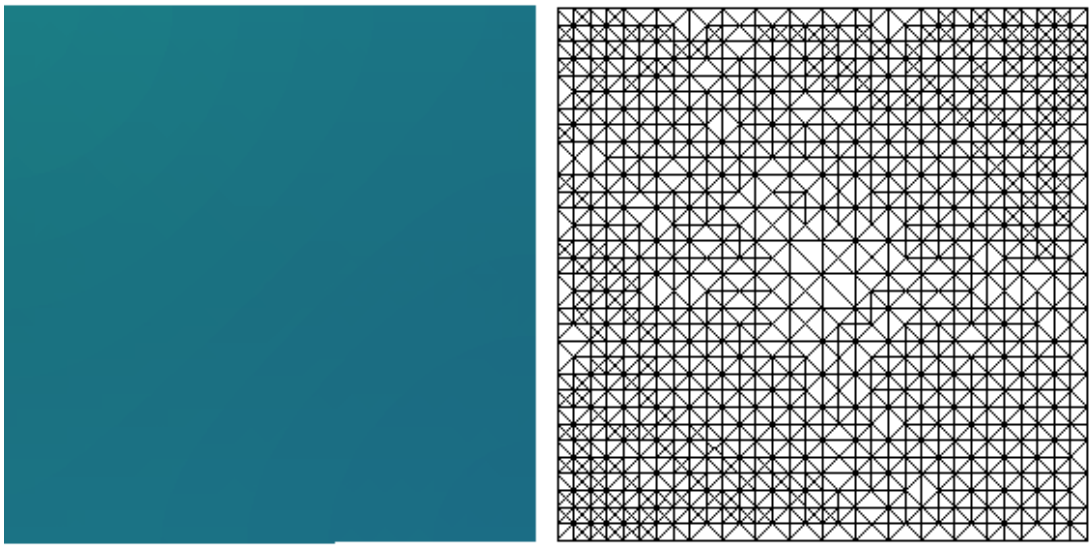

(b) $t = 1000$

Figure 5.28: (continuation of Figure 5.27) The discrete activator profile for the Schnakenberg kinetics on a domain with periodic evolution under adaptive timestep and mesh refinement (for parameter values see text). The mode transitions follow exactly that of Figures 5.3, 5.4 and 5.21.

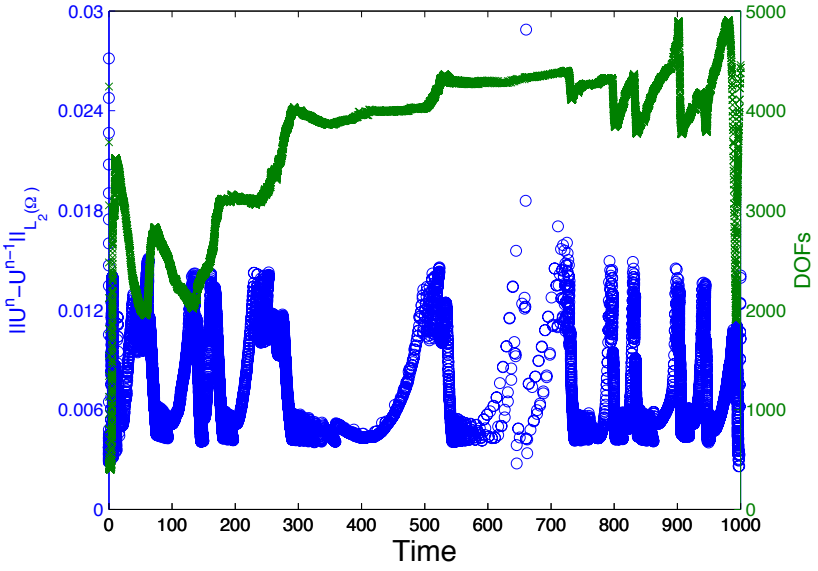

(a) Number of DOFs and change in discrete solution over time

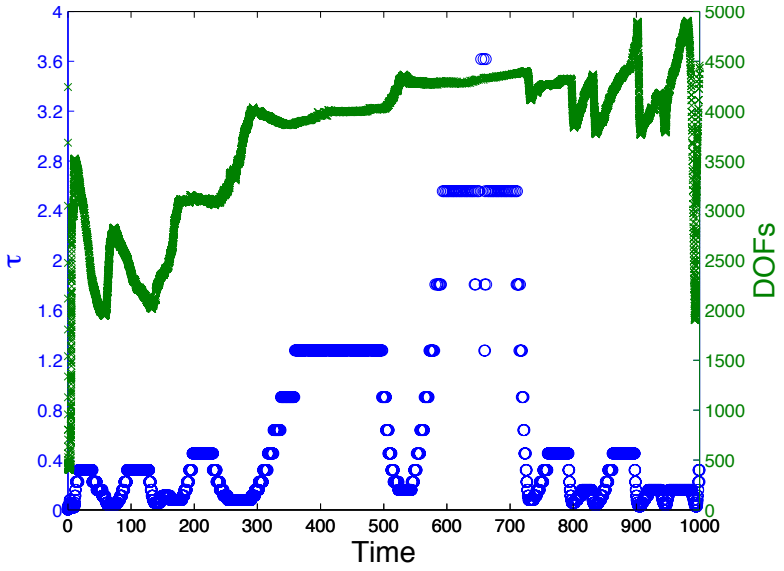

(b) Number of DOFs and timestep over time

Figure 5.29: As the domain grows ($t < 500$) the evolution of the DOFs and the change in discrete solution is similar to the space adaptive case (Figure 5.22). The timestep appears to be refined when bifurcations occur. While domain growth is slow ($400 < t < 700$) few bifurcations occur and in this period the number of DOFs stays relatively constant while the timestep selected is much larger. As the domain contracts ($t > 700$) the number of DOFs does not decline as rapidly as in the space adaptive case however by the time of the final domain on which no patterns are expressed we recover a coarse mesh.

relatively constant decreasing only as the final transition to a patternless state occurs. In Figure 5.29(b) we plot the value of the timestep and the number DOFs over time. The first striking result is that when domain growth is slow (and coincidentally the domain is large) very large timesteps are selected by the algorithm, this is consistent with intuition as at this stage ($t \in [380, 700]$) the pattern remains relatively constant with no bifurcations. The adaptive algorithm selects smaller timesteps when bifurcations occur (spikes in the number of DOFs correspond to smaller values for the timestep).

-	Uniform mesh	Space adaptive	Space-time adaptive
Time steps	100001	100001	11188
Average DOFs	8321	4326	3430
CPU time (s)	10449.40	1453.08	660.95

Table 5.1: Number of iterations, average number of DOFs and computational times for the three different schemes used to approximate the solution the Problem 5.3.2.

In Table 5.1 we report the CPU times for the three schemes used to approximate the solution to Problem 5.3.2. We observe a dramatic reduction in CPU time due to adaptivity. It is worth noting that the time adaptive strategy we have used is not especially efficient as the discrete solution must be computed at least twice in each timestep. Further speed up should be possible via a more efficient time adaptive algorithm, which we shall consider in future studies.

5.5 Discussion

In this Chapter we have conducted a series of computer experiments that firstly validate the theoretical results of preceding Chapters and secondly illustrate some of the varied spatial patterns generated by RDSs on fixed and continuously evolving domains.

To verify the accuracy of the FEM, we conducted simulations on time-independent domains verifying the resulting nonuniform steady states obtained were those predicted by linear stability analysis. We presented results on a periodically evolving domain and a suitably rescaled equation on the reference domain, the results corroborate the rescaling carried out in §2.6.

We contrasted the widely used approach of varying a scaling parameter to account for domain evolution with the simulation of RDSs on continuously evolving domains and concluded the dynamic orientation of patterns determined by domain evolution is lost under the former approach. Our results illustrate that even with relatively simple spatially linear domain evolution a variety of transient patterning phenomena occur, such as stripe to spot transitions. The periodic forms of domain evolution we considered illustrate the difference in bifurcations on growing and contracting domains. We observe the well known period-doubling phenomenon during domain growth but more interesting and surprising is the development of spot-annihilation and spot-merging phenomena during contraction. This raises new questions about bifurcation analysis on growing and contracting domains, an area in which very little work has been done and these initial numerical results indicate the need for further exploration of this area. We illustrated the versatility of the proposed FEM by considering different forms of spatially nonuniform domain evolution. Our results illustrate that the growth rate and domain shape strongly influence the patterns expressed. To investigate the role of domain symmetry on the bifurcation of solutions on growing domains,

we considered spot-splitting on a growing disc. Our results suggest that small changes in domain and mesh geometry that disrupt symmetry can significantly alter the bifurcation sequence of solutions.

The final results presented this Chapter consisted of the adaptive approximations of solutions to RDSs on evolving domains. Our adaptive algorithms perform well with the mesh being locally refined around the patterns and the space-time algorithm selecting larger timesteps during periods where no bifurcations occur. Our results suggest that on time-independent and especially on time-dependent domains spatial and temporal adaptivity (both mesh refinement and coarsening as well as variable timestep sizes) speeds up computations considerably.

The results of this Chapter illustrate that the FEM of Chapter 4 is capable of efficiently approximating the solution to RDSs on complex geometries with nonlinear evolution. Thus, it should provide a robust tool for the future investigation of biological pattern formation. We illustrate this in the next Chapter by applying the FEM to study a vertebrate skin patterning phenomena.

Chapter 6

A model for parr mark pattern formation during the early development of the Amago trout

6.1 Summary

In this Chapter we investigate the feasibility of RDSs to model an experimentally observed pattern formation process. We study the formation of the large dark patterns, known as parr marks, which form on the Amago trout as it grows from the early larval stages to adulthood. The Amago trout, known as *Oncorhynchus masou ishikawa*, exhibits stripes during the early stages of development which in turn evolve (through *reorientation and peak-insertion*) to form zigzag spot patterns as the fish grows to adulthood. By considering a standard representation of the Turing model for biological self-organisation via interacting and diffusing morphogens, we illustrate that a diffusively driven instability can generate transient patterns consistent with those experimentally observed during the process of parr mark formation in the early development of the Amago trout. Surface evolution is modelled through an experimentally-driven growth function. Our studies conclude that the surface evolution profile, the surface geometry and the curvature are key factors which play a pivotal role in RDS models of pattern formation.

The remainder of this Chapter is set out as follows; We start in §6.2 by motivating the study of skin pigmentation patterning in vertebrates. We discuss the use of RDSs to model skin pigment patterning, concentrating on fish-skin patterning, and we indicate some of the modelling novelties of our study. In §6.3 we describe the process of parr mark pattern formation on the Amago trout. We give the details of our experimental study in which we observe the parr mark formation process and record the time and size of the fish. In §6.4 we outline the method with which we seek to approximate the pattern formation process. We model the growth of the fish and construct representative models of the surface of the fish on which patterning occurs, taking into account the shape and curvature of the surface. We then define the RDS model we will be computing on an evolving surface. We conclude the section by briefly discussing the selection of parameter values for the system. In §6.5 we present the results of our computer simulations. The results are in close agreement with the experimentally observed pattern transitions. The effect of curvature on the pattern formation process is also discussed and we observe striking differences in the patterns that form on surfaces with different curvature. Finally, in §6.6 we state the conclusions of this study, primarily that an RDS on an evolving surface is a viable model for describing

the emergence of parr mark pattern formation on the Amago trout and that curvature influences patterns that arise via self-organization. We conclude this paper by discussing the implications of our results on the modelling of biological pattern formation by RDSs on continuously evolving surfaces and suggest future research directions.

6.2 Introduction

Modelling the formation of spatial pattern from homogeneity is of fundamental importance in many fields, none more so than in developmental biology. Since their seminal introduction by Turing, A. M. [1952], RDSs have constituted a standard framework for the mathematical modelling of spatial pattern formation. The theory behind RDSs as a model for biological pattern formation relies on two or more *morphogens* reacting in the presence of diffusion. The onset of a diffusion-driven instability drives a spatially homogeneous steady state of the morphogen concentration unstable. Turing's hypothesis was that one or more of the morphogens played the role of a signalling chemical, such that cell fate is determined by levels of morphogen concentration.

Turing's initial model was of an RDS with linear reaction kinetics and thus, there was no admissible spatially inhomogeneous steady state. Specifically, the onset of a diffusion-driven instability led to unbounded growth of solutions. This, together with the fact that to-date no morphogens that behave as the components of an RDS have been identified, has somewhat limited the uptake of his work amongst the biological community [Kondo and Miura, 2010]. Much of the recent interest in the Turing model as a mechanism for biological pattern formation can be attributed to the work of Gierer and Meinhardt [1972], where nonlinear reaction kinetics (which admitted a spatially inhomogeneous steady state) were considered and an RDS was used to model pattern formation in Hydra. It must be noted that RDSs are not the only candidate models for biological pattern formation. Many other models have been suggested such as, chemotactic models [Myerscough et al., 1998] where cells respond to a chemical gradient, neuronal signalling models [Swindale, 1996] where neuronal firing patterns act as signalling forces, discrete cell-based models [Chopard and Droz, 1998; Cocho et al., 1987] where cells determine their individual binary (or a finite number of) states and mechanochemical models [Murray and Maini, 1988] where physical stresses trigger cellular responses. One feature that is common to nearly all these models is *long-range inhibition and short-range activation*: the hypothesis that patterning occurs due to interactions between an activatory and an inhibitory component with the inhibitor's influence being exerted over greater distances. The underlying common patterning mechanism shared by these models makes it very hard to distinguish between them as similar patterns can result from a variety of different modelling assumptions.

Experimental studies have shown that patterns in real world systems could indeed arise as a result of diffusion-driven instability, such as the chloride-iodide-malonic-acid reaction [Vigil et al., 1992] and calcium-voltage dynamics within cardiac cells [Shiferaw and Karma, 2006]. While aesthetically attractive due to its biological economy in solving difficulties of orchestrating long range cellular interactions to induce large scale biological patterning, Turing's putative mechanism nonetheless is often considered with caution [Kerszberg and Wolpert, 2007]. In particular, the required morphogen interactions are unverified at the molecular level, even if there are potential candidates such as Nodal and Lefty gene products during mesendodermal induction [Solnica-Krezel, 2003], and questions of model sensitivity continually recur [Bard and Lauder, 1974; Bunow et al., 1980; Seirin Lee and Gaffney, 2010; Seirin Lee et al., 2010]. In contrast, numerous observations of fish skin markings can be simply explained through reaction-diffusion

frameworks emphasising that fish pigmentation at least behaves analogously to an RDS. One example includes the work of Kondo and Asai [1995], where it has been demonstrated that an RDS on a one-dimensional growing domain is consistent with stripe formation on the skin of the juvenile Pomacanthus. In a recent experimental study Yamaguchi et al. [2007] examine the effect of disrupting stripe formation on zebrafish and the resulting pattern regime that ensues is very similar to the patterns obtained by computer simulation of an RDS with disrupted patterns. This in turn, motivates further explorations of fish pigmentation to assess whether discrepancies between theory and modelling emerge, especially with modelling generalisations given the Turing instability's notorious sensitivity to initial conditions on fixed domains. Previous observations of sensitivity to factors such as domain shape [Madzvamuse, 2000; Sekimura et al., 2000] suggest that the evolving, curved geometry characterising fish skin as patterns dynamically change may increase the robustness of solutions to RDSs. Hence comparisons of models and observations in this context will offer a potential test of the theoretical framework.

The influence of curvature on pattern formation processes governed by RDSs has been investigated in other contexts (for example by Barrio et al. [2010]). However, the majority of studies of fish skin patterning by RDSs to date, have simply considered the simulation of RDSs on squares or other simple geometries. In this Chapter we simulate an observed pattern formation phenomenon in fish on a *biologically realistic* evolving surfaces and investigate the influence of domain curvature on the patterns obtained. Specifically, we shall use the FEM derived in Chapter 4 to investigate the process of parr mark pattern formation on the Amago trout [Sekimura, 2007a].

6.3 Biological observations

Our modelling is based on the Amago trout (*Oncorhynchus masou ishikawa*). The Amago is a fish species of river resident form of the Salmonidae, distributed widely in Japan from western Honshu island on the Pacific Ocean and Shikoku island, to northern Kyushu island on the Setonaikai Sea. The Amago's lifespan is between 3 and 4 years. The species is notable for remaining in freshwater during its life cycle. Adult Amagos have distinctive elliptically shaped parr marks (large dark patterns) on each side of the body. Parr mark development is completed relatively early in the fish's life cycle (6 to 7 months after hatching), hence these markings are known as "trade marks" of young fishes of Salmonidae.

In order to understand the biological evolution of parr mark formation during growth development, Sekimura recorded the parr mark formation process of around 50 Amago individuals. The specimens were tracked from shortly after the time of hatching to around seven months after birth and were photographed at monthly intervals. The individuals were placed in a glass vessel with gradations on the sides of the vessel. This allowed the collection of experimental data of the growth rates of the fish, associated patterning and geometrical descriptions during each stage of its growth development. These empirical data provide an excellent foundation for mathematical modelling of the pattern formation phenomenon during growth development. The major stages in parr mark development, which we now describe, are shown in Figure 6.1.

Upon hatching the Amago is approximately 2cm in length and for most of the first month after hatching, there are no observable parr marks on the skin (Figure 6.1(a)). During this period, the Amago's diet consists only of yolk from its egg. Towards the end of the first month after hatching, the first stage of parr mark formation occurs, with around 5 faint stripe-like parr marks appearing on both sides of the body. The stripes form perpendicular to the head-tail axis (Figures 6.1(b) and 6.1(c)). By this time, the Amago has grown to around 4cm in length. The fish has also completely

consumed its egg yolk and has started to eat food from the environment. Between the second and third month after hatching new parr marks appear, generally forming away from existing parr marks. By this stage of development, the fish has grown to around 3 to 4 times its original size (6-8cm). The parr marks are still primarily stripe-like, oriented perpendicular to the head-tail axis with 5 to 7 parr marks on both sides of the fish. On wider portions of the fish a zigzag orientation is somewhat evident (Figures 6.1(d)—6.1(g)). During the fourth and fifth month a new line of parr marks appears on the top of the fish (Figures 6.1(h) and 6.1(i)). At this stage of development the fish is around 8-10cm in length. The parr marks are now elliptical and distributed around the domain with a zigzag orientation (checkerboard pattern). Finally, around 6 to 7 months after hatching, the fish has grown to around 10-12cm and the parr mark pattern formation is completed. The fish exhibits 3 or 4 rows (along the head-tail axis) of zigzag oriented parr marks on the top portion of the body. Each row consists of 7 to 11 parr marks depending on the individual (Figures 6.1(j) and 6.1(k)). This configuration persists into maturity.

The main stages of the parr mark pattern formation process together with the time after hatching and the size of the fish during each stage are summarised in the following:

Stage 1: (2-4 cm, soon after hatching) No visible parr marks.

Stage 2: (4-6 cm, 1 to 2 months) Around 5 stripe-like parr marks appear on each side of the fish towards the top (dorsal) portion. The stripes are oriented perpendicular to the head-tail axis.

Stage 3: (6-8 cm, 2 to 3 months) 5 to 7 parr marks on each side of the fish towards the top (dorsal) portion. The parr marks are still primarily oriented perpendicular to the head-tail axis.

Stage 4: (8-12 cm, 3 to 7 months) 3 or 4 rows (parallel to the head-tail axis) of elliptical parr marks with 7 to 11 parr marks in each row. The parr marks are still all located towards the top (dorsal) portion. The parr marks are distributed in a regular zigzag orientation (checkerboard pattern), all around the top portion (dorsal region) of the body surface.

During development, the parr marks do not change significantly in size, however they change shape and reorient themselves around the surface domain. It is clear from the observations that parr mark pattern formation (or at least expression of parr marks) is restricted to the upper (dorsal) portion of the fish with no parr marks forming at any stage of development on the underside of the fish. A key facet of the parr mark formation process is the insertion of new parr marks and subsequent reorientation from vertical parr marks aligned in parallel, to elliptical parr marks with a zigzag orientation. Figure 6.2 shows a top-down perspective of an individual Amago at around 7 months after hatching. To highlight the parr marks we have included a sketch with the parr marks and the outline of the fish shaded in dark black. We clearly observe the checkerboard pattern of parr marks which arises in the latter stages of parr mark development.

6.4 Methods

The experimental results shown above clearly demonstrate that the process of Amago skin pigmentation takes place during the early stages of development with transient patterns being expressed as the fish grows. The pattern transition occurs via the insertion of new parr marks. A

(a) shortly after hatching (b) ∼30 days left (c) ∼30 days right

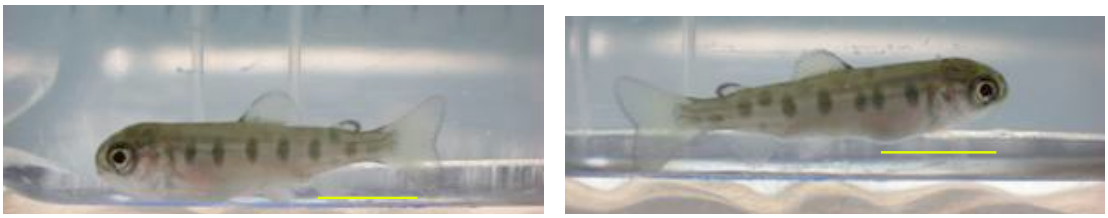

(d) ∼60 days left (e) ∼60 days right

(f) ∼90 days left (g) ∼90 days right

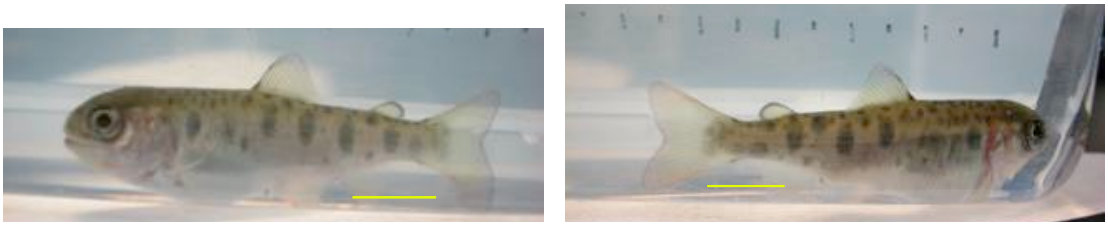

(h) ∼160 days left (i) ∼160 days right

(j) ∼200 days left (k) ∼200 days right

Figure 6.1: Amago skin pigmentation patterning during growth development (the approximate time after hatching is given in the captions and the yellow bar in the bottom right of each snapshot indicates 1cm). The figures show the left- and right-sided patterning profiles during the early stages of the Amago growth development after hatching to the juvenile period by which time patterning is complete. The fish exhibits an initial patternless state which evolves into faint vertical stripes. It can be observed that stripes evolve into spots with zigzag alignment that increase in number as the fish grows.

Figure 6.2: Top-down view of the final patterned state of the Amago and a sketch of the final patterned state on which we highlight the parr marks. A checkerboard pattern is clearly visible.

certain separation seems to be maintained between the existing and inserted patterns. The orientation of the patterns around the domain is dynamic, changing as the surface evolves. These characteristics of the pattern formation process suggest an RDS on an evolving surface as a candidate model for the pattern formation phenomenon. Firstly, since patterns that arise from RDSs (that exhibit Turing instability) have an intrinsic wavelength, some degree of separation between patterns is natural (at least for kinetics where new patterns arise via insertion). This has been used previously in modelling stripe formation on the Pomacanthus [Kondo and Asai, 1995]. Secondly and perhaps more importantly, more recent theoretical studies have shown that growth can determine the *orientation* of transient patterns [Madzvamuse et al., 2003]. This phenomenon of growth-determined orientation has also been supported experimentally by Míguez and Muñuzuri [2006] who showed that in a simplified experimental model for the formation of stripes on fish skin, the direction of domain growth could be used to determine the orientation of the resulting patterns.

We wish to investigate pattern formation on *realistic* geometries. Many studies, such as Varea et al. [1999], Chaplain et al. [2001], Plaza et al. [2004], Gjorgjieva and Jacobsen [2007], Barreira et al. [2011] and Landsberg and Voigt [2010], highlight the role of curvature on pattern formation. To properly understand the role geometry plays in the pattern formation process, the curvature of the fish should also be taken into account, motivating the modelling of RDSs on *evolving curved surfaces*.

6.4.1 Fitting a growth function to the experimental data

The experimental data allow us to estimate the surface proportions of the Amago trout through each observed stage of the parr mark formation process. Using the photographs, we measure the length and width of the fish at various stages of development. The surface proportions of the Amago appear to grow isotropically, with no obvious change in the ratio between the width and length of the fish during development. In light of this, we assume the growth of the body surface of the fish is uniform and isotropic. Another important aspect of the growth is that early in the fish's life cycle (when the fish is still feeding on its yolk), growth appears to be much faster than in later stages of development where growth occurs at a much slower rate.

A saturating growth function seems the most natural model for the observed evolution of the fish's body surface. For illustrative purposes we consider the *logistic growth function*. Under this growth profile, the fish's growth is approximately exponential initially, linear at intermedi-

ate stages and finally, saturates as the organism approaches a limiting surface size. The logistic growth function is defined by:

$$\rho(t) = \frac{e^{rt}}{1 + \frac{1}{m}\left(e^{rt} - 1\right)} \qquad \text{for } t \in [0, T]\,. \tag{6.4.1}$$

From our experimental observations we take the saturation size $m = 5.2$ to represent the nondimensional limiting surface size of the Amago fish. Fitting the logistic growth function to the experimental data as illustrated in Figure 6.3 results in the linear logistic growth rate $r = 7.5 \times 10^{-5}$. We take a computational time interval of $[0, 10^5]$, with 1 day in real time corresponding to an interval of length 500 in computational time. Figure 6.3 shows $\rho(t)$ fitted to the actual interval $[0, 200]$ (days) and the length (normalised by the initial length) of an individual Amago specimen. The function (6.4.1) appears to be a relatively good approximation to the actual growth of the fish.

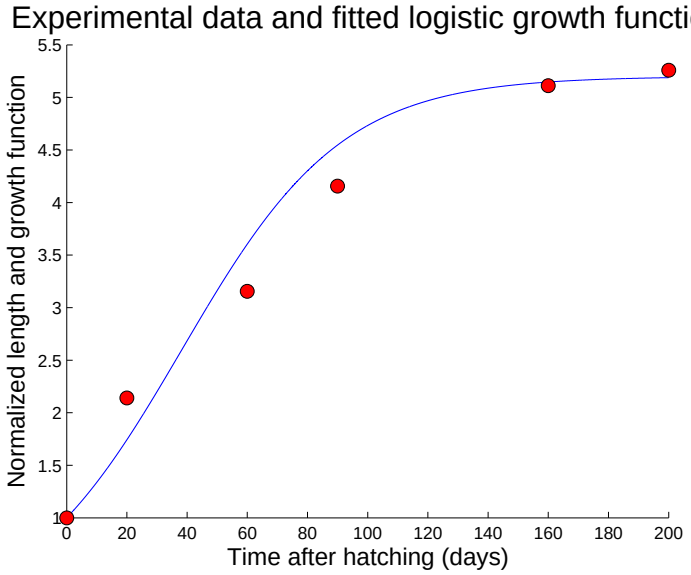

Figure 6.3: The length of a typical fish normalised by the initial length (circles) at 0, 20, 60, 90, 160 and 200 days after hatching and logistic growth as defined in (6.4.1), on the computational time interval $\left[0, 10^5\right]$ corresponding to a real time interval of $[0, 200]$ days.

6.4.2 Remark (Other growth profiles)**.** The growth of the Amago does appear to be best modelled by a saturating growth function (such as logistic growth), rather than the other standard isotropic growth profiles used in developmental biology (exponential and linear). The domain growth is sufficiently slow that the patterns that form can effectively be regarded as steady state solutions of an RDS with sharp transitions to new patterns at bifurcation points. The effects of domain growth can thus, loosely be viewed as causing transitions between series of quasi-steady state patterns and determining the continuous reorganisation of each pattern within the domain. Other growth profiles with similar features to the logistic growth could be used.

6.4.3 Modelling the patterned surface

The absence of any pattern on the underside of the fish at all stages of development is apparent in Figure 6.1. There appears to be a marked difference in coloration between the upper portion of the Amago on which patterns form and the patternless underside (most apparent in Figures 6.1(h)—6.1(k)). Recent experimental studies of the zebrafish have shown that some of the chromatophores (pigment cells) involved in the skin patterning of the fish originate from the neural crest on the dorsal (top) side of the fish and migrate to other parts of the fish in the embryonic state (see Kelsh [2004] and references therein). This may explain the lack of patterning on the underside of the fish if the pathways along which the chromatophores migrate do not extend to the ventral side (bottom) of the fish. Marked differences in colouring between the top and bottom of the fish and the absence of patterning on the underside of the fish is evident in many members of the Salmonidae, such as the white spotted char and the masou salmon [Miyazawa et al., 2010, Fig. 2a, 2b]. To the best of our knowledge, there is as yet no explanation for these phenomena in the Salmonidae and this clearly warrants further experimental research.

Our assumption is that the morphogens and chromatophores are only present in the patterned regions of the fish and migrate only along pathways within this patterned region i.e., we assume the domain on which the chromatophores form is limited and that these chromatophores are then triggered to produce pattern by the RDS which is posed on the same domain. From a modelling perspective, this is equivalent to assuming that there is no-flux of morphogens between the patterned and unpatterned regions. We therefore only consider the fish surface on which patterning occurs and impose a homogeneous Neumann boundary condition on the boundary surrounding this region.

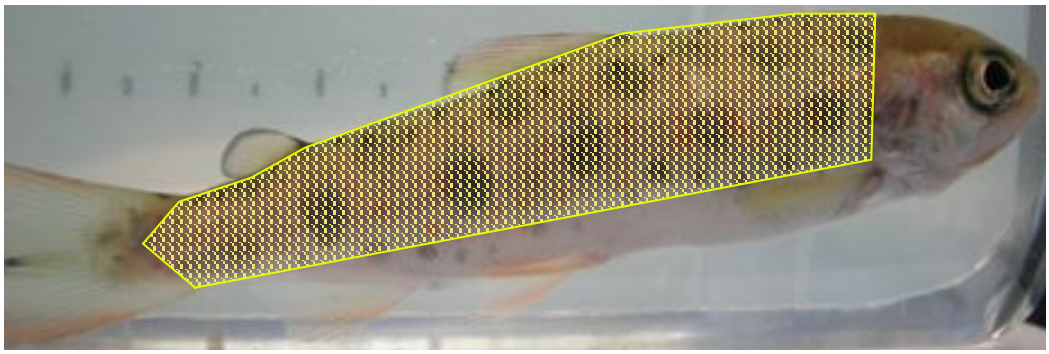

Figure 6.4: The portion of the fish that exhibits patterning, shaded in yellow. To construct an approximation to the surface of the Amago, we assume this region is symmetric about the head-tail axis of the fish and model the region by a series of surfaces with differing curvatures (Figures 6.5 and 6.7).

To model the patterned region, we first trace the portion of the two-dimensional surface of the trout on which patterns form (Figure 6.4). We assume the region is symmetric about the head-tail axis and we measure the geometry by tracing the outline of the region during the different stages of development. Our experimental observations indicate that the boundaries of the patterned portion of the fish enlarge proportionally as the fish grows. Since we assume the region as a whole grows proportionally with the fish, it is sufficient to model this surface at the initial stage of development with length and width scales that describe the skin surface of the Amago soon after hatching and then model the evolution of this surface during development with the

isotropic growth function (6.4.1). To investigate whether curvature is relevant, we first model the surface by a *planar* polygonal domain, approximating the shape of the patterned region. Figure 6.5 shows our initial triangulated planar computational domain, an approximation to the portion of the skin surface of the Amago on which patterns form (soon after hatching). We then investigate the influence of curvature by considering a series of computational domains with differing curvature, while maintaining the width and length scales which are significant in the patterning process. From inspection of the fish shape, a natural surface to investigate is a portion of the growing *elliptic cylinder* (see Figure 6.6) defined by the following parametrisation:

$$\boldsymbol{\mathcal{A}}(\boldsymbol{\xi}, t) := \rho(t) \begin{pmatrix} a\cos\left(\pi\xi_1/0.45\right) \\ b\sin\left(\pi\xi_1/0.45\right) \\ \xi_2 \end{pmatrix}, \tag{6.4.2}$$

where ξ_1 and ξ_2 are the y (width) and x (length) coordinates of the planar approximation (see Figure 6.5) and $\rho(t)$ is the logistic growth function defined in §6.4.1.

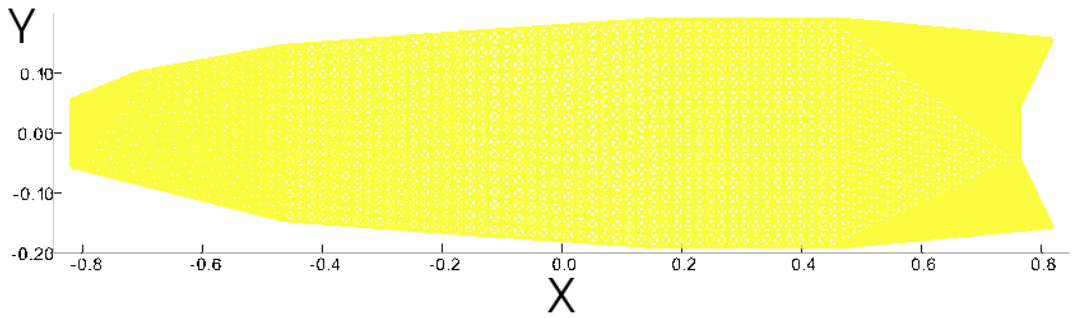

Figure 6.5: A planar approximation to the portion of the Amago trout on which patterns form. The lengths in cm represent the initial planar domain that corresponds to the surface of the Amago soon after hatching.

Since the patterning only occurs on the upper portion of the fish, we model the surface by a portion of the curved surface of the elliptical cylinder (the top half of the cylinder at its widest point). We preserve the length and width scales of the fish by constructing cylinders with the same length and width (arc length across the curved surface) as the planar triangulation. To investigate the effect of differences in curvature on pattern formation, we pick a set of values of a and b, such that the surface areas of the cylindrical surfaces obtained are approximately equal to the surface area of the planar domain.

Figure 6.7 shows the 5 different cylindrical surfaces we consider. The surfaces are shaded by the modulus of the cylindrical mean curvature, and ordered (left to right) by decreasing (modulus of) mean curvature along the central axis. The surface in the middle is the circular cylinder (of constant mean curvature). We remark that inspection of the actual fishes cross-section suggests that either the circular cylinder or the cylinder with $a = 0.14, b = 0.10$ (c.f. Figure 6.7) are the most physically realistic approximations of the fish.

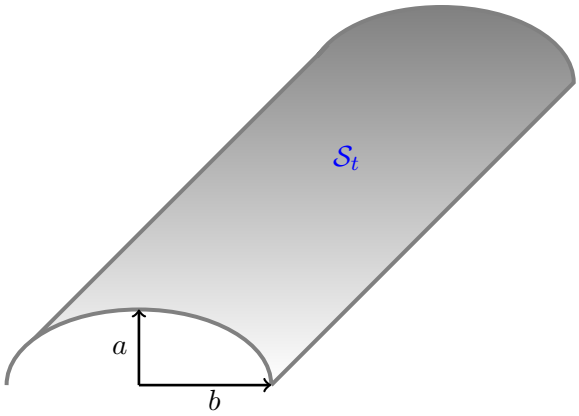

Figure 6.6: Top half of the curved surface of an elliptic cylinder.

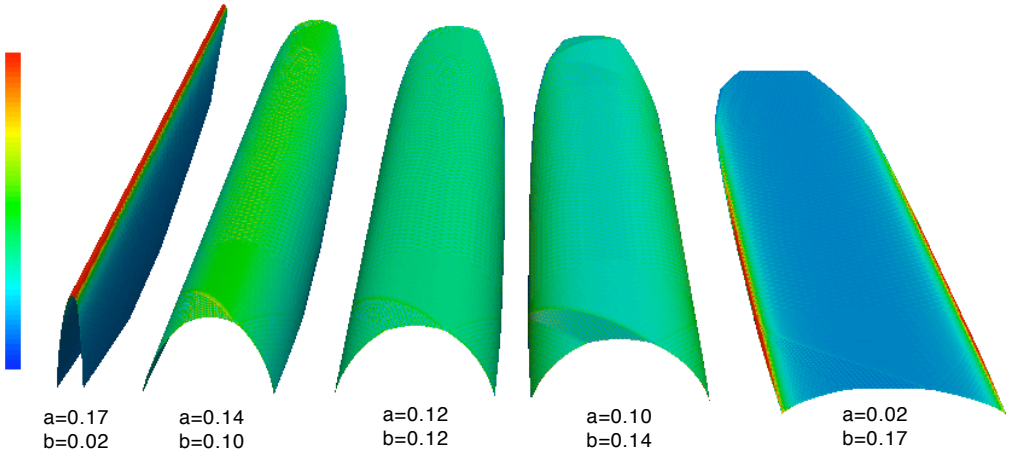

Figure 6.7: The cylindrical domains shaded by the modulus of the mean curvature.

6.4.4 Model equations

We now introduce our model, an RDS on an evolving surface. Let $\mathcal{S}_t$ be a simply connected bounded continuously deforming hypersurface embedded in $\mathbb{R}^3$ at time $t \in [0,T], T > 0$. Let $\partial\mathcal{S}_t$ be the surface boundary of $\mathcal{S}_t$. Also let $\boldsymbol{u} = \left(u_1\left(\boldsymbol{x},t\right), u_2\left(\boldsymbol{x},t\right)\right)^T$ be a vector of two chemical concentrations at position $\boldsymbol{x} \in \mathcal{S}_t$. Growth of the domain generates a flow velocity $\boldsymbol{a}(\boldsymbol{x},t)$ which we assume to be equal to the surface velocity. The generalised non-dimensionalised governing equations for an RDS on an *isotropically growing surface* were derived by Plaza et al. [2004] and take the form (see Appendix A.1 or Barreira et al. [2011] for further details):

$$\begin{cases} \partial_t u_1 + \nabla_{\mathcal{S}_t} \cdot (\boldsymbol{a} u_1) = \Delta_{\mathcal{S}_t} u_1 + \gamma f_1(\boldsymbol{u}), & \\ \partial_t u_2 + \nabla_{\mathcal{S}_t} \cdot (\boldsymbol{a} u_2) = d\Delta_{\mathcal{S}_t} u_2 + \gamma f_2(\boldsymbol{u}) & \text{in } \mathcal{S}_t, (0,T], \\ \boldsymbol{u}(\boldsymbol{x},0) = \boldsymbol{u}_0(\boldsymbol{x}), & \boldsymbol{x} \in \mathcal{S}_0, \\ [\boldsymbol{\nu} \cdot \nabla \boldsymbol{u}](\boldsymbol{x},t) = \boldsymbol{0}, & \boldsymbol{x} \in \partial\mathcal{S}_t, t > 0, \end{cases} \tag{6.4.3}$$

where d is the ratio of the diffusion coefficients, γ is a scaling parameter, $\boldsymbol{u}_0(\boldsymbol{x})$ is a well-defined positive bounded vector function. The vector $\boldsymbol{\nu}$ is the unit normal to the surface boundary $\partial\mathcal{S}_t$. The nonlinear vector valued function $\boldsymbol{f} = (f_1, f_2)^T$ represents the reaction kinetics. The only modification from the planar case is the replacement of spatial derivatives with tangential derivatives. The $\Delta_{\mathcal{S}_t} u_i$ term denotes the *Laplace-Beltrami* operator, the analogue of the Laplace operator on manifolds, defined as the divergence of the tangential gradient (see Gilbarg and Trudinger [2001, Ch 16, pg. 389]). If $\mathcal{S}_t$ is planar, then the Laplace-Beltrami operator is identical to the Laplacian and thus, from the results of Chapter 3, Problem (6.4.3) with domain growth function (6.4.1) has a classical solution (assuming the results hold on polygonal domains).

6.4.5 Remark (Isotropic growth)**.** The assumption of isotropic growth plays a central role in the model derivation. Any form of anisotropy in the growth function will affect both the dilution term (that arises when the time derivative is brought inside the integral) and crucially in this case, the curvature of the domain.

6.4.6 Remark (Alternative boundary conditions)**.** We note that without further empirical information an equally appropriate modelling assumption would have been to assume that the RDS is posed on the entire surface of the fish and some external factor suppresses patterning on the underside of the fish. This alternative modelling assumption would have major implications as we would then have to assume a domain with periodic boundaries at the sides and zero-flux boundaries at the head and tail ends or no boundary in the case of closed surfaces [Barreira et al., 2011]. Boundary conditions strongly affect the pattern formation process [Arcuri and Murray, 1986] and we shall show in the proceeding sections this effect is even more evident when curvature is included in the modelling. Further experimental evidence is needed to fully understand the appropriate boundary conditions to impose.

For our preliminary computational studies (not reported) we considered the *activator-depleted* substrate model [Gierer and Meinhardt, 1972; Lefever and Prigogine, 1968; Schnakenberg, 1979] and the Thomas [Thomas, 1975] reaction kinetics. One of the most important aspects of the patterning phenomenon is the insertion of new parr marks away from existing parr marks. This phenomenon is best captured by kinetics where new activator peaks arise due to *insertion* rather than *splitting* of existing peaks. Bifurcations on growing domains with the *activator-depleted* substrate kinetics are generally of the splitting type while the Thomas kinetics generally exhibit peak insertion [Crampin, 2000]. This was evident in our preliminary simulations and thus, we focussed on the Thomas kinetics defined as follows:

$$\begin{aligned} f_1(\boldsymbol{u}) &= \alpha - u_1 - \frac{\beta u_1 u_2}{(1 + u_1 + k u_2^2)}, \\ f_2(\boldsymbol{u}) &= c\kappa - c u_2 - \frac{\beta u_1 u_2}{(1 + u_1 + k u_1^2)}, \end{aligned} \tag{6.4.4}$$

where α, β, c, κ and k are all positive constants. It must be noted that there are many other reaction kinetics where peak splitting is observed, the celebrated Gierer-Meinhardt kinetics [Gierer and Meinhardt, 1972] being one of the most well known. Similar pattern transitions to those observed with the Thomas kinetics can arise as a result of different kinetic models where peak insertion is the dominant process.

6.4.7 Selection of parameter values

Since the morphogens that determine the patterning of the Amago trout are still unknown, the reaction kinetics we have assumed are purely hypothetical. In effect we are assuming that pat-

terning is insensitive to the physical details of the kinetics themselves, as similar patterns are generated by Turing systems with different reaction kinetics. Thus, we determined the reaction kinetic parameter values by simulating an RDS on a fixed rectangle with the same length and width scale as the fish, selecting the parameter values which best approximated the first stage of patterning of the Amago. The parameter values we selected are $\alpha = 92$, $\kappa = 64$, $k = 0.1$, $c = 1.5$, $\beta = 18.5$, $d = 9.75$ and $\gamma = 116$. With these parameter values system (6.4.3) admits a spatially homogeneous steady state $(9.93, 9.29)$ (determined by a Newton-Raphson method) valid in the absence of domain evolution. We take the initial conditions for problem (6.4.3) as small random perturbations around this homogeneous steady state.

6.5 Computer simulations

We solve the model equations (6.4.3) and (6.4.4) using the finite element method of Chapter 4. We give the details of the extension of the method to approximate the solution to RDSs on parameterisable surfaces in Appendix A.1. We only present the computed activator concentrations (u_1), the inhibitor concentrations (u_2) have been omitted as they are in phase with those of the activator. The full details of the numerical methods we use can be found in Appendix A.2.

6.5.1 Remark (Thresholding)**.** Since patterning is presumed to occur due to the morphogen concentration exceeding a certain value, the most appropriate way to visualise the results is by shading according to some threshold value. The Thomas kinetics we have used exhibit sharp gradients compared to say the Schnakenberg kinetics with similar diffusion coefficients; also the results of our simulations suggest the patterns that form with these parameter values are spots or stripes with a common amplitude. Thus, the gross pattern exhibited is relatively independent of the threshold value chosen. Although the results of the simulations appear to be relatively pixelated, this is only an artefact of the thresholding algorithm. The mesh was refined sufficiently to ensure further refinements led to only minor changes in the solution values and qualitatively the patterns expressed did not change.

6.5.2 Planar domain

Figure 6.8 shows the results of our simulation of (6.4.3) on the planar domain. We have shown snapshots of the computed activator concentrations (u_1), together with the corresponding time in days of each snapshot. The pattern transitions observed in the computer simulations are in close agreement with the transient patterns observed in Figure 6.1.

The snapshots of the simulation results at 20 and 40 days after hatching (Figures 6.8(b) and 6.8(c)) are very similar to the first parr marks that appear on the surface of the Amago towards the end of the first month (Figures 6.1(b) and 6.1(c)). At this stage of the growth development, 4 to 5 parr marks are visible along each side aligned vertically, in agreement with the experimental observations. As the computational domain grows corresponding to 60 days after hatching, new parr marks appear via insertion, Figure 6.8(d). The alignment is still primarily vertical although in the wider portions of the domain a zigzag orientation starts to appear, mirroring the experimental results in Figures 6.1(d) and 6.1(e). Further insertion of parr marks and the transition to the checkerboard configuration observed experimentally in Figures 6.1(f)—6.1(i) is clearly observable in Figure 6.8(e) as the computational domain grows. The final patterned state as the domain reaches saturation size is shown in Figure 6.8(f). We observe 3 to 4 rows (parallel to the head-tail axis) of parr marks each consisting of around 10 individual parr marks. The regular checkerboard

distribution of the parr marks is clearly evident and comparing this figure with the top-down view of Figure 6.2, we see an almost exact agreement between the final distribution of parr marks in the simulation and the observations.

The times of transition between different patterns also appear to be in accordance with the observed data with the transition from stripe-like parr marks aligned perpendicular to the head-tail axis to the checkerboard distribution of parr marks occurring between the second and fourth month after hatching both in the biological observations and the numerical simulations.

6.5.3 Cylindrical surfaces

Figure 6.9 shows the transient patterns of the activator profile, together with the corresponding time in days of each snapshot on the cylindrical surfaces. Each snapshot is arranged from bottom to top in order of increasing (modulus of) mean curvature along the central axis.

The pattern transition on the portion of the circular cylinder (middle surface) is an important benchmark for the algorithm. By construction, the portion of the circular cylinder we have considered is *isometric* to the planar domain. The Laplace-Beltrami operator is invariant under isometries as it is defined by the surface metric tensor or first fundamental form (see Appendix A.1) which is invariant under isometries [Do Carmo, 1976]. Therefore, the eigenfunctions of the Laplace-Beltrami operator on the surface of the circular cylinder under consideration are identical to the eigenfunctions of the Laplace operator on the planar domain and the pattern transitions on the circular cylinder should be identical to the planar case given identical initial conditions. Comparing Figure 6.8 and the circular cylinder (middle surface) in Figure 6.9 we see that this is indeed the case.

Generally speaking, the activator profiles on the middle 3 surfaces of Figure 6.9 are similar to the planar case with parr marks initially appearing in a vertical alignment and then reorienting into the checkerboard configuration as the surface grows. On the surface with least mean curvature along the central axis (bottom) there is a clear preference for vertical stripes (perpendicular to the head-tail axis) with the only observed pattern transition being the regular insertion of stripes as the surface grows. This is surprising as in the planar case isotropic growth would eventually lead to the reorientation of stripes or the breakdown of the stripe pattern altogether. On the surface with highest curvature along the central axis (top) there is a clear preference for spots.

Overall the number of spots (or stripes) at a given time on the surfaces in Figure 6.9 appears to increase with increasing mean curvature along the central axis, i.e., as we move from the bottom surface to the top surface. It therefore appears that on surfaces with higher curvature on the interior and smaller curvature at the boundary, patterns with higher mode-numbers (number of spots or stripes) are selected. It is worth remarking that if we had solved on the whole surface of the fish (cf. Remark 6.4.6), then the top and bottom surface would simply be rotations of each other and thus, exhibit identical patterning given identical initial conditions.

6.6 Conclusion and Discussion

Understanding the formation of spatial pattern in the early embryo is one of the central challenges in developmental biology. By virtue of their accessibility, pigmentation patterns offer a powerful paradigm model in which to propose and test various patterning hypotheses. Recent experimental evidence suggests that skin patterning in some species of fish is dynamic [Yamaguchi et al.,

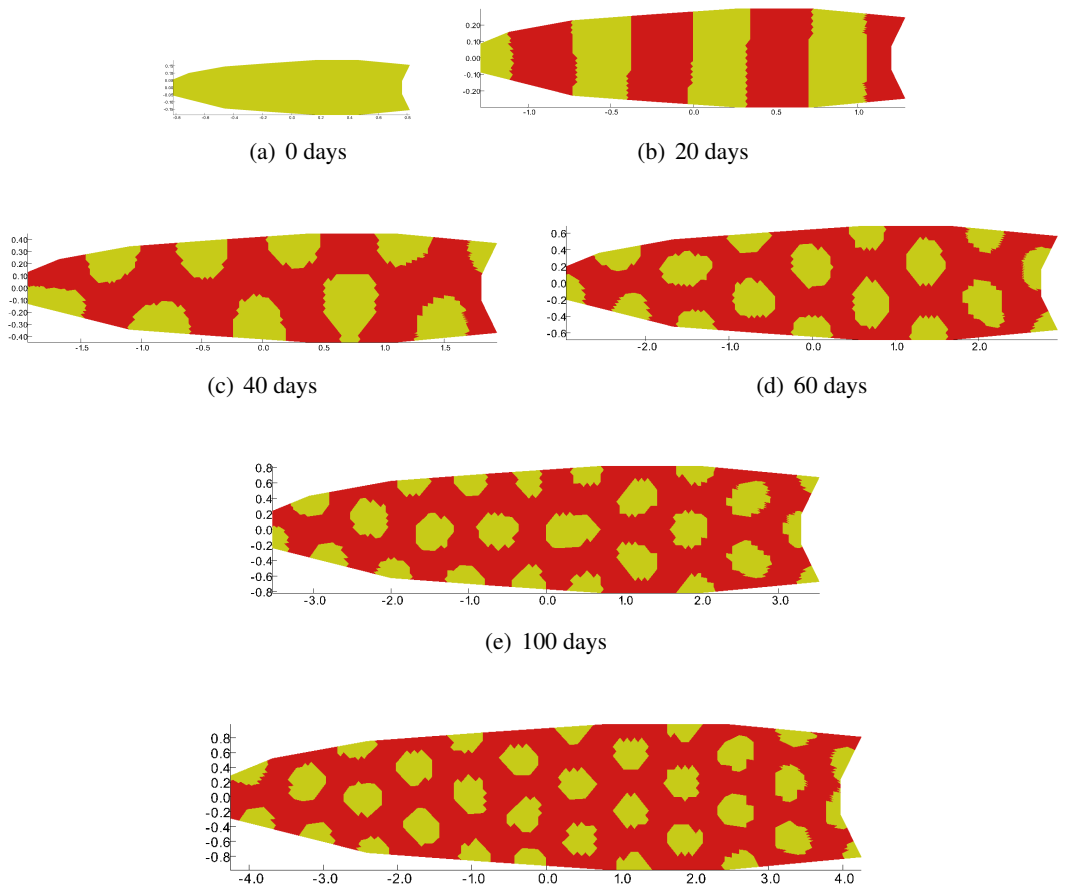

(a) 0 days

(b) 20 days

(c) 40 days

(d) 60 days

(e) 100 days

(f) 200 days

Figure 6.8: Snapshots, shaded by a threshold algorithm, of the discrete activator concentration (u_1), corresponding to the simulation of (6.4.3) on a planar domain. For parameter values see text. The simulations are in agreement with the experimental observations reported in Figure 6.1. The first pattern observed is a vertically aligned series of stripe-like parr marks with insertion of new parr marks as the domain grows. The parr marks reorient into a checkerboard configuration as the domain grows further. The number of parr marks visible at each stage of development is also in accordance with the experimental observations reported in §6.3. These patterns are relatively independent of the threshold value selected.

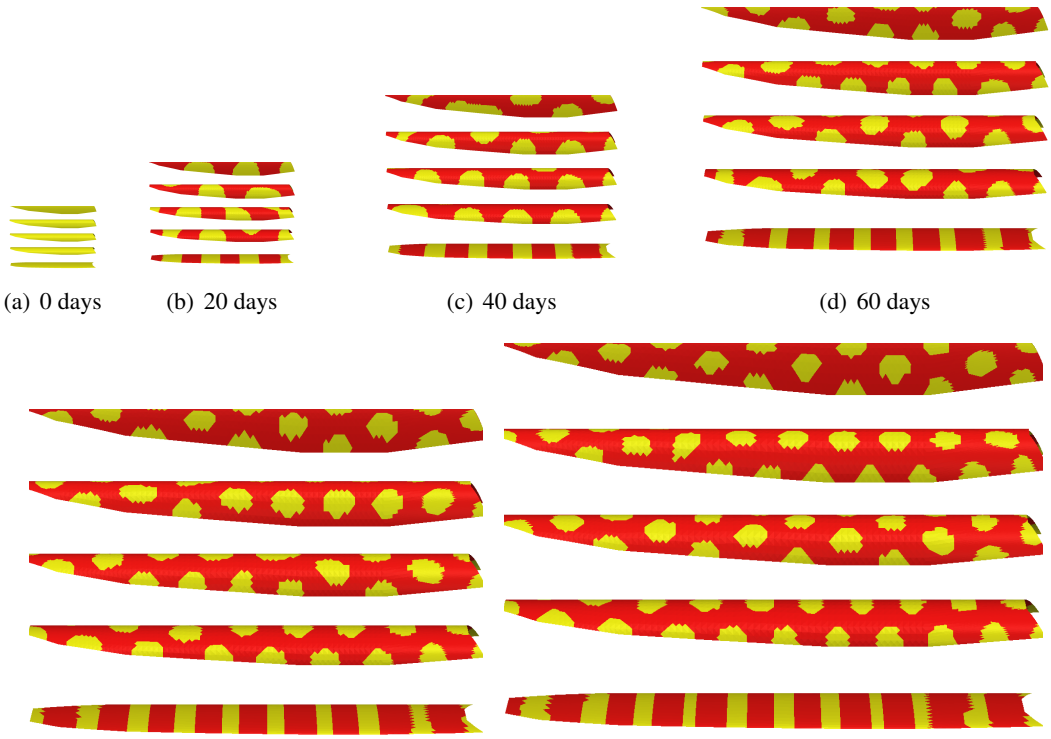

(a) 0 days (b) 20 days (c) 40 days (d) 60 days

(e) 100 days (f) 200 days

Figure 6.9: Snapshots, shaded by a threshold algorithm, of the discrete activator concentration (u_1), corresponding to the simulation of (6.4.3) on cylindrical surfaces. For parameter values see text. The timing of formation of the first patterns is identical to the planar case (Figure 6.8). The patterning on the middle three surfaces appears to be very similar to the planar case and approximates well the observed the experimental results. A striking result is the preference of stripe-like patterns with vertical alignment on the surfaces with higher curvature on the boundaries (bottom) with spots in zigzag alignment appearing to be preferred on surfaces with higher curvature along the central axis (top).

2007] i.e., fish skin patterning can be transient long after the larval stage. Fish are therefore ideally suited to the study of pattern formation as experimentalists are now able to collect data on the dynamic pattern formation behaviour from the early stages of development to adulthood. In this study we explored a reaction-diffusion model for the experimentally observed parr mark pattern formation process in the early development of the Amago trout. The assumptions we made were in the most part driven by the experimental data and an important facet of our study is the inclusion of curved surface geometry and the modelling of surface evolution of the fish. The pattern formation mechanism investigated consists of an RDS posed on a continuously evolving open curvilinear surface. The simulations indicate the importance of curvature in determining the patterns generated by RDSs and our overall conclusion is that the Turing mechanism is not inconsistent with the observed parr mark pigmentation dynamics.

The use of computer simulations of RDSs in conjunction with experimental data to approximate observed skin patterning in fish is widespread [Barrio et al., 2009; Kondo and Asai, 1995; Miyazawa et al., 2010]. The key difference between our study and existing work is that, to the best of our knowledge, this is one of the first studies that incorporates *experimentally driven modelling of growth and curvilinear geometry.* We have shown that patterns generated by an RDS can replicate experimentally observed pattern transitions, where both the growth and domain geometry are *observed experimentally and modelled mathematically*.

Our results indicate that curvature influences patterns that arise via self-organisation. For the Thomas reaction kinetics, the gross behaviour of solutions to RDSs posed on evolving surfaces is similar to the planar case with the insertion of new activator peaks as the surface evolves. However, in terms of the type of pattern generated, there does appear to be a significant sensitivity to the curvilinear geometry of the domain. In contrast to the sensitivity of RDSs to initial conditions, the sensitivity of RDSs to curvature does not appear to be ameliorated by domain evolution. We observe markedly different transient patterns on cylindrical surfaces with similar surface areas and evolution but differing nonuniform curvatures. On a circular cylinder, we observe similar transient patterns to the planar case with an initial striped pattern evolving into a spotted pattern, whereas on an evolving cylindrical surface with higher curvature on the boundary, we observe the persistence of stripes oriented perpendicular to the boundaries (where curvature is high) and no 2-dimensional patterning (spots), the pattern transitions take the form of regular stripe-insertion throughout the evolution. In light of this, further numerical investigation of RDSs posed on surfaces (other than cylinders) is warranted. Another striking result we observe is that on surfaces with higher curvature in the interior and smaller curvature at the boundary higher pattern modes are selected. This raises questions about the effect of curvature on wavenumbers of patterns that arise due to diffusion-driven instability and the linear stability analysis of RDSs posed on surfaces is an important area for future work.

Our results also suggest differences in curvature may explain some of the differences in patterning on different regions of the body surface of organisms. A tentative initial prediction we can make from the numerical results is that (at least with the reaction kinetics and cylindrical surfaces we have considered) stripes should be preferred on "flatter" regions of an organism while spots should be preferred on more "curved" regions. Consider, for example, a fish that had a striped back (dorsal portion) and spotted sides. Ogawa [2010] accounts for this type of patterning by proposing a new model of diffusion on surfaces where surface-diffusion is the limit of a three-dimensional diffusivity on an interface as the width of the interface tends to zero. Our results suggest that this difference in patterning may be explained if both the back was relatively less curved than the sides and the back and sides were effectively separate surfaces with a boundary condition at their intersection. This may explain the striped dorsal regions and spotted sides evi-

dent in many fish, such as the Char fish. We observe the persistence of a striped pattern with a fixed stripe orientation on a growing surface (the surface with least mean curvature along the central axis (bottom) in Figure 6.9). Curvature may therefore provide an explanation for the persistence of striped patterns with a fixed orientation on growing organisms, should RDSs account for skin patterning. This is an alternative hypothesis to existing studies that propose that stripe orientation in fish patterning during growth is fixed by anisotropic diffusion due to physical properties of the scales [Shoji and Iwasa, 2003; Shoji et al., 2002].

We have concentrated only on modelling the early development of the parr mark pattern formation process. After parr mark development is completed, new patterns, specifically small black and red circular spots, appear in rows parallel to the head-tail axis (Figures 6.1(j) and 6.1(k)). These new patterns generally arise around the existing parr marks. One possible extension to the model to account for this new patterning is along the lines of the model considered by Barrio et al. [2009]. They assumed a model consisting of two RDSs coupled such that the patterned state of the first system acted as a source of morphogens for the second system. The results of their simulations are similar to the new patterns observed on the Amago with new spots forming around existing spots.

There has been a plethora of recent experimental studies designed to examine the postulate of an RDS as the underlying mechanism behind patterning in fish. For example, McClure and McCune [2003] suggest that variation in patterning between zebrafish species may arise as a result of varying growth rates. Our work fits into this framework in that we have shown that experimental observations of the growth and patterning of a specific species of fish are broadly approximated by an RDS on an evolving surface. The theoretical study of RDSs provides important insight as to the likely behaviour of patterns formed by RDSs and thus, acts as an important experimental guide in hypothesis differentiation, given numerous competing hypotheses for pigmentation patterning in fish skin. It seems highly unlikely that either mathematical or experimental advances in isolation will lead to conclusive proof of the mechanism behind pattern formation. An integrative approach appears to be the way forward.

Chapter 7

Summary and Discussion

The main focus of this work is the study of RDSs as a model for spatial pattern formation on evolving domains. The main results of this work can, broadly speaking, be split into two parts. Firstly, we have presented and analysed a robust numerical method for the solution of RDSs on evolving domains, moreover our analysis gives a rigorous justification to the widespread use of numerical simulations of RDSs on evolving domains to model biological pattern formation. Secondly, our results illustrate the diverse transient patterns generated by a RDS on an evolving domain and that a RDS on an evolving surface is a feasible model of an experimentally observed pattern formation process.

To provide a mathematical foundation for the widespread use of RDSs as a model for pattern formation during growth development, we have proved the global existence of solutions to these highly nonlinear mathematical models on a class of evolving domains with no assumptions on the sign of the growth rate. We derived and analysed a numerical method for the approximation of RDSs on continuously evolving domains and given suitable assumptions on the reaction kinetics, motivated in part by the existence results, we have proved optimal convergence rates for the error in the method. To improve the efficiency of our numerical method, we derived and implemented an adaptive scheme driven by an a posteriori error estimator (valid in the space-discrete case) and an error indicator for the time discretisation.

Our results are supported by extensive computational experiments in which we seek both to validate the theoretical results and to examine some of the interesting phenomena that arise due to domain evolution, such as the effect of spatially nonuniform evolution or changes in domain shape on the solutions of RDSs on evolving domains.

In the final part of this study we investigate of parr mark pattern formation during the early development of the Amago trout. The novelties of our approach include the incorporation of realistic models of growth, geometry and curvature in the simulations made possible by the Lagrangian finite element method we utilise. The results of our study suggest a RDS is a viable model for the observed skin patterning and indicate that curvature does play an important role in determining the patterns expressed on a surface, a factor which has often been overlooked in previous studies.

We now outline possible directions for future studies:

- General evolution: The assumptions we have made on domain evolution in this work, while somewhat natural for problems posed on the surface of an organism, preclude the study of RDSs posed on evolving surfaces where the growth rate is either unknown such as stochastic or concentration-driven growth or cases where domain evolution leads to topological change in the surface. The importance of these scenarios is evident in many applications such as the

growth of solid tumours [Barreira et al., 2011] and cell motility [Stephanou et al., 2008]. Therefore, an important area for future work is the mathematical modelling of RDSs posed on surfaces with more complex evolution and the theoretical analysis of these models.

- Efficient adaptive algorithms for the solution of RDSs: We would like to extend the a posteriori error analysis presented in this study by deriving fully-discrete a posteriori error estimates for the solution of RDSs. Using a fully-discrete a posteriori error estimator, we wish to implement an efficient time-space adaptive algorithm for the solution of RDSs on continuously evolving domains.

- *Level-set* methods for RDSs posed on evolving domains or surfaces: In this study we have presented a numerical method for RDSs on evolving domains with smooth prescribed domain evolution. If we relax these assumptions on the evolution of the domain, the Lagrangian approach we use to formulate a numerical method may no longer be admissible. Numerical methods to approximate PDEs posed on surfaces or domains with evolution that results in topological change are an ongoing area of current research. One method that has proved robust in these scenarios and that we wish to implement for the solution of RDSs on evolving surfaces, is the level-set method where the evolving surface or interface is represented implicitly as a level-surface of a function [Deckelnick et al., 2005].

- The role of surface curvature in pattern formation: The results of our investigations on surfaces suggest that theoretical and experimental studies into the effect of curvature on pattern formation are warranted. We observed that changes in surface curvature strongly effect the patterns selected on a surface. An important area for future study is the linear stability analysis of RDSs posed on evolving surfaces (a natural starting point is the study of RDSs posed on fixed surfaces) and the evaluation of eigenfunctions of the Laplace-Beltrami operator on surfaces. Our results also allow the formulation of some preliminary experimental hypotheses on the role of curvature in pattern formation such as the proposition that spots should be preferred in regions of an organism that are relatively more curved with stripes on relatively flatter regions.

- Modelling skin patterning: Our results demonstrate only the feasibility but not the validity of RDSs as a model of skin patterning. To shed more light on this phenomenon we suggest experimental studies should be conducted into the transport of molecules on the surface of organisms and crucially the genetic basis of biological pattern formation. Numerical simulations of RDSs are likely to be important in this regard, as the insight they provide into possible solution behaviour can be used to devise experimental studies.

Bibliography

Acheson, D.: Elementary fluid dynamics. Oxford University Press, USA (1990).

Adams, R., Fournier, J.: Sobolev spaces, volume 140 of Pure and Applied Mathematics (2003).

Ainsworth, M., Oden, J.: A posteriori error estimation in finite element analysis. Computer Methods in Applied Mechanics and Engineering **142**(1-2), 1–88 (1997).

Ammelt, E., Astrov, Y., Purwins, H.: Stripe Turing structures in a two-dimensional gas discharge system. Physical Review E **55**(6), 6731–6740 (1997).

Arcuri, P., Murray, J.: Pattern sensitivity to boundary and initial conditions in reaction-diffusion models. Journal of mathematical biology **24**(2), 141–165 (1986).

Ascher, U.M., Ruuth, S.J., Wetton, B.T.R.: Implicit-explicit methods for time-dependent partial differential equations. SIAM J. Numer. Anal. **32**(3), 797–823 (1995). DOI http://dx.doi.org/10.1137/0732037.

Babuška, I. and Rheinboldt, W.C.: Error estimates for adaptive finite element computations. SIAM Journal on Numerical Analysis **15**, 736–754 (1978).

Baines, M.: Moving finite elements. Oxford University Press (1994).

Bänsch, E., Morin, P., Nochetto, R.: A finite element method for surface diffusion: the parametric case. Journal of Computational Physics **203**(1), 321–343 (2005).

Bard, J., Lauder, I.: How well does Turing's theory of morphogenesis work? Journal of Theoretical Biology **45**(2), 501–531 (1974).

Barrass, I., Crampin, E., Maini, P.: Mode Transitions in a Model Reaction–Diffusion System Driven by Domain Growth and Noise. Bulletin of Mathematical Biology **68**(5), 981–995 (2006).

Barreira, R., Elliott, C., Madzvamuse, A.: The surface finite element method for pattern formation on evolving biological surfaces. Journal of Mathematical Biology pp. 1–25 (2011).

Barrio, R., Baker, R., Vaughan Jr, B., Tribuzy, K., de Carvalho, M., Bassanezi, R., Maini, P.: Modeling the skin pattern of fishes. Physical Review E **79**(3), 31,908 (2009).

Barrio, R., Hernández-Machado, A., Varea, C., Romero-Arias, J., Álvarez-Buylla, E.: Flower Development as an Interplay between Dynamical Physical Fields and Genetic Networks. PloS one **5**(10), 112–114 (2010).

Barrio, R., Varea, C., Aragón, J., Maini, P.: A two-dimensional numerical study of spatial pattern formation in interacting Turing systems. Bulletin of Mathematical Biology **61**(3), 483–505 (1999).

Bendahmane, M., Saad, M.: Mathematical Analysis and Pattern Formation for a Partial Immune System Modeling the Spread of an Epidemic Disease. Acta Applicandae Mathematicae pp. 1–26 (2010a).

Bendahmane, M., Saad, M.: Mathematical analysis and pattern formation for a partial immune system modeling the spread of an epidemic disease. Acta Applicandae Mathematicae pp. 1–26 (2010b). URL `http://dx.doi.org/10.1007/s10440-010-9569-3`. 10.1007/s10440-010-9569-3.

Bergdorf, M., Sbalzarini, I., Koumoutsakos, P.: A Lagrangian particle method for reaction–diffusion systems on deforming surfaces. Journal of mathematical biology pp. 1–15 (2009).

Blowey, J., Garvie, M.: A reaction-diffusion system of λ–ω type Part I: Mathematical analysis. European Journal of Applied Mathematics **16**(01), 1–19 (2005).

Boffi, D., Gastaldi, L.: Stability and geometric conservation laws for ALE formulations. Computer methods in applied mechanics and engineering **193**(42-44), 4717–4739 (2004).

Braess, D.: Finite elements: Theory, fast solvers, and applications in solid mechanics. Cambridge Univ Pr (2001).

Brenner, S., Scott, L.: The mathematical theory of finite element methods. Texts in Applied Mathematics, vol. 15 (2002).

Brock, W., Xepapadeas, A.: Diffusion-induced instability and pattern formation in infinite horizon recursive optimal control. Journal of Economic Dynamics and Control **32**(9), 2745–2787 (2008).

Bunow, B., Kernevez, J., Joly, G., Thomas, D.: Pattern formation by reaction-diffusion instabilities: Application to morphogenesis in Drosophila. Journal of Theoretical Biology **84**(4), 629–649 (1980).

Cantrell, R., Cosner, C.: Spatial ecology via reaction-diffusion equations. Wiley (2003).

Chaplain, M., Ganesh, M., Graham, I.: Spatio-temporal pattern formation on spherical surfaces: numerical simulation and application to solid tumour growth. Journal of Mathematical Biology **42**(5), 387–423 (2001).

Chopard, B., Droz, M.: Cellular automata modeling of physical systems. Cambridge University Press Cambridge (1998).

Chueh, K., Conley, C., Smoller, J.: Positively invariant regions for systems of nonlinear diffusion equations. Indiana Univ. Math. J **26**(2), 373–392 (1977).

Clément, P.: Approximation by finite element functions using local regularization. RAIRO, Rouge, Anal. Numér. **9**(R-2), 77–84 (1975).

Cocho, G., Pérez-Pascual, R., Rius, J.: Discrete systems, cell-cell interactions and color pattern of animals. I. Conflicting dynamics and pattern formation. Journal of theoretical biology **125**(4), 419–435 (1987).

Comanici, A., Golubitsky, M.: Patterns on growing square domains via mode interactions. Dynamical Systems **23**(2), 167–206 (2008).

Crampin, E.: Reaction diffusion patterns on growing domains [PhD Thesis] (2000).

Crampin, E., Gaffney, E., Maini, P.: Reaction and diffusion on growing domains: Scenarios for robust pattern formation. Bulletin of Mathematical Biology **61**(6), 1093–1120 (1999).

Crampin, E., Gaffney, E., Maini, P.: Mode-doubling and tripling in reaction-diffusion patterns on growing domains: A piecewise linear model. Journal of Mathematical Biology **44**(2), 107–128 (2002a).

Crampin, E., Hackborn, W., Maini, P.: Pattern formation in reaction-diffusion models with nonuniform domain growth. Bulletin of mathematical biology **64**(4), 747–769 (2002b).

Crawford, J.: D4-symmetric Maps with Hidden Euclidean Symmetry. eprint arXiv: patt-sol/9310006 (1993).

Deckelnick, K., Dziuk, G., Elliott, C.: Computation of geometric partial differential equations and mean curvature flow. Acta Numerica **14**, 139–232 (2005).

Dillon, R., Maini, P., Othmer, H.: Pattern formation in generalized Turing systems. Journal of Mathematical Biology **32**(4), 345–393 (1994).

Do Carmo, M.: Differential geometry of curves and surfaces. 1976 (1976).

Donea, J., Huerta, A., Ponthot, J., Rodrıguez-Ferran, A.: Arbitrary Lagrangian-Eulerian methods. Encyclopedia of Computational Mechanics **1**, 1–25 (2004).

Estep, D., Larson, M., Williams, R.: Estimating the error of numerical solutions of systems of reaction-diffusion equations. Amer Mathematical Society (2000).

Evans, L.: A convergence theorem for a chemical diffusion-reaction system. Houston J. Math **6**(2), 259–267 (1980).

Evans, L.: Partial Differential Equations (Graduate Studies in Mathematics, Vol. 19). Dover (2009).

Formaggia, L., Nobile, F.: A stability analysis for the arbitrary Lagrangian Eulerian formulation with finite elements. East West Journal of Numerical Mathematics **7**, 105–132 (1999).

Garfinkel, A., Tintut, Y., Petrasek, D., Boström, K., Demer, L.: Pattern formation by vascular mesenchymal cells. Proceedings of the National Academy of Sciences of the United States of America **101**(25), 9247 (2004).

Garvie, M., Blowey, J.: A reaction-diffusion system of λ–ω type Part II: Numerical analysis. European Journal of Applied Mathematics **16**(05), 621–646 (2005).

Garvie, M., Trenchea, C.: Finite element approximation of spatially extended predator–prey interactions with the Holling type II functional response. Numerische Mathematik **107**(4), 641–667 (2007).

Garvie, M., Trenchea, C.: Spatiotemporal dynamics of two generic predator–prey models. Journal of Biological Dynamics **4**(6), 559—570 (2009).

Gierer, A., Meinhardt, H.: A theory of biological pattern formation. Biological Cybernetics **12**(1), 30–39 (1972).

Gilbarg, D., Trudinger, N.: Elliptic partial differential equations of second order. Springer Verlag (2001).

Gjorgjieva, J., Jacobsen, J.: Turing patterns on growing spheres: the exponential case. Dynamical Systems pp. 436–445 (2007).

Gray, P., Scott, S.: Autocatalytic reactions in the isothermal, continuous stirred tank reactor: Oscillations and instabilities. Chemical Engineering Science **39**(6), 1087–1097 (1984a).

Gray, P., Scott, S.: Isothermal autocatalysis in the CSTR: exotic stationary-state patterns (isolas and mushrooms) and sustained oscillations. Chemical instabilities: applications in chemistry, engineering, geology, and materials science p. 69 (1984b).

Gunaratne, G., Ouyang, Q., Swinney, H.: Pattern formation in the presence of symmetries. Physical Review E **50**(4), 2802–2820 (1994).

Henry, D.: Geometric theory of semilinear parabolic equations. Springer Berlin (1981).

Hestenes, M., Stiefel, E.: Methods of Conjugate Gradients for Solving Linear Systems1. Journal of Research of the National Bureau of Standards **49**(6) (1952).

Hofer, T., Maini, P.: Turing patterns in fish skin? Nature **380**(6576), 678 (1996).

Hollis, S., Martin Jr, R., Pierre, M.: Global existence and boundedness in reaction-diffusion systems. SIAM Journal on Mathematical Analysis **18**, 744 (1987).

Iron, D., Ward, M., Wei, J.: The stability of spike solutions to the one-dimensional Gierer–Meinhardt model. Physica D: Nonlinear Phenomena **150**(1-2), 25–62 (2001).

Iron, D., Wei, J., Winter, M.: Stability analysis of Turing patterns generated by the Schnakenberg model. Journal of Mathematical Biology **49**(4), 358–390 (2004).

Kelkel, J., Surulescu, C.: A weak solution approach to a reaction-diffusion system modeling pattern formation on seashells. Mathematical Methods in the Applied Sciences (2009).

Keller, E., Segel, L.: Model for chemotaxis. Journal of Theoretical Biology **30**(2), 225–234 (1971).

Kelsh, R.: Genetics and evolution of pigment patterns in fish. Pigment Cell Research **17**(4), 326–336 (2004).

Kerszberg, M., Wolpert, L.: Specifying positional information in the embryo: looking beyond morphogens. Cell **130**(2), 205–209 (2007).

Kimura, M., Komura, H., Mimura, M., Miyoshi, H., Takaishi, T., Ueyama, D.: Quantitative study of adaptive mesh FEM with localization index of pattern. Proceedings of the Czech–Japanese Seminar in Applied Mathematics (2005).

Kolokolnikov, T., Ward, M., Wei, J.: Spot Self-Replication and Dynamics for the Schnakenburg Model in a Two-Dimensional Domain. Journal of Nonlinear Science (2008).

Kolokolnikov, T., Wei, J., Winter, M.: Existence and stability analysis of spiky solutions for the Gierer-Meinhardt system with large reaction rates. Physica D: Nonlinear Phenomena **238**(16), 1695–1710 (2009).

Kondo, S., Asai, R.: A reaction–diffusion wave on the skin of the marine angelfish Pomacanthus. Nature **376**(6543), 765–768 (1995).

Kondo, S., Miura, T.: Reaction-Diffusion Model as a Framework for Understanding Biological Pattern Formation. Science **329**(5999), 1616 (2010).

Kruger, O., Picasso, M., Scheid, J.: A posteriori error estimates and adaptive finite elements for a nonlinear parabolic problem related to solidification. Computer Methods in Applied Mechanics and Engineering **192**(5-6), 535–558 (2003).

Labadie, M.: The stabilizing effect of growth on pattern formation (2008). Preprint.

Lacalli, T., Wilkinson, D., Harrison, L.: Theoretical aspects of stripe formation in relation to Drosophila segmentation. Development **104**(1), 105–113 (1988).

Ladyzhenskaya, O., Solonnikov, V., Uraltseva, N.: Linear and Quasilinear Equations of Parabolic Type.— Amer. Math. Soc., Providence, RI (1968).

Lakkis, O., Makridakis, C.: Elliptic reconstruction and a posteriori error estimates for fully discrete linear parabolic problems. Mathematics of Computation **75**(256), 1627 (2006).

Landsberg, C., Voigt, A.: A multigrid finite element method for reaction-diffusion systems on surfaces. Computing and Visualization in Science **13**(4), 177–185 (2010).

Lee, K., McCormick, W., Pearson, J., Swinney, H.: Experimental observation of self-replicating spots in a reaction-diffusion system. Nature **369**(6477), 215–218 (1994).

Lefever, R., Prigogine, I.: Symmetry-breaking instabilities in dissipative systems II. J. chem. Phys **48**, 1695–1700 (1968).

Liang, G.: A finite element method of semi-discretization with moving grid. J. Comput. Math. **4**(1), 86–96 (1986).

Mackenzie, J., Madzvamuse, A.: Analysis of stability and convergence of finite-difference methods for a reaction–diffusion problem on a one-dimensional growing domain. IMA Journal of Numerical Analysis **31**(1), 212 (2011).

Mackenzie, J., Mekwi, W.: An unconditionally stable second-order accurate ale-fem scheme for two-dimensional convection-diffusion probelms. IMA Journal of Numerical Analysis (2011). *In Print*.

Madzvamuse, A.: A Numerical Approach to the Study of Spatial Pattern Formation. Ph.D. thesis, University of Oxford (2000).

Madzvamuse, A.: Time-stepping schemes for moving grid finite elements applied to reaction-diffusion systems on fixed and growing domains. J. Comput. Phys. **214**(1), 239–263 (2006).

Madzvamuse, A.: Stability analysis of Reaction-Diffusion Systems with constant coefficients on growing domains. International Journal **1**(4), 250–262 (2008).

Madzvamuse, A., Gaffney, E., Maini, P.: Stability analysis of non-autonomous reaction-diffusion systems: the effects of growing domains. Journal of Mathematical Biology **61**(1), 133–164 (2010).

Madzvamuse, A., Maini, P.: Velocity-induced numerical solutions of reaction-diffusion systems on continuously growing domains. Journal of Computational Physics **225**(1), 100–119 (2007).

Madzvamuse, A., Maini, P., Wathen, A.: A Moving Grid Finite Element Method for the Simulation of Pattern Generation by Turing Models on Growing Domains. Journal of Scientific Computing **24**(2), 247–262 (2005).

Madzvamuse, A., Maini, P., Wathen, A., Sekimura, T., File, P.: A predictive model for color pattern formation in the butterfly wing of Papilio dardanus. Hiroshima Math. J **32**(2), 325–336 (2002a).

Madzvamuse, A., Thomas, R., Maini, P., Wathen, A.: A numerical approach to the study of spatial pattern formation in the ligaments of arcoid bivalves. Bulletin of Mathematical Biology **64**(3), 501–530 (2002b).

Madzvamuse, A., Wathen, A., Maini, P.: A moving grid finite element method applied to a model biological pattern generator. Journal of Computational Physics **190**(2), 478–500 (2003).

Maini, P.: The impact of Turing's work on pattern formation in biology. Mathematics Today **40**(4), 140–141 (2004).

Makridakis, C., Nochetto, R.: Elliptic reconstruction and a posteriori error estimates for parabolic problems. SIAM Journal on Numerical Analysis **41**(4), 1585 (2004).

Matkowsky, B., Sivashinsky, G.: Propagation of a pulsating reaction front in solid fuel combustion. SIAM Journal on Applied Mathematics **35**(3), 465–478 (1978).

McClure, M., McCune, A.: Evidence for developmental linkage of pigment patterns with body size and shape in danios (Teleostei: Cyprinidae). Evolution **57**(8), 1863–1875 (2003).

McKenna, P., Reichel, W.: Gidas–Ni–Nirenberg results for finite difference equations: Estimates of approximate symmetry. Journal of Mathematical Analysis and Applications **334**(1), 206–222 (2007).

Medina, J., Picasso, M., Rappaz, J.: Error estimates and adaptive finite elements for nonlinear diffusion-convection problems. Mathematical Models and Methods in Applied Sciences **6**(5), 689–712 (1996).

Meinhardt, H.: The algorithmic beauty of sea shells. Springer Verlag (2009).

Míguez, D., Muñuzuri, A.: On the orientation of stripes in fish skin patterning. Biophysical chemistry **124**(2), 161–167 (2006).

Miura, T., Shiota, K., Morriss-Kay, G., Maini, P.: Mixed-mode pattern in Doublefoot mutant mouse limb–Turing reaction-diffusion model on a growing domain during limb development. Journal of theoretical biology **240**(4), 562–573 (2006).

Miyazawa, S., Okamoto, M., Kondo, S.: Blending of animal colour patterns by hybridization. Nature Communications **1**(6), 1–6 (2010).

Morgan, J.: Global existence for semilinear parabolic systems. SIAM Journal on Mathematical Analysis **20**, 1128 (1989).

Morgan, J., Hollis, S.: The existence of periodic solutions to reaction-diffusion systems with periodic data. SIAM Journal on Mathematical Analysis **26**(5), 1225–1232 (1995).

Morton, K., Mayers, D.: Numerical solution of partial differential equations: an introduction. Cambridge Univ Pr (2005).

Mullins, M., Hammerschmidt, M., Kane, D., Odenthal, J., Brand, M., Van Eeden, F., Furutani-Seiki, M., Granato, M., Haffter, P., Heisenberg, C., et al.: Genes establishing dorsoventral pattern formation in the zebrafish embryo: the ventral specifying genes. Development **123**(1), 81 (1996).

Muratov, C., Osipov, V.: Stability of the Static Spike Autosolitons in the Gray-Scott Model. SIAM Journal on Applied Mathematics **62**(5), 1463–1487 (2002).

Murray, J.: How the leopard gets its spots. Scientific American **258**(3), 80–87 (1988).

Murray, J.: Mathematical biology. Springer Verlag (2003).

Murray, J., Deeming, D., Ferguson, M.: Size-dependent pigmentation-pattern formation in embryos of Alligator mississippiensis: time of initiation of pattern generation mechanism. Proceedings of the Royal Society of London. Series B, Biological Sciences **239**(1296), 279–293 (1990).

Murray, J., Maini, R.: Mechanochemical models for generating biological pattern and form in development. Physics Reports **171**(2), 59–84 (1988).

Murray, J., Myerscough, M.: Pigmentation pattern formation on snakes*. Journal of theoretical biology **149**(3), 339–360 (1991).

Myerscough, M., Maini, P., Painter, K.: Pattern formation in a generalized chemotactic model. Bulletin of mathematical biology **60**(1), 1–26 (1998).

Nagorcka, B., Mooney, J.: From stripes to spots: prepatterns which can be produced in the skin by a reaction-diffusion system. Mathematical Medicine and Biology **9**(4), 249 (1992).

Nicolis, G., Prigogine, I., Nicolis, G.: Self-organization in nonequilibrium systems: From dissipative structures to order through fluctuations. Wiley New York (1977).

Ogawa, N.: Curvature-dependent diffusion flow on a surface with thickness. Physical Review E **81**(6), 61,113 (2010).

Onishi, M., Fujibuchi, H.: Reaction-diffusion in the Cu-Sn system. Trans. JIM **16**, 539–547 (1976).

Orszag, S., Patterson, G.: Numerical simulation of turbulence. Statistical models and Turbulence pp. 127–147 (1972).

Painter, K.: Modelling of pigment patterns in fish. Mathematical Models for Biological Pattern Formation pp. 59–82 (2000).

Painter, K., Maini, P., Othmer, H.: Stripe formation in juvenile Pomacanthus explained by a generalized Turing mechanism with chemotaxis. Proceedings of the National Academy of Sciences of the United States of America **96**(10), 5549 (1999).

Pierre, M.: Global Existence in Reaction-Diffusion Systems with Control of Mass: a Survey. Milan Journal of Mathematics pp. 1–39 (2009).

Plaza, R., Sánchez-Garduño, F., Padilla, P., Barrio, R., Maini, P.: The effect of growth and curvature on pattern formation. Journal of Dynamics and Differential Equations **16**(4), 1093–1121 (2004).

Rosenberg, S.: The Laplacian on a Riemannian manifold: an introduction to analysis on manifolds. Cambridge Univ Pr (1997).

Rothe, F.: Global solutions of reaction-diffusion systems. Lecture Notes in Math **1072** (1984).

Satnoianu, R., Menzinger, M., Maini, P.: Turing instabilities in general systems. Journal of Mathematical Biology **41**(6), 493–512 (2000).

Schmidt, A., Siebert, K.: Design of adaptive finite element software: The finite element toolbox ALBERTA. Springer Verlag (2005).

Schmitt, K., Thompson, R.: Nonlinear analysis and differential equations: An introduction. Lecture Notes, University of Utah, Department of Mathematics (1998).

Schmitz, Y., Baurmann, M., Engelen, B., Feudel, U.: Pattern Formation of Competing Microorganisms in Sediments. Mathematical Modelling of Natural Phenomena **2**(4), 74–104 (2007).

Schnakenberg, J.: Simple chemical reaction systems with limit cycle behaviour. Journal of theoretical biology **81**(3), 389 (1979).

Schwab, C.: p-and hp-finite element methods: Theory and applications in solid and fluid mechanics. Oxford University Press, USA (1998).

Seirin Lee, S., Gaffney, E.: Aberrant Behaviours of Reaction Diffusion Self-organisation Models on Growing Domains in the Presence of Gene Expression Time Delays. Bulletin of Mathematical Biology pp. 1–19 (2010).

Seirin Lee, S., Gaffney, E., Monk, N.: The Influence of Gene Expression Time Delays on Gierer–Meinhardt Pattern Formation Systems. Bulletin of Mathematical Biology pp. 1–22 (2010).

Sekimura, T.: Parr mark formation in the early development of amago trout. In: CA,USA, Abstracts pp.48-49. SMB-JSMB joint meeting, San Jose. (2007a).

Sekimura, T.: Pattern Formation in Butterfly Wings: Experiments and Models. Math Everywhere pp. 207–217 (2007b).

Sekimura, T., Madzvamuse, A., Wathen, A., Maini, P.: A model for colour pattern formation in the butterfly wing of Papilio dardanus. Proceedings of the Royal Society B: Biological Sciences **267**(1446), 851 (2000).

Shiferaw, Y., Karma, A.: Turing instability mediated by voltage and calcium diffusion in paced cardiac cells. Proceedings of the National Academy of Sciences of the United States of America **103**(15), 5670 (2006).

Shoji, H., Iwasa, Y.: Pattern selection and the direction of stripes in two-dimensional Turing systems for skin pattern formation of fishes. FORMA-TOKYO- **18**(1), 3–18 (2003).

Shoji, H., Iwasa, Y., Mochizuki, A., Kondo, S.: Directionality of stripes formed by anisotropic reaction-diffusion models. Journal of theoretical biology **214**(4), 549–561 (2002).

Shoji, H., Mochizuki, A., Iwasa, Y., Hirata, M., Watanabe, T., Hioki, S., Kondo, S.: Origin of directionality in the fish stripe pattern. Developmental Dynamics **226**(4), 627–633 (2003).

Sick, S., Reinker, S., Timmer, J., Schlake, T.: WNT and DKK determine hair follicle spacing through a reaction-diffusion mechanism. Science **314**(5804), 1447 (2006).

Smoller, J.: Shock waves and reaction-diffusion equations. Springer (1994).

Solnica-Krezel, L.: Vertebrate development: taming the nodal waves. Current Biology **13**(1), R7–R9 (2003).

Sperb, R.: Maximum principles and their applications. Academic Pr (1981).

Stephanou, A., Mylona, E., Chaplain, M., Tracqui, P.: A computational model of cell migration coupling the growth of focal adhesions with oscillatory cell protrusions. Journal of theoretical biology **253**(4), 701–716 (2008).

Swindale, N.: The development of topography in the visual cortex: a review of models. Network: Computation in Neural Systems **7**(2), 161–247 (1996).

Takagi, H., Kaneko, K.: Differentiation and replication of spots in a reaction-diffusion system with many chemicals. EPL (Europhysics Letters) **56**, 145 (2001).

Takagi, I.: Point-condensation for a reaction system. Journal of differential equations **61**(2), 208–249 (1986).

Thomas, D.: Artificial enzyme membranes, transport, memory, and oscillatory phenomena. Analysis and control of immobilized enzyme systems pp. 115–150 (1975).

Thomée, V.: Galerkin finite element methods for parabolic problems, *Springer Series in Computational Mathematics*, vol. 25. Second edn. Springer-Verlag, Berlin (2006).

Turing, A. M.: The chemical basis of morphogenesis. Philosophical Transactions of the Royal Society of London. Series B, Biological Sciences **237**(641), 37–72 (1952).

Varea, C., Aragon, J., Barrio, R.: Turing patterns on a sphere. Physical Review E **60**(4), 4588–4592 (1999).

Venkataraman, C., Lakkis, O., Madzvamuse, A.: Analysis of a finite element method for semilinear reaction-diffusion systems on evolving domains. (2011a). *In preparation*.

Venkataraman, C., Lakkis, O., Madzvamuse, A.: Global existence for semilinear reaction–diffusion systems on evolving domains. Journal of Mathematical Biology pp. 1–27 (2011b). URL `http://dx.doi.org/10.1007/s00285-011-0404-x`. 10.1007/s00285-011-0404-x.

Venkataraman, C., Sekimura, T., Gaffney, E., Maini, P.K., Madzvamuse, A.: A model for parr mark pattern formation during the early development of amago trout. (2011c). *Submitted to Journal*.

Versteeg, H., Malalasekera, W.: An introduction to computational fluid dynamics: the finite volume method. Prentice Hall (2007).

Vigil, R., Ouyang, Q., Swinney, H.: Turing patterns in a simple gel reactor. Physica A: Statistical Mechanics and its Applications **188**(1-3), 17–25 (1992).

Wei, J.: Existence, stability and metastability of point condensation patterns generated by Gray-Scott system. Nonlinearity **12**(3), 593–616 (1999).

Wei, J.: Pattern formations in two-dimensional Gray–Scott model: existence of single-spot solutions and their stability. Physica D: Nonlinear Phenomena **148**(1-2), 20–48 (2001a).

Wei, J.: Spikes for the two-dimensional Gierer-Meinhardt system: The weak coupling case. Journal of Nonlinear Science **11**(6), 415–458 (2001b).

Wei, J., Winter, M.: Stationary multiple spots for reaction–diffusion systems. Journal of Mathematical Biology **57**(1), 53–89 (2008).

Wheeler, M.: A priori L 2 error estimates for Galerkin approximations to parabolic partial differential equations. SIAM Journal on Numerical Analysis **10**(4), 723–759 (1973).

Xu, G.: Discrete Laplace-Beltrami operators and their convergence. Computer Aided Geometric Design **21**(8), 767–784 (2004).

Yamaguchi, M., Yoshimoto, E., Kondo, S.: Pattern regulation in the stripe of zebrafish suggests an underlying dynamic and autonomous mechanism. Proceedings of the National Academy of Sciences **104**(12), 4790 (2007).

Zegeling, P.A., Kok, H.P.: Adaptive moving mesh computations for reaction–diffusion systems. J. Comput. Appl. Math. **168**(1-2), 519–528 (2004). DOI http://dx.doi.org/10.1016/j.cam.2003.06.013.

Zhang, K., Wong, J., Zhang, R.: Second-order implicit-explicit scheme for the Gray-Scott model. Journal of Computational and Applied Mathematics **213**(2), 559–581 (2008).

Zheng, X., Wise, S., Cristini, V.: Nonlinear simulation of tumor necrosis, neo-vascularization and tissue invasion via an adaptive finite-element/level-set method. Bulletin of mathematical biology **67**(2), 211–259 (2005).

Appendix A

Modelling Amago surface patterning

A.1 Extending the FEM to parameterisable surfaces

The model equations for a RDS on an evolving surface $\mathcal{S}_t$ can be written as [Barreira et al., 2011; Plaza et al., 2004]:

$$\frac{\mathrm{d}}{\mathrm{d}t}\int_{\mathcal{S}_t} u_i \,\mathrm{d}\mathcal{S}_t = \int_{\mathcal{S}_t} D_i \nabla_{\mathcal{S}_t}\cdot(\nabla_{\mathcal{S}_t} u_i) + f_i(\boldsymbol{u})\,\mathrm{d}\mathcal{S}_t. \tag{A.1.1}$$

We assume the surface $\mathcal{S}_t$ is parameterisable and denote by

$$\boldsymbol{\mathcal{A}} : \mathbb{R}^2 \times [0,T] \to \mathbb{R}^3, \tag{A.1.2}$$

the parameterisation. Formally, we assume there exists a reference domain $\hat{\Omega} \subset \mathbb{R}^2$ such that at each instant $t \in [0,T]$ and for each $\boldsymbol{x} \in \mathcal{S}_t$ there exists a $\boldsymbol{\xi} \in \hat{\Omega}$ such that

$$\boldsymbol{\mathcal{A}}(\boldsymbol{\xi}, t) = \boldsymbol{x}. \tag{A.1.3}$$

Moreover, we assume the parametrisation defined by $\boldsymbol{\mathcal{A}}$ is orthogonal, i.e.,

$$\partial_{\xi_1}\boldsymbol{\mathcal{A}} \cdot \partial_{\xi_2}\boldsymbol{\mathcal{A}} = 0 \text{ in } \hat{\Omega}\times[0,T]. \tag{A.1.4}$$

To construct a finite element method to approximate the solution of RDSs on parameterisable surfaces, we need the following elementary facts from differential geometry (see for example Do Carmo [1976]). The *area element* of $\mathcal{S}_t$ is given by

$$\mathrm{d}\mathcal{S}_t = \left|\partial_{\xi_1}\boldsymbol{\mathcal{A}}\right| \left|\partial_{\xi_2}\boldsymbol{\mathcal{A}}\right|. \tag{A.1.5}$$

Letting $\hat{u}_i(\boldsymbol{\xi}, t) = u_i\left(\boldsymbol{\mathcal{A}}(\boldsymbol{\xi}, t), t\right)$ then, the Laplace-Beltrami operator can be expressed on the reference frame as (see Xu [2004, (2.3)])

$$\nabla_{\mathcal{S}_t}\cdot(\nabla_{\mathcal{S}_t} u_i) = \frac{1}{2G}\nabla_{\boldsymbol{\xi}} G \cdot \left(\boldsymbol{G}^{-1}\nabla_{\boldsymbol{\xi}}\hat{u}_i\right) + \nabla_{\boldsymbol{\xi}}\cdot\left(\boldsymbol{G}^{-1}\nabla_{\boldsymbol{\xi}}\hat{u}_i\right), \tag{A.1.6}$$

where the matrix $\boldsymbol{G}$ is the matrix of coefficients of the *first fundamental form*:

$$\boldsymbol{G} = \begin{bmatrix} \left|\partial_{\xi_1}\boldsymbol{\mathcal{A}}\right|^2 & 0 \\ 0 & \left|\partial_{\xi_2}\boldsymbol{\mathcal{A}}\right|^2 \end{bmatrix}, \tag{A.1.7}$$

and

$$G = \det(\boldsymbol{g}). \tag{A.1.8}$$

Since the parameterisation is orthogonal (A.1.4), the first term on the left hand side of (A.1.6) is zero (see Xu [2004, (2.5)] for details). Thus, changing variables in (A.1.1) we obtain the following expression on the reference frame

$$\frac{\mathrm{d}}{\mathrm{d}t}\int_{\hat{\Omega}} \hat{u}_i \left|\partial_{\xi_1}\boldsymbol{\mathcal{A}}\right| \left|\partial_{\xi_2}\boldsymbol{\mathcal{A}}\right| = \int_{\hat{\Omega}} \left(D_i \nabla_{\boldsymbol{\xi}} \cdot (\boldsymbol{G}^{-1}\nabla_{\boldsymbol{\xi}} u_i) + f_i(\boldsymbol{u})\right) \left|\partial_{\xi_1}\boldsymbol{\mathcal{A}}\right| \left|\partial_{\xi_2}\boldsymbol{\mathcal{A}}\right|. \tag{A.1.9}$$

Thus, the finite element scheme to approximate $\hat{\boldsymbol{u}}$ corresponds to the finite element scheme defined in Chapter 4, where we now solve on the reference frame, with the matrix $\boldsymbol{K}$ (cf. (4.7.3)) and the determinant of the Jacobian J given by

$$\boldsymbol{K} = \begin{bmatrix} \frac{1}{\left|\partial_{\xi_1}\boldsymbol{\mathcal{A}}\right|} & 0 \\ 0 & \frac{1}{\left|\partial_{\xi_2}\boldsymbol{\mathcal{A}}\right|} \end{bmatrix}, \tag{A.1.10}$$

$$J = \left|\partial_{\xi_1}\boldsymbol{\mathcal{A}}\right| \left|\partial_{\xi_2}\boldsymbol{\mathcal{A}}\right|. \tag{A.1.11}$$

A.2 Numerical schemes for the approximation of pattern formation on the Amago

We employ a Galerkin finite element method for the spatial approximation and an implicit-explicit modified backward Euler scheme for the time integration. For the simulations on planar domains, we use the moving finite element scheme (cf. Chapter 4) which aims to find $U_1^n, U_2^n \in \mathbb{V}^n, n = 1, \cdots, N$ such that

$$\begin{cases} \frac{1}{\tau}\langle U_1^n, \Psi^n\rangle & +\langle \nabla U_1^n, \nabla \Psi^n\rangle \\ & = \gamma\left\langle \alpha - U_1^n - \dfrac{\beta U_2^{n-1} U_1^n}{1+(1+kU_1^{n-1})U_1^{n-1}}, \Psi^n \right\rangle + \dfrac{1}{\tau}\langle U_1^{n-1}, \Psi^{n-1}\rangle \\ \frac{1}{\tau}\langle U_2^n, \Psi^n\rangle & +d\langle \nabla U_2^n, \nabla \Psi^n\rangle \\ & = \gamma\left\langle c\kappa - cV_1^n - \dfrac{\beta U_1^{n-1} U_2^n}{1+(1+kU_1^{n-1})U_1^{n-1}}, \Psi^n \right\rangle + \dfrac{1}{\tau}\langle U_2^{n-1}, \Psi^{n-1}\rangle, \end{cases} \tag{A.2.1}$$

for all $\Psi^n \in \mathbb{V}^n, n = 1, \cdots, N$.

For the simulations on surfaces, the scheme we used aims to find $\hat{U}_1^n, \hat{U}_2^n \in \hat{\mathbb{V}}$, such that

$$\begin{cases} \frac{1}{\tau}\langle [J\hat{U}_1]^n - [J\hat{U}]^{n-1}, \hat{\Psi}\rangle & +\langle [J\boldsymbol{K}]^n \nabla \hat{U}_1^n, \nabla \boldsymbol{K}^n \hat{\Psi}\rangle \\ & = \gamma\left\langle \alpha - \hat{U}_1^n - \dfrac{\beta \hat{U}_2^{n-1} \hat{U}_1^n}{1+(1+k\hat{U}_1^{n-1})\hat{U}_1^{n-1}}, J^n\hat{\Psi} \right\rangle \\ \frac{1}{\tau}\langle [J\hat{U}_2]^n - [J\hat{U}_2]^{n-1}, \hat{\Psi}\rangle & +d\langle [J\boldsymbol{K}]^n \nabla \hat{U}_2^n, \nabla \boldsymbol{K}^n \hat{\Psi}\rangle \\ & = \gamma\left\langle c\kappa - cV_1^n - \dfrac{\beta \hat{U}_1^{n-1} \hat{U}_2^n}{1+(1+k\hat{U}_1^{n-1})\hat{U}_1^{n-1}}, J^n\hat{\Psi} \right\rangle, \end{cases} \tag{A.2.2}$$

for all $\hat{\Psi} \in \hat{\mathbb{V}}$.

The parameters $d, \alpha, \kappa, k, c, \beta$ and γ are as defined in (6.4.4) and J and $\boldsymbol{K}$ are as defined in (A.1.10). In both cases the finite element spaces were made up of piecewise linear basis functions. The initial data was approximated using the Lagrange interpolant. The linear systems were solved using the conjugate gradient algorithm. In both cases we took an initial triangulation $\mathcal{T}^0$ with 6897 nodes and a fixed timestep of 10^{-2}.